Deformation Processes in Great Subduction Zone Earthquake Cycles

by

Yan Hu
M.Sc., University of Victoria, 2004
B.Sc., Peking University, 1999

A Dissertation Submitted in Partial Fulfillment
of the Requirements for the Degree of

DOCTOR OF PHILOSOPHY

in the School of Earth and Ocean Sciences

Supervisory Committee

Deformation Processes in Great Subduction Zone Earthquake Cycles

by

Yan Hu
M.Sc., University of Victoria, 2004
B.Sc., Peking University, 1999

Supervisory Committee

Dr. Kelin Wang (School of Earth and Ocean Sciences)
Co-Supervisor

Dr. George D. Spence (School of Earth and Ocean Sciences)
Co-Supervisor

Dr. Stan E. Dosso (School of Earth and Ocean Sciences)
Departmental Member

Dr. Roy D. Hyndman (School of Earth and Ocean Sciences)
Departmental Member

Dr. Joanne Wegner (Department of Mechanical Engineering)
Outside Member

Abstract

Supervisory Committee
Dr. Kelin Wang (School of Earth and Ocean Sciences)
Co-Supervisor
Dr. George D. Spence (School of Earth and Ocean Sciences)
Co-Supervisor
Dr. Stan E. Dosso (School of Earth and Ocean Sciences)
Departmental Member
Dr. Roy D. Hyndman (School of Earth and Ocean Sciences)
Departmental Member
Dr. Joanne Wegner (Department of Mechanical Engineering)
Outside Member

This dissertation consists of two parts and investigates the crustal deformation associated with great subduction zone earthquake at two different spatial scales. At the small scale, I investigate the stress transfer along the megathrust during great earthquakes and its effects on the forearc wedge. At the large scale, I investigate the viscoelastic crustal deformation of the forearc and the back arc associated with great earthquakes.

Part I: In a subduction zone, the frontal region of the forearc can be morphologically divided into the outer wedge and the inner wedge. The outer wedge which features much active plastic deformation has a surface slope angle generally larger than that of the inner wedge which hosts stable geological formations. The megathrust can be represented by a three-segment model, the updip zone (velocity-strengthening), seismogenic zone (velocity-weakening), and downdip zone (velocity-strengthening). Our dynamic Coulomb wedge theory postulates that the outer wedge overlies the updip zone, and the inner wedge overlies the seismogenic zone. During an earthquake, strengthening of the updip zone may result in compressive failure in the outer wedge. The inner wedge undergoes elastic deformation. I have examined the geometry and mechanical processes of outer wedges of twenty-three subduction zones. The surface slope of these wedges is generally too high to be explained by the classical critical taper theory but can be explained by the dynamic Coulomb wedge theory.

Part II: A giant earthquake produces coseismic seaward motion of the upper plate and induces shear stresses in the upper mantle. After the earthquake, the fault is re-locked, causing the upper plate to move slowly landward. However, parts of the fault will undergo continuous aseismic afterslip for a short duration, causing areas surrounding the

rupture zone to move seaward. At the same time, the viscoelastic relaxation of the earthquake-induced stresses in the upper mantle causes prolonged seaward motion of areas farther landward including the forearc and the back arc. The postseismic and interseismic crustal deformation depends on the interplay of these three primary processes. I have used three-dimensional viscoelastic finite element models to study the contemporary crustal deformation of three margins, Sumatra, Chile, and Cascadia, that are presently at different stages of their great earthquake cycles. Model results indicate that the earthquake cycle deformation of different margins is governed by a common physical process. The afterslip of the fault must be at work immediately after the earthquake. The model of the 2004 Sumatra earthquake constrains the characteristic time of the afterslip to be 1.25 yr. With the incorporation of the transient rheology, the model well explains the near-field and far-field postseismic deformation within a few years after the 2004 Sumatra event. The steady-state viscosity of the continental upper mantle is determined to be 10^{19} Pa S, two orders of magnitude smaller than that of the global value obtained through global postglacial rebound models.

Table of Contents

List of Tables

List of Figures

Acknowledgments

First of all, I would like to thank my supervisor, **Kelin Wang**, for his invaluable guidance, inspiration and encouragements, and his patience in reviewing drafts, without which this thesis would have not been completed.

I would like to thank my committee members, **George Spence**, **Stan Dosso**, **Roy Hyndman**, **Joanne Wegner** and my external examiner, **Julia Morgan**, for their encouragements and helpful comments.

I would like to thank everyone at *Pacific Geoscience Centre, Geological Survey of Canada* for the support, especially:

Jiangheng He – for developing finite element codes and for his assistance on developing numerical models

Earl Davis, **Herb Dragert**, **Stephane Mazzotti**, **Garry Rogers**, and **Honn Kao** – for useful suggestions and discussions

Steve Taylor, **Bruce Johnson**, **Michelle Gorosh**, and **Robert Kung** – for computer support

I would like to thank the faculty and staff members at *School of Earth and Ocean Sciences, University of Victoria*, for their help and support during my Ph.D. program. I would also like to thank **David Nelles** for providing a lab-instructor Teaching Assistance (TA) position, and **Alex Vannetten** and **Alex Wong** for providing a number of TA positions.

I would also like to thank my family: my wife, **Mibo Gong**, for her endless support and encouragement, and my son **James** and daughter **Jalissa** for making the life joyful.

This thesis is dedicated to my Mom, **Wumei Chen**, and my Dad, **Guobin Hu**, for their boundless support and encouragement in the pursuit of my dreams.

Chapter 1. Introduction

1.1. Motivation and objectives

Great megathrust earthquakes are of great threat to coastal populations through generating strong ground shaking and devastating tsunami waves. Understanding the strain and stress processes associated with these earthquakes is important for hazard assessment and mitigation. Study of the deformation pattern and mechanisms is important also for understanding plate boundary dynamics.

Figure 1.1 illustrates the schematic cross-section of an active continental margin where the oceanic plate subducts beneath the continental plate. The portion of the subduction interface (the megathrust) between the two plates that produces giant earthquakes in some subduction zones is called the seismogenic zone. In the upper plate, the volcanic arc divides the overlying lithospheric plate into two parts, the forearc between the trench and the arc, and the back arc located landward of the arc. When the megathrust seismogenic zone is locked, the convergence of the two plates results in strain accumulation. The rupture of the seismogenic zone during an earthquake relieves stress that is built up before the earthquake. Repeated occurrence of earthquakes shapes the geometry of the frontal part of the forearc and causes a pattern of deformation cycle in the forearc and back arc. My Ph.D. dissertation project consists of two parts and focuses on deformation processes associated with subduction zone earthquakes at different spatial scales.

In the first part, Chapters 2 – 4, I examine the mechanics of the aseismic frontal part of the forearc where there are large accretionary prisms. As an example, cross-sections of portion of the Nankai Trough and Alaska are shown in Figure 1.2. The structure and topography of the most frontal part of the forearc, called the outer wedge, are distinctly different from those of the region further landward in most subduction zones, called the inner wedge. The surface slope angle of the outer wedge is generally larger than that of the inner wedge. Active plastic deformation is widely observed in the outer wedge (*e.g.*, *Park et al.*, 2002; *Krabbenhoft et al.*, 2004) while the inner wedge shows much less active deformation and often hosts stable sedimentary basins. The contrast of

geometry and deformation pattern between the outer and inner wedges cannot be explained by the classical critical wedge theory that relates the geometry of the wedge with the internal and basal fault strength. Permanent (plastic) deformation of the outer wedge is likely controlled by great earthquakes. The coseismic slip along the seismogenic zone together with the resistance to such slip offered by the updip aseismic portion of the fault cause compression of the outer wedge and may result in compressive failure in this region. The inner wedge undergoes mostly elastic deformation in earthquake cycles. I will investigate the strength variation and evolution of the megathrust in great earthquake cycles and their effects on the mechanics of the outer and inner wedges. The work of this part helps to understand how the geometry of the outer wedge is achieved through numerous earthquake cycles. The coseismic deformation pattern of the outer wedge as controlled by the frictional properties of the underlying subduction fault is important also to tsunami generation (*e.g.*, *Abe*, 1973; *Bilek and Lay*, 2002; *Moore et al.*, 2007a).

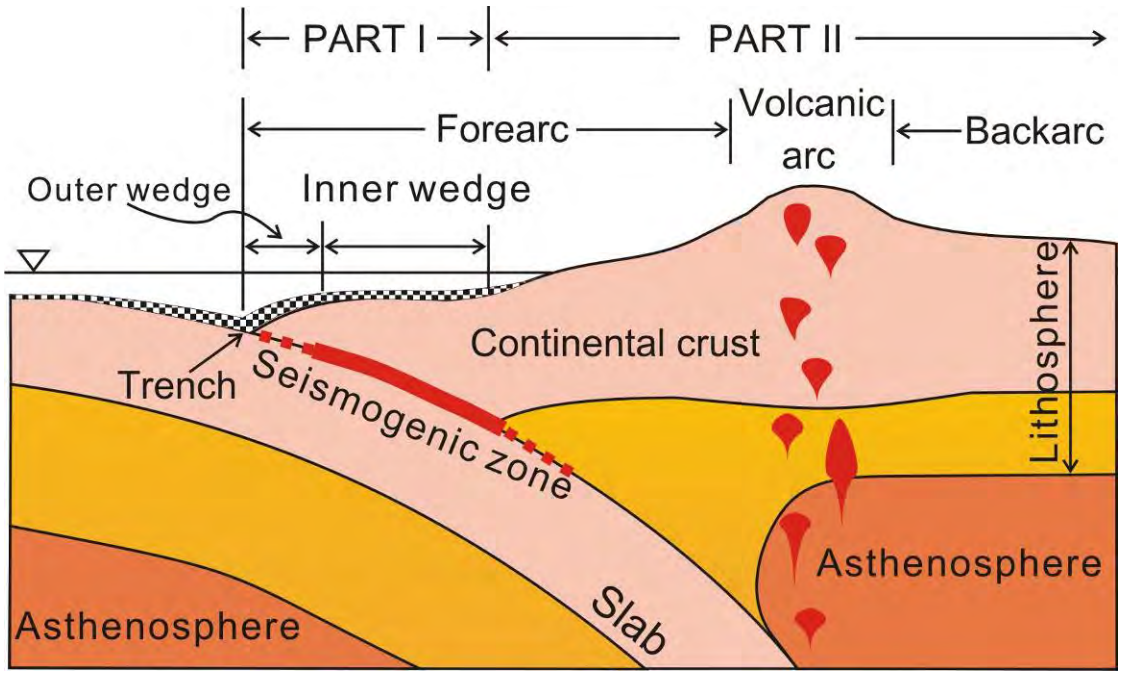

Figure 1.1. Schematic cross-section of an ocean-continent subduction zone.

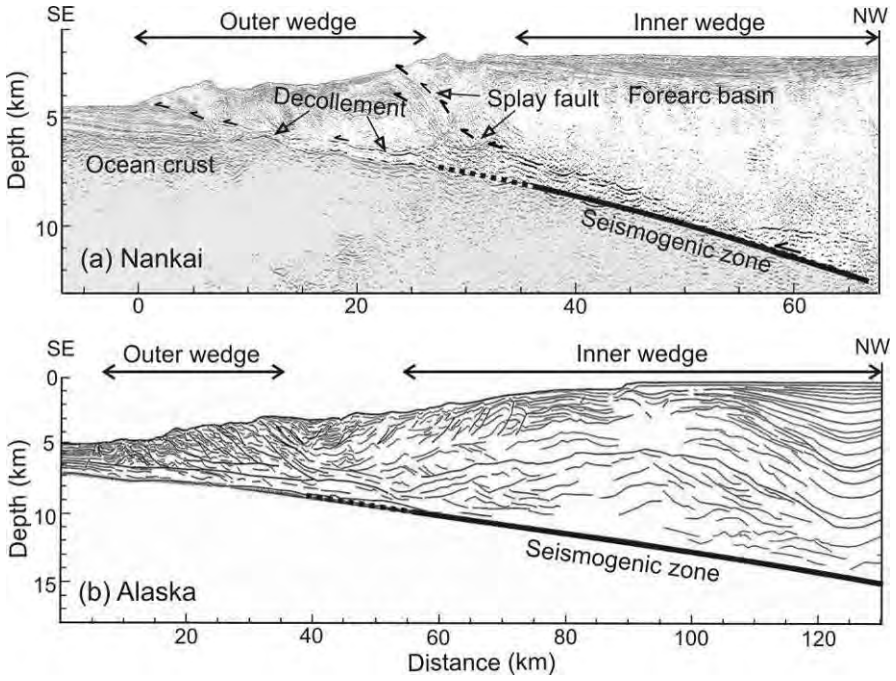

Figure 1.2. Published structure and geometry of two accretionary wedges (from *Wang and Hu*, 2006). The degree of detail depends on information provided in the original publications. The outer-inner wedge transition is narrow relative to the size of the outer wedge, but the transition cannot be defined by a vertical line. Thick black line illustrates the possible location of the seismogenic zone. (a) Nankai, based on a seismic profile off the Kii Peninsula (*Park et al*., 2002). (b) Alaska, based on a seismic profile between the Kenai Peninsula and Kodiak Island reported by *von Huene and Klaeschen* (1999), who determined that permanent shortening over the past 3 Ma occurred most within the most seaward 30-40 km (outer wedge).

The second part of this dissertation, Chapters 5 – 7, deals with viscoelastic crustal deformation in great earthquake cycles that are of a much larger scale. A sudden coseismic slip and subsequent continuous aseismic slip of the megathrust cause the upper plate to move towards the trench and also induce shear stresses in the upper mantle. For example, seaward motion has been observed at GPS stations in Sumatra where an M_w 9.2 earthquake occurred in 2004 (*e.g.*, *Chlieh et al.*, 2007; *Pollitz et al.*, 2008) (Figure 1.3a). After the earthquake, the megathrust is locked or undergoes continuous aseismic slip called afterslip. The locking of the fault causes the overlying portion of the upper plate to

move landward. At the same time, the earthquake-induced stresses relax. The stress relaxation of the mantle causes viscoelastic material flow towards the trench and results in prolonged seaward motion in the back arc and the landward portion of the forearc. Depending on the balance between the effects of the locking of the fault and stress relaxation of the mantle, the opposing motion may last less than a few years for M_w 8 earthquakes or decades for M_w 9 earthquakes. For example, the opposing motion is still observed at GPS stations in Chile more than four decades after the 1960 M_w 9.5 Chile earthquake (*e.g.*, *Hu et al.*, 2004; *Wang et al.*, 2007) (Figure 1.3b). After a long time when the earthquake-induced stresses are mostly relaxed, the effect of the locking of the fault becomes dominant, and the upper plate slowly moves landward. For example, landward motion is observed at all GPS stations in Cascadia where the last megathrust earthquake occurred more than 300 years ago in 1700 (*e.g.*, *Miller et al.*, 2001; *Mazzotti et al.*, 2003; *Wang et al.*, 2003; *McCaffrey et al.*, 2007) (Figure 1.3c).

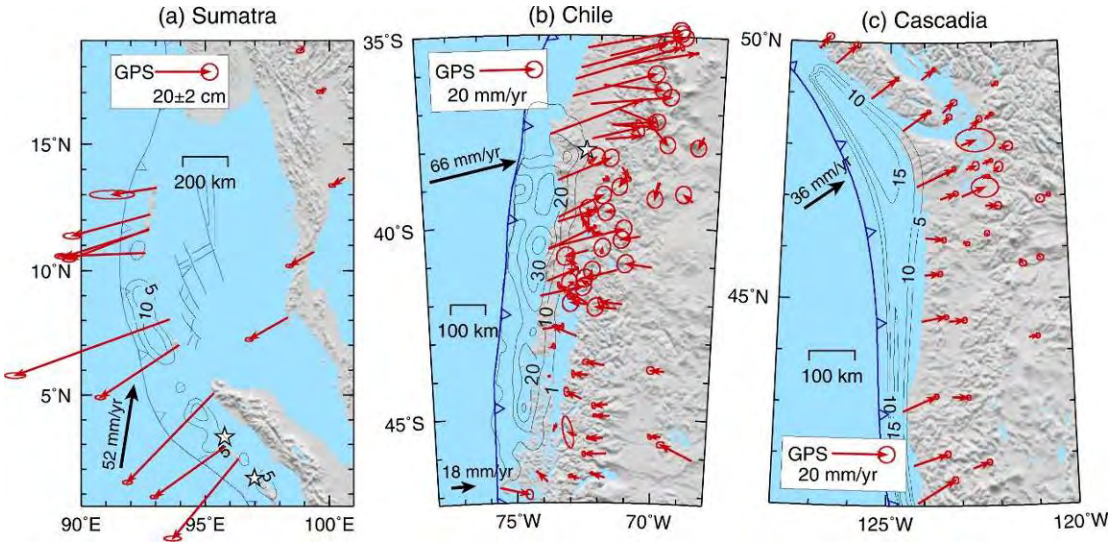

Figure 1.3. Contemporary geodetic observations in Sumatra within one year after the earthquake (a), Chile 40 years after the earthquake (b) and Cascadia 300 years after the earthquake (c). Red arrows represent GPS observations. Stars are epicentres. Contours are the coseismic slip (in meter) of the last giant megathrust earthquake that occurred in these three margins, that is, the 2004 M_w 9.2 Sumatra (*Chlieh et al.*, 2007), 1960 M_w 9.5 Chile (*Moreno et al.*, 2009), and 1700 M_w 9.0 Cascadia (*Wang et al.*, 2003) earthquakes.

Because of the limited time span of modern geodetic observations, no subduction zones have been geodetically observed for one complete earthquake cycle, particularly for giant earthquakes with recurrence intervals of centuries. However, the wealth of geodetic observations in different margins may help us link together the geodetic "snapshots" of the deformation of the earthquake cycle. Therefore, I simultaneously work on three margins, Sumatra, Chile, and Cascadia, that are presently at different stages of their earthquake cycles. In Part II, I hope to develop a unified mechanical model to unveil the underlying subduction processes that are common in convergence margins. In particular, I hope that geodetic observations at these three margins help to constrain the upper mantle viscosity and to constrain the slip evolution of the megathrust. The work of this part also helps to design the future geodetic network.

1.2. Outline of the thesis

My Ph.D. dissertation consists of two parts as discussed in previous section, and its structure is organized as follows.

The first part deals with the mechanics of the frontal part of the forearc. I use two dimensional (2D) frictional-contact finite element models to investigate the stress transfer along the megathrust during earthquakes in **Chapter 2**. In **Chapter 3**, I review the mechanics of the wedge and present the dynamic Coulomb wedge theory. On the basis of the knowledge of Chapters 2 and 3, **Chapter 4** provides the analysis of outer wedges for twenty-three margins.

The second part deals with viscoelastic finite element modelling on crustal deformation associated with subduction zone earthquakes. In **Chapter 5**, I briefly review the linear viscoelasticity, present brief descriptions on the finite element formulation, primary subduction zone processes, and the general pattern of the crustal deformation in earthquake cycles. **Chapter 6** describes the finite element model and provides comprehensive tests on model parameters. In **Chapter 7**, I use a unified mechanical model to study the contemporary crustal deformation associated with the 2004 Sumatra, 1960 Chile and 1700 Cascadia earthquakes.

In **Chapter 8**, I summarize major conclusions of this dissertation and

recommendations for future research. **Appendix A – C** provide details of the derivation of the analytical solutions and of the benchmarking of the finite element codes.

PART I: Frictional Behaviour of the Megathrust Fault and Mechanics of the Outer Wedge

This part of my dissertation deals with the mechanics of the wedge-shaped frontal forearc. Work of Part I has been published in a series of papers, *Hu and Wang* (2006), *Wang and Hu* (2006), *Wang et al.* (2006), *Hu and Wang* (2008), *Wang et al.* (2009), and *Wang et al.* (2010). This work was inspired by the pioneer efforts of *Yin* (1993) and *Yin and Kelty* (2000) who derived analytical stress solutions for uniform elastic wedges. After recognizing limitations in their papers (see discussion in Appendix B), we derived our own stress solutions with a more rigorous formulation and solution of the mechanical problems (*Hu and Wang*, 2006). Expanding the elastic wedge material with an elastic-perfectly Coulomb plastic material, we found that a subset of our stress solution is equivalent to that of the classical critical taper theory (*Davis et al.*, 1983; *Dahlen*, 1990). The critical taper theory postulates that the wedge is everywhere on the verge of plastic failure. Our solution can be used to describe the stress field of the wedge at both critical and stable states. We further examined the stress states of the wedge in earthquake cycles through the investigation of the strength change of the basal fault. We then proposed the dynamic Coulomb wedge theory that explained how the long-term deformation of the wedge is achieved during earthquake cycles (*Wang and Hu*, 2006). A static 2D frictional-contact finite element model was later developed to quantatively study the strength change of the basal fault during earthquakes (*Hu and Wang*, 2008). Based on the knowledge of the numerical modelling on the strength change and the dynamic Coulomb wedge theory, we examined the mechanics of wedges in many subduction zones (*Hu and Wang*, 2008) and the basal erosion conditions in erosional margins (*Wang et al.*, 2010). In Part I, I reorganize and reproduce these published materials. The structure and contents of Part I are based mostly on *Hu and Wang* (2008).

Wedge-shaped geological bodies are widely present at all scales, from the hanging walls of any dipping faults to accretionary prisms and thrust orogenic belts. Deformation, stress, and geometry of the wedge-shaped geological unit at the leading edge of the upper plate of subduction zones are of interest because they provide information on the frictional properties of the subduction fault. Over the past two decades, a number of models have been used to study wedge mechanics. Analytical stress solutions have been

obtained for elastic wedges (*Liu and Ranalli*, 1992; *Yin*, 1993; *Yin and Kelty*, 2000), viscous wedges (*Platt*, 1993), and critically tapered Coulomb (plastic) wedges (*Davis et al.*, 1983; *Dahlen*, 1984; *Dahlen*, 1990). Some numerical models have also dealt with the mechanics of wedge-shaped bodies with frictional basal faults (*e.g.*, *Wang and He*, 1999). Most studies investigating the mechanics of the wedge only address the long-term state of stress averaged over numerous earthquake cycles, because the wedge is assumed to be always on the verge of Coulomb failure. In 2006, we (*Wang and Hu*, 2006) proposed the dynamic Coulomb wedge theory to address the effects of stress changes along the subduction fault in great earthquake cycles on wedge mechanics.

The heterogeneity of the seismogenic behaviour of the megathrust is illustrated in Figure 1.4a. The seismogenic zone of the subduction fault exhibits a rate-weakening behaviour to produce earthquakes, that is, its frictional strength decreases with increasing slip rate. When the fault is locked, the shear stress on the seismogenic zone builds up toward the level of failure, but the stress drops to a small value during an earthquake (lower panel of Figure 1.4b). Because seismic rupture of subduction faults does not extend all the way to the trench (or deformation front of accretionary prisms), the most updip segment of the faults must have a rate-strengthening behaviour (see discussion by *Wang*, 2007). During an interseismic period when the seismogenic zone is locked, this updip segment may have little or no slip rate (*Wang and Dixon*, 2004), and hence the shear stress on the fault may become low. During an earthquake when the updip segment is forced to slip by the rupture of the downdip seismogenic zone, its strength must increase to resist slip (upper panel of Figure 1.4b) (*Marone*, 1998; *Scholz*, 1998, 2003). Direct and indirect evidence for this rate-strengthening behaviour has been summarized by *Wang and He* (2008). The segment of the fault downdip of the seismogenic zone also exhibits rate strengthening, and materials at even great depths undergo viscoelastic deformation, a subject that will be addressed in Part II of this dissertation. The updip and downdip limits of the seismogenic zone are thought usually to be thermally and petrologically controlled (*e.g.*, *Hyndman and Wang*, 1993; *Hyndman et al.*, 1997).

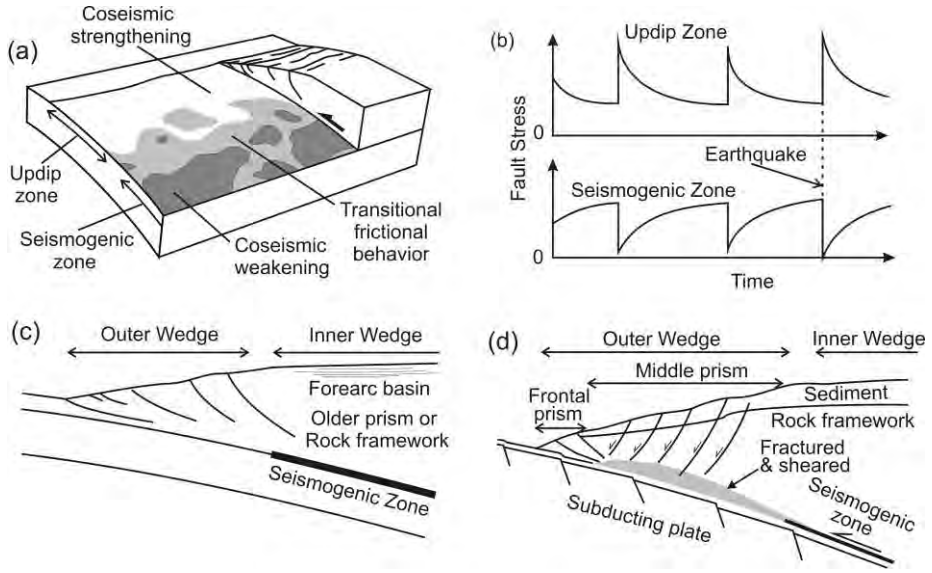

Figure 1.4. Sketch of the seismogenic behaviour of a subduction fault and main tectonic features of accretionary and erosional margins (from *Wang and Hu*, 2006; *Wang et al.*, 2010). (a) Cartoon showing spatial variations in seismogenic behaviour of a subduction fault, based on a similar figure by *Bilek and Lay* (2002). (b) Schematic illustration of shear stress variations along the two parts of the fault shown in (a). Coseismic stress drop in the seismogenic zone is accompanied with stress increase in the updip segment. (c) 2D simplification of the system shown in (a) for accretionary margins. (d) 2D simplification for erosional margins.

Subduction zones can be roughly grouped into the accretionary (Figure 1.4c) and erosional (Figure 1.4d) types (*von Huene and Scholl*, 1991; *Clift and Vannucchi*, 2004), depending on whether there is net accretion of material or continuing removal of material from the underside of the upper plate, respectively, in the recent geological past. Regardless of the difference between accretion and erosion, the most frontal part of the overlying plate, referred to as the outer wedge, features active ongoing permanent deformation, while the part further landward, referred to as the inner wedge, usually shows much less recent permanent deformation (*von Huene and Klaeschen*, 1999; *Park et al.*, 2002; *Krabbenhöft et al.*, 2004) (Figure 1.4). In addition, the surface slope of the outer wedge is generally steeper than that of the inner wedge. *Wang and Hu* (2006) postulate that the structural and topographic contrasts are associated with the frictional-

property change along the subduction fault: The outer wedge overlies the aseismic updip zone, and the inner wedge overlies the seismogenic zone (Figure 1.4). It is the coseismic strengthening of the shallow aseismic zone that repeatedly drives the outer wedge into a failure state and controls its long-term geometry.

However, the coseismic stress increase in the updip zone cannot be arbitrarily large; it is related to the size of the earthquake. Questions to be addressed include how the coseismic stress changes in different parts of the subduction fault are “coordinated” in an earthquake, what part of the shallow segment experiences strengthening during an earthquake, how much driving force an earthquake can provide to deform a wedge of given strength, and what parameters of the earthquake control the driving force.

In Part I, I first present a static 2D frictional-contact finite element model to investigate how stress is transferred from the seismogenic zone to the shallow segment during earthquakes in Chapter 2. In Chapter 3, I summarize theories of wedge mechanics in the literature including the dynamic Coulomb wedge theory that we proposed in 2006 (*Wang and Hu*, 2006). In Chapter 4, I describe the geometry of outer wedges of twenty-three subduction zones and apply the model results obtained in Chapter 2 and the theory of wedge mechanics in Chapter 3 to the analyses of the mechanics of these outer wedges.

Chapter 2. Model of Coseismic Strength Change Along the Subduction Fault

The dynamic Coulomb wedge theory postulates that the outer wedge of an accretionary prism overlies the velocity-strengthening part of the subduction fault where slip instability (earthquake nucleation) cannot occur; the inner wedge overlies the stick-slip, i.e., velocity-weakening, part of the subduction fault: the seismogenic zone (Figure 1.2). The actual coseismic behaviour of the most updip part of subduction faults has never been directly observed, but studies of tsunamis and seismic waves generated by great earthquakes all seem to indicate that subduction faults do not rupture all the way to the toe of the wedge (*Hsu et al.*, 2006; *Wang and He*, 2008). Various models have been proposed to explain the velocity-strengthening behaviour of the updip segment, such as low strength of the poorly consolidated sediments (*Byrne et al.*, 1988), presence of slippery minerals (*Hyndman and Wang*, 1993; *Hyndman et al.*, 1997; *Oleskevich et al.*, 1999; *Hyndman and Peacock*, 2003), and a combination of diagenetic, metamorphic, and hydrological conditions (*Moore and Saffer*, 2001).

In this chapter, I use a static 2D plane-strain finite element model of elastic material to model the net stress change along the fault during earthquakes. In Chapter 4, I will study the consequence of this stress change to the mechanics of the outer wedge, and the fault stress studied here will be used as a boundary condition at the base of the wedge. The strategy of separately studying the stress transfer along the fault and the mechanics of the wedge greatly simplifies the problem. A disadvantage of this separation is that the elastic stress transfer model does not account for any permanent coseismic deformation of the outer wedge and its potential nonlinear effect on fault stress. However, permanent wedge deformation during an individual earthquake is very small, and this second-order effect should introduce little error to the stress transfer modelling. Another simplification is to consider internal pore fluid pressure only in the Coulomb wedge model but ignore it in the stress transfer model. Pore fluid pressure can modify the elastic deformation in the stress transfer model only slightly, but its effect on the yield strength of a Coulomb wedge is of first order and cannot be ignored. Similarly, pore fluid pressure along the fault zone has a first-order impact on fault strength and cannot be ignored. Its effect is

included in the effective coefficient of friction μ_b' of the fault, which is the ratio of the shear strength and normal stress and is a composite parameter.

2.1. 2-D finite element model of stress transfer

In this work, the frictional behaviour of the subduction fault is described using a simple three-segment model including a rate-weakening seismogenic zone between updip and downdip rate-strengthening segments (Figure 2.1). Seismic slip along the seismogenic zone represents a sudden decrease in its frictional strength (rate-weakening) (lower panel of Figure 2.1). The aseismic updip and downdip zones experience an increase in shear stress during an earthquake, but the coseismically increased stress must relax after the earthquake. Because of rate-strengthening, the frictional strength of the segments updip and downdip suddenly increases during the earthquake to resist slip (lower panel of Figure 2.1). Therefore, the shear stress over the seismogenic zone is coseismically transferred to the updip and downdip segments. Detailed stress evolution along the fault, which can be modelled using the rate- and state-dependent friction law (*Ruina*, 1983; *Dieterich*, 1992, 1994), is dynamic and nonlinear. To investigate how the coseismic strengthening of the shallow part of the subduction fault is related to the stress drop over the seismogenic zone, we only need to know the net change in the shear stress along the fault, and we do not model the actual dynamic evolution of fault friction. It is this net change that controls the overall coseismic deformation of the overlying outer and inner wedges.

Except for a planar fault, which is sufficient for the purpose of the present work, our model setup follows that of *Wang and He* (2008). The method of Lagrange-multiplier Domain Decomposition (*Wang and He*, 1999) is used to handle the frictional contact between the two converging plates. The model boundaries are set to be very far away from the area of interest, the updip zone and seismogenic zone of the megathrust, in order to minimize potential artifacts of these boundaries. The resultant very large vertical dimension of the model domain would lead to very large lithostatic pressures at large depths and cause numerical problems to the calculation of shear stresses if gravity were directly included. Therefore, we invoke gravity (assuming a rock density of 2800 kg/m^3) only when determining yield stresses along the fault and exclude it from deformation

calculation.

Modelling of the stress transfer includes two steps, fault locking (interseismic) followed by an earthquake (coseismic). The interseismic stress build-up is modelled by moving the remote seaward and landward model boundaries towards each other against a locked fault (Figure 2.1). Based on the weak-fault arguments as summarized in *Wang and Hu* (2006), we use the effective basal friction coefficient $\mu_b' = 0.04$ (for definition of μ_b', please see (3-3b)) for the updip and seismogenic zones. The stress in the deeper creeping segment is expected to be mostly relaxed a long time after the earthquake, and we use $\mu_b' = 0.004$ to represent its perhaps finite but nearly zero strength. However, the absolute strength of the fault does not affect the model results in this section. The coseismic stress transfer depends only on the incremental change of the fault strength during the earthquake.

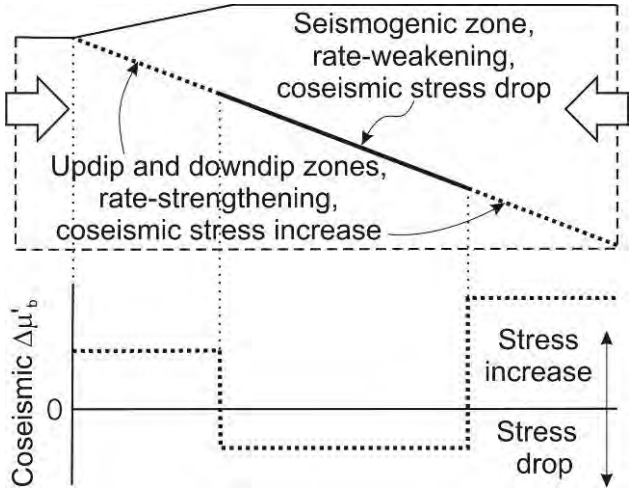

Figure 2.1. Schematic illustration of the stress transfer model considered in this work. Large arrows represent interseismic strain accumulation. An earthquake is simulated by imposing a sudden decrease in the effective friction coefficient μ_b' of the seismogenic zone by the amount of $\Delta\mu_b'$. Coseismic strengthening of the updip and downdip zones is simulated by imposing a sudden increase in their μ_b' values.

The earthquake is simulated by imposing a sudden decrease in the effective friction

coefficient of the seismogenic zone, that is, a negative $\Delta\mu_b'$ (Figure 2.1). The elastic strain accumulated in the system at the interseismic step will then cause the fault to slip. Coseismic stress drops as constrained by seismological studies vary with the types and magnitudes of earthquakes from a few KPa to a few tens of MPa (*e.g.*, *Kanamori*, 1994; *Luttreall et al.*, 2010). In this work, $\Delta\mu_b'$ along the seismogenic zone is chosen to produce a stress drop of a few MPa, typical of great subduction earthquakes. The corresponding strengthening of the updip and downdip segments is simulated by imposing a positive $\Delta\mu_b'$ (Figure 2.1). Different values of $\Delta\mu_b'$ are applied to the shallow segment updip of the seismogenic zone to represent different degrees of coseismic strengthening. The exact degree of strengthening of the aseismic segment downdip of the seismogenic zone is less important for the purpose of this study, and a sufficiently large $\Delta\mu_b'$ is used to prevent it from having any coseismic slip. This model of stress transfer is a hybrid of the frictional contact model and the classical crack model. A comparison of this model with other frequently used models for the same system is presented in Appendix A. The central part of the finite element mesh is shown in Figure 2.2a. The Coulomb wedge model to be used in Chapters 3 and 4 is illustrated in Figure 2.2b for comparison with the finite element model in this chapter.

2.2. Stress transfer and slip distribution

For a reference earthquake model, we use horizontal widths of 30 km and 120 km for the updip zone and the seismogenic zone, respectively. Based on observed average geometry of subduction zone forearcs (to be explained in Section 4.1), we assume surface slope angles α = 4º and 0º for the outer wedge and areas further landward, respectively, and a constant basal dip β = 5º for the subduction fault. Following *Wang and He* (2008), we use a moderate rigidity of 40 GPa and a Poisson's ratio of 0.25. For simplicity, uniform material properties are used, but the effects of a heterogeneous rigidity structure will be discussed in Section 2.5.3. The effects of other model parameters will be tested by varying parameter values based on the reference earthquake model. The results of the reference earthquake model are shown in both Figures 2.3a and 2.3b using solid lines.

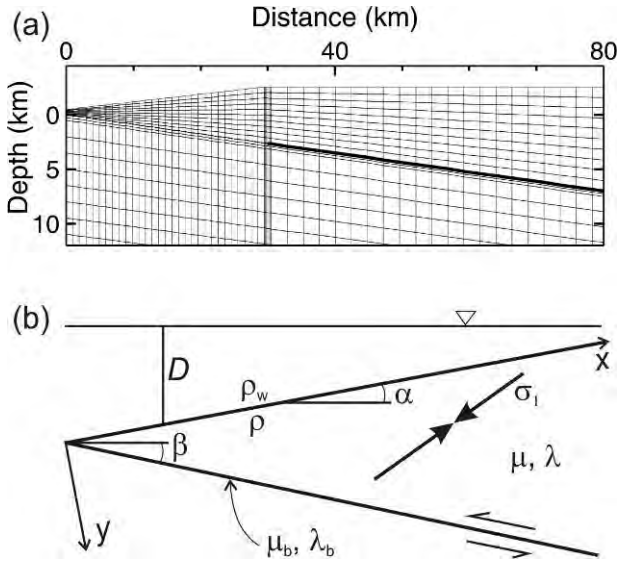

Figure 2.2. (a) Central part of the finite element mesh for the stress-transfer model. Thick solid line along the megathrust fault (≥ 30 km distance) marks the location of the seismogenic zone. (b) Illustration of the Coulomb wedge model for the most frontal part of the upper plate to be discussed in Chapters 3 and 4, showing the coordinate system (x, y), example maximum compressive stress σ_1, angles α and β, and water depth D. ρ and ρ_w are densities of the wedge material and overlying water, respectively. μ_b and λ_b are friction coefficient and pore fluid pressure ratio along the basal fault, respectively. μ and λ are internal friction coefficient and internal pore fluid pressure ratio, respectively.

For the reference earthquake, $\Delta\mu_b' = -0.01$ is applied to the seismogenic zone, leading to an average stress drop of 2.8 MPa (solid lines in Figure 2.3). A strengthening of the updip zone by $\Delta\mu_b' = 0.052$ causes the coseismic slip to taper to zero at the trench (bottom panels of Figure 2.3, solid line). If the model earthquake rupture is 500 km long in strike direction, this reference earthquake would have a moment magnitude $M_w = 8.8$. For simplicity and for the convenience of directly applying the model results to wedge mechanics in later sections, here we assume a constant $\Delta\mu_b'$ for each fault segment. The normal stress along the fault is determined mainly by the weight of the rock column above and shows little change during the earthquake, except in the vicinity of the transition between rate-strengthening and -weakening zones. The shear stress increase or

decrease with trench-normal distance follows a linear trend, indicating that the fault segments are everywhere at frictional failure. By using a heterogeneous $\Delta\mu_b'$, we could also produce a uniform stress drop along the seismogenic zone, simulating the classical crack model (see Appendix A). The abrupt stress change between the strengthening and weakening segments as shown in Figure 2.3 is the consequence of the abrupt change in $\Delta\mu_b'$ across segment boundaries. As will be discussed in Section 2.5.2, a more gradual $\Delta\mu_b'$ change between segments will lead to a smoother stress change along the fault.

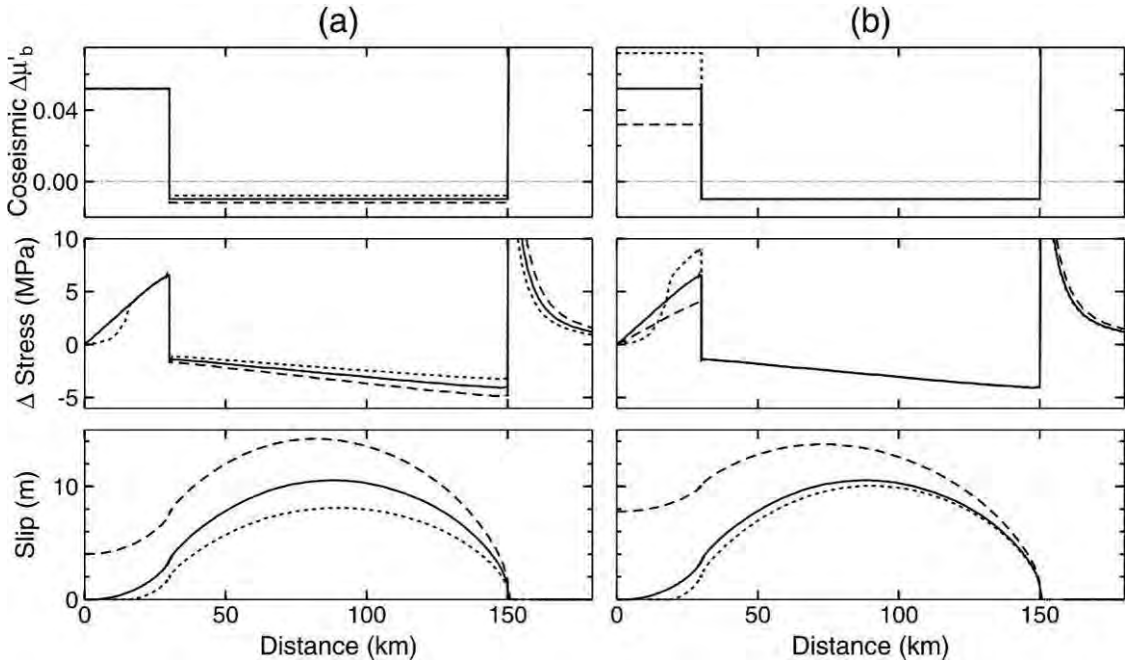

Figure 2.3. Examples to illustrate the effects of earthquake size and the degree of the coseismic strengthening of the updip zone. (a) Identical strengthening of the updip zone but different stress drops in the seismogenic zone. (b) Identical stress drop in the seismogenic zone, but different degrees of strengthening of the updip zone. Upper panels: coseismic strength change $\Delta\mu_b'$ along the fault. Middle panels: stress change. Lower panels: slip distribution. Solid lines represent the reference earthquake model. The central part of the finite element mesh for these models is shown in Figure 2.2a.

The value of coseismic $\Delta\mu_b'$ for the shallowest part of a real subduction interface is yet to be constrained by observations (discussion by *Wang and He*, 2008). To assess whether a strengthening of $\Delta\mu_b' \approx 0.05$ is unrealistically large in terms of rate- and state-dependent friction, we use this value to estimate the composite parameter (a – b) in the rate-and-state friction law using the well known equation $\Delta\mu_b' = (a-b)\ln(V_{cs}/V_0)$ (*e.g.*, *Marone et al.*, 1991; *Marone and Saffer*, 2005), where V_0 is the (nearly zero) interseismic slip rate, and V_{cs} is the coseismic peak slip rate before the slip drastically slows down due to rate strengthening. If we use $V_0 = 6.3 \times 10^{-11}$ m/s and $V_{cs} = 0.2$ m/s, parameters that *Marone et al.* (1991) used to model the rate-strengthening behaviour of the shallowest portion of a continental strike-slip fault, a $\Delta\mu_b'$ value of 0.052 leads to $(a - b) = 0.002$, well below the maximum $(a - b)$ values considered by *Marone et al.* (1991).

2.3. Coseismic strengthening of the updip zone and stress drop in the seismogenic zone

For the same degree of strengthening of the updip zone, different levels of stress drop in the seismogenic zone lead to different states of frictional failure in the updip zone. The three examples shown in Figure 2.3a have the same $\Delta\mu_b'$ value for the updip zone but different $\Delta\mu_b'$ values for the seismogenic zone. For the reference earthquake model (solid lines in Figure 2.3), the entire updip zone is at frictional failure. A larger earthquake occurring on the same seismogenic zone also pushes the entire updip zone to failure (dashed line in Figure 2.3a), but the stress increase in the updip zone is the same as for the reference earthquake. The larger earthquake does not transfer more stress to the updip zone because the stress increase in the updip zone is limited by its $\Delta\mu_b'$. Instead, the "extra" stress due to the larger earthquake causes the entire updip zone to slip for a distance. A smaller earthquake only causes a deeper portion of the updip zone to fail (dotted line in Figure 2.3a). In this case, the stress increase in this deeper portion is sufficient to resist the earthquake push, and it serves to create a stress "shadow" to protect the rest of the updip zone.

Conversely, for the same stress drop in the seismogenic zone, different degrees of strengthening of the updip zone lead to different states of frictional failure of this zone.

The three examples shown in Figure 2.3b have the same $\Delta\mu_b'$ value for the seismogenic zone but different $\Delta\mu_b'$ values for the updip zone. Given the stress drop shown in Figure 2.3b, the value of updip zone $\Delta\mu_b' = 0.052$ used for the reference earthquake model (solid lines) is the maximum strengthening with which the entire updip zone is at failure. Such a $\Delta\mu_b'$ value, denoted $\Delta\mu_{b\_c}'$, is called the critical strengthening in this work. If $\Delta\mu_b'$ is greater than $\Delta\mu_{b\_c}'$, such as 0.072, the strengthening is too large to allow the stress to be transferred to the entire updip zone, and the shallowest portion of the updip zone is in the stress shadow (dotted line in Figure 2.3b). The critical strengthening is also the minimum strengthening required to prevent the rupture from breaking the trench. If $\Delta\mu_b'$ is lower than $\Delta\mu_{b\_c}'$, such as 0.032, the resultant stress increase is too small to resist the push from the seismogenic zone, and the rupture breaks to the trench (dashed line in Figure 2.3b). Similarly, the trench-breaking rupture of the dashed-line model in Figure 2.3a indicates that the $\Delta\mu_b'$ value of 0.052 assigned to the updip zone must be smaller than the critical strengthening for the larger earthquake. The slip distribution in these two trench-breaking rupture models (dashed lines in Figure 2.3) is similar to the results obtained by *Liu and Rice* (2007) using the rate- and state-dependent friction law for a model including a small, moderately rate-strengthening updip segment.

In general, for a state with $\Delta\mu_b' \le \Delta\mu_{b\_c}'$, the whole updip zone is at frictional failure. For a state with $\Delta\mu_b' > \Delta\mu_{b\_c}'$, its shallowest part is in a stress shadow. It needs to be pointed out that for states of $\Delta\mu_b' > \Delta\mu_{b\_c}'$, potential permanent deformation of the overlying outer wedge must be localized to the area around the termination of the coseismic slip where large shear stress increase takes place (*e.g.*, the “spike” of the dotted line immediately updip of the seismogenic zone in Figure 2.3b). The exact Coulomb wedge solution (*Dahlen*, 1984; *Wang and Hu*, 2006) that we will use in later sections assumes a uniform wedge whose basal fault is either nowhere or everywhere at failure. To be able to combine the results of our finite element modelling with the Coulomb wedge solution, we focus only on the states of $\Delta\mu_b' \le \Delta\mu_{b\_c}'$. In the following sections, we mainly examine the state of $\Delta\mu_b' = \Delta\mu_{b\_c}'$, which is also representative of the states of

$\Delta\mu_b' < \Delta\mu_{b\_c}'$. States of $\Delta\mu_b' > \Delta\mu_{b\_c}'$ may sometimes be applicable to real subduction zones and will be discussed in Section 2.5.1.

2.4. Critical strengthening of the updip zone and force drop in the seismogenic zone

In this section, we investigate how the critical strengthening of the updip zone is related to the stress drop and the size of the seismogenic zone. In comparison with the reference earthquake model, we consider two models in which the seismogenic zone is either wider or narrower than the reference earthquake by 40 km (dashed and dotted lines in Figure 2.4). The seismogenic zone $\Delta\mu_b'$ values are chosen so that these two models and the reference model all have the same "force drop" ΔF, defined as the product of the average stress drop and the area of the seismogenic zone. The ΔF for all the three models shown in Figure 2.4 is identically 3.3×10^{11} N per unit strike-length. The model results show that all these models yield the same critical strengthening $\Delta\mu_{b\_c}' = 0.052$ for the updip zone (Figure 2.4a). Although these model earthquakes produce the same ΔF, their moment magnitudes are different, with the widest seismogenic zone (dotted lines) producing the largest M_w. It is the total push represented by ΔF, not M_w, that the updip zone "feels" from the seismogenic zone. $\Delta\mu_{b\_c}'$ is thus a function of ΔF only.

Further model tests reveal a linear relationship between $\Delta\mu_{b\_c}'$ and ΔF (Figure 2.5). For a given width of the updip zone, an earthquake with a larger ΔF requires a greater $\Delta\mu_{b\_c}'$ to prevent the rupture from breaking the trench. For the same earthquake force drop ΔF, a narrower updip zone requires a greater $\Delta\mu_{b\_c}'$, since a narrower updip zone is easier to be pushed to complete failure.

With the horizontal width of the updip zone fixed, Figure 2.6 shows the effects of surface slope angle α and fault dip β on $\Delta\mu_{b\_c}'$. If α is larger, the fault is more deeply buried for the same horizontal distance from the trench. The greater normal stress makes the fault stronger, and therefore a smaller $\Delta\mu_{b\_c}'$ is sufficient to prevent trench-breaking rupture (Figure 2.6a). A larger β has a similar effect on $\Delta\mu_{b\_c}'$ (Figure 2.6b). Conversely, it

is easier to drive the basal fault of a more narrowly tapered wedge to failure, and thus a greater $\Delta\mu'_{b\_c}$ is required to resist the earthquake push. Given the geometry of the system, a higher ΔF leads to a greater $\Delta\mu'_{b\_c}$, consistent with the results shown in Figure 2.5. For small-taper wedges with $\alpha + \beta < 10^{o}$, $\Delta\mu'_{b\_c}$ is greatly affected by wedge geometry as well as the earthquake force drop. For wedges with larger tapers, $\Delta\mu'_{b\_c}$ is less sensitive to further changes in wedge geometry.

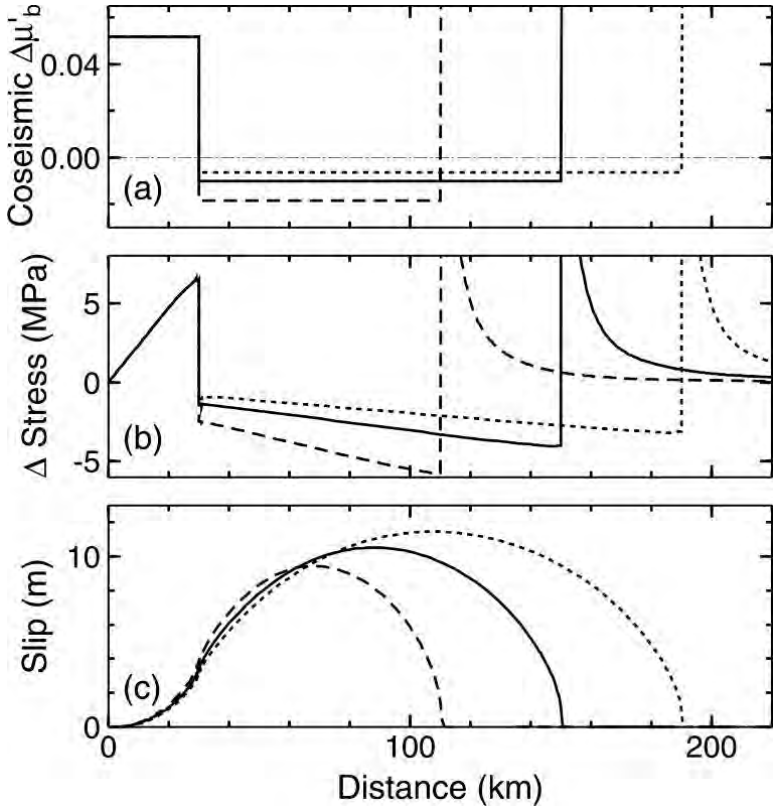

Figure 2.4. Three examples with different seismogenic zone widths but the same force drop $\Delta F = 3.3 \times 10^{11}$ N. (a) Coseismic $\Delta\mu'_b$ along the subduction fault. (b) Shear stress change along the fault. (c) Slip distribution. Results for the reference earthquake model shown in Figure 2.3 are reproduced here using solid lines. Models with seismogenic zone widths of 80 km and 160 km are represented by the dashed and dotted lines, respectively.

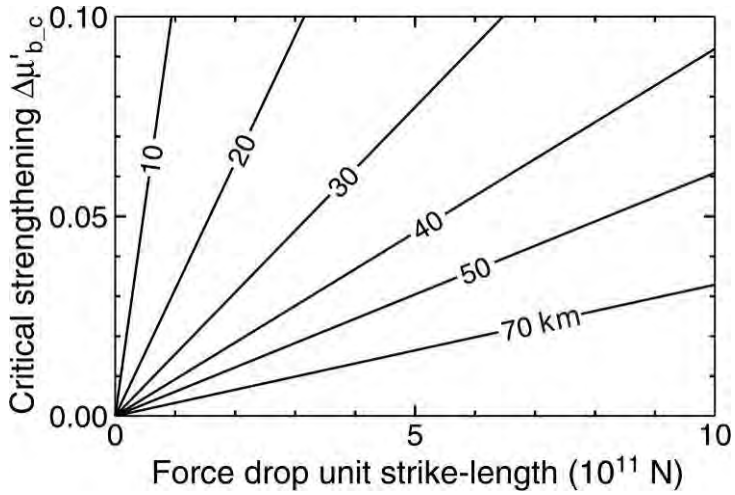

Figure 2.5. Relation of the critical strengthening $\Delta\mu'_{b\_c}$ of the updip zone with the force drop ΔF over the seismogenic zone. Given trench-normal width (km) of the shallowest updip aseismic segment (labelled on each line), $\Delta\mu'_{b\_c}$ scales linearly with ΔF.

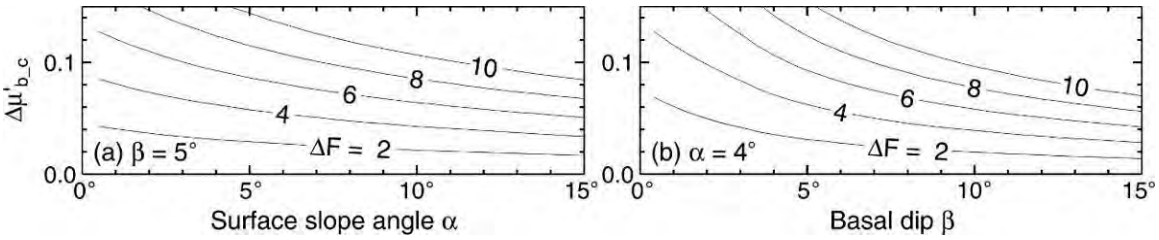

Figure 2.6. Effects of wedge geometry on the critical strengthening $\Delta\mu'_{b\_c}$ of the updip zone. (a) Effects of surface slope angle α for a fixed basal dip β = 5º. (b) Effects of β for a fixed α = 4º. Each curve represents a model with the labelled force drop ΔF ($\times 10^{11}$ N) along the seismogenic zone per unit strike length.

2.5. Discussion

2.5.1. Coseismic strengthening greater than $\Delta\mu'_{b\_c}$

In Section 2.3, we examined the effects of an earthquake rupture on the outer wedge assuming the entire updip zone of the fault is at Coulomb failure, that is, its coseismic strengthening is equal to or less than $\Delta\mu'_{b\_c}$. If the strengthening is greater than $\Delta\mu'_{b\_c}$, the

increase in shear stress takes place mainly in the deeper portion of the updip zone, and the shallower portion is in a stress shadow (*e.g.*, models represented by dotted lines in Figure 2.3). The localized large shear stress increase has two effects. First, it may cause localized compression and permanent deformation of the overlying wedge material. Repeated occurrences of the localized permanent deformation may explain the presence of an outer ridge between the outer wedge and inner wedge at some subduction zones such as Tonga. Second, relaxation of the large shear stress in this region after the earthquake will result in a delayed stress transfer to the shallower part of the updip zone that was in the stress shadow during the earthquake. This will gradually and temporarily increase compression in the more frontal part of the outer wedge. The timescale of the delayed stress transfer is an interesting subject of future research.

2.5.2. Transitional change of $\Delta\mu_b'$ between the strengthening and weakening segments

In a real subduction zone, the frictional property of the megathrust is likely to change more gradually between the updip and the seismogenic zones than portrayed by the simplified model shown in Figures 2.3 and 2.4. To demonstrate the effect of a more gradual change, we compare the reference earthquake model with a model in which the strengthening of the updip zone ($\Delta\mu_b' > 0$) linearly changes to the weakening of the seismogenic zone ($\Delta\mu_b' < 0$) over a horizontal distance of 20 km (Figure 2.7a). Other model parameters are the same as in the reference earthquake model. The transitional change of $\Delta\mu_b'$ leads to a stress change that is less abrupt than in the reference earthquake model (Figure 2.7b). The addition of this transition makes the seismogenic zone slightly narrower, and the resultant smaller force drop in the seismogenic zone is unable to push the updip zone into complete failure given the same degree of strengthening. Except for these minor details, the abrupt changes in $\Delta\mu_b'$ assumed in Sections 2.2 – 2.4 do not significantly bias the results. However, in reality, the more gradual stress change may result in a more gradual change in the topography between the outer and inner wedges over numerous earthquake cycles. In some accretionary margins, such as Alaska, Barbados, and Kurile, the surface slope angle of the outer wedge changes to the smaller

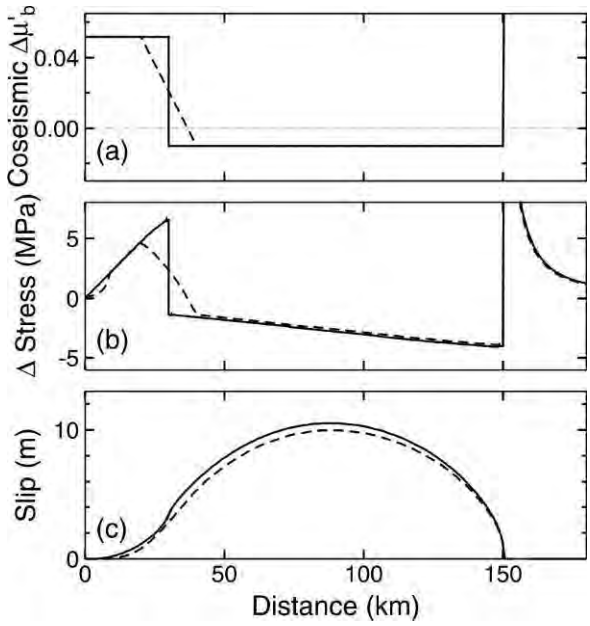

Figure 2.7. An example (dashed line) illustrating the effects of a more gradual change in fault friction than assumed for the reference earthquake model shown in Figures 2.3 and 2.4 (reproduced here also using solid lines). (a) Coseismic strength change $\Delta\mu_b'$ along the fault. (b) Shear stress change along the fault. (c) Slip distribution.

value of the inner wedge indeed very gradually.

2.5.3. Effects of rigidity

A moderate rigidity 40 GPa is used for all the tests in Sections 2.2 – 2.4. Here we investigate how material rigidity affects the results of the stress transfer modelling. In comparison with the reference earthquake model, we consider two models of different rigidity values (Figure 2.8). The rigidity in one of them is assumed to be 20 GPa (dashed lines), similar to what was used by *Geist and Bilek* (2001), and in the other assumed to be 60 GPa (dotted lines), similar to the Preliminary Reference Earth Model (*Dziewonski and Anderson*, 1981). Because of the same fault-strength decrease over the same seismogenic zone, the three earthquake models have the same stress drop and hence force drop. The same force drop gives rise to larger deformation in a material of lower rigidity and hence greater maximum slip along the fault. However, $\Delta\mu_{b\_c}'$ of the updip zone in these three

models are identically 0.052, unaffected by the changes in rigidity.

For a model with the rigidity linearly increasing from 20 GPa at the surface to 60 GPa at depths of ≥ 30 km (grey line in Figure 2.8), the shallowest portion of the updip zone is in the stress shadow, indicating that its $\Delta\mu'_{b\_c}$ must be smaller than 0.052, consistent with the slightly smaller force drop ΔF. Another slight difference of this model from the other models is that the slip distribution is skewed towards the trench (grey line in Figure 2.8c). This is because a fault in the more rigid deeper part of the model tends to slip less than in the less rigid shallower part.

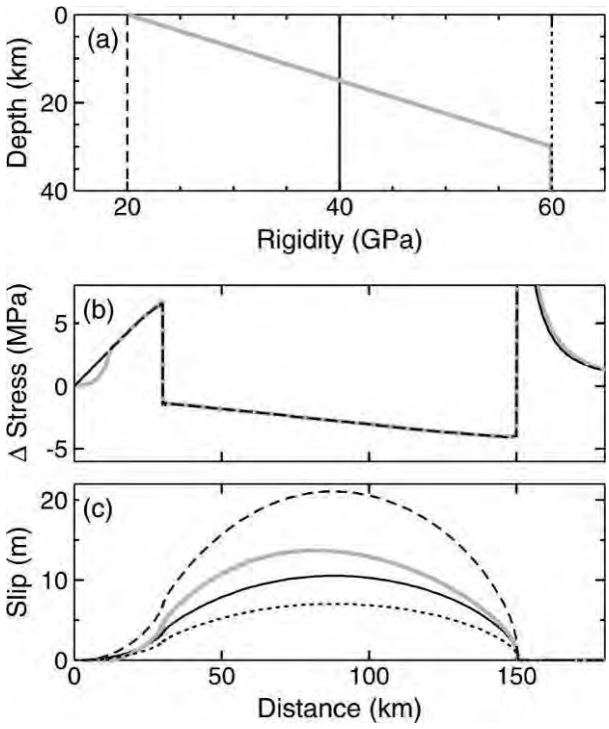

Figure 2.8. Examples to illustrate the effects of material rigidity. (a) Four rigidity models. (b) Stress change along the fault. (c) Slip distribution. Dashed, solid, and dotted dark lines represent models of uniform rigidities 20 GPa, 40 GPa (the reference earthquake model), and 60 GPa, respectively. Grey lines represent a model in which the rigidity increases with depth.

Chapter 3. Wedge Mechanics

In Chapter 2, I have described models that quantify stress transfer along the subduction fault during earthquakes. Here I briefly review the wedge mechanics theory to explain how stresses and stress changes along the fault control the stress field of the overlying wedge. In this chapter, I first summarize the classical Coulomb wedge theory. Then I will present a new stress function solution of an elastic perfectly-Coulomb-plastic wedge and the work of the dynamic Coulomb wedge theory (*Hu and Wang*, 2006; *Wang and Hu*, 2006).

3.1. Classical Coulomb wedge theory

As applied, the classical Coulomb wedge theory describes an end-member scenario in which the subduction fault slips at a constant shear stress and the wedge is in a critical state. Except for the situation of purely aseismic subduction, the theory is understood to address a long-term process averaged over numerous earthquake cycles. Some of the applications to submarine wedges are summarized in Table 3.1.

Table 3.1. Some applications of classical Coulomb wedge theory to submarine wedges.

Reference	Subduction Zones	μ	μ_b	Notes
Davis et al. (1983)	Japan, Java, Sunda, Peru, Makran, Aleutian, Barbados, Oregon	1.03	0.85	$\lambda = \lambda_b$
Dahlen (1984)	Above + Guatemala	1.1	0.85	$\lambda = \lambda_b$
Zhao et al. (1986)	Mostly Barbados	0.85, 0.4	0.85, 0.4	$\lambda = \lambda_b, \mu = \mu_b$
Davis and von Huene (1987)	Aleutian	0.45	0.3-0.45	$\lambda \leq \lambda_b$
Dahlen (1990)	Barbados	0.27-1.57	0.27-0.85	$\lambda = \lambda_b = 0.95$
Breen and Orange (1992)	Barbados	0.45-1.1	0.45,0.85	
Lallemand et al. (1994)	21 trenches	0.52	$\mu_b' = 0.029$	$\lambda = 0.88$
Adam and Reuther (2000)	Northern Chile	0.7	0.7	$\lambda, \lambda_b \leq 0.83$
Kukowski et al. (2001)	Makran	0.42	0.22	$\lambda = 0.42$-0.6
Saffer and Bekins (2002)	Mexico, Cascadia, Nankai, Nankai	0.85	0.55, 0.85	$\lambda = \lambda_b$ (variable)
Haywood et al. (2003)	Barbados	0.85	0.85	$\lambda \approx$ hydrostatic
Kopp and Kukowski (2003)	Sunda	0.31	0.135	$\lambda \approx \lambda_b = 0.47$

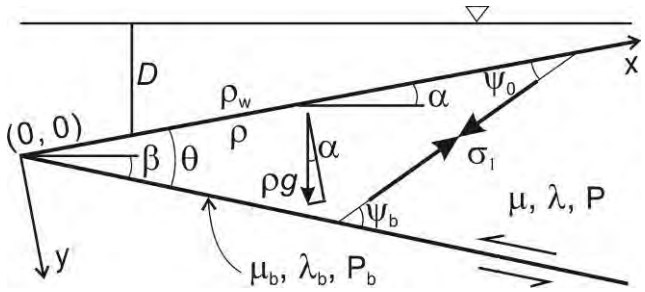

Figure 3.1. Coulomb wedge model for the outer wedge showing the coordinate system (x, y), maximum compressive stress σ_1, angles α, β, θ, ψ_b, ψ_0, pore fluid pressure within the wedge P and along the basal fault P_b, internal (λ) and basal (λ_b) pore fluid pressure ratio, coefficients of internal μ and basal μ_b friction. ρ and ρ_w are densities of the wedge material and overlying water, respectively, and g is gravitational acceleration.

Here I summarize the widely used exact stress solutions of *Dahlen* (1984) and *Zhao et al.* (1986), although various simpler or more refined analytical and numerical versions are also available (*Davis et al.*, 1983; *Dahlen et al.*, 1984; *Fletcher*, 1989; *Dahlen*, 1990; *Breen and Orange*, 1992; *Willett et al.*, 1993; *Wang and Davis*, 1996; *Enlow and Koons*, 1998). Exactly the same formulation will be used for our new stress solution in Section 3.2.

Consider a two-dimensional wedge with an upper slope angle α and basal dip β in the (x, y) coordinate system illustrated in Figure 3.1. The wedge is subject to gravitational force ρg per unit volume, where ρ is the density of the wedge material and g is gravitational acceleration. Pore fluid pressure P within the wedge is parameterized using a generalized Hubbert-Rubey fluid pressure ratio defined as (*Dahlen*, 1984)

$$\lambda = \frac{P - \rho_w g D}{-\sigma_y - \rho_w g D} \tag{3-1}$$

where D and ρ_w are water depth and density (ρ_w = 0 for a subareal wedge), respectively, and σ_y is normal stress in the y direction (negative if compressive). A similar definition of the pore fluid pressure ratio λ_b along the fault had been proposed by *Wang et al* (2006):

$$\lambda_b = \frac{P_b - \rho_w g D + \lambda H}{-\sigma_y - \rho_w g D + H} \tag{3-2a}$$

$$H = \frac{\sigma_y - \sigma_n}{1-\lambda} \tag{3-2b}$$

where P_b is pore fluid pressure along the basal fault. The definition (3-2) allows us to establish a precise relationship between the shear stress τ_n along the fault and the effective normal stress $\overline{\sigma}_n (= \sigma_n + P)$ just above the fault. The relationship between τ_n and $\overline{\sigma}_n$, stemming from the Coulomb friction criterion for the subduction fault, can be written as (*e.g.*, *Byerlee*, 1978)

$$\tau_n = -\frac{\mu_b (1-\lambda_b)}{1-\lambda}(\sigma_n + P) = -\mu_b' \frac{\overline{\sigma}_n}{1-\lambda} \tag{3-3a}$$

where $\mu_b = \tan\varphi_b$ is the friction coefficient along the fault with φ_b being angle of the basal friction, and μ_b' is the effective friction coefficient along the fault defined as

$$\mu_b' = \tan\varphi_b' = (1-\lambda_b)\mu_b \tag{3-3b}$$

Note that in *Dahlen* (1984), *Hu and Wang* (2006), *Wang and Hu* (2006), and *Wang et al.* (2006), parameter $\mu_b'/(1-\lambda)$ was called the effective friction coefficient and denoted μ_b'. A negative μ_b' represents a normal fault (*Xiao et al.*, 1991).

If the wedge is uniformly Coulomb-plastic with its cohesion proportional to depth and is everywhere on the verge of failure, an exact stress solution can be obtained (*Zhao et al.*, 1986). If we write cohesion S_0 in the following form,

$$S_0 = \eta(1-\lambda)\mu\rho g y \cos\alpha \tag{3-4}$$

where the cohesion gradient η is a dimensionless constant and $\mu = \tan\varphi$ is the coefficient of internal friction, the solution of *Zhao et al.* (1986), in terms of effective stresses, can be written as

$$\overline{\sigma}_x = -m^c(1-\lambda)\rho g y \cos\alpha \tag{3-5a}$$

$$\overline{\sigma}_y = -(1-\lambda)\rho g y \cos\alpha \tag{3-5b}$$

$$\tau_{xy} = (1-\rho')\rho g y \sin\alpha \tag{3-5c}$$

where

$$m^c = 1 + \frac{2(1+\eta)}{\csc\varphi \sec 2\psi_0^c - 1} \tag{3-6a}$$

$$\rho' = \rho_w / \rho \tag{3-6b}$$

with ψ_0^c being the uniform angle between the most compressive principal stress σ_1 and the upper surface and *c* denoting a critical wedge. ψ_0^c is given by the following relation

$$\frac{\tan 2\psi_0^c}{\csc\varphi\sec 2\psi_0^c - 1} = \frac{\tan\alpha'}{1+\eta} \tag{3-7}$$

where

$$\tan\alpha' = \frac{1-\rho'}{1-\lambda}\tan\alpha \tag{3-8}$$

is the constant ratio of $\tau_{xy}/\left(-\overline{\sigma}_y\right)$ ("modified surface slope" in *Dahlen* (1984)). Note that $\overline{\sigma}_x = m^c\overline{\sigma}_y$, $\tau_{xy} = -\overline{\sigma}_y\tan\alpha'$, and $S_0 = -\eta\mu\overline{\sigma}_y$. The taper angle of the critical wedge is

$$\alpha + \beta = \psi_b^c - \psi_0^c \tag{3-9}$$

where ψ_b^c is the angle between σ_1 and the basal surface and is directly related to μ_b' as well as μ. For η = 0, the above solution reduces to that of a noncohesive Coulomb wedge earlier obtained by *Dahlen* (1984).

3.2. Stress function solutions of an elastic perfectly-Coulomb-plastic wedge

In the classical theory, the wedge is perfectly Coulomb-plastic. The Coulomb failure criterion defines a yield surface in the stress space, and the solution (3-5) describes the state of stress on this yield surface. Beyond the yield surface, the wedge is unstable. Within the yield surface, the wedge is stable, but the stress is not defined because no constitutive relation has been specified for the stable regime.

The most reasonable candidate for the constitutive relation of a stable wedge is that of linear elasticity. Assuming elastic behaviour for the stable regime, *Wang and Hu* (2006) define an elastic – perfectly Coulomb-plastic rheology for the wedge. The stress-strain relationship for this rheology is schematically illustrated in Figure 3.2. In the elastic loading phase leading up to failure (point A), stress increases linearly with strain, following Hooke's law. When the stress reaches the yield envelope (point B), further deformation is perfectly plastic, and the stress stays constant, as represented by the flat line. This state (point B or B') is described by the critical wedge solution of (3-5). Upon unloading, the wedge returns to the elastic state (*e.g.*, point A'). The state of stress in the

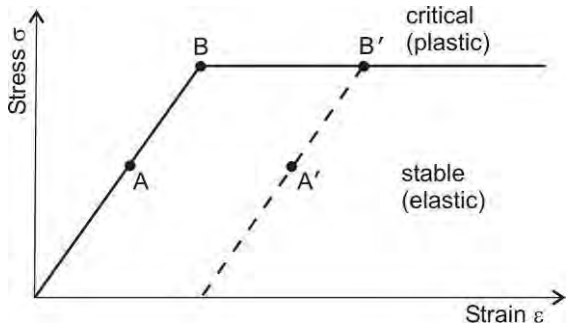

Figure 3.2. Schematic illustration of stress-strain relation for an elastic – perfectly plastic material (from *Wang and Hu*, 2006). Points A and A' are in the elastic regime. Despite a difference in permanent strain, they have an identical state of stress that can be described using an elastic solution. Points B and B' are in the plastic regime (*i.e.*, in a critical state). They also have an identical state of stress that can be described using either an elastic or a plastic solution.

elastic regime depends on current boundary conditions only and is not affected by permanent deformation in the past, that is, stresses for points A and A' are identical.

Figure 3.2 also illustrates that for any critical-wedge stress solution (B or B') there must be an equivalent elastic solution, and that the elastic solution for a stable wedge (A or A') must have a similar form to the elastic equivalence of the critical-wedge solution. I first present a general elastic solution in section 3.2.1 (*Hu and Wang*, 2006). Section 3.2.2 provides a subset of the general solution for noncohesive critical or stable wedges (*Wang and Hu*, 2006).

3.2.1. Infinite elastic wedge

The formulation of the problem is identical to that of *Dahlen* (1984) for a critically tapered Coulomb wedge (section 3.1) except that the wedge is elastic (Figure 3.1). For a submarine wedge, water load at the upper surface is $\rho_w g D$, where $D = D_0 - x\sin\alpha$ is water depth above the upper surface, with D_0 being the depth at the toe of the wedge ($x = y = 0$). The solution presented here can be used for a subareal wedge if we let $\rho_w = 0$.

Assuming plane strain, the stress equilibrium equations are as follows.

$$\frac{\partial \sigma_x}{\partial x} + \frac{\partial \tau_{xy}}{\partial y} - \rho g \sin\alpha = 0 \tag{3-10a}$$

$$\frac{\partial \tau_{xy}}{\partial x} + \frac{\partial \sigma_y}{\partial y} + \rho g \cos\alpha = 0 \tag{3-10b}$$

where $-\rho g \sin\alpha$ and $\rho g \cos\alpha$ are the x and y components of ρg, respectively. Tensile normal stress is defined to be positive in this work. Stresses in the wedge can be written as follows from an Airy stress function $\Phi(x, y)$ (*e.g.*, *Fung*, 1965).

$$\sigma_x = \frac{\partial^2 \Phi}{\partial y^2} + \rho g x \sin\alpha \tag{3-11a}$$

$$\sigma_y = \frac{\partial^2 \Phi}{\partial x^2} - \rho g y \cos\alpha \tag{3-11b}$$

$$\tau_{xy} = -\frac{\partial^2 \Phi}{\partial x \partial y} \tag{3-11c}$$

From (3-1), the pore fluid pressure P in the wedge can be written as

$$P = -\lambda \sigma_y + (1-\lambda)\rho_w g D \tag{3-12}$$

The relationship between stress σ and effective stress $\bar{\sigma}$ is:

$$\begin{cases} \bar{\sigma}_x = \sigma_x + P \\ \bar{\sigma}_y = \sigma_y + P \end{cases} \tag{3-13}$$

The boundary condition along the upper surface ($y = 0$) is simply pressure due to the weight of the water column above, that is,

$$\sigma_y\big|_{y=0} = -\rho_w g D = -\rho_w g D_0 + \rho_w g x \sin\alpha \tag{3-14}$$

$$\tau_{xy}\big|_{y=0} = 0 \tag{3-15}$$

The basal boundary ($y = x\tan\theta$, where $\theta = \alpha + \beta$) is assumed to be a planar fault to which a static friction law $|\tau_n| = |\mu_b(\sigma_n + P_b)|$ applies, where τ_n and σ_n are shear and normal tractions, respectively. If we define thrust-type shear traction (for $\beta > 0$) to be positive as shown in Figure 3.1, and because $\bar{\sigma}_n \le 0$, the static friction law along this boundary can be rewritten in (3-3a).

Here effective normal traction on the boundary is represented by the effective normal stress just above the basal fault. If the basal boundary is a normal fault (for $\beta > 0$), we can

use the same expression for the shear traction by allowing negative values for μ_b.

The previous section elucidated that basal traction of a uniform critically tapered Coulomb wedge was a linear function of distance. The linearity is a consequence of the absence of any natural scale length, not of the Coulomb-plastic rheology; basal traction simply scales with the thickness of the wedge, that is, the weight of the rock column above. In the absence of special local processes, a linear basal traction is generally applicable also to a uniform elastic wedge. With the assumption of a constant pore fluid pressure ratio, linear boundary tractions must lead to linear distributions of stress and fluid pressure, such that the effective basal normal stress is also linear. A constant gradient *a* is used to describe this distribution

$$\overline{\sigma}_n = \sigma_n + P = -a\rho g x \tan\theta \tag{3-16}$$

Here $\overline{\sigma}_n$ at distance *x* is expressed as a fraction (*a*) of the weight of the rock column (in the *y* direction) above. Under special conditions that may introduce a scale length, boundary tractions and thus stresses within the wedge may deviate from a linear distribution. A stress solution for a quadratic boundary traction can be found in *Hu and Wang* (2006).

Obviously, $\sigma_x = \sigma_y = -\rho_w g D_0$ at the wedge tip ($x = y = 0$) (Figure 3.1). Because of the linear boundary conditions, stresses σ_x or σ_y within the wedge must be linear functions of *x* and *y* but with a constant term $-\rho_w g D_0$. Therefore, the lowest-order terms in stress function $\Phi(x, y)$ must be of the form $\rho_w g D_0 x^2$ and $\rho_w g D_0 y^2$. The following function is thus considered.

$$\Phi = -\frac{1}{2}\rho_w g D_0\left(x^2 + y^2\right) + \frac{\rho g}{2}\left(k_1 x^2 y + k_2 x y^2\right) + \frac{\rho g}{6}\left(k_3 x^3 + k_4 y^3\right) \tag{3-17}$$

where k_i ($i = 1, 4$) are constants to be determined from boundary conditions. According to (3-11), stresses are derived from Φ as

$$\sigma_x = -\rho_w g D_0 + \left(k_2 + \sin\alpha\right)\rho g x + k_4 \rho g y \tag{3-18a}$$

$$\sigma_y = -\rho_w g D_0 + k_3 \rho g x + \left(k_1 - \cos\alpha\right)\rho g y \tag{3-18b}$$

$$\tau_{xy} = -\rho g\left(k_1 x + k_2 y\right) \tag{3-18c}$$

Using (3-14), we immediately obtain $k_1 = 0$ and $k_3 = \rho' \sin\alpha$.

The two remaining unknown constants k_2 and k_4 can be determined from the basal

boundary condition. The relationship between boundary tractions and internal stresses along the basal boundary is

$$\sigma_n = \sigma_x \sin^2\theta + \sigma_y \cos^2\theta - \tau_{xy} \sin 2\theta \tag{3-19a}$$

$$\tau_n = -\frac{1}{2}(\sigma_x - \sigma_y)\sin 2\theta + \tau_{xy} \cos 2\theta \tag{3-19b}$$

Combining (3-3a), (3-12), (3-13), (3-16), (3-18), and (3-19), we obtain the following two equations.

$$[3k_2 + k_4 \tan\theta + (1-\rho')\sin\alpha]\sin^2\theta + (\lambda \tan\theta - \sin\theta\cos\theta)\cos\alpha = -a\tan\theta \tag{3-20a}$$

$$(k_2 \tan\theta - k_4 - \cos\alpha)\sin^2\theta - \left[k_2 + \frac{1}{2}(1-\rho')\sin\alpha\right]\sin 2\theta = \frac{\mu_b'}{1-\lambda} a \tan\theta \tag{3-20b}$$

k_2 and k_4 can be readily determined from these two equations as

$$k_2 = \frac{-a(1-\mu_b' \tan\theta) + (1-\lambda)^2 \cos\alpha}{(1-\lambda)\tan\theta} \tag{3-21a}$$

$$k_4 = \frac{a[3(1-\lambda-\mu_b' \tan\theta)\cos^2\theta - 1 + \lambda]}{(1-\lambda)\sin^2\theta} - \frac{2(1-\lambda)\cos\alpha}{\tan^2\theta} - \lambda\cos\alpha - \frac{(1-\rho')\sin\alpha}{\tan\theta} \tag{3-21b}$$

From (3-12) and (3-18), the pore fluid pressure is found to be

$$P = \rho_w g D + \lambda \rho g y \cos\alpha \tag{3-22}$$

From (3-13), (3-18), and (3-22), the effective stresses are found to be

$$\bar{\sigma}_x = [k_2 + (1-\rho')\sin\alpha]\rho g x + (k_4 + \lambda\cos\alpha)\rho g y \tag{3-23a}$$

$$\bar{\sigma}_y = -(1-\lambda)\rho g y \cos\alpha \tag{3-23b}$$

$$\tau_{xy} = -k_2 \rho g y \tag{3-23c}$$

with k_2 and k_4 given in (3-21). Given geometry and material properties, there is only one free parameter, a, in the above solution. Comparisons with other relevant solutions are provided in Appendix B.

Solution (3-23) has a very similar form to the stress solution (3-5) for a uniform critical Coulomb wedge. In fact, the $\bar{\sigma}_y$ expression is identical with that of the critical wedge solution. Similar to the critical wedge solution, an important property is that along any straight line radiating from the toe of the wedge, the effective stresses simply scale with x, since $y = x \tan\gamma$, where γ is the angle between the line and the upper surface. The

fundamental mechanics is thus independent of the wedge size. This is also a demonstration of the absence of any natural scale length.

The elastic wedge has been assumed to be infinite in deriving (3-23), but the solution is applicable to finite wedges as well. We have also presented a subset of the general solution (3-23) for finite elastic wedges and discussions on the bending-like behaviour of elastic wedges. For details, please refer to *Hu and Wang* (2006).

3.2.2. Noncohesive critical or stable wedge

In the previous section, I presented a general stress solution for an elastic wedge using the Airy stress function. The formulation of the problem is identical to that described by Figure 3.1 and equations (3-5), except that the basal normal traction needs to be explicitly specified using a constant gradient *a*. In this section, I show that a subset of the general solution of the previous section is the solution for stable and critical wedges.

If $\bar{\sigma}_x = 0$ at $y = 0$, the necessary condition for a wedge lacking surface cohesion, the constant *a* is not an independent parameter but is determined by wedge geometry, pore fluid pressure, and basal friction. Using (3-23a), this condition gives,

$$k_2 = -(1-\rho')\sin\alpha \tag{3-24}$$

(3-24) and (3-21a) lead to

$$a = \frac{(1-\rho')\tan\theta\sin\alpha + (1-\lambda)\cos\alpha}{1-\dfrac{\mu_b'}{1-\lambda}\tan\theta} \tag{3-25}$$

Substituting (3-25) into (3-21b) and after some algebraic manipulation, we obtain

$$k_4 = -\left[m(1-\lambda)+\lambda\right]\cos\alpha \tag{3-26}$$

where *m* is called the effective stress ratio and can be written as

$$m = 1 + \frac{2\left[(1-\lambda)\tan\alpha' + \mu_b'\right]}{\sin 2\theta\left(1-\lambda-\mu_b'\tan\theta\right)} - \frac{2\tan\alpha'}{\tan\theta} \tag{3-27}$$

Therefore, the form of (3-23) that is applicable to a wedge lacking surface cohesion is

$$\bar{\sigma}_x = -m(1-\lambda)\rho g y\cos\alpha \tag{3-28a}$$

$$\bar{\sigma}_y = -(1-\lambda)\rho g y\cos\alpha \tag{3-28b}$$

$$\tau_{xy} = (1 - \rho')\rho g y \sin\alpha \tag{3-28c}$$

If the wedge is in a yield state (critical wedge), it obeys the Coulomb failure criterion. If it is not in a yield state (stable wedge), it obeys Hooke's law of elasticity. The effective stress ratio m determines whether the wedge is stable (elastic deformation) or critical (at Coulomb failure). For a wedge of fixed geometry and material strength, this parameter has two critical values, denoted m^c, with which the wedge is in a critical state (*Wang and Hu*, 2006). The smaller m^c, corresponding to a weaker basal fault, represents an extensionally critical state in which the wedge is everywhere on the verge of gravitational collapse. The larger m^c, corresponding to a stronger fault, represents a compressively critical state in which the wedge is everywhere on the verge of compressive failure. For any m value between these two m^c values, the wedge is in a stable state and undergoes elastic deformation. A change in μ_b' and/or λ results in a change in m and thus may cause the wedge to switch between stable and critical states. Repeated Coulomb failure of the wedge material over geological times gradually shapes the wedge taper.

If $m = m^c$, (3-28) becomes identical with (3-5) and thus is the elastic equivalence of the critical wedge solution (points B and B' in Figure 3.2). This means, for any critical wedge solution in the form of (3-5), we can always find an equivalent elastic solution for the same wedge geometry by equating (3-6) and (3-28). In the elastic equivalence, internal friction is no longer relevant; it is expressed in terms of other parameters through the relation $m = m^c$. If a critical wedge exists for a given wedge geometry and strength, there are typically two m^c values corresponding to compressively and extensionally critical states, depending on basal friction μ_b'. If the value of m falls between the two m^c values, (3-28) represents the state of stress in a stable wedge (points A and A' in Figure 3.2).

Even for $m \neq m^c$, (3-28) and (3-5) share all fundamental features. For example, just like in a critical wedge, the angle ψ_0 between σ_1 and the upper surface (Figure 3.1) in a stable wedge must be uniform, and, similar to (3-9), we must have

$$\alpha + \beta = \psi_b - \psi_0 \tag{3-29}$$

where ψ_b is the angle between σ_1 and the basal surface of the stable wedge (Figure 3.1). The physical meaning of this similarity can be made more intuitive by comparing Mohr

circle illustrations of (3-5) and (3-28). Figure 3.3 represents states of stress in two wedges with identical geometry and basal friction angle φ_b. Figure 3.3a shows a critical state with cohesion S_0 defined in (3-4) and internal friction $\mu = \tan\varphi$, but Figure 3.3b shows a stable state. For the stable state, if we define a pseudo-internal friction $\mu^p = \tan\varphi^p$ (dotted line tangential to the Mohr circle in Figure 3.3b), the two states in Figure 3.3are completely analogous. Angle ψ_0 is thus determined from the following equation similar to (3-7)

$$\frac{\tan 2\psi_0}{\csc\varphi^p \sec 2\psi_0 - 1} = \frac{\tan\alpha'}{1+\eta} \tag{3-30}$$

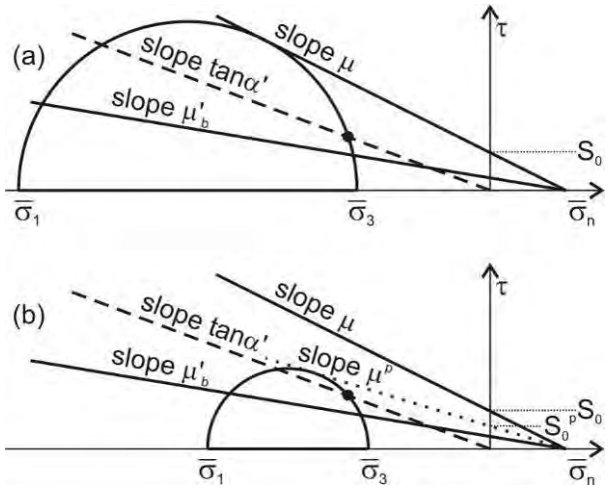

Figure 3.3. Mohr circles to illustrate the state of stress in critical and stable wedges with the same geometry and basal friction coefficient μ_b (from *Wang and Hu*, 2006). (a) Stresses in a critically tapered Coulomb wedge. S_0 is cohesion, and μ is the coefficient of internal friction. (b) Stresses in a stable wedge. S_0^p is pseudo-cohesion and μ^p is the pseudo-coefficient of internal friction. In both (a) and (b), the solid circle marks invariant point $(\bar{\sigma}_y, \tau_{xy})$.

One may be puzzled why the cohesion gradient η appears in the equation for an elastic wedge. In fact, the pseudo-internal friction must be accompanied by a pseudo-cohesion S_0^p (Figure 3.3b). It can be shown that S_0^p has an identical form to S_0 as defined by (3-4), except that μ is replaced with μ^p, and therefore η here appears also as a pseudo-

parameter. By invoking φ^p, (3-27) can be written into a form similar to (3-6a)

$$m = 1 + \frac{2(1+\eta)}{\csc\varphi^p \sec 2\psi_0 - 1} \tag{3-31}$$

If $\varphi^p = \varphi$, we have $\psi_0 = \psi_0^c$, $\psi_b = \psi_b^c$, and $m = m^c$. Using the Mohr circle, we readily obtain

$$\sin^2\varphi^p = \frac{(m-1)^2 + 4\tan^2\alpha'}{(2\eta + m + 1)^2} \tag{3-32}$$

Expanding a well known example of *Dahlen* (1984), we demonstrate how stresses in a wedge of given geometry change elastically from one critical state to another in response to changing basal friction conditions (Figure 3.4). The hypothetical wedge is assumed to be noncohesive ($\eta = 0$) with $\beta = 5°$, $\alpha = 4°$, $\mu = 0.7$, and $\lambda = 0.8$. The same parameter set will be used in Chapter 4. The critical taper theory (3-5) shows that this wedge is compressively critical if $\mu_b' = 0.11$ (Figure 3.4a) but extensionally critical if μ_b' is decreased to 0.019 (Figure 3.4e). Using (3-29), we have calculated stresses in stable wedges for three values of μ_b' between the two critical values. If the angle between σ_1 and the upper surface $\psi_0 < 45°$, the wedge is compressively stable (Figure 3.4b). If $\psi_0 > 45°$, the wedge is extensionally stable (Figure 3.4d). If $\psi_0 = 45°$, it is in a neutral state (Figure 3.4c). The value of μ_b' at the neutral state, denoted μ_{b-N}', is related to other parameters by the following equation

$$\mu_{b-N} = \frac{(1-\lambda)\cos 2\theta}{\cot\alpha' + \sin 2\theta} \tag{3-33}$$

The change of ψ_0 with μ_b', referred to as the elastic stress path, for this wedge is shown in Figure 3.5a (thick solid line), together with stress paths for other surface slopes. For each geometry, ψ_0 changes between its two critical values corresponding to the two critical μ_b' values. The end points of all curves (connected by a dashed line) outline the stable region. The α - β plot for the same wedge material but $\mu_b' = 0.1$ is shown in Figure 3.5b, with the stable region "filled" with contours of ψ_0 determined using (3-23), in conjunction with (3-27) and (3-32).

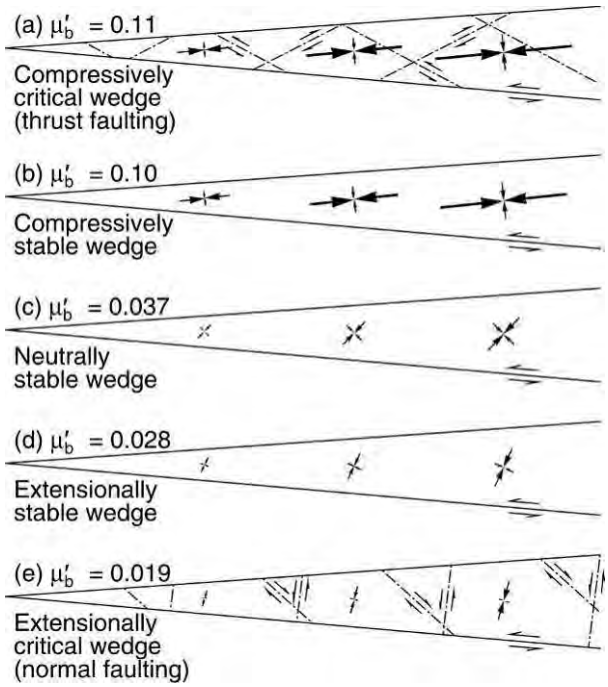

Figure 3.4. An example to show how stresses in an elastic – perfectly Coulomb-plastic wedge, with $\alpha = 4^o$, $\beta = 5^o$, $\mu = 0.7$, and $\lambda = 0.8$, are affected by basal friction μ_b'. Converging arrows represent principal stresses, with the larger one being σ_1. (a) Compressively critical state. (b) Compressively stable state. (c) Neutral state (σ_1 is at 45° with the upper surface). (d) Extensionally stable state. (e) Extensionally critical state. In (a) and (e), dot-dashed lines are plastic slip lines.

Two special critical states are marked in Figure 3.5, featuring basal erosion (Figure 3.5a) and the angle of repose (Figure 3.5b), respectively. The angle of repose is the maximum value of α for the given set of material properties, reached in the extensionally critical state in which $\tan\alpha' = \mu$, that is, one the two conjugate sets of plastic slip lines becomes parallel with the upper surface. "Basal erosion" is often used as a generic term to indicate removal of materials from the underside of the wedge (see discussion in section 4.3.1). Here it is used to indicate a specific compressively critical state in which $\mu_b' = \mu(1-\lambda)$, that is, one set of plastic slip lines in the critical wedge becomes parallel with the basal thrust (*Dahlen*, 1984). At this μ_b', no elastically stable surface slope exists.

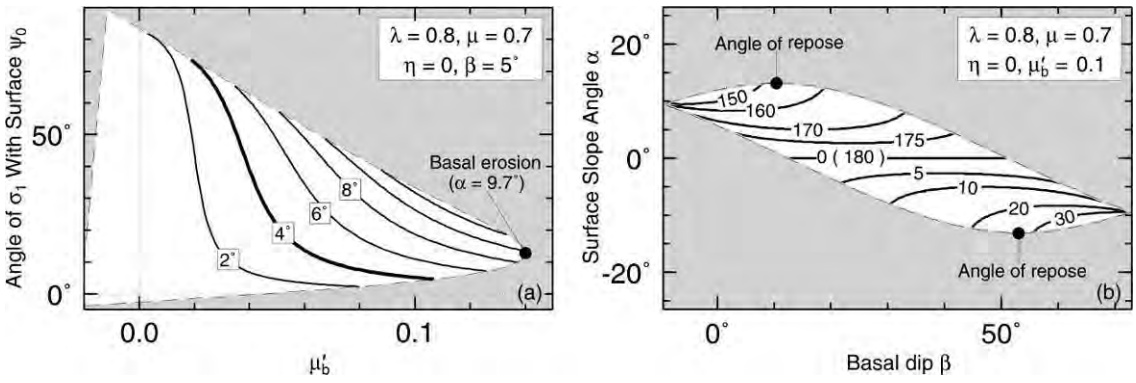

Figure 3.5. Stability diagrams of intermediate-strong wedge material. (a) Plot of the angle of σ_1 with the upper surface ψ_0 (defined in Figure 3.1) vs. basal friction μ_b' (the elastic stress path) for the wedge in Figure 3.4 (thick solid line) and similar wedges but with different surface slopes (thin solid lines). Each stress path is terminated at the extensionally critical state at a lower μ_b' and the compressively critical state at a higher μ_b'. The end points (connected by a dashed line) outline the stable region of α for the given β value (= 5º) in the $\psi_0 - \mu_b'$ space. (b) Plot of α vs. β for the same wedge material with μ_b' = 0.1, with ψ_0 contours (in degrees) in the stable region encompassed by the line of critical states (dashed line). In both (a) and (b), the unstable region is shaded.

3.3. The dynamic Coulomb wedge theory

The theory of critically tapered Coulomb wedge (section 3.1) has met great success in its application to deformation processes at convergent margins. However, not addressed by the theory is one of the most important processes in subduction zones: great earthquakes. It is the purpose of this work to expand the classical Coulomb wedge theory and to establish a conceptual framework for studying mechanical processes of submarine wedges throughout earthquake cycles.

Fluctuations of fault stress in earthquake cycles must affect wedge mechanics. Because of the fluctuation of basal stress, the wedge cannot always be in a critical state, and therefore the mechanics of a stable wedge also needs to be considered. In this section, the two accretionary wedges shown in Figure 1.2 are used as an example to elucidate our theory of dynamic Coulomb wedge (*Wang and Hu*, 2006). Although the

theory is based on static stress equilibrium and ignores inertial forces and seismic wave propagation, we use the word “dynamic” to emphasize the importance of temporal changes in the state of stress and deformation mechanism (elastic vs. plastic).

In this section, the inner and outer wedges are treated independently for simplicity. The state of stress in each of them is assumed to depend only on the basal stress directly beneath. In reality, there is stress transfer between the two parts (see Chapter 2). For example, the state of stress in the inner wedge depends not only on the shear stress of the megathrust seismogenic zone directly beneath, but also on stresses in the outer wedge.

3.3.1. Outer wedges in earthquake cycles

Velocity-strengthening of the basal fault of the outer wedge implies that μ_b' decreases with decreasing slip rate. In the later part of an interseismic period long after a previous earthquake, the updip segment is “protected” by the locking of the seismogenic part of the fault further downdip. If this updip segment has little slip, μ_b' is expected to be low, *e.g.*, around the reference value of 0.04 or lower. Stress paths for the two outer wedges of Figure 1.2 with $\mu = 0.7$ are shown in Figure 3.6 for a few λ values. In most of the interseismic period, they are expected to be in the stable regime (point A or A' in Figure 3.2) for a wide range of μ_b' and λ values.

During an earthquake, as the updip segment of the fault is forced to slip, it suddenly becomes stronger. The increase in μ_b' may be due to the intrinsically velocity-strengthening nature of μ_b and perhaps also a decrease in fault-zone fluid pressure. The outer wedge is elastically compressed at the beginning of the coseismic slip.
If μ_b' increases to the end of the elastic stress path (Figure 3.6), the wedge enters a critical state and compressive failure occurs (point B or B' in Figure 3.2). If the earthquake is too small to push the outer wedge into the critical state, the wedge simply experiences a brief phase of elastic compression.

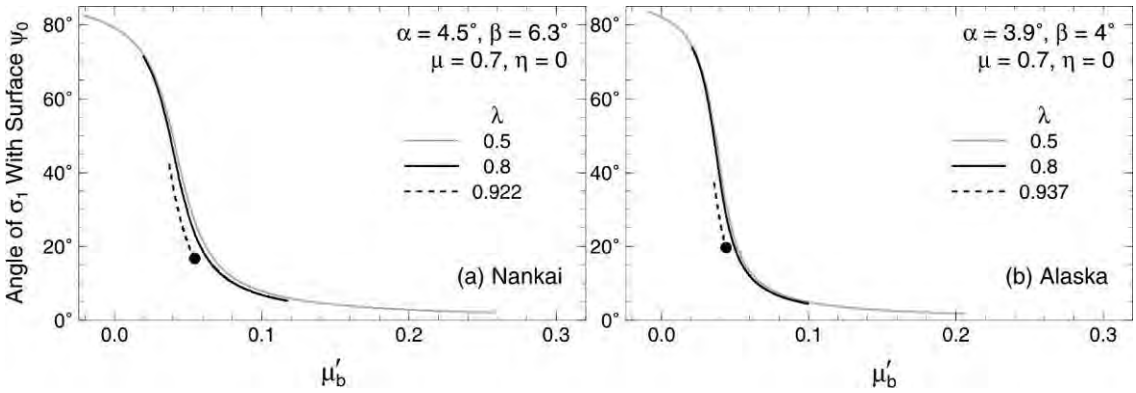

Figure 3.6. Elastic stress paths for the outer wedges of the two prisms in Figure 1.2 with μ = 0.7, η = 0. Solid circle marks the state of basal erosion.

After the earthquake, when the seismogenic part of the fault is locked, the updip velocity-strengthening segment is expected to creep to relax the coseismically generated stress in the outer wedge. Any relaxation immediately brings a critical wedge back to the stable elastic regime.

If λ stays constant in this cycle, wedge stress simply moves back and forth along one stress path (Figure 3.6). However, pore fluid pressure within the wedge must increase during coseismic compression of the wedge and decrease afterwards. A proper treatment of the fluid pressure pulse in a stable wedge requires the theory of poroelasticity, and λ must be stress-dependent. For example, for elastic coseismic deformation, in which the system can usually be assumed to be undrained, $P = \gamma(\Delta\sigma_x + \Delta\sigma_y + \Delta\sigma_z)/3$, where γ is the (three-dimensional) loading efficiency (or the Skempton coefficient) (*Wang*, 2007), and $\Delta\sigma_i$ (i = *x*, *y*, *z*) is incremental stress in the fluid-solid mixture. In order to obtain the exact stress solution of (3-28), we have to assume a constant λ. But on the basis of this simple solution we may qualitatively predict the effect of fluid pressure variation: During an earthquake, wedge stress should move on to stress paths for higher λ values (Figure 3.6). For a higher λ, the critical state is reached at a lower μ_b'. After the earthquake, wedge stress should gradually move to stress paths for lower λ values because of stress relaxation and fluid drainage.

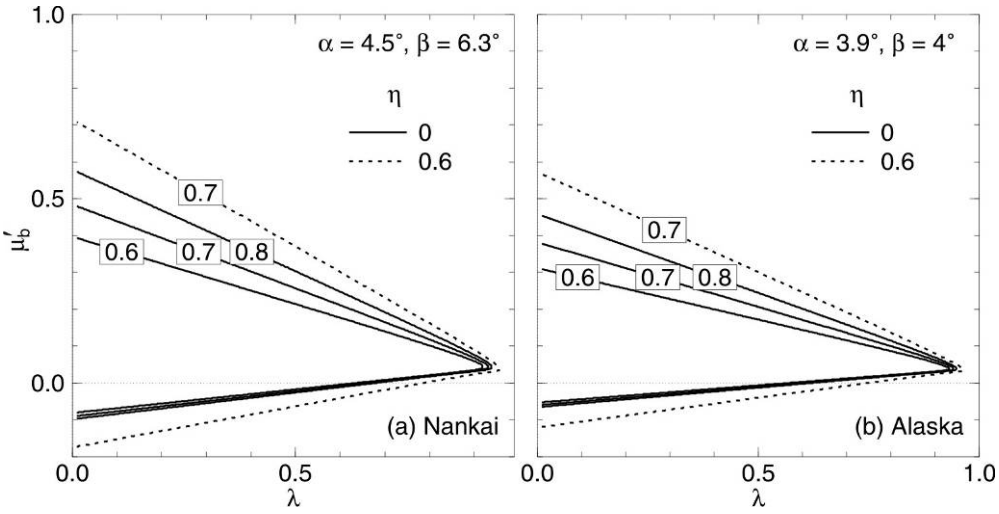

Figure 3.7. Critical values of basal μ_b' as a function of pore fluid pressure ratio λ for the Nankai and Alaska outer wedges with different internal frictions μ (labelled on each curve). (a) Nankai outer wedge. (b) Alaska outer wedge.

Figure 3.7 shows how the critical value of μ_b' depends on λ. This plot also shows the sensitivity of the results to the choice of internal friction μ and cohesion gradient η. For each μ or η, there are two branches of μ_b' as a function of λ encompassing the stable region, with the upper branch for compressively and lower branch for extensionally critical states, respectively. Greater pore fluid pressure makes the wedge weaker, so that compressive failure can occur at a lower basal friction, and gravitational collapse can occur at a higher basal friction.

Coseismic increase in λ can also provide the condition for basal erosion. The state of basal erosion (defined at the end of Section 3.2) requires not only a high enough μ_b', but also a high λ. For μ = 0.7, basal erosion for our Nankai cross-section requires λ = 0.92 (Figures 3.6a). Although this is unlikely to happen for the whole Nankai outer wedge, it may locally occur just above the basal decollement during an earthquake.

In summary, the sediment accretion, permanent outer-wedge deformation, and limited basal erosion take place mainly during great earthquakes, and the observed surface slope of an outer wedge is determined by the peak value of μ_b' reached at the time of the largest earthquakes.

3.3.2. Inner wedge in earthquake cycles

In the conceptual model shown in Figure 2.1, we only consider the core region of the seismogenic zone. The transition from the updip velocity-strengthening segment to this core region awaits more detailed future studies. The downdip limit of the seismogenic zone (*Hyndman and Wang*, 1993; *Peacock and Hyndman*, 1999) is less important to the subject of this study.

In the end-member scenario we are considering, the stick-slip segment of the subduction fault is in a locked state or slips extremely slowly in the interseismic period. The peak shear stress that the fault can sustain is probably represented by low μ_b' values such as 0.04 discussed in Section 3.3.1. Because the subduction fault fails (and ruptures) at such a low μ_b', the inner wedge never comes close to compressive failure. This explains the general lack of recent contractile structure in inner wedges. Stress paths of the two inner wedges of Figure 1.2 for $\lambda = 0.5$ are shown in Figure 3.8. We include models with the cohesion $\eta = 0.6$ to account for the possible greater strength of inner wedges than outer wedges. A greater η makes it more difficult to cause Coulomb failure (*i.e.*, the wedge is stable over a wider range of μ_b') but does not affect the shape of elastic stress paths. The exact interseismic μ_b' value is obviously unimportant in keeping the inner wedge in the stable regime, because the stability occurs over a very wide range of μ_b' values.

Because of the velocity-weakening nature of the seismogenic zone, μ_b' decreases during a great earthquake, and the wedge follows the stress path in the direction toward low μ_b' and high ψ_0, opposite of the coseismic behaviour of the outer wedge, and the wedge becomes more extensional.

Even the weakest inner wedge assumed ($\eta = 0$) stays in the stable regime throughout great earthquake cycles (Figure 3.8). The inner wedge thus provides a stable environment for the formation of forearc sedimentary basins, which explains the correlation between the downdip positioning of megathrust rupture with the location of forearc basins observed at many accretionary margins (*Wells et al.*, 2003). *Wells et al.* (2003) noticed that the second-order, along-strike positioning of patches of greater coseismic fault slip

also seems to correlate with the location of forearc basins. The mechanism for this correlation, if confirmed, deserves further study, and the key question may be about what leads to the anomalous areas between basins. The stability of the inner wedge also helps explain the presence of an apparent "dynamic backstop" landward of the outer wedge (*Kopp and Kukowski*, 2003). In addition to a landward increase in consolidation state of wedge sediments, the seismogenic behaviour of the subduction fault can cause a change in structural style and even a surface slope break around the outer-inner wedge transition. In fact, the stable environment of the inner wedge should facilitate consolidation.

The case of $\mu_b' = 0$, *i.e.*, zero shear stress, represents complete stress drop of the seismogenic zone during an earthquake. It is theoretically possible to cause extensional failure by coseismically raising λ to 0.99 and 0.69 for Nankai and Alaska inner wedges, respectively, although near-lithostatic fluid pressures are very unlikely. Of course, the applicability of the wedge model decreases as we go landward, because the rheology of the deeper region may increasingly deviate from Coulomb.

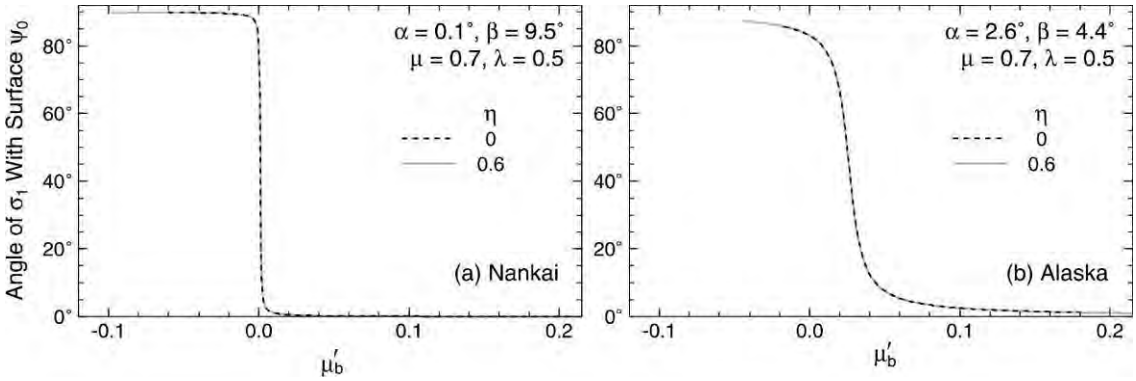

Figure 3.8. Elastic stress paths for the inner wedges of the two prisms in Figure 1.2, with $\mu = 0.7$, $\lambda = 0.5$.

Chapter 4. Geometry and Stability of Outer Wedges in Subduction Zones

Based on the knowledge of stress transfer along the megathrust during earthquakes in Chapter 2, I use the dynamic Coulomb wedge theory described in Chapter 3 to investigate the stability of outer wedges in subduction zones in this chapter. I first present the measurement on the geometry of outer wedges in twenty-three margins. I then describe the application of wedge mechanics to these outer wedges. The work of this chapter has been published in *Journal of Geophysical Research* in 2008 (*Hu and Wang*, 2008).

4.1. Observed geometry of outer wedges

In order to apply the wedge mechanics described in Chapter 3 and what we have learned from the stress transfer modelling in Chapter 2 to real subduction zones, I compiled published seismic-survey depth sections and measured the geometry of the outer wedge for twenty-three margins. I first determined the location of the transition of the outer and inner wedges on the basis of the deformation pattern of the forearc as described by the authors who published these sections as well as a surface slope break. An outer wedge shows active permanent deformation and evidence for out-of-sequence faults, and its surface slope is usually steeper than that of the inner wedge. I then drew linear outlines to approximate the wedge surface and the subduction interface and determined α and β from these straight lines. For a subduction zone with several seismic survey profiles less than 100 km apart, I measured all the profiles but only present an average of these measurements. Obviously, the shape of the seafloor is generally more accurate than the shape of the subduction fault in seismic sections. Considering the uncertainties in the travel-time to depth conversion in published papers and in the measurements in this work, I estimate the errors in α and β to be at least $\pm 1.0^{o}$ and $\pm 2^{o}$, respectively. Additionally, along-strike variations in α often exceed measurement uncertainties from a single profile, and it should be cautioned that the geometry determined from a single profile may not represent the along-strike average.

Measurements of α and β involving different trench-normal distances may yield different results. For example, for a profile across the Nankai Trough, I obtained $\alpha = 4.5°$ and $\beta = 5.3°$ for an outer wedge of 20 km width. For the same profile, *Lallemand et al.* (1994) obtained $\alpha = 4.0°$ and $\beta = 5.5°$ for a wedge of 40 km width by measuring a segment from the trench to a position corresponding to a decollement depth of 10 km below seafloor. Surface slope values reported by *Lallemand et al.* (1994) for various subduction zones are generally slightly smaller than ours, because all their measurements were made over a larger region including the most seaward part of the inner wedge.

Measurements of twelve accretionary outer wedges (Table 4.1) give an average surface slope angle $\alpha = 4.0°$ and basal dip $\beta = 4.8°$ (Figure 4.1). It is interesting to note that most of the recent devastating megathrust earthquakes of M_w 9 or greater have occurred at accretionary margins, such as the 1700 Cascadia, 1960 Chile, 1964 Alaska, and 2004 Sumatra earthquakes. Overall, outer wedges of margins that produced large megathrust earthquakes, such as Alaska, southern Chile, southwestern Japan, and southern Cascadia (Oregon), feature larger surface slope angles, comparing to those with smaller historical megathrust earthquakes, such as Barbados, Kurile, Kermadec, and Hikurangi. This suggests a connection between outer wedge geometry and maximum size of megathrust earthquakes, although there are also exceptions. At some accretionary margins, such as north-central Cascadia (*Davis and Hyndman*, 1989; *Hyndman et al.*, 1993; *Flueh et al.*, 1998; *Spence et al.*, 2001) and Makran (*Kopp et al.*, 2000; *Kukowski et al.*, 2001), there is a section of very thick, nearly horizontally-layered oceanic sediments (≥2 km) between the deformation front and the point where the surface slope sharply steepens and seismic reflectors in the sediments become disordered. In this work, I assume that the outer wedge at these margins start from where the surface slope sharply steepens.

Outer wedges at some erosional margins, such as Costa Rica, North Chile, and Peru, include a frontal prism consisting mainly of land-derived debris and a middle prism consisting mainly of the rock frame of the upper plate (Figure 1.4d). Where possible, the geometry of both the frontal and middle prisms is measured in this work. The surface slope of the frontal prism is generally steeper than that of the middle prisms (Figure 4.1). Excluding the frontal prisms, measurements of eleven erosional outer wedges (Table 4.2)

give an average $\alpha = 6.0^{o}$ and $\beta = 7.2^{o}$.

Table 4.1. Surface slope angle (α, ±1º), basal dip (β, ±2º), and trench-normal width (km) of outer wedges at twelve accretionary subduction margins.

Name	Location[a]	width	α	β	Source[b]
Barbados	15º30'N-58º40'W	25	2.3	1.3	1
Nankai	33ºN-136º50'E	30	4.5	6.3	2-4
	32º20'N-134º40'E	35	3.5	3.6	2-4
Alaska	57º30'N-147º50'W	25	3.5	2.4	3,5-6
	59º10'N-145º50'W	25	8.7	4.7	3,5-6
Aleutian	54º10'N-157º20'W	35	4.0	5.9	7-8
	50º30'N-175ºW	35	5.7	8.6	7-8
S. Chile	33º10'S-72º40'W	25	4.7	5.8	3,9
Sunda	6º50'S-102º10'E	40	5.1	4.5	10
	8ºS-104ºE	35	3.6	4.3	10
	9º10'S-106º20'E	40	4.4	5.9	10
N. Cascadia	47º20'N-125º30'W	15	2.5	2.4	11-14
S. Cascadia	44º40'N-125º20'W	20	7.2	4.7	15-16
Kurile	43ºN-148º20'E	30	4.1	6.2	17-18
Kermadec	26º20'S-175º20'W	30	3.0	8.6	19
C. Hikurangi	39º20'S-178º40'W	>15	0.7	3	20
S. Hikurangi	41ºS-178ºW	35	1.7	4.5	21
Makran	24º10'N-62º50'E	30	1.5	3.3	22-23

[a] Location is where the profile crosses the trench.

[b] References for numbered sources are 1, *Moore et al.* (1995); 2, *Park et al.* (2002); 3, *von Huene and Ranero* (2003); 4, *Bangs et al.* (2006); 5, *von Huene and Klaeschen* (1999); 6, *Fruehn et al.* (1999); 7, *Bruns and von Huene* (1986); 8, *Scholl et al.* (1986); 9, *Laursen et al.* (2002); 10, *Kopp and Kukowski* (2003); 11, *Davis and Hyndman* (1989); 12, *Hyndman et al.* (1993); 13, *Flueh et al.* (1998); 14, *Spence et al.* (2001); 15, *Snavely Jr. et al.* (1986); 16, *Gerdom et al.* (2000); 17, *Klaeschen et al.* (1994); 18, *Schnürle et al.* (1995); 19, *von Huene and Scholl* (1991); 20, *P. Barnes,* 2006, personal communication; 21, *Davey et al.* (1986); 22, *Kopp et al.* (2000); 23, *Kukowski et al.* (2001).

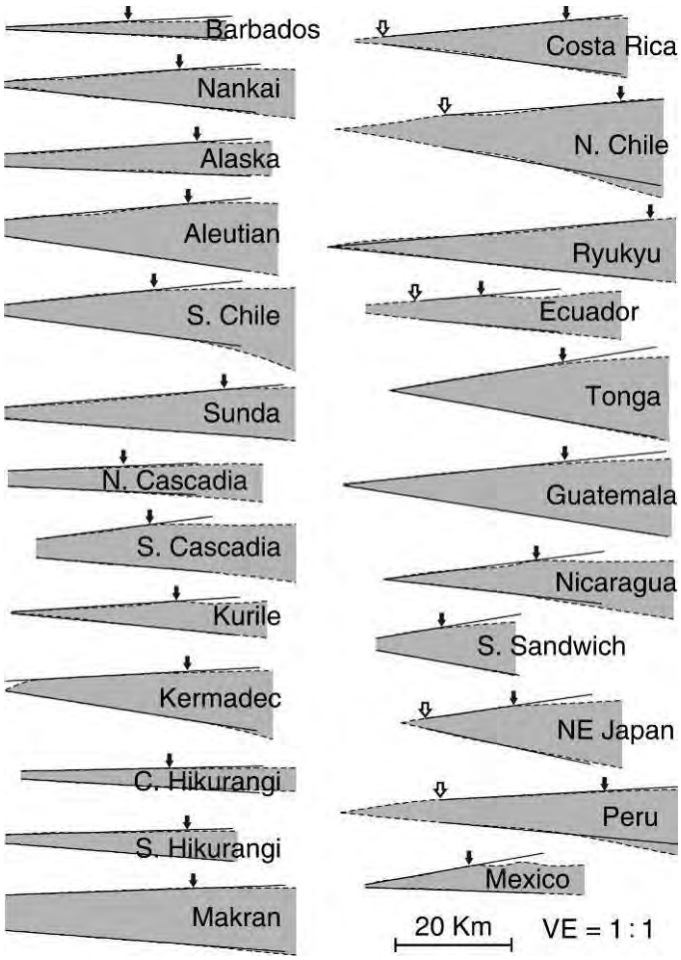

Figure 4.1. Observed geometry of subduction zone wedges based on published seismic sections referenced in Tables 4.1 and 4.2 (shaded area with dashed outline) and linear approximations of their upper and lower surfaces used in this work (solid lines). (left) Accretionary margins and (right) predominantly erosional margins. The transition between outer and inner wedges for each margin is approximately marked by a solid arrow. For erosional margins, where a frontal sedimentary prism can be clearly discerned on the seismic section, the limit of the prism is marked by a hollow arrow. If there are multiple seismic sections, only one of them is shown here. There is no vertical exaggeration.

Table 4.2. Surface slope angle (α, ±1°), basal dip (β, ±2°), and trench-normal width (km) of outer wedges at eleven erosional subduction margins.

		Frontal prism			Middle prism			
Name	Location[a]	width	α	β	width	α	β	Source[b]
Costa Rica	9°40'N-86°10'W	5	7.4	4.9	30	4.5	7.2	1-3
	9°10'N-85°40'W	10	5.0	3.8	30	3.0	5.9	1-3
	8°50'N-85°30'W	8	5.0	4.8	15	5.9	5.6	1-3
N. Chile	23°20'S-71°20'W	15	8.5	5.5	35	5.5	12.0	4
Ryukyu	25°20'N-128°20'E	<5			30	4.9	5.2	5
Ecuador	3°20'N-79°W	10	5.5	6.1	20	5.5	5.2	6-7
Tonga	23°30'S-174°50'W	<3			30	9.0	10.6	8
Guatemala	13°N-91°W	<3			45	6.2	9.7	9
Nicaragua	11°20'N-87°30'W	<5			25	7.6	7.0	10
S. Sandwich	~57°S-24°30'W	5			20	8.0	10.0	11
NE Japan	40°5'N-144°20'E	5	7.4	11.7	10	6.7	12.6	12
	39°40'N-144°20'E	<10	8.1	4.6	25	4.7	5.5	13
Peru	8°30'S-81°W	15	7.9	5.5	35	5.0	8.3	14
	11°40'S-79°10'W	15	9.1	3.5	30	3.2	5.3	14
	13°30'S-78°W	15	6.9	4.8	50	2.8	8.7	14
Mexico	15°50'N-99°W	<3			20	10.6	1.7	15

[a]Location is where the profile crosses the trench.

[b]References for numbered sources are 1, *Ye et al.* (1996); 2, *Christeson et al.* (1999); 3, *Ranero et al.* (2008); 4, *Sallarès and Ranero* (2005); 5, *Kodaira et al.* (1996); 6, *Collot et al.* (2004); 7, *B. Marcaillou*, 2007, personal communication; 8, *von Huene and Scholl* (1991); 9, *Aubouin et al.* (1984); 10, *Ranero et al.* (2000); 11, *Vanneste and Larter* (2002); 12, *von Huene et al.* (1986); 13, *von Huene et al.* (1994); 14, *Krabbenhöft et al.* (2004); 15, *Collins and Watkins* (1986).

In Figure 4.2a, I compare the geometry measurements with a reference wedge model using the Coulomb wedge theory. For the reference wedge model, I assume an internal friction coefficient $\mu = 0.7$, internal pore fluid pressure ratio $\lambda = 0.8$, and basal effective friction coefficient $\mu_b' = 0.04$ (the same as that of the updip zone in the interseismic phase assumed in Chapter 2) (*Wang and Hu*, 2006). Accretionary outer wedges accumulate materials and deform by compressive failure and therefore are expected to be compressively critical. Erosional outer wedges must also be overall compressively critical, although they may sometimes become extensionally critical in an extremely relaxed state in great earthquake cycles (*Wang et al.*, 2010). Therefore, each data point in Figure 4.2 is expected to be on a line of compressively critical states similar to the lower

solid trajectories shown in Figure 4.2. However, Figure 4.2a would indicate that the outer wedges of most subduction zones are in a stable state (white area). For the weak-wedge model of *Lallemand et al.* (1994) shown in Figure 4.2b, most wedges would be stable or gravitationally unstable. Figure 4.2 indicates that, with reasonable parameter values, the steady-state Coulomb wedge theory cannot fully explain the mechanics of outer wedges.

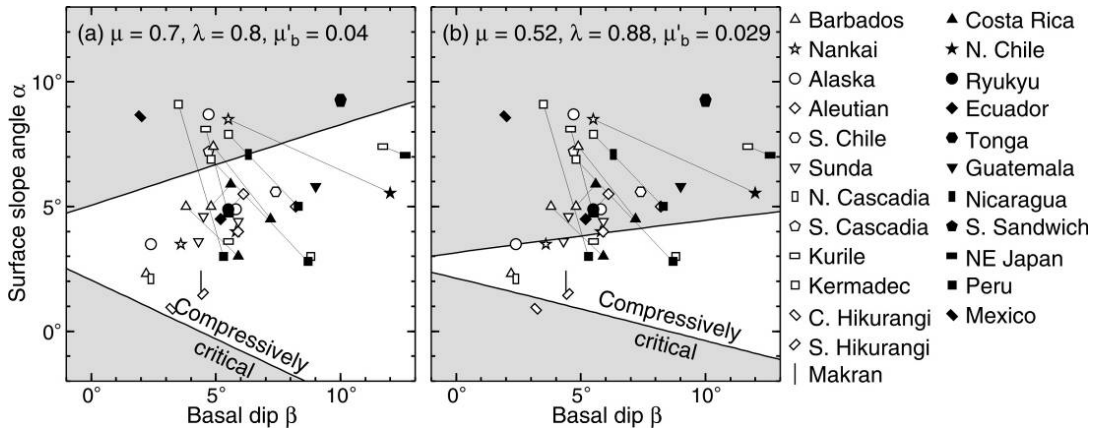

Figure 4.2. Surface slope angle α versus basal dip β for outer wedges of twenty-three subduction zones compared with Coulomb wedge models. (a) Comparison with the reference wedge model. (b) Comparison with the weak wedge model of *Lallemand et al.* (1994). Isolated open and solid symbols represent accretionary and erosional margins, respectively. For erosional margins where frontal prisms are wider than 10 km, the middle prism (solid symbol) and the frontal prism (open symbol) are both shown and linked with a thin line. The pair of thick solid lines brackets the stable region of a Coulomb wedge model with the shown set of material parameters. The top one of the pair represents extensionally critical states (on the verge of gravitational collapse), and the bottom one represents compressively critical states.

4.2. Application of wedge mechanics theory to outer wedges

How do we make the outer wedges compressively critical, that is, how is the line of the compressively critical states in Figure 4.2 moved upward? I vary parameter values of the reference wedge model to illustrate their roles in achieving this goal. For each panel of Figure 4.3, the solid trajectories represent the reference wedge model in Figure 4.2a,

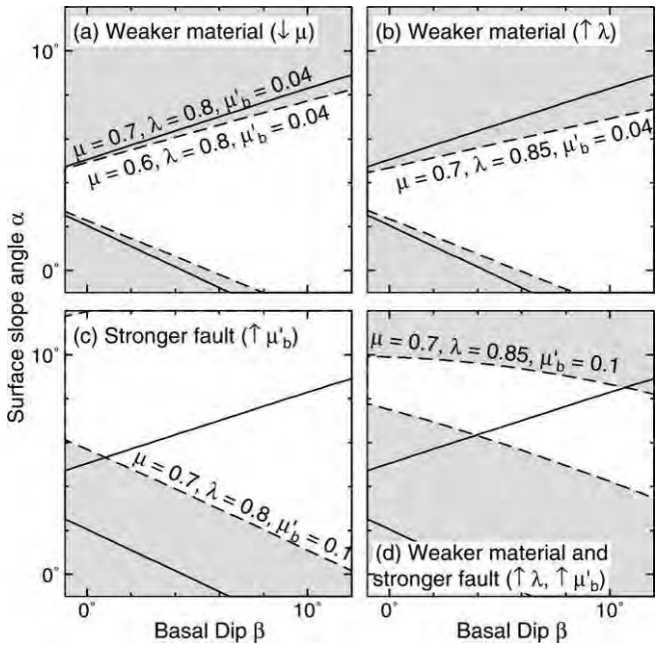

Figure 4.3. Surface slope angle α versus basal dip β for models with different parameter combinations (labelled on the critical state trajectories). Solid lines represent the reference wedge model shown in Figure 4.2a. Dashed lines dividing stable (white) and unstable (shaded) regions are critical state trajectories of models with one or two parameters different from the reference model. (a) Effects of a weaker wedge due to a smaller μ. (b) Effects of a weaker wedge due to a greater λ. (c) Effects of a stronger basal fault due to a greater μ_b'. (d) Combined effects of a stronger basal fault (greater μ_b') and a weaker wedge (greater λ).

and the dashed trajectories represent a model with one or more parameters differing from the reference model. The models of a weaker wedge, either with a smaller internal friction coefficient μ = 0.6 (Figure 4.3a) or a greater internal pore fluid pressure ratio λ = 0.85 (Figure 4.3b) move the line of compressively critical states slightly upward. The model of a stronger basal fault with friction μ_b' = 0.1(Figure 4.3c) moves it upward significantly. The combined effect of a weaker wedge and a stronger basal fault is even greater (Figure 4.3d). Therefore, a model with a stronger basal fault (larger μ_b') and/or a weaker wedge (larger μ and/or λ) is required to drive an outer wedge towards

compressive failure. As discussed in Chapter 2, a stronger basal fault can be achieved through coseismic strengthening.

In the following, we discuss how the moderate coseismic strengthening discussed in Chapter 2 can drive the outer wedge into a compressively critical state. For the model wedge, I assume $\alpha = 4^o$ and $\beta = 5^o$, the same as for the stress transfer model shown in Figure 2.2a and similar to the observed average geometry of the accretionary outer wedges shown in Figure 4.2. The model shown in Figure 4.4a is the reference wedge model, with material property values given in Figure 4.2a, for the specified geometry. For an interseismic strength of the basal fault $\mu_b' = 0.04$, the outer wedge is stable as shown in Figure 4.4a, similar to those falling in the white region of Figure 4.2a for a wide range of wedge geometry.

With the strength of the wedge material fixed, a strengthening of the updip zone of the basal fault by $\Delta\mu_b' = 0.052$ as in the reference earthquake model (Figure 2.3, solid lines) is not sufficient to push the outer wedge into a compressively critical state (Figure 4.4b). By simply strengthening the basal fault alone, a critical wedge of the given geometry and material properties requires an increase in fault strength by $\Delta\mu_b' = 0.067$ (Figure 4.4c), greater than that of the reference earthquake by a factor of 1.3. Figure 2.5 (the 30-km line) shows that this requires the force drop of the earthquake to be greater by at least the same factor, by increasing either the stress drop or downdip width of the seismogenic zone. As explained in Section 2.3, if $\Delta\mu_b' < \Delta\mu_{b\_c}'$, a greater force drop would only cause the updip zone to slip for a larger distance without further increasing the fault stress, such as the cases shown using dashed lines in Figure 2.3.

An earthquake not only causes strengthening of the updip fault zone, but also causes weakening of the wedge material because coseismic compression of the outer wedge leads to an increase in its internal pore fluid pressure (*Wang and Hu*, 2006). As shown in Figure 4.4d, a combination of fault strengthening and wedge weakening has a much greater tendency to make the wedge critical than does fault strengthening alone. For example, for the reference earthquake shown in Figure 2.3 (solid lines), the wedge will become compressively critical if the wedge material is weakened by coseismically

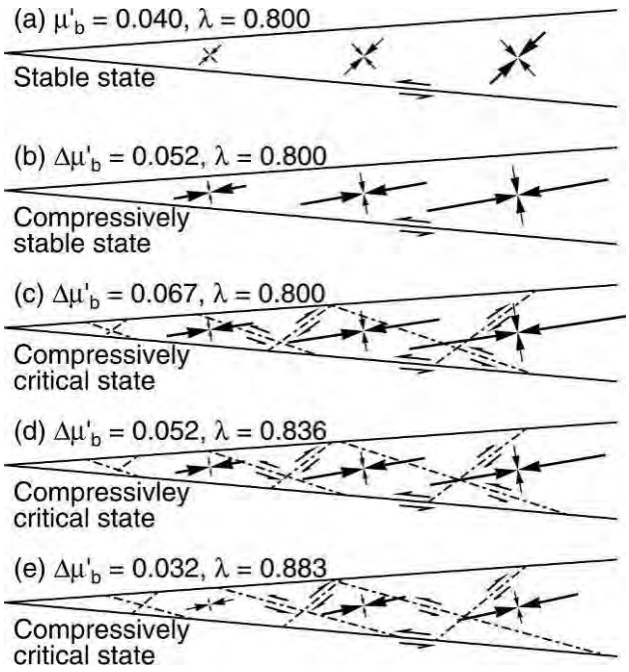

Figure 4.4. Stress field in a wedge with $\alpha = 4^{o}$, $\beta = 5^{o}$, and $\mu = 0.7$ for different λ and μ_b' values as labelled. (a) A compressively stable wedge representing the interseismic stage. (b) With coseismic strengthening of the basal fault $\Delta\mu_b' = 0.052$ (i.e., $\mu_b' = 0.092$) but without increasing pore fluid pressure ratio λ, the wedge is still compressively stable. (c) With greater coseismic strengthening $\Delta\mu_b' = 0.067$ (i.e., $\mu_b' = 0.107$) and without increasing λ, the wedge is compressively critical. (d) With moderate strengthening $\Delta\mu_b' = 0.052$ and an increase in λ, the wedge is compressively critical. (e) With a low degree of strengthening $\Delta\mu_b' = 0.032$ (i.e., $\mu_b' = 0.072$) but a greater increase in λ, the wedge is compressively critical. Dot-dashed lines in (c), (d) and (e) represent potential faulting directions.

increasing λ to 0.836 (Figure 4.4d). The amount of increase from 0.8 to 0.836 shown here is an arbitrarily assumed scenario for the purpose of illustrating the point. Given $\Delta\mu_b'$, the increase in λ required to bring the wedge into a critical state depends on the initial value of λ. For example, if λ is initially 0.835, an increase of merely 0.001 will suffice. Even for the model earthquake of a much lesser degree of strengthening of $\Delta\mu_b' = 0.032$, shown

using dashed lines in Figure 2.3b, increasing λ to 0.883 can also result in a compressively critical wedge (Figure 4.4e). The comparison between Figures 4.4d and 4.4e illustrates the trade-off between $\Delta\mu_b'$ and λ.

The fundamental mechanics of the results displayed in Figure 4.4 can be better explained using the effective stress ratio *m* (equation 3-27). Still with $\beta = 5°$, $\lambda = 0.8$, and $\mu = 0.7$, we show *m* as a function of the effective friction coefficient μ_b' in Figure 4.5a for different α values, using expressions of *m* given in (3-27). Given α, the stress ratio varies along a nearly straight line in the stable area in response to changes in basal fault friction. Points A and B along the line of $\alpha = 4^o$ represent the stable states shown in Figures 4.4a and 4.4b, respectively, and point C represents the critical state shown in Figure 4.4c. In a somewhat speculative situation, if several earthquakes occur sequentially in the same area, and the stress induced by each event does not fully relax, the wedge may gradually evolve from state A to state C due to the cumulative effects of these earthquakes. Without coseismically increasing λ, a coseismic fault strengthening of $\Delta\mu_b' = 0.052$ will move the wedge from state A to state B. With an increase of λ to 0.836 as well, the same earthquake theoretically moves the wedge from state A in Figure 4.5a to the compressively critical state D in Figure 4.5b (with stresses displayed in Figure 4.4d).

4.3. Discussion

4.3.1. Shallow subduction erosion driving by megathrust earthquakes

Subduction erosion occurs at many convergent margins, resulting in seafloor subsidence and landward migration of the trench axis and volcanic arc (*von Huene and Scholl*, 1991; *Clift and Vannucchi*, 2004). Basal erosion is a process of continual removal of materials from the underside of the upper plate by the subducting plate and differs from frontal erosion caused by the subduction of anomalous seafloor features such as seamounts. Figure 1.4d summarizes essential features of end-member erosion-dominated subduction zones such as northern Chile (*von Huene and Ranero*, 2003; *Salares and Ranero*, 2005), Peru (*von Huene and Lallemand*, 1990; *Clift et al.*, 2003; *Krabbenhöft et al.*, 2004), Costa Rica (*Ranero and von Huene*, 2000), Ecuador (*Sage et al*., 2006), Kuril (*Klaeschen et al.*, 1994), and Northeast Japan (*von Huene et al.*, 1994).

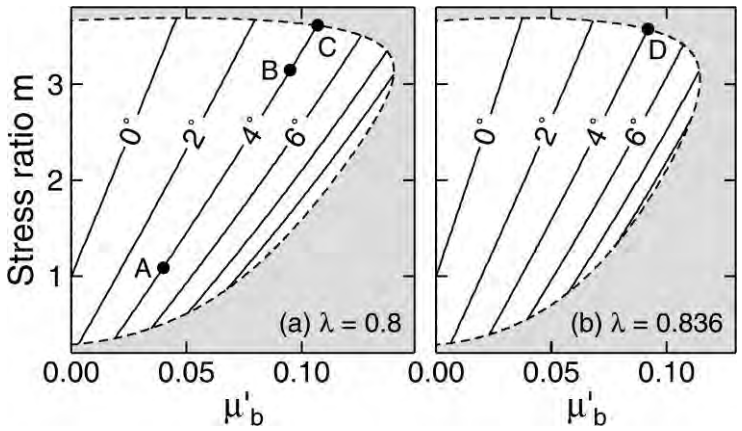

Figure 4.5. Stress ratio *m* as a function of effective friction coefficient μ_b' for wedges with $\beta = 5°$ and $\mu = 0.7$ but different α values. (a) Internal pore fluid pressure ratio $\lambda = 0.8$. (b) $\lambda = 0.836$. The dashed trajectory representing critical states divides areas of stable states (white) and unstable states (shaded). Stresses for states A, B, C and D are illustrated in Figures 4.4a, 4.4b, 4.4c and 4.4d, respectively.

In the middle prism (Figure 1.4d), under a sediment cover are crystalline-basement or older sedimentary rocks that are fractured predominantly by deep-cutting normal faults. These faults were initiated when the rocks of the present middle-prism were still in the shelf area (*Vannucchi et al.*, 2004). As basal erosion proceeds, small incremental motion of these faults accommodates the gradual subsidence of the seafloor. The shallow basal erosion in the middle prism area is the focus of this work, although basal erosion also occurs further downdip, along the seismogenic zone of great interplate earthquakes and at the base of the overriding mantle wedge (*Kukowski and Oncken*, 2006; *Tonarini et al.*, 2007). The very frontal part of the upper plate is the frontal prism (Figure 1.4d), consisting mostly of down-slope debris derived from land and retaining a quasi-constant size (*von Huene et al.*, 2004).

Wang et al. (2010) proposed that stress fluctuations in earthquake cycles may cause the state of the middle prism to alternate among states of stable, extensionally and compressively critical states. During earthquakes, strengthening of the basal fault and/or weakening of the wedge material may drive the middle prism into a compressively critical state including basal erosion. After earthquakes, the basal fault becomes weak

because of the very low or zero slip rates, and hence the overlying middle prism is in a stable state or an extensionally critical state. We also argue that basal erosion tends not to occur in accretionary prisms featuring flatter surface slopes unless conditions are unusual.

We use the middle prism of northern Chile with $\alpha = 5.5^{o}$ and $\beta = 12^{o}$ (Table 4.2) as an example to demonstrate its stress state in earthquake cycles (Figure 4.6). Given the material strength (*e.g.*, the same $\mu = 0.7$ and $\lambda = 0.8$ as in Chapter 3), the wedge has two critical states depending on basal friction: an extensionally critical (EC) state if the basal friction is sufficiently low (Figure 4.6a) and a compressively critical (CC) state if the basal friction is sufficiently high (Figure 4.6c). For intermediate basal friction, the wedge is in a stable state enduring only elastic deformation (Figure 4.6b).

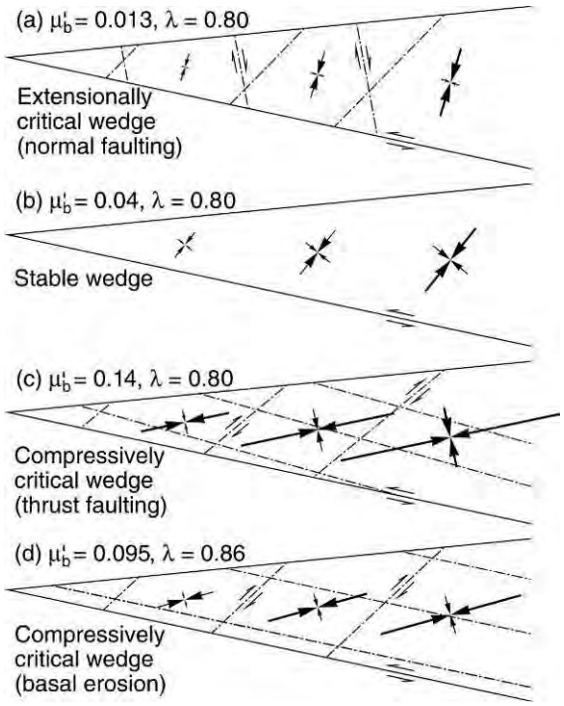

Figure 4.6. State of stress in a uniform noncohesive Coulomb wedge with $\alpha = 5.5^{o}$ and $\beta = 12^{o}$, representative of the middle prism at northern Chile (Table 4.2). Converging arrows represent principal stresses, with the larger pair being σ_1. $\mu = 0.7$. (a) Extensionally critical (EC) state. (b) Stable state. (c) Compressively critical (CC) state. (d) Ideal state of basal erosion, a special CC state. In (a), (c), and (d), dot-dashed lines are plastic slip lines (potential failure planes).

The existence of a basal fault means $\mu_b' < \mu(1-\lambda)$, that is, the fault is weaker than the wedge material. If $\mu_b' = \mu(1-\lambda)$, that is, if the fault is as strong as the wedge, there is no mechanical distinction between the two, and one of the two conjugate sets of potential failure plane (plastic slip lines) is parallel with the basal fault (Figure 4.6d). This is the ideal state of basal erosion. The basal fault cannot become any stronger, because a new decollement will be formed up in the wedge. "The precise location of the decollement will be governed by pre-existing weaknesses, but the net result will always be basal erosion" (*Dahlen*, 1984). In real subduction zones, basal erosion represents a mechanical state close to the ideal state, that is, $\mu_b' \approx \mu(1-\lambda)$. It requires one or both of the two conditions: (1) a relatively strong fault and (2) relatively weak wedge material, particularly the wedge material in proximity to the fault. *Wang et al.* (2010) argue that the basal fault is weak and the middle prism is relatively strong in the interseismic period, but strengthening of the basal fault and hydraulic weakening of the prism can both occur during great earthquakes (*e.g.*, Figure 4.6d). With this mechanism, erosion of the base of the middle prism does not occur continuously but in brief episodes of coseismic deformation. The mechanism does not require extreme conditions such as near-lithostatic pore fluid pressures.

4.3.2. Very low frequency earthquakes in the outer wedge at Nankai

The dynamic Coulomb wedge theory (*Wang and Hu*, 2006) suggests that an earthquake slip along the seismogenic zone induces large shear stress at the shallowest aseismic portion of the subduction fault and may push the outer wedge to compressive failure. After the earthquake, the induced stresses relax in the form of afterslip. Based on continuous GPS observations at sites close enough to the trench, *Hsu et al.* (2006) showed that the shallowest segment of the subduction fault did not rupture during the 2005 M_w 8.6 Nias-Simeulue earthquake, but it exhibited significant afterslip logarithmically decreasing with time. This is consistent with the prediction of the dynamic Coulomb wedge theory (*Wang and Hu*, 2006). However, in 2003 and 2004, *Obara and Ito* (2005) and *Ito and Obara* (2006) observed very-low-frequency (VLF) earthquakes exhibiting thrust faulting distributed at ~10 km depth, above the surface of

the subducting Philippine Sea Plate, within the outer wedge at Nankai Trough (Figure 4.7). The last megathrust event that occurred in this part of the Nankai Trough is the 1944 M_w 8.3 Tonankai earthquake (*Kanamori*, 1972; *Satake*, 1993; *Sagiya and Thatcher*, 1999), and on the basis of the record of paleoseismology, the repeating cycle of megathrusts in the Nankai Trough is believed to be around 180 years (*Ando*, 1975). The newly observed VLF thrust faulting events indicate that the outer wedge of the Nankai Trough is still on the verge of compressive failure 60 years after the earthquake, which is not consistent with the prediction of stress relaxation by the dynamic Coulomb wedge theory. One may argue that several decades after the 1944 earthquake, the earthquake-induced stresses may still have not relaxed. Nevertheless, relaxation of the earthquake-induced stresses postulated by the dynamic Coulomb wedge theory (*Wang and Hu*, 2006) may not be used to explain the phenomenon of VLF thrust faulting events within the accretionary prism. The following three possible mechanisms responsible for the VLF events need to be investigated in the future.

(1) Interseismic slip of the seismogenic zone. The seismogenic zone is locked after the earthquake, but whether the fault is always fully locked over the interseismic period is still debatable. It may have some very slow slip in the interseismic period (partial locking). An aseismic slip, similar to a small earthquake, along the seismogenic zone may not be sufficient to drive forearc prisms into a critical state from a fully relaxed interseismic state (from state A to A' in Figure 3.2). However, if the earthquake-induced stress is not fully relaxed, and may still be close to a critical state, for example, a state close to states A or E in Figure 3.4, a small perturbation from the seismogenic zone may drive parts of the outer wedge into compressive failure. *Davis et al.* (2006) observed fluid pressure changes in borehole sites close to the trench of Nankai Trough, in spatial and temporal correlation with a cluster of VLF events, which may reflect an episode of aseismic unlocking of a part of the seismogenic zone. GPS observations over a hundred kilometres from the trench are frequently interpreted to indicate that the subduction fault is fully locked. Land-based GPS observations are not adequate to resolve slip behaviour of the subduction fault close to the trench (*Wang*, 2007). Near-field data, such as data from seafloor borehole strainmeters or fluid pressure sensors, are required to determine the locking state of the shallow part of the subduction fault.

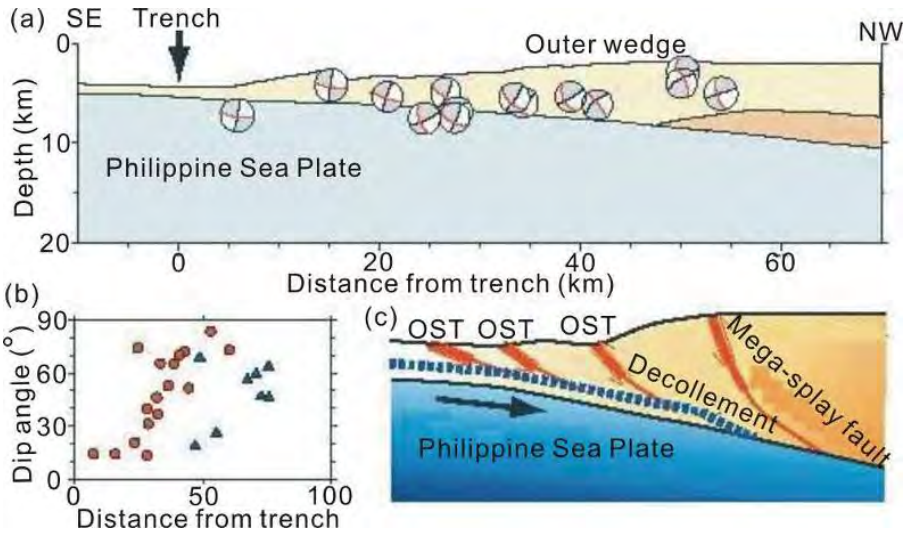

Figure 4.7. Crustal structure of the Nankai trough and distribution of the VLF earthquakes (from *Ito and Obara*, 2006). (a) Crustal structure and focal mechanisms of the VLF events. (b) Dipping angle of the fault plane for VLF events in the areas of the Kii peninsula (red circles) and Hyuga-nada (blue triangles). (c) Schematic cross-section showing a source model for the VLF earthquakes. OST: out-of-sequence faults.

(2) Delayed transfer of earthquake-induced stresses. As described in section 2.3, an earthquake slip along the seismogenic zone results in strengthening of the shallowest portion of the updip subduction fault (Figure 2.3b). The induced stresses may transfer slowly updip instead of instantaneously. Depending on material property of the overlying plate and the frictional property of the fault, the transferred shear stress may induce compression of the outer wedge and cause thrust failure.

(3) Slab shortening. In all studies of the outer wedge, no attention has been paid to the deformation of the subducting oceanic slab associated with great subduction zone earthquakes. The earthquake slip along the seismogenic zone causes a stretch of the subducting plate updip of the rupture zone during and immediately after the earthquake. During the interseismic period, when the seismogenic zone is locked, ongoing plate convergence causes this part of the plate to shorten. This slab shortening results in a compression of the outer wedge and may produce thrust faulting events in the outer wedge. Because of the coupling of the slab with the underlying upper mantle which

experiences viscoelastic postseismic relaxation of the stress induced by the earthquake, interseismic shortening of the slab in earthquake cycles is time-dependent.

4.3.3. Normal faulting in the inner wedge at Nankai

Recent seismic surveys showed the presence of normal faults in the most seaward part of the Nankai inner wedge. For example, several normal faults cut through young sediments of ages within tens of thousands of years in the Kumano basin of Nankai trough as shown in Figure 4.8 (*Moore et al.*, 2007b). The profile shown in Figure 4.8 is part of the proposed profile for the IODP drilling project NanTroSEIZE shown in Figure 1.2a. Normal faulting in the compressive subduction zone environment is an apparent paradox. The observed normal faulting at Nankai is certainly not due to slope failure. Normal faults are also observed at other margins such as Cascadia (*López et al.*, 2010). The following two possible mechanisms need to be investigated.

(1) Underplating of the subducted sediments leads to “bending” of the upper plate and thus results in extension in the shallow part of the inner wedge. 2-D and 3-D seismic surveys have revealed the subduction of pelagic and terrestrial sediments (*Park et al.*, 2002; *Moore et al.*, 2007b). Geochemistry data also indicate that subduction of the oceanic plate does carry sediments down to greater depths (*Shipley et al.*, 1982; *von Huene and Scholl*, 1991; *Clift and Vannucchi*, 2004). The subducting sediments may not go down all the way smoothly and may be accreted to the underside of the upper plate at certain depths. This will generate an upward push and thus the “bending” effect mentioned above. Sediment underplating thus results in a locally extensional stress field although the regional stress may still be compressive. The seismic survey profile shown in Figure 4.9b appears to indicate that the normal faults indicating extensional stress do not extend to deeper than about 2 km. This is consistent with the “bending” model. However, because of the uncertainties of seismic survey data at greater depths, whether the normal faults penetrating to depths of a few kilometres in the seismic survey profiles actually reaches the subduction interface has yet to be investigated.

(2) If the normal faults cut through the entire upper plate, it will indicate that the stress within the whole wedge in the normal faulting area is extensional (*i.e.*, vertical stress is greater than horizontal stress). To this scenario, mechanism (1) discussed above

does not apply. Relaxation of the earthquake-induced stresses is another potentially viable option to explain this scenario. On the basis of a model with a uniform wedge, *Wang and Hu* (2006) demonstrated that the stress relaxation cannot produce extensional failure within the inner wedge. However, the uniform geometry assumption of *Wang and Hu* (2006) excludes the effects of the adjacent outer wedge. Further investigation including the stress interaction between the outer and inner wedges is required.

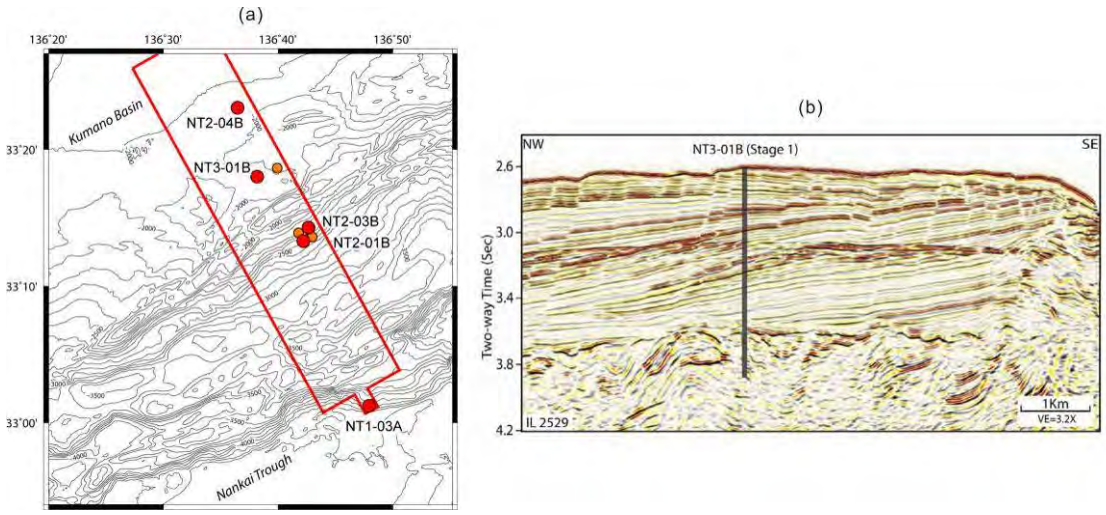

Figure 4.8. Observation of normal faulting in the forearc basin in the Nankai trough (from *Moore et al.*, 2007b). (a) Regional bathymetric map of Kumano Basin. Red dots represent proposed drilling sites for IODP project. (b) Two-way seismic reflection profile through the proposed drilling site NT3-01B shown in (a).

PART II: Viscoelastic Finite Element Model of Postseismic and Interseismic Crustal Deformation Associated with Megathrust Earthquakes

In PART I, I examined how stress is transferred from the seismogenic zone to the updip zone and its effect on the overlying outer wedge. In part II, I will investigate the deformation associated with subduction zone earthquakes in a much broader area (the forearc and the back arc) and at a much larger time scale including postseismic and interseismic deformation.

In Chapter 5, I will review the theory of the linear viscoelasticity and briefly describe the pattern of the viscoelastic deformation in earthquake cycles. In Chapter 6, I will construct simple finite element models to test model parameters. In Chapter 7, based on the knowledge of Chapter 6, I will use a unified mechanical model to examine contemporary crustal deformation at three margins, Sumatra, Chile and Cascadia, that are presently at distinctively different stages of earthquake cycles.

Chapter 5. Linear Viscoelasticity and its Application to Subduction Zone Studies

5.1. Linear viscoelasticity

Rheology governs how the Earth material deforms in response to imposed stresses. *Wang et al.* (1979), *Kirby* (1983), *Karato and Wu* (1993), *Ranalli* (1995), *Blenkinsop* (2000), *Turcotte and Schubert* (2002), *Wang* (2007), *Bürgmann and Dresen* (2008), and *Karato* (2008, 2010) have provided comprehensive discussions on rock deformation and rheology. In this section, I briefly review their conclusions that are relevant to this work.

Time-dependent deformation of solids was first recognized for metals. Viscoelastic deformation of rock and metal samples has been widely studied in laboratory experiments. Figure 5.1 illustrates the evolution of uniaxial strain ε of a rock sample subject to a constant differential stress $\sigma = \sigma_0 = \sigma_1 - \sigma_3$, where σ_1 and σ_3 are the axial and confining stresses, respectively. The instantaneous response to the suddenly imposed σ_0 is elastic and results in strain ε_0 in the rock sample (the dot A in Figure 5.1). In instantaneous response of rocks to a sudden stress perturbation such as an earthquake or

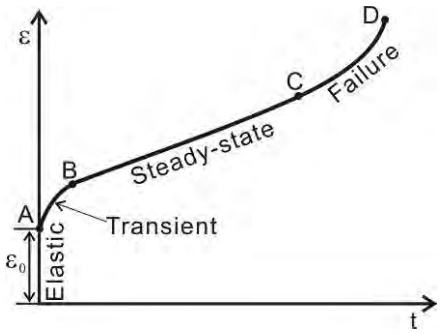

Figure 5.1. Sketch of the evolution of uniaxial strain ε of a rock sample subject to a constant differential stress σ_0 (after *Wang et al.* (1979)).

rapid deglaciation, the deformation is elastic. The elastic deformation is due to a small displacement of atoms from their stable positions to new equilibrium positions. If the imposed stress is removed, the atoms move back to their original positions, and there is no permanent deformation. The elastic deformation is governed by Hooke's law:

$$\varepsilon_{ij} = s_{ijkl}\sigma_{kl} \tag{5-1a}$$

where ε_{ij} and σ_{kl} are the strain and stress tensors, respectively, and s_{ijkl} is the compliance tensor. For the widely used isotropic material, the general Hooke's law in (5-1a) can be written in terms of Young's modulus E and Poisson's ratio ν as follows.

$$\begin{cases} \varepsilon_{11} = \dfrac{1}{E}\left[\sigma_{11} - \nu(\sigma_{22} + \sigma_{33})\right] \\ \varepsilon_{22} = \dfrac{1}{E}\left[\sigma_{22} - \nu(\sigma_{33} + \sigma_{11})\right] \\ \varepsilon_{33} = \dfrac{1}{E}\left[\sigma_{33} - \nu(\sigma_{11} + \sigma_{22})\right] \\ \varepsilon_{12} = \dfrac{2(1+\nu)\sigma_{12}}{E}; \varepsilon_{23} = \dfrac{2(1+\nu)\sigma_{23}}{E}; \varepsilon_{31} = \dfrac{2(1+\nu)\sigma_{31}}{E} \end{cases} \tag{5-1b}$$

From A to B, strain increases with time, but the strain rate decreases rapidly with time. This is the transient deformation. Rocks of the lower crust or mantle may undergo transient deformation after a stress perturbation. Microscopic mechanisms for transient deformation are still under intense investigation. *Andrade* (1910) observed the initial transient creep of Pb and Cu at room temperature and proposed a flow law:

$$\varepsilon = A\left[\left(1 + at^{1/3}\right)\exp(bt) - 1\right] \tag{5-2a}$$

where A, a, and b are constants, and *t* is time. For creep of metals at high-temperatures appropriate for the lower crust and mantle, strain in the transient phase may follow t^m, with $1/3 < m < 2/3$ (*e.g.*, *Weertman*, 1955; *Weertman and Weertman*, 1975; *Ranalli and Schloessin*, 1989) or other forms. The transient deformation of rocks may be represented by the linear Kelvin viscoelasticity (*e.g.*, *Pollitz*, 2003; *Pollitz et al.*, 2006). For a constant stress load σ_0, a transient flow law can be written as follows:

$$\varepsilon = \frac{\sigma_0}{2\mu}\left[1 - \exp\left(-t / \tau_K\right)\right] \tag{5-2b}$$

where $\tau_K = \eta_K / \mu$, and η_K and μ are the transient viscosity and shear modulus, respectively.

From B to C, strain increases with time at a constant rate. This type of deformation is called steady-state deformation. Deformation of Earth rocks at long times (*e.g.*, $t > 10^1$ yr) after a perturbation is commonly assumed to be in the steady-state phase. At the microscopic scale, the steady-state deformation of mantle rocks may be described primarily by diffusion and dislocation creep. The diffusion creep is the stress-driven diffusive mass transfer from a highly concentrated region to a less concentrated region through interiors of crystal grains (Nabarro-Herring creep) or along grain boundaries (Coble creep). The dislocation creep is a collective motion of the movements of dislocations in crystal lattice structure. A flow law for both diffusion and dislocation creep based on laboratory experiments can be written as follows (*e.g.*, *Kirby*, 1983).

$$\dot{\varepsilon} = A\left(\frac{\sigma_0}{\mu}\right)^n \left(\frac{b}{d}\right)^m \exp\left(-\frac{E_0 + PV_0}{RT}\right) \tag{5-3a}$$

where $\dot{\varepsilon}$ is rate of the uniaxial strain, *A* is a parameter with the dimension of frequency, μ is shear modulus, *b* is length of the Burghers vector (~0.5 nm), *d* is grain size, *n* and *m* are stress and grain-size exponents, respectively, E_0 is activation energy, V_0 is activation volume, *P* is confining pressure, *R* is the universal gas constant (8.31 J $mol^{-1}K^{-1}$), and *T* is absolute temperature. If we ignore the grain size effect, a more general expression of the steady-state flow law in (5-3a) can be written as follows (*e.g.*, *Melosh*, 1980; *Wu*, 1992):

$$\dot{\varepsilon}_{pq} = B\sigma_{II}^{n-1}\sigma_{pq} \tag{5-3b}$$

where ε_{pq} and σ_{pq} are components of the deviatoric strain and stress tensors, respectively,

B is a parameter with contributions of *A* and *T*, and σ_{II} is the second stress invariant. An effective viscosity $\eta(n)$ can be defined as

$$\eta(n) = \frac{\sigma_{pq}}{2\dot{\varepsilon}_{pq}} = \frac{1}{2B\sigma_{II}^{n-1}} \tag{5-4a}$$

Given suddenly imposed and fixed strain, the induced stresses relax with time. The time scale of the stress relaxation is characterized by the Maxwell time $\tau(n)$ (*e.g.*, *Melosh and Raefsky*, 1983)

$$\tau(n) = \frac{\eta(n)}{\mu} = \frac{1}{2B\mu\sigma_{II}^{n-1}} \tag{5-4b}$$

For the linear Maxwell viscoelasticity, $n = 1$, and $\eta(1)$, the Newtonian viscosity, is a stress-independent constant. For the nonlinear (power law) rheology, $n > 1$, and the Maxwell time depends on the initial stress perturbation. Because of the power-law relation, the effective viscosity in areas of high stresses such as around the edges of the rupture zone is small and results in fast deformation. However, as the stresses relax, and hence the effective viscosity increases, the deformation slows down. Compared with the Newtonian rheology, the power-law rheology is characterized by very fast initial deformation and much slower later deformation. It has been argued that the Newtonian rheology may be adequate in modelling viscoelastic deformation due to small stress perturbations at time scales of $10^1 – 10^4$ years (*e.g.*, *Melosh and Raefsky*, 1983; *Wang*, 2007). The power-law rheology may be required in modelling geodynamic processes of time scales of millions of years, such as in thermal models (*e.g.*, *Currie et al.*, 2004; *Wada and Wang*, 2009).

From C to D, strain increases rapidly with time, and the rock sample disintegrates. The process is complicated and is not dealt with in this study.

Linear viscoelastic deformation may be represented by two fundamentally different physical bodies, Maxwell (flow law written in (5-3b) with $n = 1$) (Figure 5.2a) and Kelvin (flow law written in (5-2b)) (Figure 5.2b) bodies. A Maxwell body is a spring (shear modulus μ) in series with a dashpot (viscosity η_{M}). A Kelvin body is a spring (μ) in parallel with a dashpot (η_{K}). The characteristic time of the stress relaxation of the Maxwell and Kelvin bodies are $\tau_M = \eta_M / \mu$ and $\tau_K = \eta_K / \mu$, respectively. The Maxwell

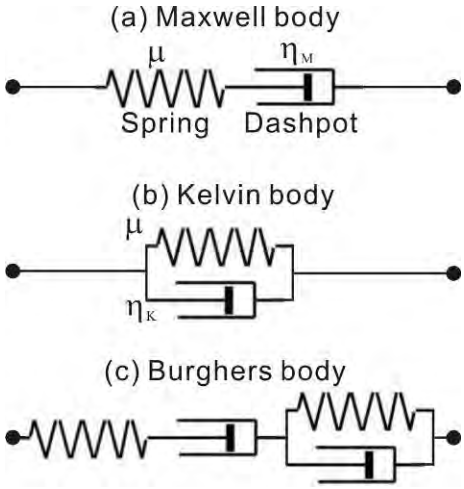

Figure 5.2. Sketch of three physical bodies, Maxwell (a), Kelvin (b), and Burghers (c) bodies.

body behaves like an elastic material at the short-time scale ($t = \tau_M$) and like a viscous material at the long-time scale ($t >> \tau_M$). The viscous deformation of the Maxwell body can occur indefinitely without any threshold strain (or stress). In other words, under constant stress the strain rate of the Maxwell body is initially zero and then increases to a value constant with time. The Kelvin body behaves like a viscous material at the short-time scale ($t = \tau_K$) and like an elastic material at the long-time scale ($t >> \tau_K$). Karato (2010) elucidated that the viscous motion of "defects" in the Kelvin body creates a "back-stress", and after a long time when the created "back-stress" balances with the imposed stress, the viscous deformation stops. Under constant stress, the strain rate of the Kelvin body is initially very large and then decreases to zero.

Newtonian Maxwell rheology is widely used in subduction zone earthquake models. However, recent geodetic observations such as in Sumatra (*e.g., Gahalaut et al.,* 2006; *Jade et al.,* 2007) have revealed that the crust deforms very fast within a few years after an earthquake and deforms slowly at longer times. The very rapid deformation at the short-time scale may be represented by a Kelvin body (*e.g., Pollitz,* 2003; *Pollitz et al.,* 2006) or a Maxwell body with a very low viscosity. The slower deformation at the long-time scale may be represented by a Maxwell body with an intermediate viscosity (*e.g., Wahr and Wyss,* 1980; *Miyashita,* 1987; *Ueda et al.,* 2003; *Hu et al.,* 2004). Therefore,

the viscoelastic deformation associated with the earthquake at the short-time and long-time scales cannot be described by a single Maxwell body. However, they can be described by the transient rheology. The transient rheology may be represented by a Burghers body (*e.g.*, *Yuen et al.*, 1986; *Lakki et al.*, 1998; *Pollitz*, 2003), a Maxwell body in series with a Kelvin body (Figure 5.2c). The transition of the behaviour from the Kelvin mode to the Maxwell mode described by the Burghers body corresponds to the change of the transient to steady-state creep (*e.g.*, *Karato*, 2010). Note that the steady-state power-law rheology is characterized by a deformation pattern similar to that of the transient rheology, with fast initial deformation and slow later deformation (*e.g.*, *Freed et al.*, 2006). However, the applicability of the steady-state power law to describing the transient creep is questionable. The transient rheology is increasingly preferred by the scientific community (e.g., *Freed et al.*, 2010; *Pollitz*, 2003).

5.2. Mathematical formulation of finite element models

The finite element source code PGCvise2 by Dr. *Jiangheng He*, Geological Survey of Canada, Pacific Geoscience Centre (GSC-PGC) is an expansion of the code PGCvise1 used in my M.Sc. program finished in early 2004. Improvements on the model used in my previous project include two main aspects. (1) Linear transient rheology (Figure 5.2c) is incorporated into the new code that can model the transient deformation after an earthquake as well as the long-term deformation. (2) A spherical coordinate system is used in the new code to better represent the Earth. Studies of crustal deformation associated with recent earthquakes recorded by modern geodetic networks indicate that short-term postseismic deformation decays much faster with time than can be represented by the Maxwell rheology. Transient rheology that can be used to represent short-term as well as long-term viscoelastic deformation is incorporated into my finite element model. Benchmarking of PGCvise2 is presented in Appendix C.

The mathematical formulation of PGCvise1 was presented in my M.Sc. thesis in 2004 (*Hu*, 2004). In this section, I expand the discussion of the mathematical formulation of my M.Sc. thesis to account for the incorporation of the transient rheology in PGCvise2.

The stress equilibrium equation for a hydrostatically pre-stressed continuum is the same as in *Hu* (2004):

$$\nabla \cdot \sigma - \rho g \nabla w = 0 \tag{5-5}$$

where ρ and g are density and gravitational acceleration, respectively, and w is vertical displacement. The stress tensor in this equation is the non-hydrostatic (or non-lithostatic) stress; that is, the hydrostatic component has been subtracted. If the equation were to describe the total stress, the second term would just be $\rho\vec{\mathbf{g}}$. Although the hydrostatic component is removed, its effect of tending to bring a perturbed system back to the hydrostatic state should be retained, which results in the second term $-\rho g \nabla w$ (*Peltier*, 1974). Therefore (5-5) describes a system different from one that completely ignores gravity.

With the matrix notation that is widely used in the finite element theory, the strain tensor is written as a 6 × 1 single-column matrix and called a six-dimensional (6-D) strain vector $\boldsymbol{\varepsilon} = [\varepsilon_{xx}, \varepsilon_{yy}, \varepsilon_{zz}, \varepsilon_{xy}, \varepsilon_{yz}, \varepsilon_{zx}]^{\tau}$, where τ denotes transpose operation. Similarly, stress is written as a 6-D stress vector $\boldsymbol{\sigma} = [\sigma_{xx}, \sigma_{yy}, \sigma_{zz}, \sigma_{xy}, \sigma_{yz}, \sigma_{zx}]^{\tau}$.

PGCvise2 solves for the displacement field, the same as in PGCvise1. Other desired quantities such as velocity, strain, and stress are derived from the displacement solution. The relation between displacement and (infinitesimal) strain is:

$$\boldsymbol{\varepsilon} = \mathrm{L}\mathbf{U} \tag{5-6}$$

where $\mathbf{U} = [u, v, w]^{\tau}$ is the 3-D displacement vector, and L is a 6 × 3 matrix of linear differentiation operator defined by

$$\mathrm{L} = \begin{pmatrix} \frac{\partial}{\partial x} & 0 & 0 & \frac{\partial}{2\partial y} & 0 & \frac{\partial}{2\partial z} \\ 0 & \frac{\partial}{\partial y} & 0 & \frac{\partial}{2\partial x} & \frac{\partial}{2\partial z} & 0 \\ 0 & 0 & \frac{\partial}{\partial z} & 0 & \frac{\partial}{2\partial y} & \frac{\partial}{2\partial x} \end{pmatrix}^{\tau}$$

The strain $\boldsymbol{\varepsilon}$ consists of three components, $\boldsymbol{\varepsilon}_e$ (the elastic response that is constant with time), $\boldsymbol{\varepsilon}_M$ (the viscoelastic response of the Maxwell body) and $\boldsymbol{\varepsilon}_K$ (the viscoelastic response of the Kelvin body):

$$\boldsymbol{\varepsilon} = \boldsymbol{\varepsilon}_e + \boldsymbol{\varepsilon}_M + \boldsymbol{\varepsilon}_K \tag{5-7}$$

where

$$\begin{cases} \boldsymbol{\varepsilon}_e = D_1^{-1}\boldsymbol{\sigma} \\ \boldsymbol{\varepsilon}_M = \dfrac{1}{2\eta_M} D_v\boldsymbol{\sigma} \\ 2\eta_K \mathbf{I}\dot{\boldsymbol{\varepsilon}}_K + D_2\boldsymbol{\varepsilon}_K = \boldsymbol{\sigma} \end{cases} \tag{5-8}$$

where **I** is identity matrix, and D_1, D_2 and D_v are material matrices defined as

$$D_1 = \frac{E_M}{(1+\nu_M)(1-2\nu_M)} \begin{pmatrix} 1-\nu_M & \nu_M & \nu_M & 0 & 0 & 0 \\ \nu_M & 1-\nu_M & \nu_M & 0 & 0 & 0 \\ \nu_M & \nu & 1-\nu_M & 0 & 0 & 0 \\ 0 & 0 & 0 & \dfrac{1-2\nu_M}{2} & 0 & 0 \\ 0 & 0 & 0 & 0 & \dfrac{1-2\nu_M}{2} & 0 \\ 0 & 0 & 0 & 0 & 0 & \dfrac{1-2\nu_M}{2} \end{pmatrix} \tag{5-9a}$$

$$D_2 = \frac{E_K}{(1+\nu_K)(1-2\nu_K)} \begin{pmatrix} 1-\nu_K & \nu_K & \nu_K & 0 & 0 & 0 \\ \nu_K & 1-\nu_K & \nu_K & 0 & 0 & 0 \\ \nu_K & \nu & 1-\nu_K & 0 & 0 & 0 \\ 0 & 0 & 0 & \dfrac{1-2\nu_K}{2} & 0 & 0 \\ 0 & 0 & 0 & 0 & \dfrac{1-2\nu_K}{2} & 0 \\ 0 & 0 & 0 & 0 & 0 & \dfrac{1-2\nu_K}{2} \end{pmatrix} \tag{5-9b}$$

$$D_v = \begin{pmatrix} \frac{2}{3} & -\frac{1}{3} & -\frac{1}{3} & 0 & 0 & 0 \\ -\frac{1}{3} & \frac{2}{3} & -\frac{1}{3} & 0 & 0 & 0 \\ -\frac{1}{3} & -\frac{1}{3} & \frac{2}{3} & 0 & 0 & 0 \\ 0 & 0 & 0 & 1 & 0 & 0 \\ 0 & 0 & 0 & 0 & 1 & 0 \\ 0 & 0 & 0 & 0 & 0 & 1 \end{pmatrix} \tag{5-9c}$$

Note that in PGCvise1, $\boldsymbol{\varepsilon} = \boldsymbol{\varepsilon}_e + \boldsymbol{\varepsilon}_M$. For simplicity, the Kelvin body is assumed to be incompressible. Differentiating (5-7) and combining it with (5-8), we obtain the constitutive equation

$$2\eta_K \mathbf{I}\ddot{\boldsymbol{\varepsilon}} + D_2\dot{\boldsymbol{\varepsilon}} = 2\eta_K \mathbf{I}\ddot{\boldsymbol{\varepsilon}}_e + D_1\dot{\boldsymbol{\varepsilon}}_e + 2\eta_K \mathbf{I}\ddot{\boldsymbol{\varepsilon}}_M + D_2\dot{\boldsymbol{\varepsilon}}_M + \boldsymbol{\sigma} \tag{5-10}$$

The finite element method does not solve partial differential equations like (5-5). Instead, it solves an equivalent integral equation based on the virtual work principle (*Yin*, 1987). The virtual work equation associated with (5-5) can be written as

$$\int_V \delta\boldsymbol{\varepsilon}^\tau \cdot \boldsymbol{\sigma} dV - \int_V \delta\mathbf{U}^\tau \cdot \rho g \nabla w dV - \int_S \delta\mathbf{U}^\tau \cdot \mathbf{f} ds = \mathbf{0} \tag{5-11}$$

where V is volume, S is the portion of boundary of V where traction boundary condition is prescribed, $\mathbf{f}$ is the boundary force applied, and $\delta\boldsymbol{\varepsilon}$ and $\delta\mathbf{U}$ are virtual strain and virtual displacement, respectively. Mathematically, they are the variations of the strain and displacement functionals. The physical meaning of (5-11) is that the total virtual work done on the system by external forces in virtual deformation equals the total incremental virtual energy. Equation (5-11) differs from (5-5) in that the physical quantities involved are no longer required to be differentiable. For this reason, this "weak form" equation is a more general and hence a more fundamental statement of the physical problem. The finite element method determines the displacement function that satisfies (5-11) in the functional space.

In the finite element method, the model domain is divided into a number of elements, each having a number of nodal points. Displacement $\mathbf{U}$ in element e is represented by nodal values using polynomial shape (or interpolation) functions. If there are M nodal points in the element

$$\mathbf{U} = \mathrm{N}\mathbf{U}_e \tag{5-12}$$

where $\mathbf{U}_e = [u_1, v_1, w_1, u_2, v_2, w_2, \ldots, u_M, v_M, w_M]^\tau$ is the $3M \times 1$ one-column matrix containing element nodal displacements, and N is a $3 \times 3M$ matrix consisting of shape functions. Thus (5-6) becomes

$$\boldsymbol{\varepsilon} = \mathrm{LN}\mathbf{U}_e \equiv \mathrm{B}\mathbf{U}_e \tag{5-13}$$

The interpolation of the vertical displacements in the element is

$$w = \mathrm{I}_w\mathbf{U} = \mathrm{I}_w\mathrm{N}\mathbf{U}_e \tag{5-14}$$

where $\mathrm{I}_w = [0,0,1]$. Note that the $1 \times 3M$ matrix $\mathrm{I}_w\mathrm{N}$ is simply the third row of N.

Combining (5-11) and (5-13), noting that $\boldsymbol{\delta\varepsilon} = \mathrm{B} \cdot \boldsymbol{\delta}\mathbf{U}$, and dropping the resultant common factor $\boldsymbol{\delta}\mathbf{U}_e$, we obtain the following virtual work equation for element e:

$$\int_e \mathrm{B}^\tau \boldsymbol{\sigma} dV - \int_e \mathrm{N}^\tau \rho g \nabla(\mathrm{I}_w\mathrm{N})\mathrm{U}_e dV = \int_{S\cap e} \mathrm{N}^\tau \mathbf{f} ds \tag{5-15}$$

where $\nabla = \left[\frac{\partial}{\partial x}, \frac{\partial}{\partial y}, \frac{\partial}{\partial z}\right]^{\tau}$ is understood to be a 3 × 1 matrix operator. Equation (5-15) is identical in both PGCvise1 and PGCvise2.

To use our specific constitutive relation with (5-10), we need to deal with the time dependence in the transient rheology. To do this, we apply a backward difference scheme for the time to (5-11), which yields

$$\begin{aligned}\boldsymbol{\sigma}^{n+1} = D^{-1}\left(AD_1 + E\right)\boldsymbol{\varepsilon}^{n+1} - D^{-1}\left(2AD_1 + E\right)\boldsymbol{\varepsilon}^{n} + \\ D^{-1}AD_1\boldsymbol{\varepsilon}^{n-1} + D^{-1}\left(2A + B\right)\boldsymbol{\sigma}^{n} - D^{-1}A\boldsymbol{\sigma}^{n-1}\end{aligned} \tag{5-16}$$

where

$$\begin{cases} A = \dfrac{2\eta_K}{\left(\Delta t\right)^2}\mathbf{I} \\ B = \dfrac{1}{\Delta t}\left(D_2 + D_1 D_v \dfrac{\eta_K}{\eta_M}\right) \\ C = \dfrac{1}{2\eta_M} D_1 D_2 D_v \\ D = A + B + C \\ E = \dfrac{1}{\Delta t} D_1 D_2 \end{cases} \tag{5-17}$$

where Δt is time step length, which does not have to be constant. Equation (5-16) shows that stress at a given time step can be determined from strain of the same time step and stress and strain of the previous time step.

Substituting (5-16) into (5-15) at time step n +1 and writing strain in terms of nodal displacement using (5-13), we obtain

$$\mathrm{K}_e^{\,n+1}\mathbf{U}_e^{\,n+1} = \mathbf{F}_e^{\,n+1} \tag{5-18}$$

where

$$\mathrm{K}_e^{\,n+1} = \int_e \mathrm{B}^{\tau}\mathrm{D}_{\mathbf{s}}^{-1}\mathrm{D}\mathrm{B}dV - \int_e \mathrm{N}^{\tau}\rho g\nabla(\mathrm{I}_w\mathrm{N})dV$$

is the elemental stiffness matrix, and

$$\mathbf{F}_e^{\,n+1} = \int_{S\cap e} \mathrm{N}^{\tau}\mathbf{f}ds + \int_e \mathrm{B}^{\tau}\mathrm{D}_s^{-1}\mathrm{D}\boldsymbol{\varepsilon}^{n}dV - \int_e \mathrm{B}^{\tau}\mathrm{D}_s^{-1}\boldsymbol{\sigma}^{n}dV$$

is the elemental equivalent nodal force vector. The global stiffness matrix K^{n+1} and nodal force vector $\mathbf{F}^{n+1}$ are obtained by summing up elemental $\mathbf{K}_e^{n+1}$ and $\mathbf{F}_e^{n+1}$, respectively, over all elements. That is, for each time step we solve the global algebraic system

$$\mathrm{K}^{n+1}\mathbf{U}^{n+1} = \mathbf{F}^{n+1} \tag{5-19}$$

for the global nodal displacement vector $\mathbf{U}^{n+1}$. Pre-stress σ_0 at $n = 0$ may or may not be zero. Displacement at each time step is calculated from (5-19). Strain and stress at the corresponding time step are determined from (5-15) and (5-16), respectively. Note that the elements in the matrixes K_e^{n+1}, F_e^{n+1} of (5-18) and K^{n+1}, F^{n+1} of (5-19) are different in PGCvise1 and PGCvise2 although the form of these two equations is identical in both programs. The split-node method (*Melosh and Raefsky*, 1981) is used in the finite element code to model discontinuous displacements (slip) along faults.

5.3. Crustal deformation associated with great subduction zone earthquakes

Although in general the crust at shallow depths deforms elastically in earthquake cycles, it is coupled with the more viscous rocks at greater depths (lower crust and the mantle). The rheology of the upper mantle may play an essential role in controlling postseismic and interseismic deformation of the upper crust. For models with a purely elastic medium (*e.g.*, the dislocation model), given medium properties, fault geometry and plate convergence rate, the model results are controlled only by the position and size of the locked zone and a transition between zones of no slip and full slip. But for models with a viscoelastic medium (*e.g.*, the model used in this work), stress relaxation of the viscoelastic medium greatly contributes to the postseismic and interseismic crustal deformation. “Relaxation” means that stress decreases with time subject to an externally imposed and fixed displacement field. The work of Part II focuses on crustal deformation associated with great subduction zone earthquakes. The significant crustal deformation associated with great earthquakes prevails over deformations due to other tectonic processes in great earthquake cycles and thus helps to glean underlying fundamental subduction zone processes.

After a great subduction zone earthquake, there are three primary processes that

control the crustal deformation (Figure 5.3). After the earthquake, segments of the megathrust surrounding the coseismic rupture zone may undergo continuous aseismic slip that is called afterslip (process numbered “1” in Figure 5.3). Afterslip of the fault is believed to decay rapidly with time (see discussion in section 6.6) and causes the upper plate to move towards the trench at high velocities. Segments of the megathrust that do not undergo afterslip must be re-locked to accumulate strain for next events. The re-locking of the fault (process numbered “3” in Figure 5.3) causes the upper plate to move slowly landward. At the coseismic stage, the earthquake induces shear stresses in the upper mantle. The subsequent stress relaxation (process numbered “2” in Figure 5.3) causes areas farther away from the trench to move slowly seaward to catch up with the seaward coseismic motion.

At different stages of the earthquake cycle, portions of the contributions of these three processes to the crustal deformation are different. A general pattern of crustal deformation associated with great subduction zone earthquakes in earthquake cycles is illustrated in Figure 5.4. A brief description of the crustal deformation at different stages of the earthquake cycle is as follows (*e.g.*, *Wang*, 2007).

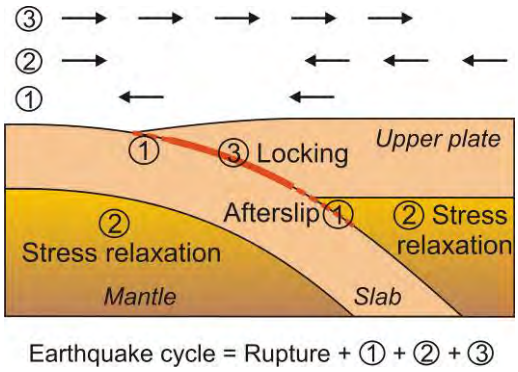

Figure 5.3. Sketch of three primary processes after a great subduction zone earthquake. Aseismic afterslip occurs around the rupture zone (denoted “1”). The coseismically stressed mantle undergoes viscoelastic relaxation (denoted “2”). The fault is relocked (denoted “3”).

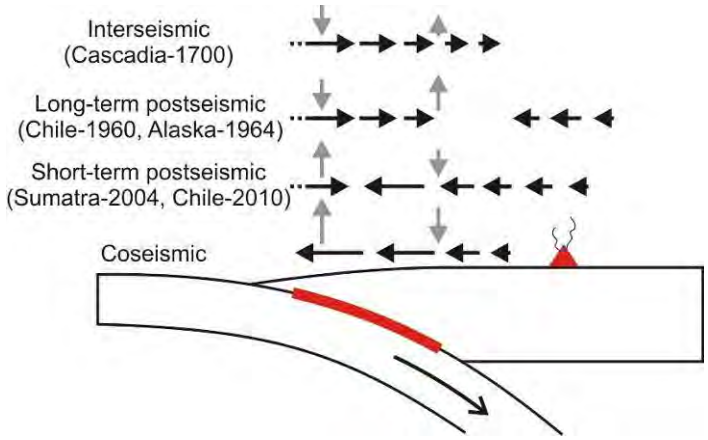

Figure 5.4. Sketch of crustal deformation in great subduction zone earthquake cycles. Black and light-shaded arrows at the top show the sense of horizontal and vertical motion of Earth's surface in an earthquake cycle, respectively. Red thick line and red solid triangle illustrate locations of the seismogenic zone and the arc.

(1) Coseismic stage: A sudden coseismic slip of the seismogenic zone stretches the overlying continental plate and results in seaward crustal motion mostly near the rupture zone although deformation by giant M_w 9 events such as the 2004 M_w 9.2 Sumatra earthquake (*Chlieh et al.*, 2007) can be detected at rather large distances from the rupture zone. For vertical deformation, maximum subsidence occurs roughly above the downdip termination of the coseismic slip. At this stage, deformation of the upper mantle is comparably small because shear stresses are induced to resist the coseismic deformation.

(2) Short-term postseismic stage: Depending on the earthquake size, time for the deformation at this stage to be detectable spans from a few days to a couple of years. At this stage, the fault is re-locked ("3" in Figure 5.3) or undergoes afterslip especially just downdip of the rupture zone ("1" in Figure 5.3). Depending on the interplay of the coseismic deformation and the plate convergence rate, the re-locking of the fault may result in landward movement of the coastal area within a few years after the earthquake. The viscoelastic relaxation of the earthquake-induced stresses in the mantle ("2" in Figure 5.3) at this stage results in the seaward motion in a broad area (*e.g.*, the back arc) catching up with the coseismic motion. Because of the combined effects of the afterslip of the fault and the transient creep of the upper mantle, deformation at this stage is much

faster than decades or centuries later.

(3) Long-term postseismic stage: The fault is locked, and the upper mantle undergoes steady-state viscoelastic deformation. The coastal area moves landward due to the locking of the fault while the inland area still slowly moves seaward due to the stress relaxation. The detectable opposing motion may last less than a couple of years for M_w 8 earthquakes or decades for giant M_w 9 earthquakes. For the vertical deformation, the region of maximum coseismic subsidence bounces back to become a region of uplift, and the region of coseismic uplift that is near the trench becomes a region of subsidence. Detailed evolution of the vertical deformation during this period may depend on the Earth structure, physical properties of the rocks, and the earthquake size, and is still under investigation.

(4) Interseismic stage: The earthquake-induced stresses are mostly relaxed, and the upper plate moves slowly landward due to the locking of the fault. For the vertical deformation, the uplift in the vicinities of the downdip edge of the seismogenic zone slows down.

In addition to the above main characteristics, there may be significant differences between different convergence margins or between different segments of the same margin. The differences between different margins may be related to specific tectonic settings at each margin such as the plate convergence rate and properties of the incoming plate (the age, sediment thickness, sea mounts, etc) (*e.g.*, *Demets et al.*, 1994; *Goldfinger et al.*, 2003; *Wang*, 2007). An earthquake may rupture only segments of the megathrust, and thus different segments of the same margin may be at different stages of the earthquake cycle (*e.g.*, *Thatcher*, 1984; *Newcomb and McCann*, 1987; *Cisternas et al.*, 2005; *Kelsey et al.*, 2005). Note that time scales of the crustal deformation associated with small earthquakes are different from those shown in Figure 5.4. For small earthquakes, seaward motion of the inland area disappears shortly after the earthquake (see discussion in *Hu et al.*, 2004). For example, the whole upper plate started to move landward a couple of years after the 1995 M_w 8.0 Antofagasta earthquake (*Delouis et al.*, 1998; *Klotz et al.*, 1999), a scenario of interseismic deformation shown in Figure 5.4.

Chapter 6. Finite Element Models of Subduction Earthquake Cycles in a Spherical Earth

The crustal deformation in response to a megathrust earthquake depends on the structure of the Earth, the physical properties of the rock and the coseismic slip of the fault. Before I examine the great earthquakes in real subduction zones in Chapter 7, I use simple generic models to investigate the effects of various model parameters in this chapter in order to understand the fundamentals of the earthquake-related processes. Knowledge of tests in this chapter help to understand the modelling results of real subduction zones.

6.1. Model concept

We focus on the first-order pattern of crustal deformation in earthquake cycles, and ignore fine details of the heterogeneity. Simplifications allow us to focus on the essential aspects of the fundamental physical processes. The conceptual model used by *Hu et al.* (2004) is schematically shown in Figure 6.1. The model consists of an elastic upper plate, an elastic subducting plate including the slab, a viscoelastic continental upper mantle, and a viscoelastic oceanic upper mantle. Lateral and downdip variation of the viscosity of the upper mantle will be investigated in section 6.4. Otherwise, material in each of these tectonic units is assumed to be uniform.

For a subduction fault in the interseismic period, a shallow portion is assumed to be locked (locked zone), and from a certain depth downdip, the fault is assumed to slip aseismically at the full plate convergence rate. In the locked zone, the slip deficit accumulated during the interseismic period is assumed to be completely recovered in future earthquakes. After removing steady state plate convergence, the locked zone of the fault can equivalently described as to slip backwards slowly, and the slip deficit becomes backslip (*Savage*, 1983). In reality, the fault slip over the locked zone is likely to be time dependent and may be better described with a laboratory-derived time- and state-dependent friction law (*Ruina*, 1983; *Dieterich*, 1978, 1994). The present work is designed to understand the crustal deformation in response to given faulting motion, not the mechanics of the fault itself. Therefore, slip along the fault is kinematically prescribed using the split-node method (*Melosh and Raefsky*, 1981). The fault at shallow depths is

assigned with a uniform slip (rupture zone), and at greater depths, the fault slip is assumed to taper linearly to zero (transition zone).

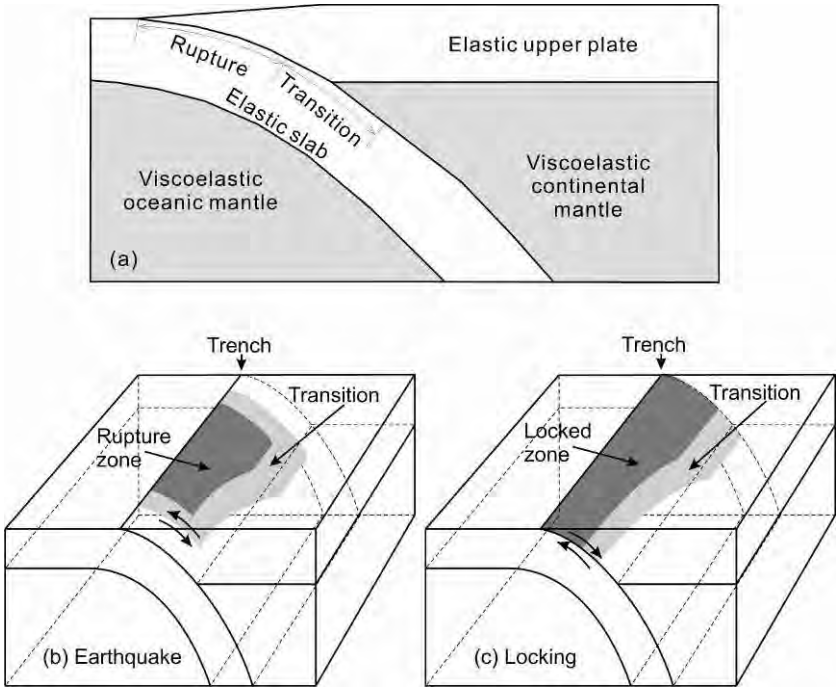

Figure 6.1. A conceptual finite element model of subduction zone earthquake cycles. (a) Conceptual representation of the subduction zone model (from *Hu et al.*, 2004). (b) Coseismic slip model. (c) Backslip model for fault locking after the earthquake. Slip in (b) or backslip rate in (c) tapers to zero over the transition zone (lighter shading).

The simplest view of an earthquake cycle is that the fault is completely locked during the interseismic period, and the accumulated slip deficit is completely recovered during an earthquake. This process can be illustrated by the stairway case in Figure 6.2a. The other end-member scenario is that the fault slips continuously and aseismically at all times, as shown by the straight dashed line in Figure 6.2a. The dot-dashed line in Figure 6.2a describes an intermediate case in between. In the real Earth, the fault slip distribution is likely to be a complicated function of space and time. For example, some parts of the locked zone may slip aseismically before and/or after an earthquake; some parts of the locked zone may slip aseismically during an interseismic period; and the size

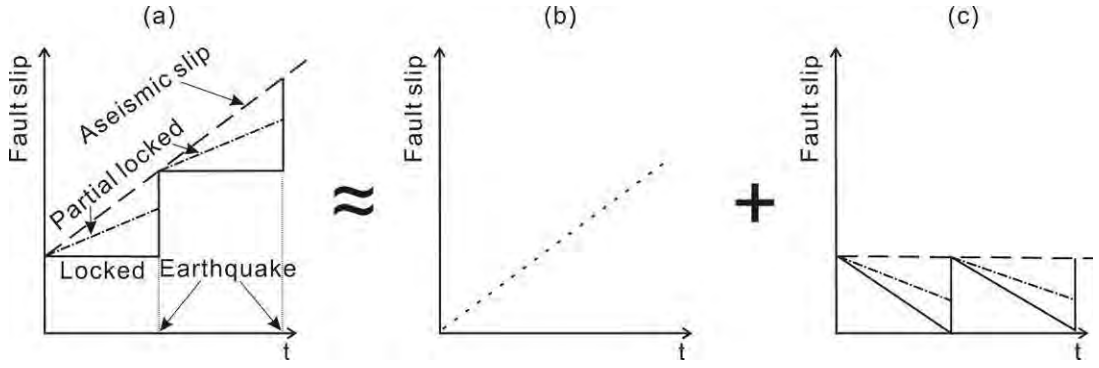

Figure 6.2. Decomposition of the fault slip into a steady slip and a sawtooth motion. Dashed and solid lines represent aseismic slip and purely seismic slip, respectively, and dash-dotted line represents an intermediate case.

of the locked zone may change with time in response to thermal, chemical, and hydrogeological processes. My work focuses on the first-order behaviour of the mechanical system. For simplicity, the faulting behaviour has been idealized. In the model, any aseismic slip is averaged over the entire interseismic period, such that the fault slips interseismically at a constant rate that is less than the plate convergence rate ("partial locking"). The same treatment of fault motion was used by *Zheng et al.* (1996).

The slip budget in Figure 6.2a can be described as a superposition of steady plate motion shown in Figure 6.2b and repetitive cycles of a sudden forward slip (earthquake) followed by backward slow slip (slip deficit) shown in Figure 6.2c. It is assumed that the steady motion component has no contribution to crustal deformation in earthquake cycles and is subtracted from the model. Therefore, we only need to consider the sawtooth cyclic component. With this decomposition, the aseismic component of the fault motion (assumed to be continuous slow slip) in the interseismic period is removed as part of the steady state plate motion. In other words, the effect of partial aseismic interseismic slip is modelled using a slower backslip rate. Deformation of a viscoelastic Earth in an earthquake cycle (the sawtooth fault motion) is therefore a combination of two components, that caused by the coseismic forward slip (earthquake) and that caused by the interseismic backslip (locking). These two components are modelled separately in this work (Figures 6.1b and 6.1c), and the total effect is a linear combination. This chapter

focuses on investigation of effects of the model geometry, the rock physical property and the fault slip pattern, and the conclusion drawn in this chapter applies to both earthquake and backslip models. Therefore, only the earthquake component is presented in this chapter to avoid redundancy.

Following *Wang et al.* (2001), the Young's modulus of the elastic plates and upper mantle are assumed to be 120 GPa and 160 GPa, respectively, and the Poisson's ratio and rock density are assumed to be 0.25 and 3.3 g/cm^3, respectively, for the entire system. The gravitational acceleration is assumed to be 10 m/s^2. Gravity is not directly modelled as a body force, but its effect of tending to bring a perturbed system back to the hydrostatic state is modelled using a pre-stress advection approach (*Peltier*, 1974; *Wang et al.*, 2001). For simplicity, viscoelastic behaviour of the upper mantle is represented by Maxwell rheology (see discussion in section 5.1). The upper mantle represented by the transient rheology will also be tested. Based on *Hu et al.* (2004), viscosities of the oceanic and the continental mantle are 10^{20} Pa s and 10^{19} Pa s, respectively. The above physical properties are denoted as a reference testing model in this chapter. Other testing models with one or more variable modified from this reference testing model will be examined. The finite element program PGCvise2 is used in Part II.

6.2. Comparison between spherical and flat Earth models

A flat Earth in the Cartesian coordinate system is widely used in models of crustal deformation at small spatial scales in which the curvature of the Earth can be ignored. Appendix C2.2 demonstrates that in a 10 km^3 cubic box, uniform constant slip over a rectangular fault leads to the same viscoelastic deformation in both the spherical and flat Earth. At larger scales, approximating the spherical Earth with a flat Earth results in distortion of model geometry, and the further away from the model centre, the larger the distortion. In this section, I will investigate the effects of the geometrical distortion using models involving either constant surface loading or thrust faulting.

6.2.1. Uniform constant pressure on top surface

In this test, I examine the surface deformation of a box subject to a uniform constant pressure σ_0 over the top surface in both the spherical and flat Earth (Figure 6.3). For the

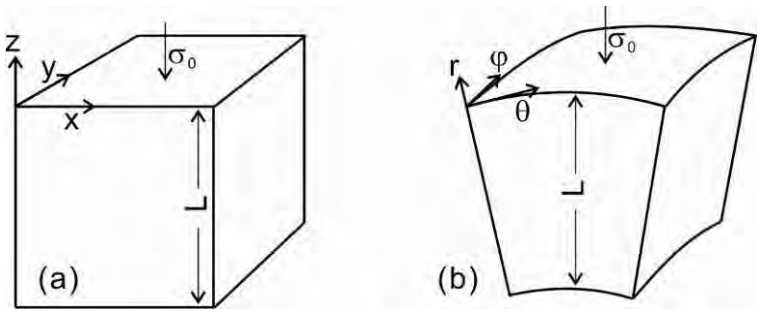

Figure 6.3. Sketch of the testing models in the flat (a) and spherical (b) Earth. The Cartesian coordinate system *x*-*y*-*z* and the spherical system r-θ-φ are used in the flat and spherical Earth, respectively. A uniform pressure load σ_0 is applied to the top surface.

surrounding and bottom surfaces, displacements are fixed at zero in the normal direction and are free in directions parallel to the surface. Gravitational acceleration is assumed to be zero. The vertical dimension of the box is denoted *L* (Figure 6.3). First, I will examine the elastic deformation, the instantaneous response to σ_0, using analytical solutions for the same box models as shown in Figure 6.3. The analytical solutions are free of numerical artefacts and serve to benchmark the numerical solutions. They also provide convenience in exploring the parameter space to understand the fundamental mechanics. With a good understanding of the elastic deformation, I will then examine the viscoelastic deformation in numerical models.

In a flat Earth, the testing model is a cubic box (Figure 6.3a). The vertical elastic deformation U_z of the top surface can be written from the strain-stress relationship,

$$U_z = -\frac{\sigma_0 L(1+\upsilon)(1-2\upsilon)}{E(1-\upsilon)} \tag{6-1a}$$

where v and E are the Poisson's ratio and the Young's modulus, respectively. The normal stresses in the box are uniform,

$$\begin{cases} \sigma_x = \sigma_y = \dfrac{v\sigma_0}{1-v} \\ \sigma_z = \sigma_0 \end{cases} \tag{6-1b}$$

For v = 0.25, the magnitude of the two identical horizontal stresses is one third of the vertical stress σ_0.

In the spherical Earth, the box is part of a spherical shell (Figure 6.3b), and (6-1) does not apply. *Xu* (1979) presented a stress solution for an elastic spherical shell subject to surface and bottom pressures. By replacing the bottom pressure in *Xu*'s solution (1979) with a zero displacement, the radial (vertical) elastic deformation U_r of the top surface can be obtained as

$$U_r = -\frac{\sigma_0 L(1+\upsilon)(1-2\upsilon)}{E(1-\upsilon)} \frac{(1-\upsilon)(\delta^2+\delta+1)}{1+\upsilon+2\delta^3(1-2\upsilon)} = U_z \frac{(1-\upsilon)(\delta^2+\delta+1)}{1+\upsilon+2\delta^3(1-2\upsilon)} \tag{6-2}$$

where $\delta = 1 - L/R$, and R is the radius of the Earth. From (6-1a) and (6-2), the ratio of U_r over U_z is

$$\frac{U_r}{U_z} = \frac{(1-\upsilon)(\delta^2+\delta+1)}{1+\upsilon+2\delta^3(1-2\upsilon)} \tag{6-3}$$

In contrast to the uniform stresses in the flat Earth, both the vertical (radial) stress σ_r and the horizontal (tangential) stresses $\sigma_\theta = \sigma_\varphi$ in the spherical Earth, where σ_θ and σ_φ are normal stresses in the west-east and south-north directions (Figure 6-3b), respectively, depend on depth d:

$$\begin{cases} \sigma_r = \dfrac{\sigma_0 \left[\dfrac{(1-2\upsilon)\left((R-L)^3 + 2R^3 - 2r^3\right)}{r^3(1+\upsilon)} - \dfrac{1}{2\delta^3} - \dfrac{1}{2} \right]}{(1-\delta^3)\left(\dfrac{1}{2\delta^3} + \dfrac{1-2\upsilon}{1+\upsilon} \right)} \\ \sigma_\theta = \sigma_\varphi = \dfrac{\sigma_0 \left[(R-L)^3 - R^3 \right] \left[\dfrac{1}{(R-L)^3} - \dfrac{(1-2\upsilon)}{r^3(1+\upsilon)} \right]}{2(1-\delta^3)\left(\dfrac{1}{2\delta^3} + \dfrac{1-2\upsilon}{1+\upsilon} \right)} \end{cases} \tag{6-4}$$

where $r = R - d$.

For $R = 6.378 \times 10^6$ m and $E = 160$ GPa, U_r / U_z as a function of v is shown in Figure 6.4a for different L values. The range between the upper and lower bounds of U_r / U_z increases with increasing L values (Figure 6.4b). For $L = 500$ km, approximating the spherical Earth with a flat Earth results in a maximum of ~8 percent difference in the model results (Figure 6.4b). If $v = 0.25$, U_r / U_z is greater than unity but is less than 1.04 for L up to 2000 km.

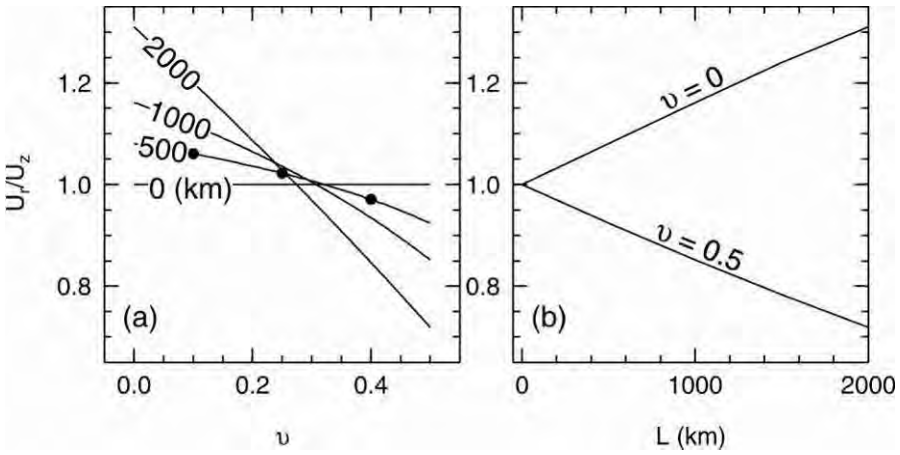

Figure 6.4. Comparison of the elastic deformation of the top surface due to a uniform pressure σ_0 in the flat or spherical Earth. Results shown are produced by the analytical solutions, but the FEM would give the same solutions with numerical errors less than 10^{-5} m. (a) Ratio of surface displacements in the spherical (U_r) and flat (U_z) Earth as a function of the Poisson's ratio ν for different L values. Three black dots represent $\nu = 0.1$, 0.25, 0.4 for L = 500 km, respectively, for which the subsequent viscoelastic deformation will be examined (Figure 6.5). (b) For different L values, upper ($\nu = 0$) and lower ($\nu = 0.5$) bounds of U_r / U_z.

If the material is fully compressible ($\nu = 0$), the horizontal stresses are zero, and the vertical deformation is controlled only by the vertical stress. Because the area of surface-parallel cross-sections decreases with increasing depth in the spherical Earth, the vertical stress increases with depth compared to the uniform vertical stress in the flat Earth. This results in a larger averaged vertical stress in the spherical Earth, and thus a larger surface displacement U_r ($U_r / U_z > 1.0$). If the material is not fully compressible ($\nu > 0$), the vertical deformation is controlled by the horizontal stresses as well as the vertical stress. Under the same vertical loading, the horizontal strain in the spherical Earth is not zero because arc length in the θ and φ directions shortens with increasing depth. The total effect is to have a greater resistance to deformation and hence a smaller U_r. Thus U_r / U_z decreases with increasing ν. If $\nu = 0.5$ representing an incompressible material, U_r / U_z is the smallest and is less than 1. To have $U_r = U_z$, we must have

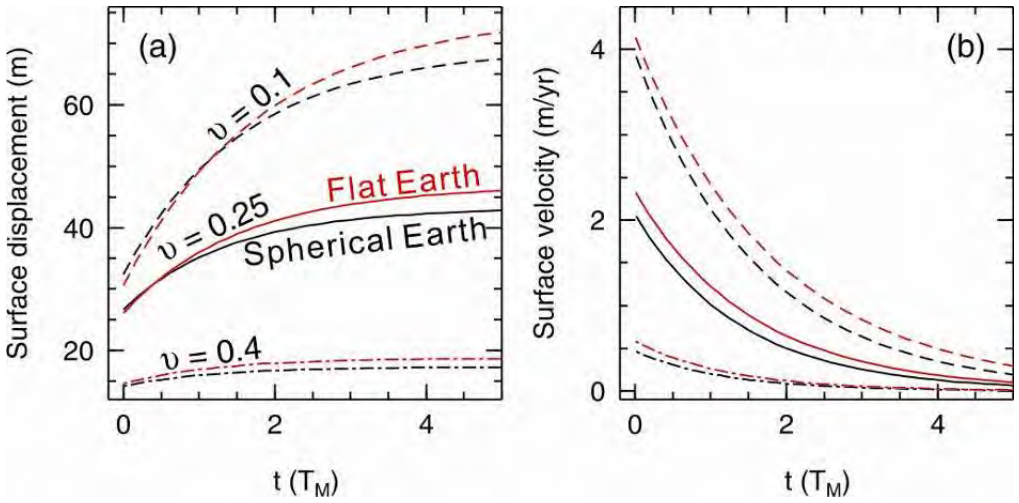

Figure 6.5. Comparison of the viscoelastic deformation of the top surface of the box models of Figure 6.3 in the flat or spherical Earth. The results are produced using numerical models. (a) Viscoelastic evolution of the surface vertical displacement in the spherical (black) and the flat (red) Earth for three different v values as labelled. The U_r/U_z of the elastic deformation of these three models is illustrated in Figure 6.4a. Time t is in terms of T_M = 5.0 yr. (b) Surface vertical velocities of the same solutions as in (a).

$$v = 1 - \frac{1 + \delta + \delta^2}{1 + 1.5\delta + 2\delta^2} \tag{6-5}$$

For the same models, the finite element models (FEM) reproduce the analytical elastic-deformation solutions almost exactly with errors less than 10^{-5} m (time t = 0 in Figure 6.5a). With the FEM nicely benchmarked against the analytical solutions, we can confidently use the finite element models to examine the viscoelastic deformation (t > 0 in Figure 6.5a). Assuming L = 500 km, a Maxwell viscosity 10^{19} Pa s (corresponding to a Maxwell relaxation time T_M = 6.0 yr if v = 0.25), R = 6.378 × 10^6 m, and E = 160 GPa, three examples for v = 0.1, 0.25, and 0.4 are shown in Figure 6.5a.

Although U_r /U_z of the elastic deformation (t = 0) may be greater or less than unity, the viscoelastic deformation (t > 0) in the spherical Earth is always smaller than in the flat Earth after a certain time depending on model parameters (no later than t = 1.5 T_M in the examples of Figure 6.5a). All the three models in Figure 6.5b produce smaller surface velocity in the spherical Earth than that of the flat Earth.

After a long time when the viscoelastic creeping of the boxes shown in Figure 6.3 stops (zero surface velocity), the final stress state in the fully relaxed boxes must be a "hydrostatic" state in which the normal stresses equal the external pressure load σ_0 in all directions. For the same top surface area, the volume of any testing box in the spherical Earth (Figure 6.4a) is smaller than in the flat Earth (Figure 6.4b). The smaller volume of the box in the spherical Earth requires less vertical displacement of the surface to reach the final "hydrostatic" state. This lower velocity in the spherical Earth is because the non-uniform stresses due to the initial elastic deformation necessitates less material flow within the box.

6.2.2. Uniform slip of a rectangular fault

Following the model in Figure 6.1b, a testing model in this section includes an elastic subducting slab, an elastic upper plate, a viscoelastic continental upper mantle and a viscoelastic oceanic upper mantle (Figure 6.6). Except for the free top surface, boundary conditions for the other surfaces are the same, that is, displacement is fixed at zero in the normal direction and is free in directions parallel to the surface. A 20-m uniform slip is applied over a rectangular fault at $t = 0$, 100 km wide (W) in the downdip direction and 400 km long in the striking direction (N-S). The fault slip tapers linearly with depth to zero in a 50 km wide transition zone downdip of the full rupture zone. There is no further fault slip at $t > 0$. The model boundaries are placed very far away from the rupture zone to minimize the boundary effects. The Young's modulus is 160 GPa for the viscoelastic upper mantle and 120 GPa for the elastic slab and the upper plate. The Poisson's ratio is 0.25 for the entire system. The upper mantle is assumed to have the Maxwell rheology with a viscosity of 10^{19} Pa s (T_M = 5.0 yr) for both the continental and the oceanic upper mantle. Although the testing model is three dimensional (3D), only the surface deformation along the trench-normal line bisecting the rupture zone will be presented for the purpose of examining the geometry effect.

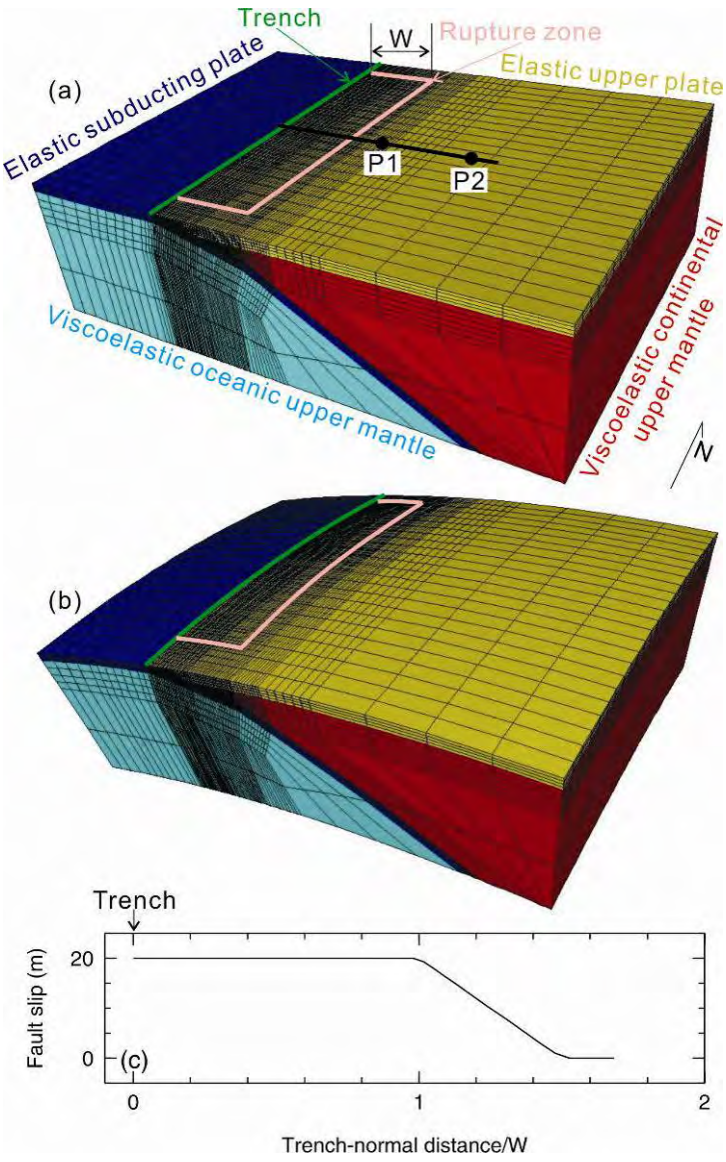

Figure 6.6. Central part of the three-dimensional finite element mesh and the coseismic slip distribution of the fault. (a) Finite element mesh in the flat Earth. (b) Finite element mesh in the spherical Earth. Tectonic units labelled in (a) have the same colours in (b). Surface deformation along the thick black line will be presented in Figure 6.7. Horizontal trench-normal width of the rupture zone is denoted *W*. Deformation evolution of surface points P1 and P2, 1.5W and 3W away from the trench, respectively, will be presented in Figure 6.8. (c) Illustration of the coseismic slip distribution in the trench-normal direction along the fault.

For both models in Figure 6.6, the instantaneous elastic response (time $t = 0$) to the sudden slip over the fault is shown in Figure 6.7a (green solid line). The slight difference between elastic solutions in the spherical and flat Earth is not visible at the plot scale. In section 6.2.1, the model box undergoes creeping deformation under the fixed external pressure σ_0, and the elastic deformation of the box is different between the spherical and flat Earth. In the present test, the model box undergoes relaxation of the stresses induced by the fixed displacement field, the fault slip, and the elastic deformation is thus almost identical in the two models. In the strike-normal direction, the whole area landward of the trench undergoes seaward deformation. In the vertical direction, areas immediately landward of the trench undergo uplift, and areas further landward undergo subsidence. This elastic deformation can be exactly reproduced using an analytical dislocation solution (*Okada*, 1985). Shear stresses at greater depths downdip of the fault and in the upper mantle are induced to resist the coseismic deformation. After the earthquake, the stress relaxes and causes prolonged seaward deformation in the areas landward of the rupture zone (Figure 6.7b).

For the viscoelastic deformation ($t > 0$), the horizontal displacement in the spherical Earth is smaller than in the flat Earth for the time covered by the model runs (upper panel of Figure 6.7a). I have run the models to $t = 1200$ yr, and the model behaviour is qualitatively the same. The horizontal velocity in the spherical Earth is also smaller (upper panel of Figure 6.7b). The vertical displacement in the spherical Earth is approximately the same as in the flat Earth in the vicinities of the trench, but is larger in areas further landward (lower panel of Figure 6.7a). The pattern of the vertical velocity is more complex (lower panel of Figure 6.7b).

The difference between the two models is further demonstrated by the deformation evolution of two surface points whose locations are shown using solid circles in the top panel of Figure 6.6a. Elastic deformation is the same in both models ($t = 0$ in Figure 6.8a), as already shown in Figure 6.7a. For the viscoelastic deformation ($t > 0$) in the horizontal direction, the seaward displacement in the spherical Earth decreases with time more slowly than in the flat Earth (upper panel of Figure 6.8). For the viscoelastic deformation ($t > 0$) in the vertical direction, the velocity in the spherical Earth is generally smaller than in the flat Earth (lower panel of Figure 6.8b). The vertical

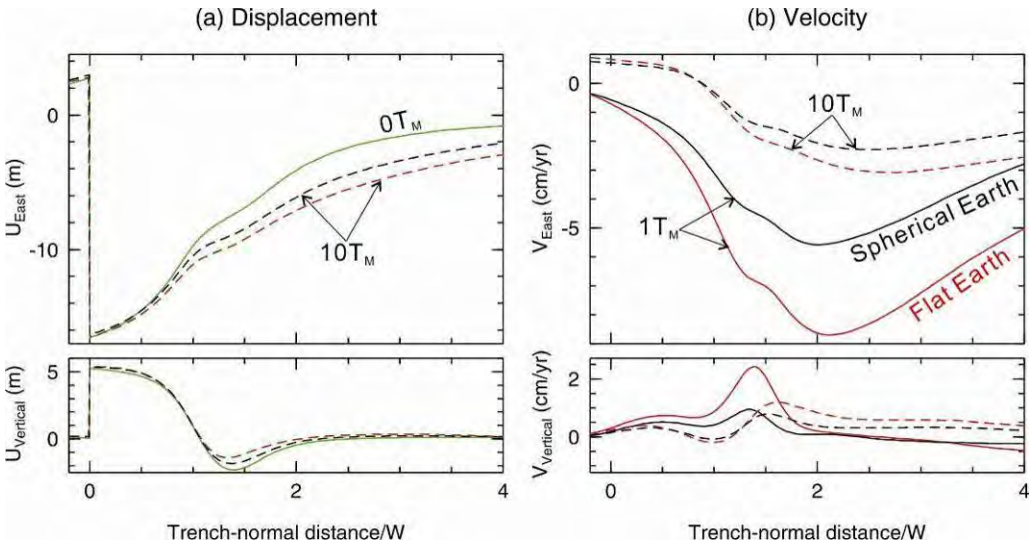

Figure 6.7. Comparison of surface deformation between the spherical and flat Earth. (a) Surface displacements along a trench-normal line shown as a thick black line in Figure 6.6. Note that the coseismic deformations (the green solid line) in both models are almost identical and are shown as a single curve. (b) Surface velocities of the same solutions as in (a). Upper and lower panels illustrate deformation in the trench-normal and vertical (up is positive) directions, respectively. In both (a) and (b), black and red colours represent results in the spherical and flat Earth, respectively. Solid and dashed lines represent results at different times as labelled. T_M = 5.0 yr.

displacement in the spherical Earth is larger or smaller than in the flat Earth, and the deformation pattern is more complex.

From this test, we have learned the following points. For the elastic deformation (t = 0) under thrust faulting, approximating the spherical Earth with a flat Earth results in negligible differences. For the viscoelastic deformation (t > 0), the velocity difference between the two models is the largest shortly after the earthquake event and diminishes with time (*e.g.*, surface V_{East} in the spherical Earth is 0% – ~40% of that of the flat Earth at $t = 1T_M$ shown in Figure 6.7). The difference in the vertical deformation is the largest just landward of the rupture zone.

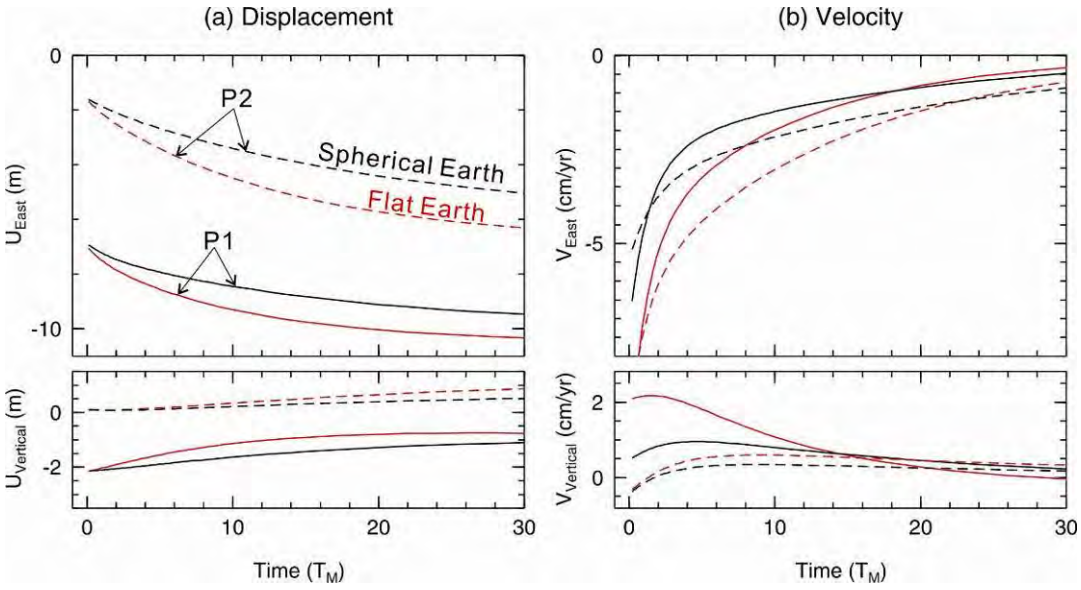

Figure 6.8. Comparison of deformation evolution of two surface points between the spherical (black) and flat (red) Earth. Displacement and velocity evolution are plotted in (a) and (b), respectively. Upper and lower panels represent deformation in the strike-normal and vertical directions, respectively. Solid and dashed lines represent deformation at surface points P1 and P2, respectively, whose locations are shown in Figure 6.6a.

6.3. Effects of the existence and the thickness of the subducting slab

Layered-Earth models neglecting the existence of the subducting slab (*e.g.*, *Pollitz*, 2003; *Wang et al.*, 2003, 2006) are widely used to study the crustal deformation associated with megathrust earthquakes. However, a subducting slab may play an important role in the viscoelastic crustal deformation because the slab affects the pattern of the material flow due to the relaxation of the earthquake-induced stresses in the upper mantle. In this section, the effects of the existence of the slab and the effects of the thickness of the slab will be examined.

A reference testing model (REF) in the spherical Earth is shown in Figure 6.9. Compared to the 3D testing model in section 6.2.2 shown in Figure 6.6b, the REF is a 3D "slice" with only one finite element in the strike direction. For the thrust faulting, the deformation in the strike direction is much smaller than in the trench-normal direction, and the "two-dimensional" ("2D") REF is adequate for investigating the effects of model

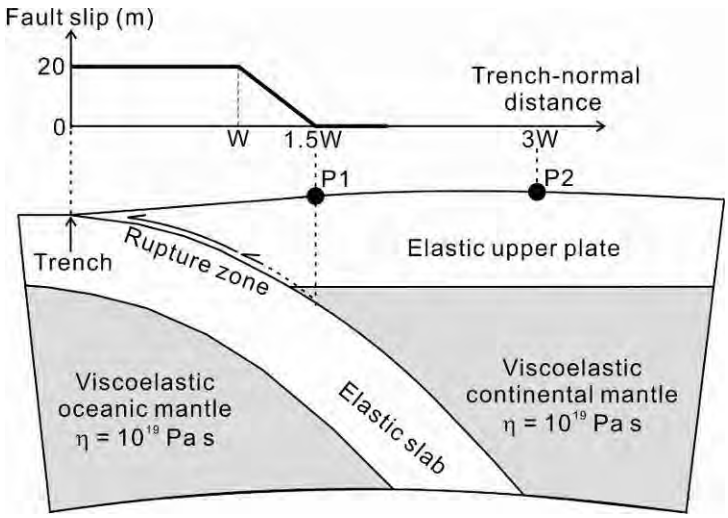

Figure 6.9. Sketch of the reference testing model (REF). The horizontal width of the rupture zone assigned with a 20-m uniform slip is *W*. Trench-normal distances of surface points P1 and P2 are 1.5W and 3W, respectively. Locations of P1 and P2 are also shown in Figure 6.6a.

parameters. Note that in the spherical Earth, there is no such thing as the plane strain condition. Other model parameters in the REF, such as, the structure of the Earth, rock physical properties, and boundary conditions, are the same as the testing model shown in Figure 6.6b. Testing models in the remaining sections of this Chapter are based on the REF with one or more model parameters varied.

The REF in which the slab extends to the bottom of the model domain of 500 km depth is compared with a layered Earth testing model without a slab. In the no-slab model, except for the absence of the subducting slab, all the model parameters are the same as in the REF. As expected, the elastic response ($t = 0$) to the megathrust slip is almost identical in both models (green line in Figure 6.10a). For the viscoelastic deformation ($t > 0$), there are dramatic differences in the velocities and the vertical displacement between the two models. The vertical displacement near the landward edge of the rupture zone is ~1 m in the no-slab model in contrast to ~–2 m in the REF at $t = 10$ T_M (lower panel of Figure 6.10a). The vertical velocity in the same area in the no-slab model is ~10 times that of the REF for t up to 10 T_M (lower panel of Figure 6.10b).

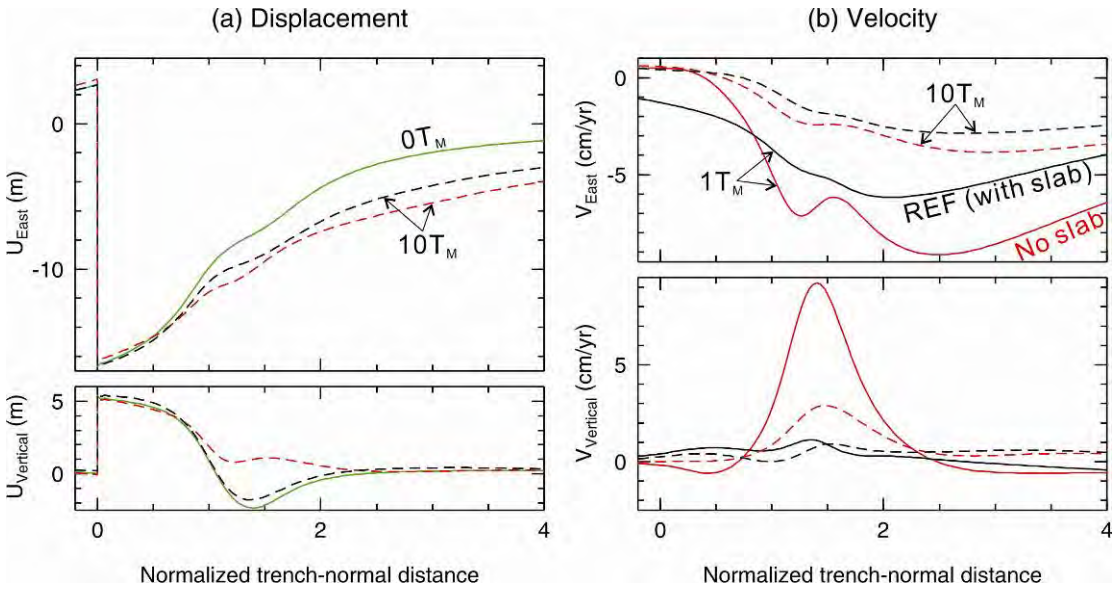

Figure 6.10. Comparison of surface deformation between the REF (with slab, black) and the no slab model (red). Surface displacements and surface velocities are plotted in (a) and (b), respectively. Upper and lower panels illustrate deformation in the trench-normal and vertical directions, respectively. Maxwell relaxation time of the continental upper mantle T_M is 5.0 yr. Coseismic deformations of both models are almost identical (green line in (a)) and are shown as a single curve.

Shortly after the earthquake, *e.g.*, $t = 1\ T_M$, the horizontal velocity in the no-slab model is ~50% larger than that in the REF (upper panel of Figure 6.10b). After a longer time, *e.g.*, $t = 10\ T_M$, the difference in the horizontal velocity becomes small. A testing model in which the slab extends only to a depth of 200 km produces viscoelastic surface deformation almost identical with the REF (results not shown). Note that the deformation of the "2D" REF shown in Figure 6.10 is almost identical with the 3D testing model in the spherical Earth shown as black lines in Figure 6.7.

A sudden slip of the megathrust induces stresses in the upper mantle, and these induced stresses serve to resist coseismic deformation. The earthquake-induced stress field is almost identical in both the REF and the no-slab model because the coseismic slip distribution along the fault is the same. However, the pattern of material flow caused by the subsequent viscoelastic relaxation of the stresses is dramatically different in these two

models. The elastic subducting slab acts as a flow barrier to slow down the flow of material in the viscoelastic upper mantle. Without a slab, the flow of the material in the upper mantle is faster, allowing the elastic upper plate to move towards the trench and upward at a greater speed.

The subducting slab in “cold” subduction zones such as Northeast Japan subduction zone is much thicker than that of warm subduction zones such as Cascadia and South Chile. Another testing model (thicker-slab model) in which the slab thickness is 60 km is used to compare with the REF with a 30-km thick slab. In contrast to the significant difference between the REF and no-slab models shown in Figure 6.10, the REF and the thicker-slab model produce very similar deformation (Figure 6.11).

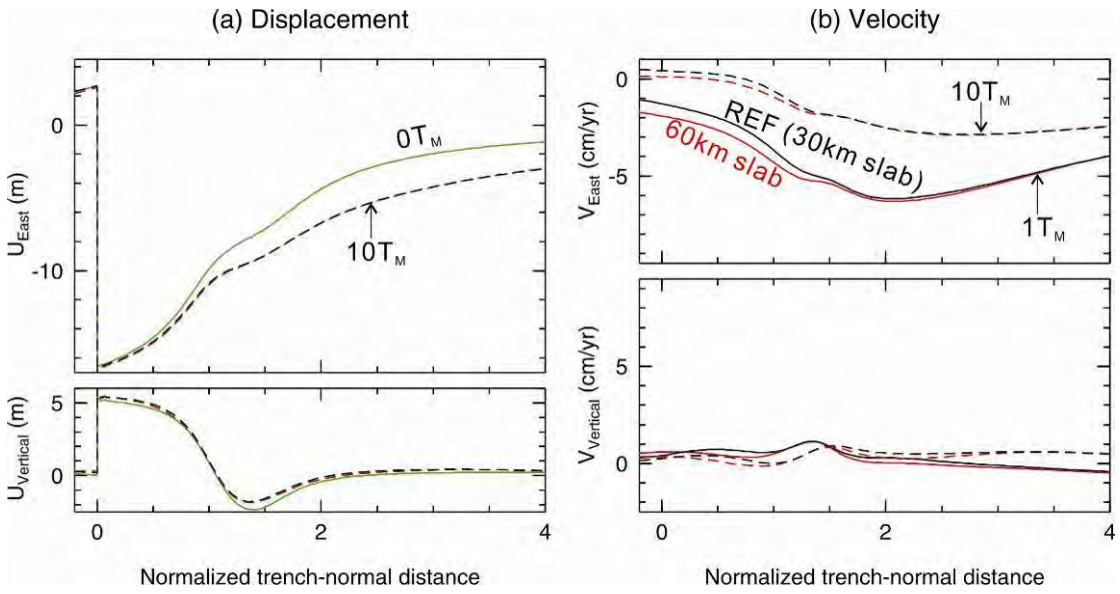

Figure 6.11. Comparison of surface deformation between the REF (30 km slab, black) and the 60-km slab model (red). Surface displacements and surface velocities are plotted in (a) and (b), respectively. Upper and lower panels illustrate deformation in the trench-normal and vertical directions, respectively. Coseismic deformations of both models are almost identical (green line in (a)).

Points that we have learned from this test are as follows. For the elastic response to the earthquake faulting (t = 0), changes in the structure of the Earth, such as the existence

of the subducting slab or the slab thickness, result in negligible differences. For the viscoelastic deformation ($t > 0$), the absence of the slab has a dramatic effect. The vertical velocity of the no-slab model is much larger than that of the REF for t up to $10^1\ T_M$. The difference in the horizontal velocities in both the REF and the no-slab model is large at times of $10^0\ T_M$ and is acceptable at longer times $t > 10^1\ T_M$. Variations on the slab thickness result in slight differences in the viscoelastic deformation.

6.4. Effects of the heterogeneous viscosity of the upper mantle

In the previous section, it is demonstrated that the existence of the subducting slab greatly affects the pattern of material flow during the relaxation of the earthquake-induced stresses in the upper mantle. The rate of the stress relaxation is controlled by the rheology of the upper mantle, such as the Maxwell rheology in the previous section. The viscosity may vary in the lateral or depth directions. In this section, I will examine the effects of the heterogeneous viscosity and the "cold" wedge corner between the elastic upper plate and subducting slab.

Global post-glacial rebound models are constrained by data mostly from continental interiors (cratons) and are widely used to examine crustal deformation at time scales of $10^3 – 10^4$ yr. Global post-glacier rebound models give viscosity values of the order of $10^{20} – 10^{21}$ Pa s (*e.g.*, *James and Ivins*, 1998; *Peltier*, 2004). Subduction zone earthquake models are constrained by data mostly from continental margins and are used to examine crustal deformation at time scales of 10^2 yr. Subduction zone earthquake models give viscosity values of the order of 10^{19} Pa s (*e.g.*, summarized by *Wang*, 2007). The order of magnitude difference in the viscosity values indicates that the viscosity of the upper mantle must increase from low values at the continental margin to high values below the continental interior. To address this viscosity difference, I derive a testing model (VS1) with variations in the viscosity values in the lateral direction (Figure 6.12b). In VS1, the upper mantle farther than 900 km from the trench has a viscosity 10^{20} Pa s, one order of magnitude larger than that within 800 km of the trench. The region in between is a transition zone in which the viscosity increases linearly from the lower value to the higher value. The structure of the upper mantle in the real Earth has yet to be well understood. The structure of the upper mantle in this test is based on the location of the

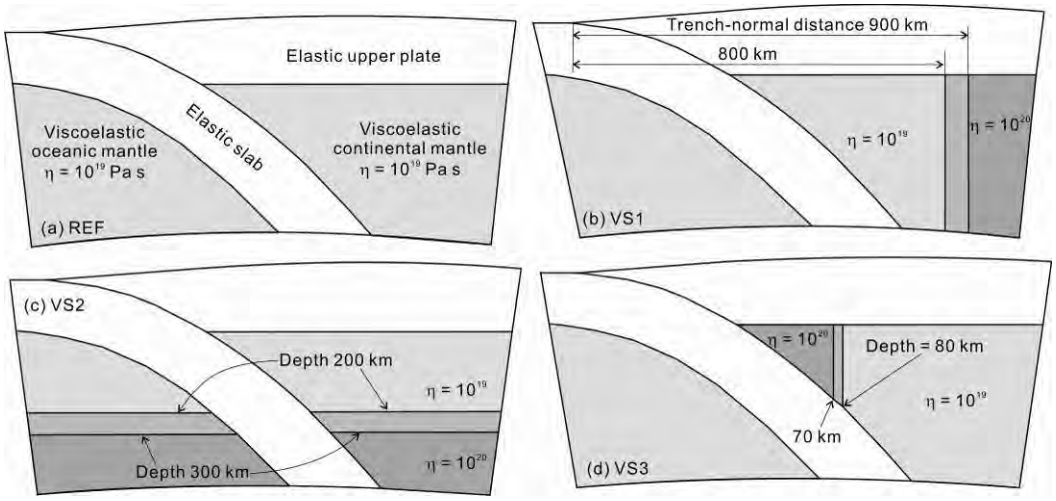

Figure 6.12. Sketch of four testing models. (a) The reference testing model (REF), the same as in Figure 6.9. The mantle viscosities in the other three testing models will be varied based on REF. (b) Lateral variation of the mantle viscosity (VS1). The viscosity of the mantle farther than 900 km from trench is assumed to be 10^{20} Pa s, one order of magnitude larger than that within 800 km. The viscosity of the region in between increases linearly from the lower value to the higher value. (c) Variation of the viscosity in the depth direction (VS2). The viscosity at depths $\geqslant$300 km is 10^{20} Pa s one order of magnitude larger than that at depths $\leqslant$200 km. A transition zone is placed in between. (d) Model of a cold wedge corner (VS3). The viscosity of the most seaward part of the mantle wedge where the slab is less than the depth 70 km is 10^{20} Pa s, one order of magnitude larger than that where the slab is greater than the depth 80 km.

North America craton relative to the Cascadia subduction zone (*e.g.*, *Currie, et al.*, 2004).

Layered-Earth models are widely used in the literature for post-glacier rebound modelling (*e.g.*, *James and Ivins*, 1998; *Peltier*, 2004) and earthquake modelling (*e.g.*, *Pollitz*, 2003; *Wang et al.*, 2003; *Pollitz et al.*, 2006; *Wang et al.*, 2006). A testing model (VS2) with variations in the viscosity in the depth direction is shown in Figure 6.12c. In VS2, the viscosity is 10^{20} Pa s at depths $\geqslant$300 km, one order of magnitude larger than that of depths $\leqslant$200 km. Similar to VS1, the region in between is a transition zone. The viscosity variation in the depth direction in VS1 is based on the work of *Pollitz* (2003).

The vertical variation of the viscosity in the real Earth is more complex (*e.g.*, *Dziewonski and Anderson*, 1981). The simplified viscosity variation in VS2 serves to demonstrate the salient effects of the viscosity layering.

Numerous thermal models of subduction zones have been used to study geodynamic processes of time scales of millions of years. *Wada and Wang* (2009) developed thermal models for many subduction zones and reported a common maximum depth of 70 – 80 km of the decoupling of the subduction interface. At depths shallower than 70 – 80 km, the material of the mantle wedge overlying the subduction interface is comparably cold and stays stagnant, that is, the mantle wedge is decoupled from the subduction interface. At depths greater than 70 – 80 km, the material is hot and flows with the subducting slab, that is, the mantle wedge is coupled with the subduction interface. Although the thermal models at time scales of 10^6 yr examine processes different from the subduction zone earthquake models, it is still of interest to examine how the "cold" wedge corner that is required by the thermal models may affect the viscoelastic deformation in subduction zone earthquake cycles. A testing model including a "cold" wedge corner (VS3) is shown in Figure 6.12d. In VS3, the viscosity of the most seaward part of the mantle wedge where the slab is shallower than 70 km is 10^{20} Pa s, one order of magnitude larger than farther landward where the slab is deeper than 80 km. The region in between is a transition zone.

Other model parameters in VS1, VS2 and VS3 are the same as in REF. These three testing models are compared with REF (Figure 6.13). Both VS1 and VS2 produce deformations vary similar to REF (Figure 6.13). At $t = 1\ T_M$, the horizontal velocity of VS3 is much smaller than that of REF (Figure 6.13a). The wavelength of the vertical velocity variation, the trench-normal distance between two neighbouring peak values, is larger in VS3. At $t = 30\ T_M$, the differences in the horizontal and vertical velocities between VS3 and REF becomes small (Figure 6.13b). However, the difference in the vertical velocity near the "cold" wedge corner is still large.

The viscosity variation in the lateral (VS1) or depth (VS2) directions has very small effects on the viscoelastic deformation. At short times after the earthquake, the higher viscosity of the wedge corner in VS3 causes the material to deform more slowly and thus results in lower velocities. At longer times, the "cold" wedge corner has much less

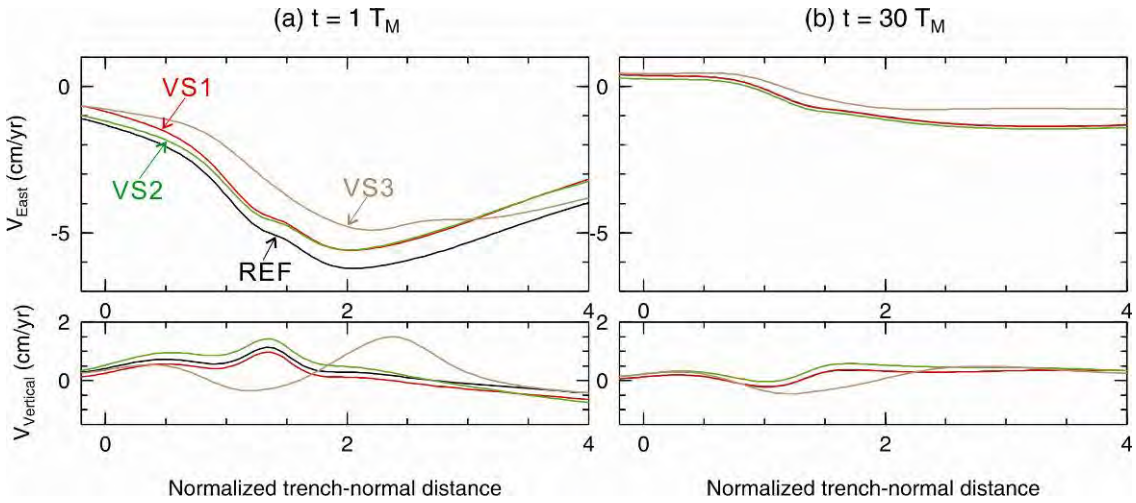

Figure 6.13. Comparison of the surface deformation between the four testing models shown in Figure 6.12. Surface velocities are plotted at t = 1 T_M (a) and t = 30 T_M (b). Upper and lower panels illustrate the velocities in the trench-normal and vertical directions, respectively. The four testing models are colour-coded and labelled in the upper panel of (a).

influence on the horizontal deformation but still strongly affects the vertical deformation. Note that these models only model the effects due to an earthquake. The effects due to the re-locking of the fault are not modelled in this chapter. It will be demonstrated in Chapter 7 that the effects of the "cold" wedge corner due to the earthquake and the re-locking of the fault largely cancel out.

We have learned the following points from these tests. The higher viscosity of the "cold" wedge corner (VS3) greatly affects the vertical viscoelastic deformation. The "cold" wedge corner has large effects on the horizontal deformation at short times (*e.g.*, t = 1 T_M) but smaller effects at longer times (*e.g.*, t = 30 T_M). Variations in the viscosity of the upper mantle in the lateral or depth directions have very small effects on the viscoelastic deformation.

6.5. Effects of the transient rheology

It is reported that a short time after a megathrust earthquake such as days to a few years, the crust deforms rapidly with time (*e.g.*, *Gahalaut et al.*, 2006; *Jade et al.*, 2007).

The very rapid deformation to some extent indicates very fast relaxation of the earthquake-induced stresses in the upper mantle. If the upper mantle is represented by the Maxwell rheology, the viscosity must be small, on the order of 10^{17} – 10^{18} Pa s. However, after a longer time, decades to centuries after the earthquake, the crust deforms more slowly, and a higher viscosity on the order of 10^{19} Pa s is required. Therefore, the viscoelastic deformation at short and long time scales cannot be described using a single model with the Maxwell rheology. However, they may be described using a single model with the transient rheology. As discussed in section 5.1, the transient rheology may be represented by a Burghers body, that is, a Maxwell body in series with a Kelvin body. A testing model (TR1) with the transient rheology is used to compare with REF of the Maxwell rheology. Following previously published papers (*e.g.*, *Pollitz et al.*, 2008; *Panet et al.*, 2010), I used a viscosity 5×10^{17} Pa s for the Kelvin body in TR1 (corresponding to a Kelvin relaxation time $T_K = 0.25$ yr). The Maxwell body in TR1 has the same viscosity 10^{19} Pa s ($T_M = 5$ yr) as in REF. With these values, $T_M = 20\ T_K$. Other model parameters in TR1 are the same as in REF.

As expected, the elastic coseismic deformation of TR1 is identical with REF (green line in Figure 6.14a). For the viscoelastic deformation at short times after the earthquake (*e.g.*, $t = 2\ T_K = 0.1\ T_M$ in Figure 6.14a), the variation in the vertical velocity in TR1 is much greater than in REF. The horizontal velocity in areas landward of the rupture zone in TR1 is about one order of magnitude larger than in REF. Areas over the rupture zone in TR1 at first move landward with very high velocity values while areas farther landward move seaward. The high landward velocities in these areas decrease rapidly with time (Figure 6.15). The opposite short-term surface deformation (Figures 6.14b and 6.15) is due to the motion of the fault slip, that is, the hanging wall moves seaward, and the foot wall moves landward. However, with dip slip faulting, the symmetric point for the surface deformation is not the trench. If the fault were vertical (the trench were the symmetric point), the deformation would be symmetric. At $t = 20\ T_K$ (or $t = 1\ T_M$), the area near the trench in TR1 moves seaward with velocity values similar to those in REF (Figure 6.14b). The surface horizontal velocity farther landward in TR1 is smaller than in REF. At longer times after the earthquake (*e.g.*, $t = 200\ T_K = 10\ T_M$ in Figure 6.14c), both models produce similar horizontal and vertical velocities. The differences in the

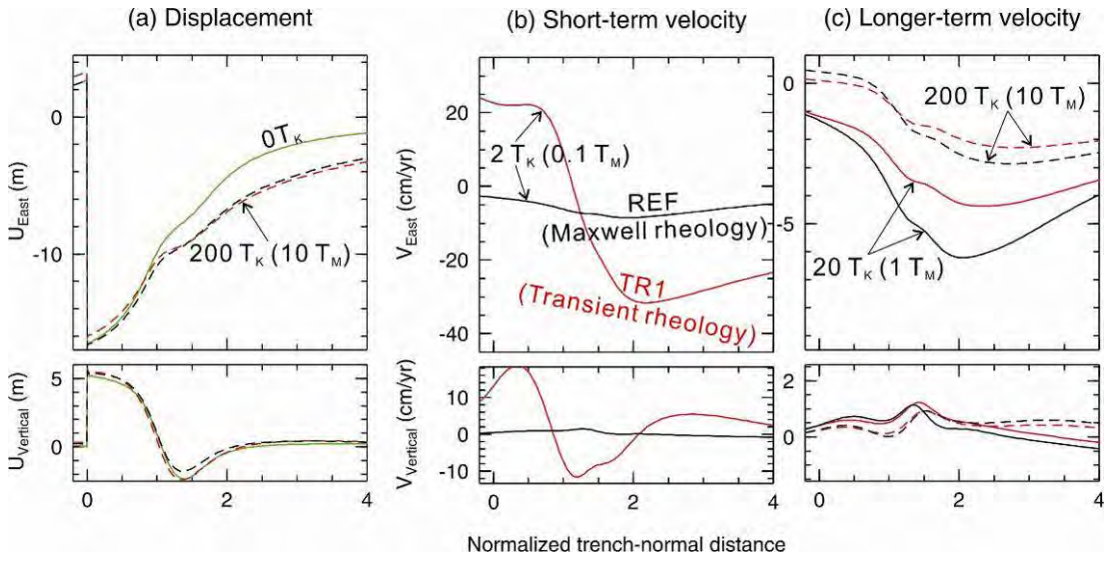

Figure 6.14. Comparison of the surface deformation between REF (black) and TR1 (red). Surface displacements and velocities are plotted in (a) and (b), respectively. Upper and lower panels demonstrate the deformation in the trench-normal and vertical directions, respectively. T_K = 0.25 yr (T_M = 20 T_K). Coseismic deformation of both models are identical (green line in (a)).

displacements between the two models are small (Figure 6.14a).

The evolution of the viscoelastic deformation of two surface points whose locations are shown in Figure 6.9 is shown in Figure 6.16. At $t < 3\ T_K$ (or $t < 0.15\ T_M$), both the horizontal and vertical velocities in TR1 is about one order of magnitude larger than in REF (Figure 6.16b). At ~5 $T_K < t <$ ~200 T_K (or ~0.25 $T_M < t <$ ~10 T_M), the velocities in TR1 is smaller than in REF (Figure 6.16c). At longer times (*e.g.*, $t >$ ~200 T_K, or $t >$ ~10 T_M), the differences in the velocities between the two models are small (Figure 6.16c). The displacements in both models are almost identical (Figure 6.16a). Using other values for the transient viscosity (Kelvin) in TR1 greatly affects deformations at short times, and deformations at longer times are almost the same (results not shown).

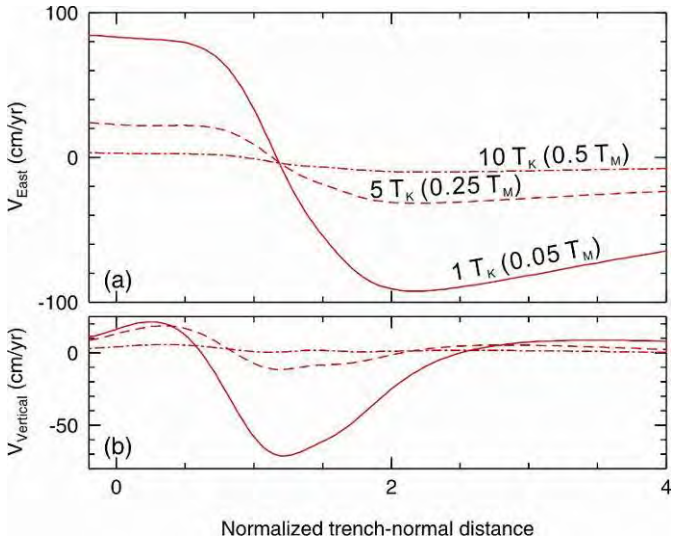

Figure 6.15. Surface velocities of TR1 at short times. Surface velocities in the trench-normal and vertical directions are plotted in (a) and (b), respectively. Solid, dashed and dot-dashed lines represent surface velocities at t = 1 T_K, 5 T_K and 10 T_K, respectively.

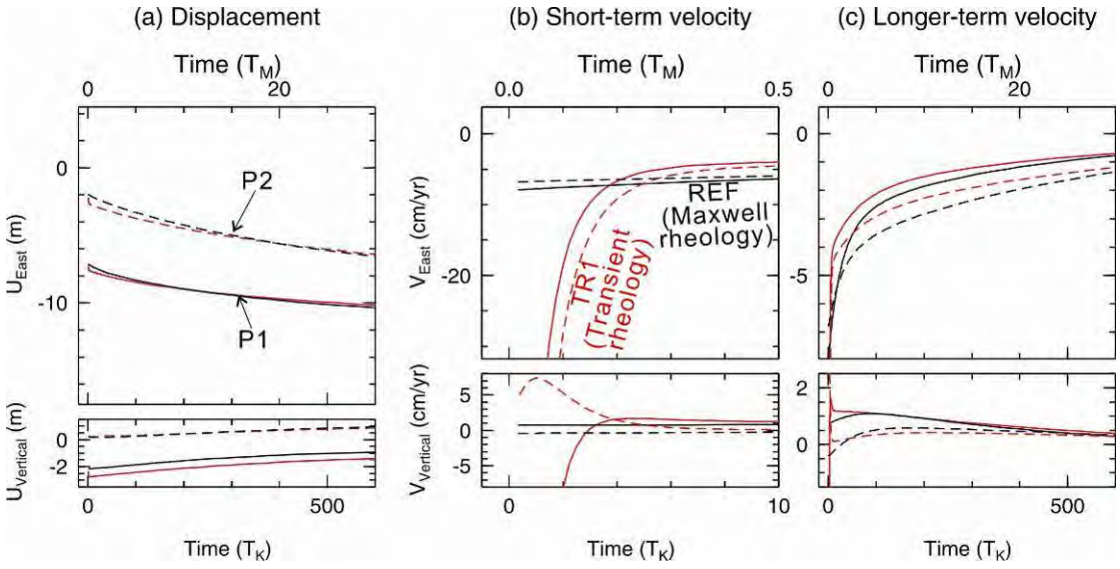

Figure 6.16. Comparison of the deformation evolution of surface points P1 (solid lines) and P2 (dashed lines) between REF (black) and TR1 (red). Locations of P1 and P2 are shown in Figures 6.6a and 6.9. (a) Displacements of t = 0 to 600 T_K. (b) Velocities of t = 0 to 10 T_K. (c) Velocities of t = 0 to 600 T_K. T_K = 0.25 yr (T_M = 20 T_K). Upper and lower panels represent deformation in the trench-normal and vertical directions, respectively.

We have learned the following points from this test. If the upper mantle is represented by the transient rheology, the viscoelastic deformation at short times (*e.g.*, $t < 5\ T_K$) is much faster than that of the Maxwell rheology. At times of ~5 T_K – 200 T_K, the viscoelastic deformation in the transient rheology model is slower than in the Maxwell rheology model. At longer times ($t > 200\ T_K$), the transient stresses (Kelvin body) are mostly relaxed, and the viscoelastic deformation is controlled mainly by the steady-state rheology (Maxwell body) which has a higher viscosity. The long-term viscoelastic deformation thus may be represented by either the transient rheology or the steady-state (Maxwell) rheology.

6.6. Effects of aseismic afterslip

The subduction fault may show downdip and along-strike variations in its seismogenic behaviour at various time scales (*Wang and Hu*, 2006; *Bilek*, 2009). A megathrust earthquake may rupture segments of the fault. After the earthquake, areas surrounding the rupture zone may undergo continuous aseismic slip which is called afterslip (*e.g.*, *Melbourne et al.*, 2002). In this section, I will investigate the effects of various temporal decay functions of afterslip and compare the effects of afterslip and the mantle rheology.

The afterslip of the fault in the real Earth must be complex and is a function of both space and time. For demonstration purposes, the application of a model afterslip is shown in Figure 6.17a. The coseismic distribution shown as a solid line in Figure 6.17a is applied over the fault at $t = 0$. The segment downdip of the rupture zone slips continuously to a level represented by the dashed line in Figure 6.17a. The characteristic time T_A of afterslip is assumed to be 1 year. $T_A = 1$ yr in this test is based on the fact that the crustal deformation at geodetic sites decreases rapidly within a couple of years after a megathrust earthquake (*e.g.*, *Gahalaut et al.*, 2006; *Jade et al.*, 2007). The exact value of T_A in the real Earth may vary from place to place. The seismic moment associated with the afterslip shown in Figure 6.17a is 40% of the main shock. Surface horizontal and vertical displacements in a purely elastic model due to the main shock alone and with the additional afterslip are shown in Figures 6.17b and 6.17c, respectively. The effect of the afterslip is to produce larger horizontal displacements and to move the location of the

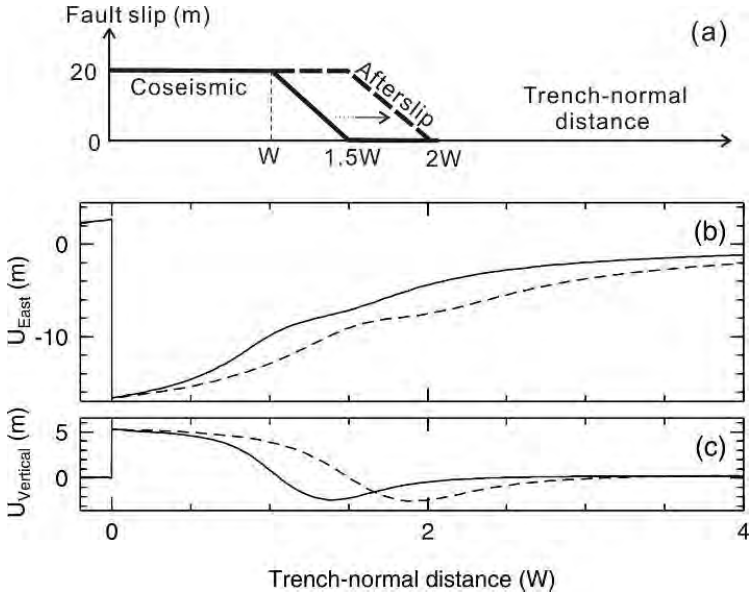

Figure 6.17. Illustration of the application of afterslip. (a) Distributions of coseismic slip (solid line) and afterslip (dashed line) along the fault. The fault slips continuously from the solid line at t = 0 yr to the dashed line. The characteristic time T_A of afterslip is 1 yr. (b) Surface elastic displacements in the trench-normal direction. Solid and dashed lines represent models with the main shock alone (solid line in (a)) and with the addition of afterslip (dashed line in (a)), respectively. (c) Surface elastic displacements in the vertical direction for the same models as in (b).

maximum subsidence farther away from the trench. In the following, I will show the effects of afterslip using viscoelastic models.

How the afterslip zone slips aseismically with time is not well known. Four temporal-decay functions of afterslip are listed in (6-6). Except for the power-law decay function that I have derived, the other three decay functions are widely used in the literature.

$$\begin{cases} U_s = A\times\left[1-\left(1-\dfrac{t}{4T_A}\right)^n\right] \quad (n=1,2...,t \le 4T_A) & \text{(Power law)} \\ U_s = A\times\left[1-\exp\left(-t/T_A\right)\right] & \text{(Exponential)} \\ U_s = A\times\log\left(1+t/T_A\right) & \text{(Logarithmic)} \\ U_s = A\times\left(1-1/\left(1+t/T_A\right)\right) & \text{(Ohmori's law)} \end{cases} \tag{6-6}$$

where U_s is the afterslip as a function of space and time, A is the magnitude of the

afterslip that is a function of space, and t is time since the earthquake. Note that for the power-law function, the fault slip is fixed at the value $U_s\big|_{t=T_A}$ when $t > 4T_A$. For the power-law function with $n = 1$, afterslip increases linearly with time. For $A = 1$, afterslip with different decay functions in (6-6) is shown in Figure 6.18. The change of the fault slip in the power-law function with $n = 1$ is abrupt at $t = T_A$ (results not shown) and is thus unphysical.

REF plus afterslip are used in testing models to examine the effects of different afterslip decay functions. Deformation evolution of the surface point P2 in these models is shown in Figure 6.19. The decay functions greatly affect the viscoelastic deformation at $t < 2T_A$. At $t = 4T_A$ the change of the horizontal velocity is abrupt in the power-law model with $n = 2$ and is thus unphysical. At $t > 4T_A$, differences in the velocities in all the five models become small. For margins in which last megathrust earthquake occurred >5 T_A ago such as Chile and Cascadia, either of the decay functions in (6-6) may be adequate in modelling the contemporary crustal deformation. For margins with the occurrence of the last event <5 T_A such as Sumatra, one of the decay functions has to be constrained by geodetic data. In Chapter 7, I will demonstrate that the power-law function with $n = 3$ provides best fit to GPS time series. In the following tests, the power-law function with $n = 3$ will be used in models with afterslip.

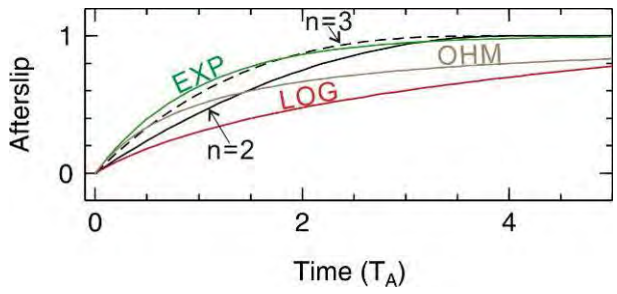

Figure 6.18. Illustration of unit afterslip with different temporal decay functions. Different colours represent different functions in (6-6). The abbreviation of the functions includes LOG for “logarithmic”, EXP for “Exponential”, and OHM for “Ohmori’s law”. Different orders n for the power-law function (black lines) are also labelled.

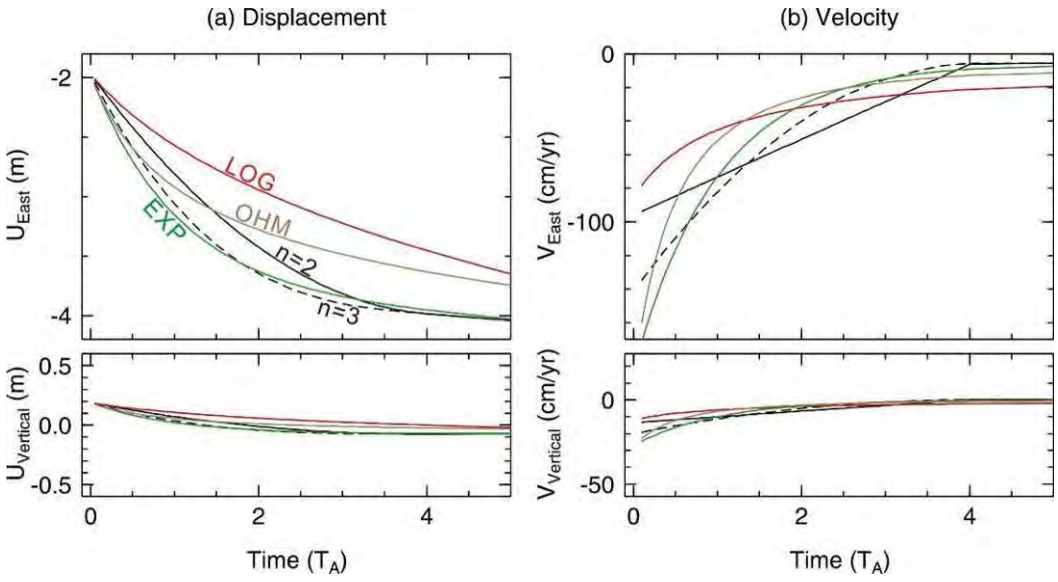

Figure 6.19. Comparison of the deformation evolution of the surface point P2 between models with different afterslip decay functions. The location of P2 is shown in Figures 6.6a and 6.9. Displacements and velocities are plotted in (a) and (b), respectively. Upper and lower panels demonstrate deformation in the trench-normal and vertical directions, respectively. The colour coding of these models is the same as in Figure 6.18.

Two testing models are used to compare with REF and the transient-rheology model TR1 in the previous section (Table 6.1). AS1 is simply REF plus afterslip, and the afterslip shown in Figure 6.17a is applied to the fault. AS2 is TR1 plus afterslip. With T_K = 0.25 yr and T_M = 5 yr, the T_A = 1 yr of the afterslip in these models is 4 T_K or 0.2 T_M.

Table 6.1. Fault slip and mantle rheology in REF, TR1 and two testing models. Viscosity values are in Pa s.

Model	Afterslip	Maxwell (10^{19})	Transient (10^{19}, 5×10^{17})	Notes
REF	×	√		Reference testing model
TR1	×		√	Same model as in section 6.5
AS1	√	√		
AS2	√		√	

Surface displacements of these models are similar to those shown in Figure 6.17 and are not presented. At very short times after the earthquake (*e.g.*, t = 0.25 T_A = 1 T_K in

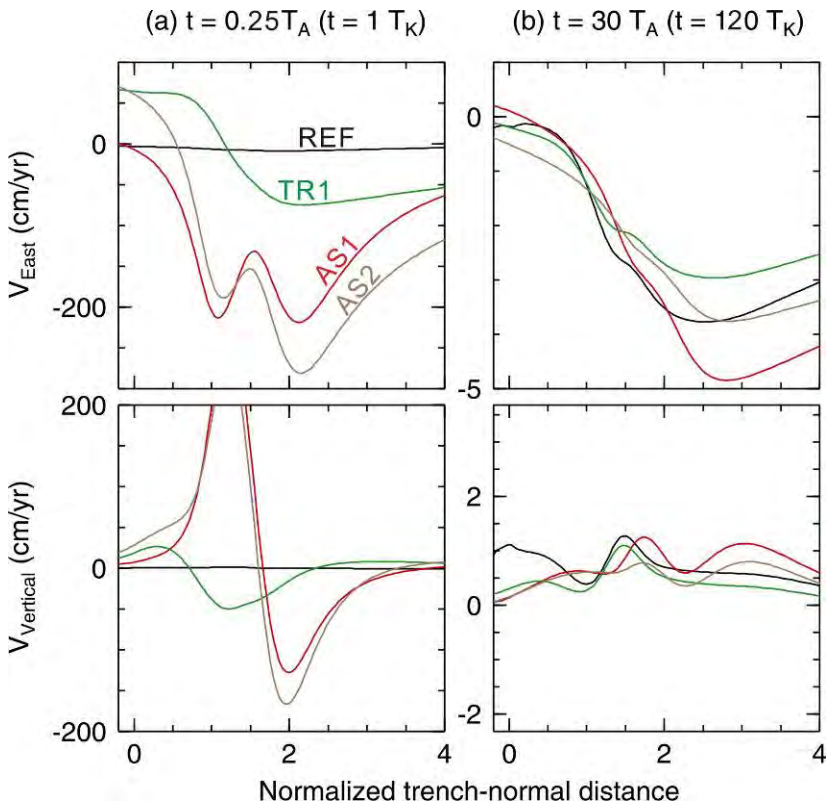

Figure 6.20. Comparison of the surface deformation between the four testing models in the Table 6.1 at very short and very long times. (a) Surface velocities at t = 0.25 T_A= 1 T_K. (b) Surface velocities at t = 30 T_A= 120 T_K. Upper and lower panels illustrate deformations in the trench-normal and vertical directions, respectively.

Figure 6.20a), the effect of afterslip is very significant, producing the horizontal and vertical velocities much larger than in REF and in TR1. At much longer times (*e.g.*, t = 30 T_A = 120 T_K in Figure 6.20b), the application of afterslip has a very small effect in the velocities in areas over the rupture zone but still has a large effect in areas farther landward. The application of the transient rheology is to produce velocities generally smaller than in REF at longer times.

At times in between, time scales of a few T_A or a few T_K, the application of afterslip or the transient rheology has different effects on the horizontal velocities in the rupture zone (near-field areas) and in areas farther landward (far-field areas) (Figure 6.21). At t = 2.5 T_A, the application of afterslip (AS1) has large effects on the near-field horizontal

velocity and very small effects on the far-field velocity (Figure 6.21a). At t = 10 T_A, the horizontal velocity in both the near-field and far-field areas in AS1 is slightly larger than in REF. The slighter larger velocity in the far-field in AS1 reflects a prolonged response to the afterslip. At t = 2.5 T_K, the application of the transient rheology (TR1) has large effects on both the near-field and the far-field horizontal velocities (Figure 6.21b). At t = 10 T_K, the horizontal velocity in TR1 is smaller than in REF. At the same t = 10 T_K= 2.5 T_A, the application of afterslip and the transient rheology (AS2) produce horizontal velocities generally larger than that in REF. At t = 40 T_K= 10 T_A, the horizontal velocity in AS2 is almost the same as in REF. The application of the transient rheology (TR1) or afterslip (AS1) results in maximum uplift and subsidence larger than in REF (low panels in Figures 6.21a and 6.21b). The combined effect (AS2) on the vertical velocity is even larger (lower panel in Figure 6.21c).

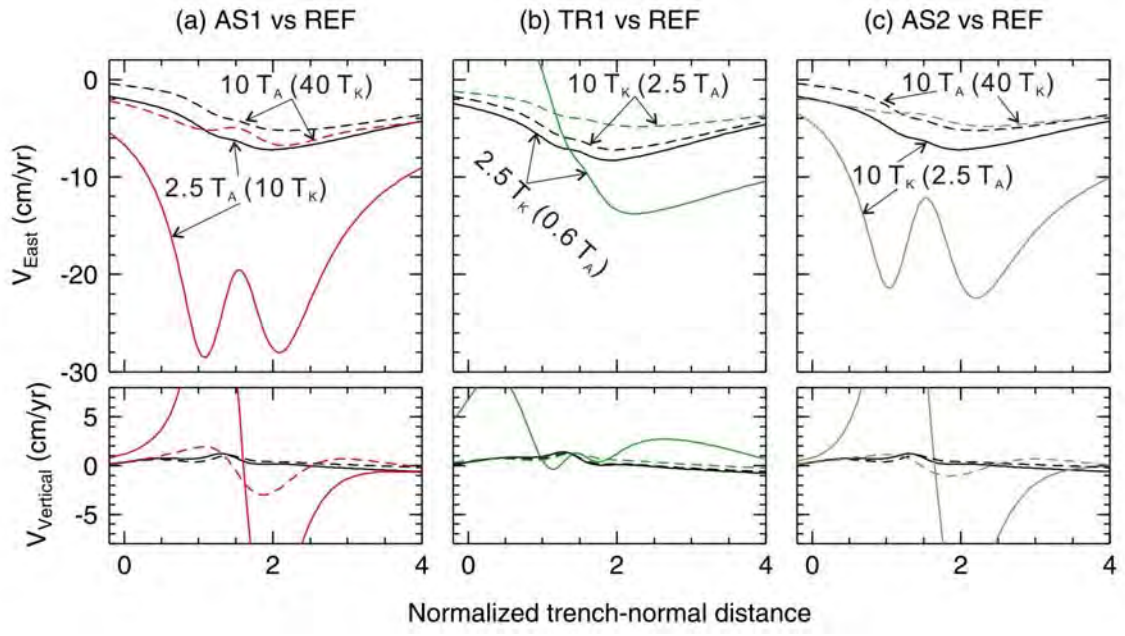

Figure 6.21. Comparison of the surface deformation of AS1, TR1 and AS2 with REF at times of a few T_A or a few T_K. (a) AS1 versus REF. (b) TR1 versus REF. (c) AS2 versus REF. Upper and lower panels illustrate deformations in the trench-normal and vertical directions, respectively. Colour coding of these four models is the same as in Figure 6.20.

The deformation contrast of the four testing models is further illustrated through the deformation evolution of the surface point P2 (Figure 6.22). The application of the afterslip results in displacements larger than that in models without afterslip (Figure 6.22a). The application of the transient rheology results in larger displacements at short times and almost the same displacements at longer times. The application of either the afterslip or the transient rheology greatly affects the velocities at $t < 1\ T_A$ (or $t < \sim 3\ T_K$) (Figure 6.22b). The effect of the afterslip with $T_A = 1$ yr greatly overshadows the effect of the transient rheology ($T_K = 0.25$ yr). At longer times (*e.g.*, $t = 30\ T_A$), the horizontal velocities in models with afterslip are larger than in models without afterslip (Figure 6.22c). The vertical velocities in these models are almost the same.

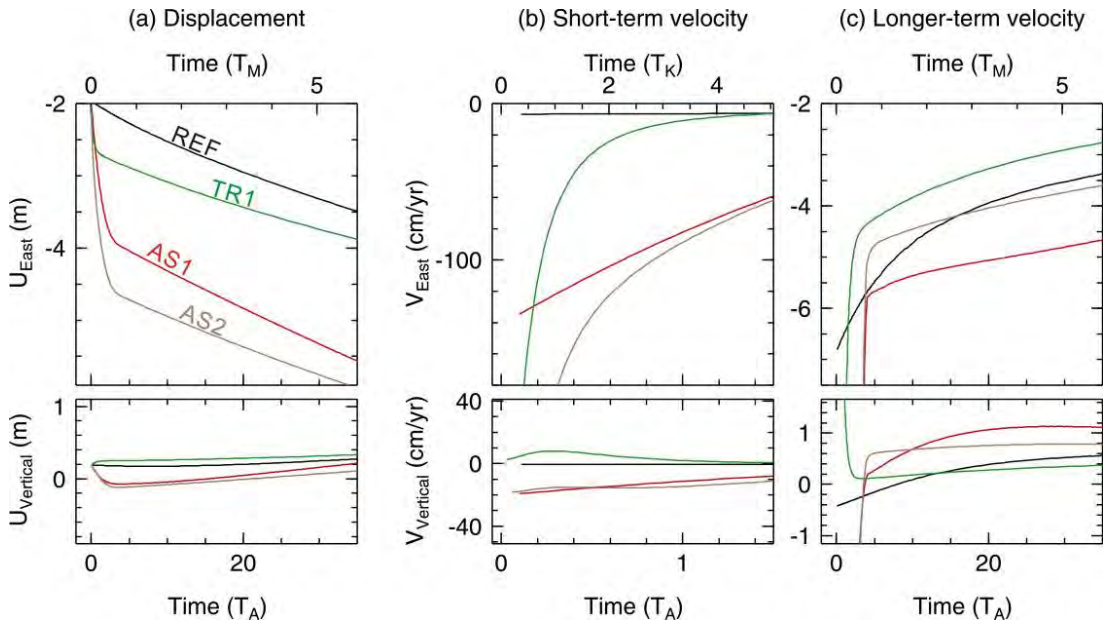

Figure 6.22. Comparison of the deformation evolution of the surface point P2 between the four testing models in Table 6.1. The location of P2 is shown in Figures 6.6a and 6.9. (a) Displacements. (b) Short-term velocities. (c) Longer-term velocities. Upper and lower panels illustrate deformation in the trench-normal and vertical directions, respectively. Colour coding of these models is the same as in Figures 6.20 and 6.21 and is labelled in (a).

From this test, we have learned the following points. At very short times (less than 1 T_A or 3 T_K), the application of the afterslip or the transient rheology greatly affects the whole surface area. At time scales of a few T_K or a few T_A, the application of the afterslip greatly affects the viscoelastic deformation near the rupture zone while the transient rheology greatly affects the deformation in the whole surface area. At longer times (*e.g.*, $t > 30\ T_A$ or $t > 120\ T_K$), the application of either the afterslip or the transient rheology produces the viscoelastic deformation almost identical with the REF.

6.7. Effects of the heterogeneity of the coseismic slip distribution

An earthquake may rupture multiple segments of a megathrust fault (*e.g.*, *Zweck et al.*, 2002; *Ammon et al.*, 2005), or several earthquakes may rupture different segments of the fault (*e.g.*, *Yamanaka and Kikuchi*, 2004). The heterogeneity of the coseismic slip results in heterogeneous elastic deformation and induces a heterogeneous stress field in the mantle. Subsequent relaxation of the earthquake-induced stresses then produces heterogeneous viscoelastic crustal deformation. However, how long the heterogeneity of the viscoelastic crustal deformation persists after a megathrust earthquake is not well known. In this section, I will use a 3D finite element model to examine this problem.

The first heterogeneous slip model (HS1) in this section includes three rupture patches (Figure 6.23). Each patch is 150 km wide in the downdip direction and 150 km long in the strike direction. Ten-metre uniform slip is assigned to the rupture zones. The fault slip tapers to zero in a 50 km-wide transition zone surrounding the 150 × 150 km full-slip rupture zone (Figure 6.23). Re-locking of the fault is assumed at a subduction rate 4 cm/yr, similar to Cascadia. The locked zone is 150 km wide in the downdip direction and the entire length of the model domain in the strike direction. Other model parameters in HS1 are the same as in REF. Note that the mantle in both HS1 and REF has a Maxwell viscosity 10^{19} Pa s (T_M = 5 yr). Because of the symmetry of the model in the strike direction, only the northern half part is modelled. Effects due to the earthquake (Figure 6.1b) and re-locking of the fault (Figure 6.1c) are modelled separately. The re-locking of the fault is modelled as backslip of the fault at the subduction rate as explained in section 6.1. The total effect is a linear combination of the effects of the earthquake and the re-locking of the fault (Figure 6.23).

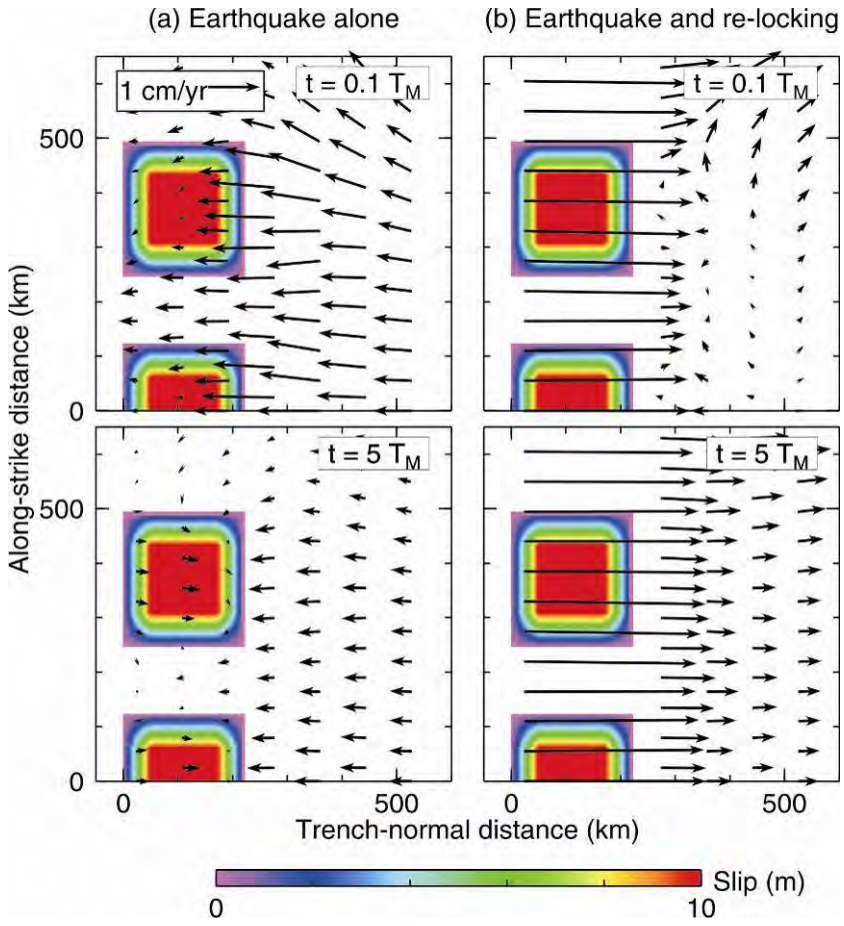

Figure 6.23. Surface velocities of HS1 due to the earthquake of three rupture patches and uniform re-locking of the fault. Only the northern half part of the model is modelled and presented. (a) Surface velocities due to the earthquake alone. (b) Surface velocities due to the earthquake and re-locking of the fault. Upper and lower panels are velocities at t = 0.1 T_M and 5 T_M, respectively. Coloured contours represent the plan view of the coseismic slip distribution. The width of the rupture patches in the trench-normal direction is less than 250 km because of the dipping of the fault.

At t = 0.1 T_M, significant variations of deformation in the strike direction exist for the effect of the earthquake alone (upper panels in Figure 6.23a) and the combined effect of earthquake and re-locking (upper panel in Figure 6.23b). The heterogeneous surface deformation obviously results from the heterogeneous distribution of the coseismic slip. For the combined effect of the earthquake and re-locking, the area over the locked zone

moves landward at almost a uniform velocity ~4 cm/yr which is due to the re-locking of the fault. Further landward, there is significant along-strike variation in the velocity field. At this time, the effect of fault-locking cannot yet fully overcome the effect of the earthquake in this area. In some places, velocity vectors are still oriented in the seaward direction, the same as coseismic displacements.

At $t = 5\ T_M$, the along-strike variations of the surface deformation is negligible (lower panels of Figure 6.23). For the effect of earthquake alone, the area landward of the rupture patches moves seaward at almost the same velocity ~0.2 cm/yr (lower panel in Figure 6.23a) because of continuing mantle stress relaxation. For the combined effect (lower panel in Figure 6.23b), this area moves landward at almost a uniform velocity, although with values slightly smaller than that north of the rupture zones that is not affected by the earthquake. At this time, it would be difficult to use surface velocity to tell how the coseismic rupture varied along strike.

Using different values for the viscosity of the upper mantle slightly changes the time span of the existence of the deformation contrast in the strike direction (results not shown). If the locations of the centres of the rupture patches are the same as in HS1, but the along-strike length of each patch is shorter, which means, larger gaps between the rupture patches, the along-strike deformation contrast disappears more quickly (results not shown).

The second testing model (HS2) has only one rupture zone patch. The width of the rupture zone in the downdip dimension in HS2 is the same as in HS1. The along-strike length in HS2 is 450 km, a sum of the lengths of the rupture patches in HS1. Other model parameters in HS2 are the same as in HS1. At $t = 5\ T_M$, the along-strike contrast of the surface deformation is still significant for both the effect of the earthquake alone and the combined effect (upper panels in Figure 6.24). At $t = 15\ T_M$, the along-strike deformation contrast becomes small.

We have learned the following points from these tests. The heterogeneity of the crustal deformation due to the heterogeneous distribution of the fault slip is very small at $t > 5\ T_M$. The time span of the along-strike contrast of the surface deformation is longer for earthquakes with larger along-strike rupture length but still rather short-lived. It is absolutely impossible to use contemporary geodetic deformation to infer the slip

distribution of an earthquake hundreds of years ago. Such an effort was made by *Pollitz et al.* (2010) for the Cascadia subduction zone, but largely unsuccessfully.

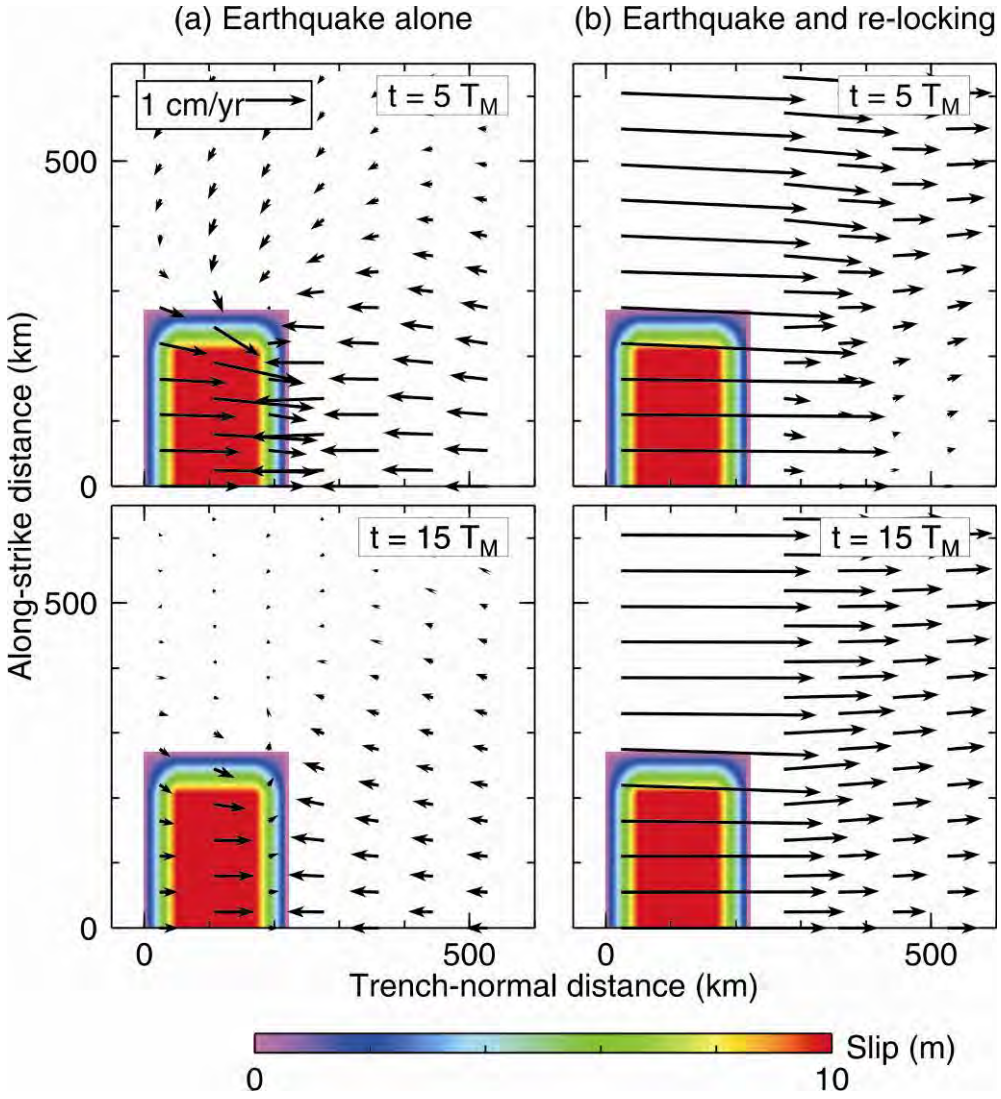

Figure 6.24. Similar to Figure 6.23, surface velocities of HS2 due to the earthquake of one rupture patch and uniform re-locking of the fault. (a) Surface velocities due to the earthquake alone. (b) Surface velocities due to the earthquake and re-locking of the fault. Upper and lower panels are velocities at t = 5 T_M and 15 T_M, respectively.

Chapter 7. Crustal Deformation Associated with Great Subduction Zone Earthquakes in Earthquake Cycles

Because of the limited time span of modern geodetic observations such as GPS, no subduction zones have been observed geodetically and continuously over a complete earthquake cycle. However, the poor temporal coverage can be compensated by a better spatial coverage. Earthquake cycles of all subduction zones should be governed by the same fundamental mechanics. For example, previously published subduction zone earthquake models on different margins, such as Alaska (*Zweck et al.*, 2002), southern Chile (*Khazaradze et al.*, 2002; *Hu et al.*, 2004), and Cascadia (*Wang et al.*, 2001), gave similar values of the upper mantle viscosity at the order of 10^{19} Pa s (*e.g.*, summarized by *Wang*, 2007). Differences in their deformation patterns are due only to specifics in their tectonic settings. By simultaneously studying subduction margins that are presently at different stages of the earthquake cycle, we can understand their common underlying physical process and in effect piece together a full deformation cycle for great megathrust earthquakes. In this chapter, I will examine three margins, Sumatra, southern Chile and Cascadia, which produced great earthquakes in 2004, 1960, and 1700, respectively, and are presently at distinctly different stages of the earthquake cycle. I will use a unified mechanical model to explain the vastly different contemporary deformation patterns at those three margins. Future geodetic observations will provide further tests for the numerical model presented in this work.

7.1. Common parameters for subduction zone earthquake models

Subduction zone earthquake models in this chapter are based on the conceptual model in Figure 6.1a. Only the model parameters that are common to models of the three margins, Sumatra, Chile and Cascadia, are summarized in this section. The upper mantle is assumed to have the transient rheology to model both the short-term and long-term deformation. The viscosity values of the Maxwell and Kelvin components are 10^{19} Pa s (T_M = 5 yr) and 5×10^{17} Pa s (T_K = 0.25 yr), respectively. Geometric parameters, rock physical properties and boundary conditions follow the reference testing model (REF) in Chapter 6 and are listed in Table 7.1.

The geometry of the fault, the distributions of the coseismic slip and afterslip, and the subduction rate of the oceanic plate are different between the three margins and will be discussed in later sections. An earthquake ruptures the shallow portion of the megathrust (Figure 6.1b). The continuous and aseismic slip of the areas surrounding the coseismic rupture zone is assumed to follow the power-law decay function with $n = 3$ in (6-6) with a characteristic time of 1.25 years ($T_A = 1.25$ yr).

Locking of the fault in this work adopts the approach elaborated by Hu et al. (2004) (also discussed in section 6.1). In the dip direction, the megathrust slips backward at the plate convergence rate in the fully locked zone, and the back-slip rate decreases linearly to zero over the transition zone (Figure 6-1c). In strike direction, the entire margin is assumed to be locked.

Table 7.1. Common geometric parameters and rock physical properties. η_M and η_K are the viscosities of the Maxwell and Kelvin bodies (Pa s), respectively, E is the Young's modulus (GPa), υ is the Poisson's ratio, ρ is the rock density (g/cm^3) and g is the gravitational acceleration (m/s^2).

	Thickness (km)	η_M	η_K	E	υ	ρ	g
Elastic continental plate	40	∞	∞	120	0.25	3.3	10
Elastic oceanic plate	30	∞	∞	120	0.25	3.3	10
Continental mantle	up to 500 km	10^{19}	5×10^{17}	160	0.25	3.3	10
Oceanic mantle	up to 500 km	10^{20}	5×10^{17}	160	0.25	3.3	10

7.2. Sumatra: Short-term post-seismic deformation

7.2.1. Tectonic background

At the Sumatra subduction zone, the Indo-Australian plate subducts obliquely beneath the Sunda block at a rate of 52 mm/yr (*Larson et al.*, 1997). The angle between the subduction direction and the strike of the trench varies from ~70° north of Sumatra to ~0° at the Andaman Islands (Figure 7.1). The motion of the overlying plate, the Sunda block,

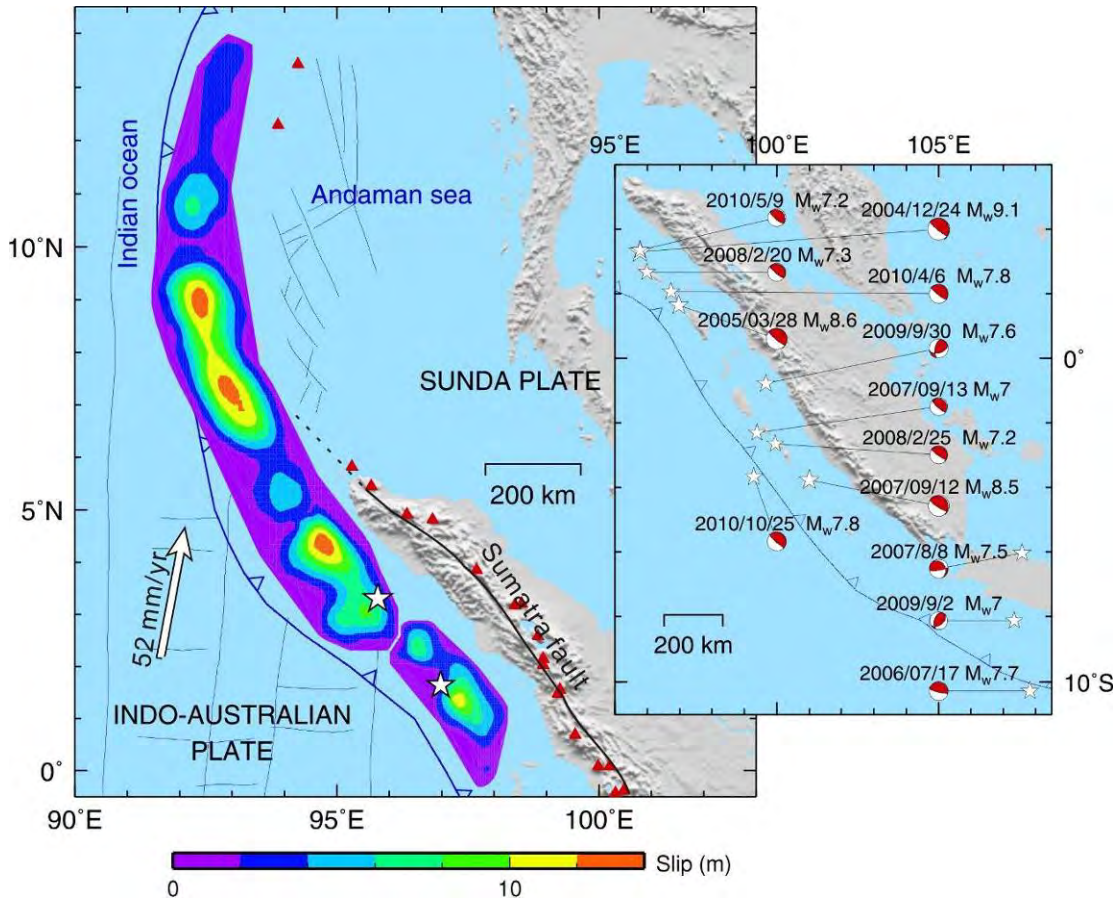

Figure 7.1. Coseismic distributions of the 2004 Sumatra earthquake based on *Chlieh et al.* (2007) and of the 2005 Nias earthquake (*Hsu et al.*, 2006). Large white arrow represents the subduction direction of the Indo-Australia plate with the subduction rate labelled (*Larson et al.*, 1997). Focal mechanisms of the 2004 and 2005 events are from the global CMT (http://www.globalcmt.org). Red triangles represent arc volcanoes.

is estimated to be about 2.5 cm/yr in the International Terrestrial Reference Frame 2000 (ITRF2000) (*Altamimi et al.*, 2002). In the upper plate, there is a right-lateral shear motion fault system, the Sumatra fault, of a few tens of kilometres width co-located with the volcanic arc (*Bellier et al.*, 1997; *Curray*, 2005). The Sumatra fault extends from latitudes ~5°S to ~5°N. Its northern termination is yet to be understood. *McCaffrey et al.* (2000) reported that about two-thirds of the margin-parallel component of the relative plate motion is accommodated by the Sumatra fault. Slip partitioning of this type is a common feature of obliquely convergent margins (*Fitch*, 1972; *Jarrard*, 1986; *Yu et al.*,

1993). It is also observed at Cascadia (*Wells et al.*, 1998; *Wang et al.*, 2001; *McCaffrey*, 2005) and Chile (*Cembrano et al.*, 2002; *Hoffmann-Rothe et al.*, 2006; *Wang et al.*, 2007). However, compared to the hundreds of centimetres of coseismic displacements and tens of centimetres a year of the short-term postseismic deformation, the slip of the Sumatra fault at <2.5 cm/yr is negligible. Also, only a small southern portion of the rupture zone of the earthquake to be investigated in this section coincides with the latitudes of the northern Sumatra fault. In addition, only few of campaign GPS stations used in this work are located between the trench and the Sumatra fault. Effects of the Sumatra fault on the deformation at other GPS stations that are hundreds of kilometres away are very small. Therefore, the motion of the Sumatra fault is not important for the model of this section.

The devastating Sumatra-Andaman earthquake of December 26, 2004, the first event of $M_w > 9$ in the era of modern space geodesy, ruptured ~1300 km of the megathrust with an average slip of 10 m (*Ammon et al.*, 2005; *Banergee et al.*, 2005). This giant earthquake and its accompanying tsunami (*Satake et al.*, 2005, 2006) caused more than 230,000 fatalities in this region. The rupture started at the megathrust below Nias Island, propagated in the north direction and lasted more than 1000 s (*Lay et al.*, 2005; *Ammon et al.*, 2005). *Stein and Okal* (2005) reported a seismic moment of $M_0 = 1.2 \times 10^{23}$ Nm (M_w 9.3) inferred from very-long-period data, three times the initial Harvard CMT estimate of scalar seismic moment. The moment magnitude based on geodetic data does not exceed 9.2 (*Banerjee et al.*, 2005; *Vigny et al.*, 2005; *Subarya et al.*, 2006). Inferred from combined inversion of seismic data and geodetic data, the estimated moment magnitude for this event is ~9.15 (*Chlieh et al.*, 2007).

About three months after the 2004 event, the March 28 2005 Nias-Simeulue earthquake ($M_w = 8.6$) ruptured more than 400 km of the megathrust, to the immediate south of the 2004 event (*Briggs et al.*, 2006; *Hsu et al.*, 2006) (Figure 1). Since the 2004 and 2005 events, several M_w 7 events and one M_w 8 event have repeatedly ruptured this margin (information from global CMT, http://www.globalcmt.org) (Figure 7.1). In 2007, two M_w 7 and one M_w 8 events ruptured segments of this margin further south of the 2005 event. In 2008, one M_w 7 event ruptured the megathrust at the immediate northern termination of the 2005 event, and the other M_w 7 event ruptured farther south of the

2005 event. In 2009, two M_w 7 events occurred a few hundreds of kilometres south of the hypocentre of the 2005 event. In 2010, two M_w 7 events occurred at almost the same locations of the 2004 and 2005 events.

In the 400-year written history of Indonesia, the country that suffered the most in the 2004 earthquake, there was no mention of an event of similar size as the 2004 event. Based on the analysis of the 1000-year tsunami sediment record, *Monecke et al.* (2008) and *Jankaew et al.* (2008) both reported two historical events with similar severity rupturing this margin in 1290-1400 and in 780-990. The repeat time for an M_w 9 event is thus 500 – 600 years. Such a long accumulation of strain could explain the size of the 2004 event.

7.2.2. Observed crustal deformation in Sumatra

The 2004 Sumatra earthquake caused crustal deformation detectable at GPS stations over 3,000 km from the epicentre (*Catherine et al.*, 2005; *Boschi et al.*, 2006; *Hashimoto et al.*, 2006; *Jade et al.*, 2007). Ideally, coseismic displacements of a GPS station may be described as the static offsets between times just prior to and a few minutes after the earthquake. However, the background noise at stations hundreds of kilometres from the rupture zone is comparable with the order of the coseismic displacements, and it is reported that slow slip of the megathrust lasted on the order of one hour (*Bilham*, 2005; *Bilham et al.*, 2005; *Stein and Okal*, 2005) or longer (*Banerjee et al.*, 2005). Therefore, *Vigny et al.* (2005) reported static offsets averaged one day before and after the 2004 event at 79 continuously operating GPS stations hundreds of kilometres away from the rupture zone (their SEAMERGES GPS and International GPS Service networks) (red arrows in Figure 7.2a). After analyzing 41 stations of the network used by *Vigny et al.* (2005), 11 regional CGPS stations and 11 campaign-mode stations, *Banerjee et al.* (2007) reported geodetic offsets at these stations similar to those of *Vigny et al.* (2005). If a GPS station is used by both *Vigny et al.* (2005) and *Banerjee et al.* (2007), the data of *Vigny et al.* (2005) are used in this work. After removing duplicated data and ignoring data at stations too far from the epicentre, coseismic deformation data at 45 GPS stations are used in this work and are shown as red arrows in Figure 7.2a.

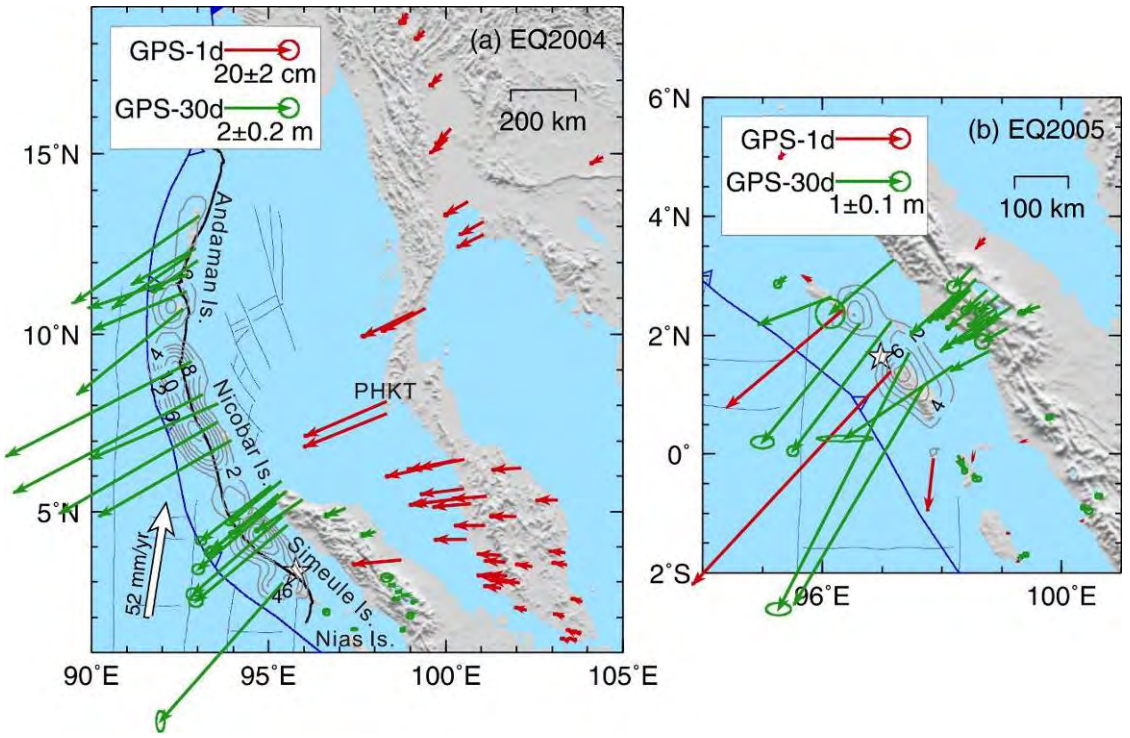

Figure 7.2. Coseismic GPS displacements of the 2004 Sumatra earthquake (a) and the 2005 Nias earthquake (b). Red arrows represent offsets at continuously operating stations one day before and one day after the 2004 event (*Vigny et al.*, 2005; *Banerjee et al.*, 2007) and the 2005 event (*Hsu et al.*, 2005; *Kreemer et al.*, 2006). Green arrows represent offsets at campaign stations surveyed a few days to around a month after the 2004 event (*Gahalaut et al.*, 2006; *Subarya et al.*, 2006) and the 2005 event (*Kreemer et al.*, 2006). See text for detailed discussion on the GPS data. Grey contour lines with 2 m intervals represent the coseismic slip distributions of the 2004 event (*Chlieh et al.*, 2007) and the 2005 event (*Hsu et al.*, 2005). White stars represent epicentres.

At the time of the 2004 event, there were no continuous GPS stations near the rupture zone. Campaign GPS stations in the rupture zone or less than 200 km away from the epicentre were surveyed several months to more than ten years before the earthquake (*Banerjee et al.*, 2005; *Gahalaut et al.*, 2006; *Subarya et al.*, 2006; *Jade et al.*, 2007; *Rajendran et al.*, 2007; *Gahalaut et al.*, 2008). A few days to almost one month after the event, these stations were surveyed again. The geodetic offset between the two campaign

surveys before and after the earthquake includes the interseismic deformation before, coseismic deformation during, and postseismic deformation after the earthquake. The procedure to correct for the interseismic deformation was reported as follows (*e.g., Subarya et al.*, 2006; *Banerjee et al.*, 2005). Some of the GPS stations were surveyed more than once before the earthquake and thus yielded interseismic velocities. These GPS-derived interseismic velocities were used to construct a kinematic model of interseismic deformation. The model interseismic motion was then subtracted from data from each station. The corrected measurements thus include coseismic and up to one month short-term postseismic deformations of the 2004 event. I use the corrected GPS data of *Subarya et al.* (2006) (green arrows south of latitude 6° in Figure 7.2a) and of *Gahalaut et al.* (2006) (green arrows north of latitude 6° in Figure 7.2a). Other publications (*e.g., Jade et al.*, 2007; *Rajendran et al.*, 2007; *Gahalaut et al.*, 2008) reported GPS data with values similar to those from these two groups.

In addition to GPS, three types of observations are used in the literature to constrain uplift and subsidence associated with the 2004 earthquake, that is, maximum growth elevation of coral heads or microatolls, remote sensing images, and field observations of sea-level changes. Corals grow up to a certain elevation with respect to the lowest annual tide level. Above this maximum elevation, corals cannot survive. Differences in the maximum elevations of the growth of the coral head or microatoll before and after an earthquake give a record of uplift or subsidence associated with the earthquake. The accuracy of this method is about 5 cm (*Zachariasen et al.*, 2000). Field measurements of uplift made on coral heads around Simeulue Island indicated 0.2 to 1.5 m uplift in this region (*Subarya et al.*, 2006). Colour and brightness of satellite images depend on water depth above coral reefs, and thus satellite images can be used to deduce coseismic vertical deformation. The accuracy of this method is 5-10 cm (*Meltzner et al.*, 2006). Comparing satellite images (ASTER, SPOT, IKONOS, QUICKBIRD, and LANDSAT) acquired prior to the 2004 earthquake with images acquired between 28 December 2004 and 26 March 2005, *Meltzner et al.* (2006) reported the pivot line (the line dividing areas of coseismic uplift and subsidence) of the 2004 event, shown as a black line in Figure 7.2a. Based on field observations of sea-level change, *Bilham et al.* (2005) reported a maximum subsidence of 4 m at Nicobar Islands, and from a maximum subsidence of 1.5

m to a maximum uplift of 2 m at Andaman Islands.

Rapid postseismic motion in the seaward direction, the same direction as the coseismic motion, has been observed at continuous GPS stations. *Vigny et al.* (2005) reported that a total displacement of about 10% of the coseismic displacement was detected at station PHKT over a 15-day period after the 2004 event. *Hashimoto et al.* (2006) reported that at the same station (PHKT), total postseismic displacement over a 30-day period after the 2004 event was up to ~25% of the coseismic displacement. Based on campaign-mode GPS data, *Gahalaut et al.* (2008) reported postseismic velocities of ~20 cm/yr in 2006 and of ~5 cm/yr in 2007 at Andaman Islands.

Pollitz et al. (2008) reported displacement accumulated from about 40 days to 11 months after the 2004 events at various continuously operating GPS stations and a few campaign stations (Figure 7.3a). The station GOVI moves in a direction dramatically different from the neighbouring stations. Therefore, the displacement vector of GOVI may be in error. The GPS data shown in Figure 7.3a are corrected for effects of the locking of the fault and the 2005 event, but details of the correction are not available. Stations SAMP and LHWA are a few hundred kilometres from the southern edge of the rupture zone of the 2004 earthquake, but their reported displacements are even larger than those within the rupture zone. The displacement vectors at these two stations may be over-corrected for the 2005 event. The postseismic displacements at these three stations, GOVI, SAMP and LHWA, will not be used in the later comparison with model results. *Panet et al.* (2010) later reported time series from 2005 to 2008 at three stations BNKK, CPN, and PHKT (Figure 7.3b). GPS data in *Pollitz et al.* (2008) (Figure 7.3a) and in *Panet et al.* (2010) (Figure 7.3b) are processed by the same research group, and the same correction for interseismic deformation and the 2005 event is applied in both papers.

Models predict crustal deformation with respect to the distant stable area of the upper plate, the Sunda block, while all the GPS data shown in Figures 7.2 and 7.3 are processed in ITRF2000 (*Altamimi et al.,* 2002). For the coseismic deformation, the motion of ~2.5 cm/yr of the Sunda block in ITRF2000 is negligible.

For the postseismic deformation, GPS data without the correction for the interseismic deformation represent the combined effects of three factors: the earthquake, the locking of the fault, and the secular motion of the Sunda block. The “interseismic motion”

derived by *Apel et al.* (2006) from velocities at GPS stations actually includes the deformation due to the locking of the fault as well as the motion of the Sunda block. The data that have been corrected for this "interseismic deformation" as shown in Figure 7.3 are thus due only to the earthquake with respect to the "fixed" upper plate. Therefore, direct comparison of model-predicted postseismic deformation with GPS observations is also possible.

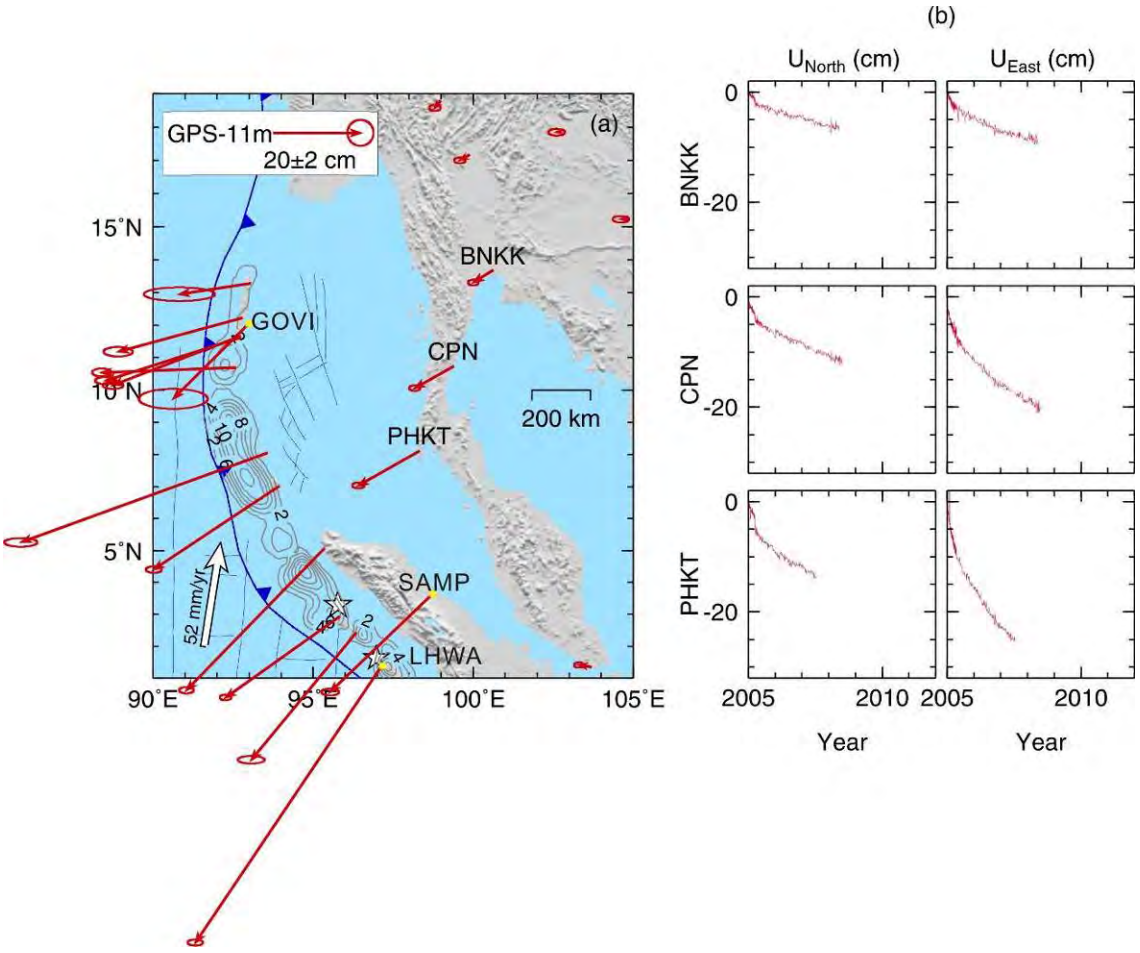

Figure 7.3. Postseismic deformation of the 2004 Sumatra earthquake. (a) Cumulative postseismic displacements from ~40 days to 11 months after the 2004 Sumatra earthquake (*Pollitz et al.*, 2008). GPS data at stations, GOVI, SAMP and LHWA, whose locations are highlighted by yellow dots will be ignored in later plots (see text for discussion). (b) Time series of three continuously operating GPS stations, BNKK, CPN, and PHKT whose locations are shown in (a) (*Panet et al.*, 2010). Left and right panels represent displacements in the north and east directions, respectively.

The elastic dislocation model is widely used to model coseismic deformation. In the work of *Vigny et al.* (2006) and *Chlieh et al.* (2007), the megathrust is approximated by a few rectangular patches. Static displacement due to slip along each of the patches is separately calculated in a uniform (*Okada*, 1985, 1992) or stratified (*Xie and Yao*, 1989) elastic half-space. The total deformation is a combination of the calculated displacements due to the slip of all the patches. On the basis of this approach, source models inverted from seismic and/or geodetic data produce a good fit to coseismic GPS data. For the postseismic deformation, section 6.5 demonstrates that the steady-state (Maxwell) rheology is not appropriate to modelling the short-term transient deformation, but the transient rheology is. Incorporating the transient rheology, an analytical solution for viscoelastic relaxation in a spherically-layered Earth was developed by *Pollitz* (1992, 1997). However, the importance of the presence of the subducting oceanic plate (the slab) was ignored (see discussion in section 6.3). *Pollitz et al.* (2008) later reported a model including a slab (code not published), but their model provided a rather poor fit to the GPS data. In this section, I will demonstrate that our 3D viscoelastic finite element model described in section 7.1 provides a much better fit to the coseismic and postseismic data shown in Figures 7.2 and 7.3.

7.2.3. Fault slip and model mesh

Model parameters used for this margin are summarized in section 7.1. Coseismic distribution of the 2004 Sumatra earthquake is based on *Chlieh et al.* (2007) who derived the slip vectors by inverting geodetic observations, most of which are shown in Figure 7.2. For the inversion, they used three planar rectangular fault blocks to approximate the long and curved megathrust. I smoothed the overlapping parts of, and gaps between, these blocks and mapped the resultant slip distribution onto the three-dimensionally curved fault. The model directly using the slip distribution from *Chlieh et al.* (2007) overestimates the coseismic deformation at GPS stations. The reason is not clear. If their slip vectors are scaled down by 80%, the model provides the best fit to the geodetic data. The modified slip distribution is shown in Figure 7.1. Coseismic distribution of the 2005 Nias earthquake is from *Hsu et al.* (2006), and no modification is required to fit the GPS data. On the basis of the available geodetic data shown in Figures 7.2 and 7.3, both

coseismic and postseismic deformation associated with the 2004 event are modelled, and only the coseismic deformation is modelled for the 2005 event.

There is no reported model of aseismic afterslip in areas surrounding the rupture zones. In this work, the afterslip along the megathrust is determined by fitting the postseismic deformation shown in Figure 7.3 using a trial-and-error approach. Direction of afterslip is based on the direction of near-field postseismic GPS data shown in Figure 7.3a and is approximately margin-normal. The design of a spatial distribution of total afterslip is as follows. I use the modified rupture model of the 2004 event (*Chlieh et al.*, 2007) to define a coseismic slip residue for any nodal point on the shallow (< 70 km) part of fault, that is, the difference between the peak slip (at 4.3°N, 94.8°E) of the entire earthquake event, and the cosesimic slip at the given nodal point. The maximum depths of ~70 km of the afterslip is consistent with the common maximum depth of 70 – 80 km of the decoupling of the subduction interface proposed by *Wada and Wang* (2009) through thermal models of many subduction zones. At the latitude of the peak slip, I fix the residue to be zero at distances 50 km farther away from the peak slip than the 0.1 m coseismic slip contour. This distance is then used to define the zero-residual line relative to the trench for the entire rupture zone. I then modify the residue slip distribution by letting it taper to zero linearly from the location of the 0.1 m coseismic slip contour to the zero-residual line, in both downdip and updip directions. The modified residual slip multiplied by a percentage factor is the assigned total afterslip. The percentage factor is allowed to vary along strike and is obtained by comparing model results with GPS data on a trial-and-error basis. For the Sumatra model, the percentage factor varies from 0% to 30% along strike with an average of about 15%. Coseismic and afterslip of the fault is assumed to be truncated at the location of the trench, that is, fault slip extends no farther seaward than the trench. The total slip including the coseismic slip and afterslip is shown in Figure 7.4a. Two latitude-parallel profiles are shown in Figures 7.4b and 7.4c as examples. Because the two events in Figure 7.1 occurred only a few years ago, deformation due to the fault locking (Figure 6.1c) is negligible, and thus only the effect of the earthquake (Figure 6.1b) is modelled in this margin.

Based on relocated seismicity data (*Engdahl et al.*, 1998), previously published slab geometry (*Gudmundsson and Sambridge*, 1998; *Hippchen and Hyndman*, 2008), and

locations of the trench (*Bird*, 2003) and the arc, I compiled the geometry of the subduction interface for this margin (Figure 7.5). I tried to make the following efforts to reconcile all the available data in the literature in the manual derivation of twenty-eight latitude-parallel cross-sections of the slab interface (only three of them shown in Figure 7.5b). (1) At shallow depths, I tried to derive the slab interface on the basis of previous work and the seismicity data. (2) I assume that the depth of the slab beneath the arc is ~100 – 120 km. (3) I tried to smooth the curve of each slab profile such that dip of the slab gradually increases from low values (<10°) at shallow depths to larger values (~40°) at greater depths. These profiles were then used to construct the 3D mesh of the model. The finite element model spans longitudes 84°E – 115°E and latitudes 7°S – 24°N. It consists of 173,453 nodal points in 20,370 elements. The central part of the mesh is shown in Figure 7.6. Computing time of one model on a PC cluster with 5 dual-core computers is ~8 hours.

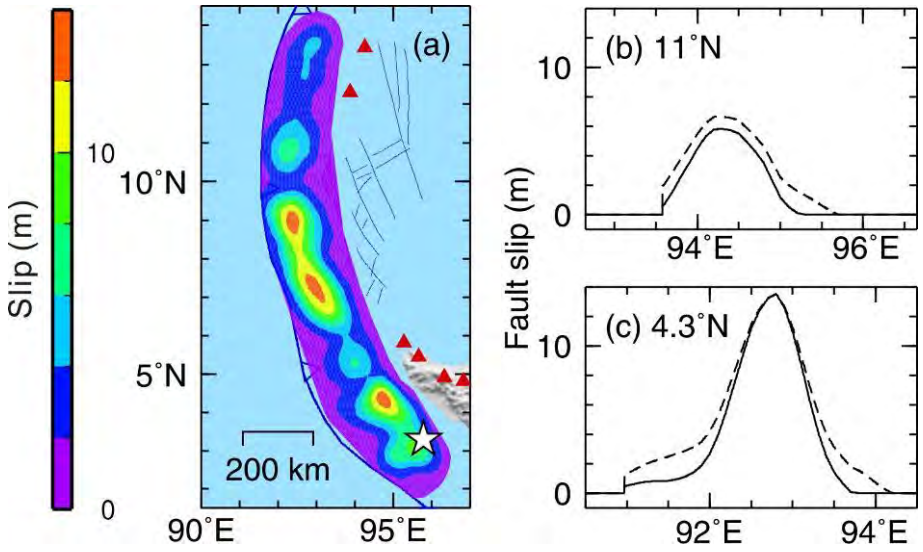

Figure 7.4. (a) Total slip of the megathrust including the coseismic slip showing in Figure 7.1 and afterslip. Open stars represent epicentres of the 2004 and 2005 events. (b) Total slip (dashed line) and the coseismic slip (solid line) along a surface line A-B shown in (a). The fault slips continuously and aseismically from the solid line towards the dashed line following the power-law decay function with T_A = 1.25 yr.

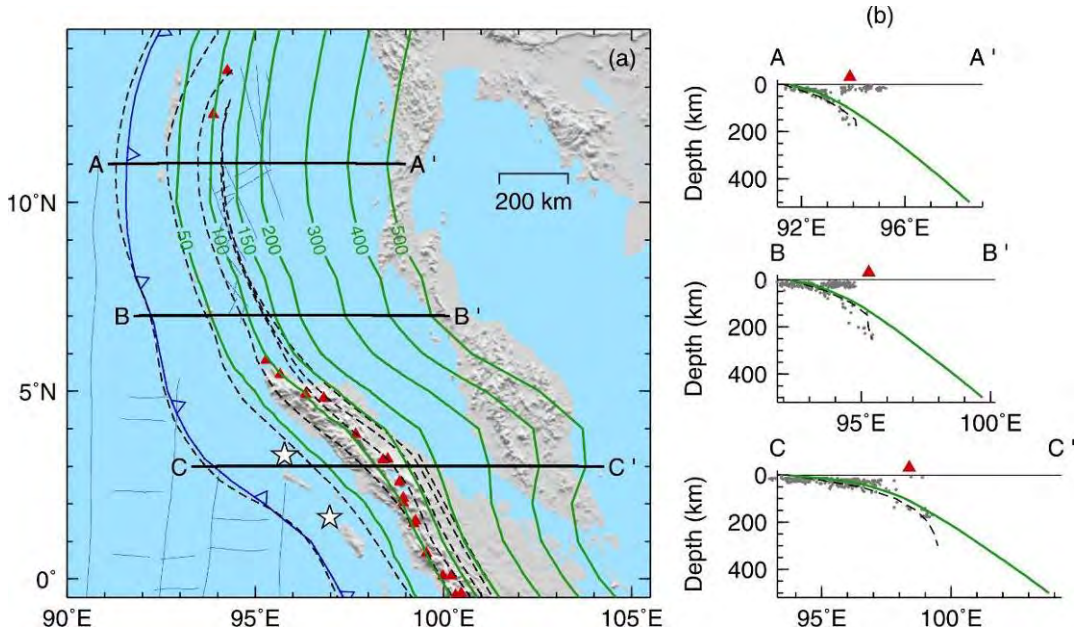

Figure 7.5. Geometry of the subduction interface in Sumatra. (a) Contour of the depth of the subduction interface. Solid green and dashed black lines represent this work and work of *Gudmundsson and Sambridge* (1998), respectively. Red triangles represent locations of the arc volcanoes. Open white stars represent the epicentres of the 2004 Sumatra and 2005 Nias events. (b) Cross-sections of three slab profiles along lines of AA′, BB′ and CC′ in (a). The red triangle represents the location of the volcanoes of the arc closest to the slab profile. Small solid gray dots represent relocated earthquakes by *Engdahl et al.* (1998).

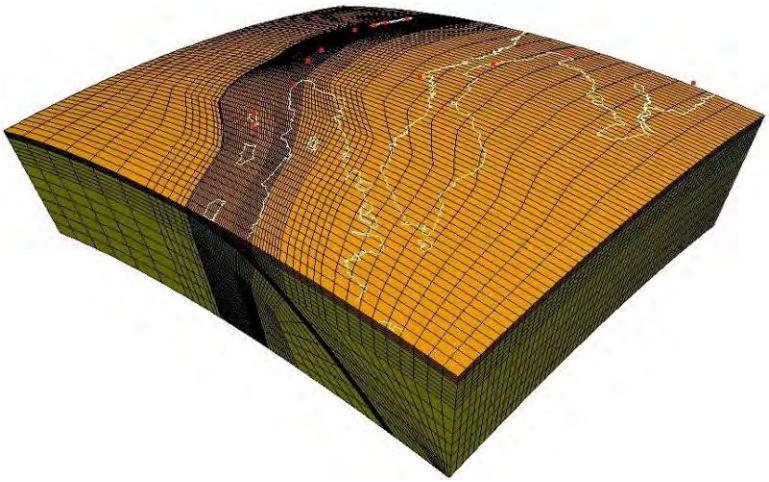

Figure 7.6. Central part of the finite element mesh for the Sumatra margin. White lines on the top surface represent the coast lines in this region. Red dots represent locations of the GPS stations shown in Figure 7.3a.

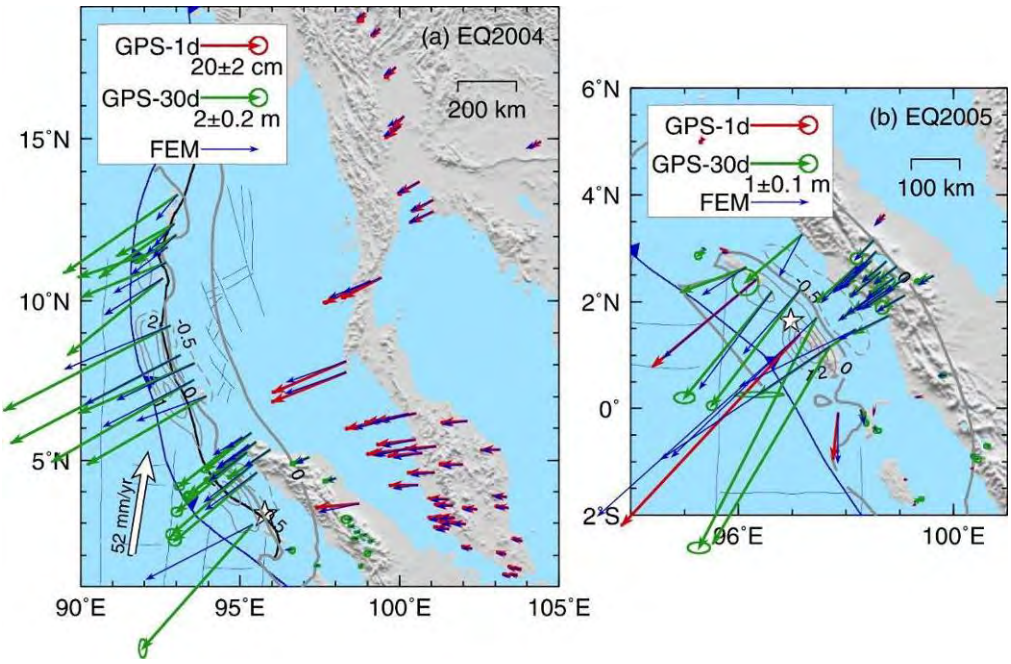

Figure 7.7. Comparison of GPS observations with model produced coseismic deformation. (a) Coseismic deformation associated with the 2004 M_w 9.1 Sumatra earthquake. (b) Coseismic deformation associated with the 2005 M_w 8.6 Nias earthquake. GPS vectors are the same as in Figure 7.2. Blue vectors represent model predicted coseismic displacements. Contours of surface uplift (solid grey lines) and surface subsidence (dashed grey lines) are in 1 m and 0.5 m intervals, respectively. Solid black and solid grey lines represent the pivot lines obtained by satellite images (*Meltzner et al.*, 2006) and by the model of this work, respectively.

7.2.4. Model results

The model well reproduces coseismic deformation at GPS stations as shown in Figure 7.7. The same poor fit to the campaign-mode GPS data in the rupture zone as in *Chlieh et al.* (2007) is because those GPS data include postseismic deformation for about one month. In Figure 7.7a, the model-predicted pivot line generally coincides with that obtained through satellite images (*Meltzner et al.*, 2006).

Model-produced postseismic deformation agrees well with the GPS observations as shown in Figure 7.8b. The model also matches the shape of the time series at the three

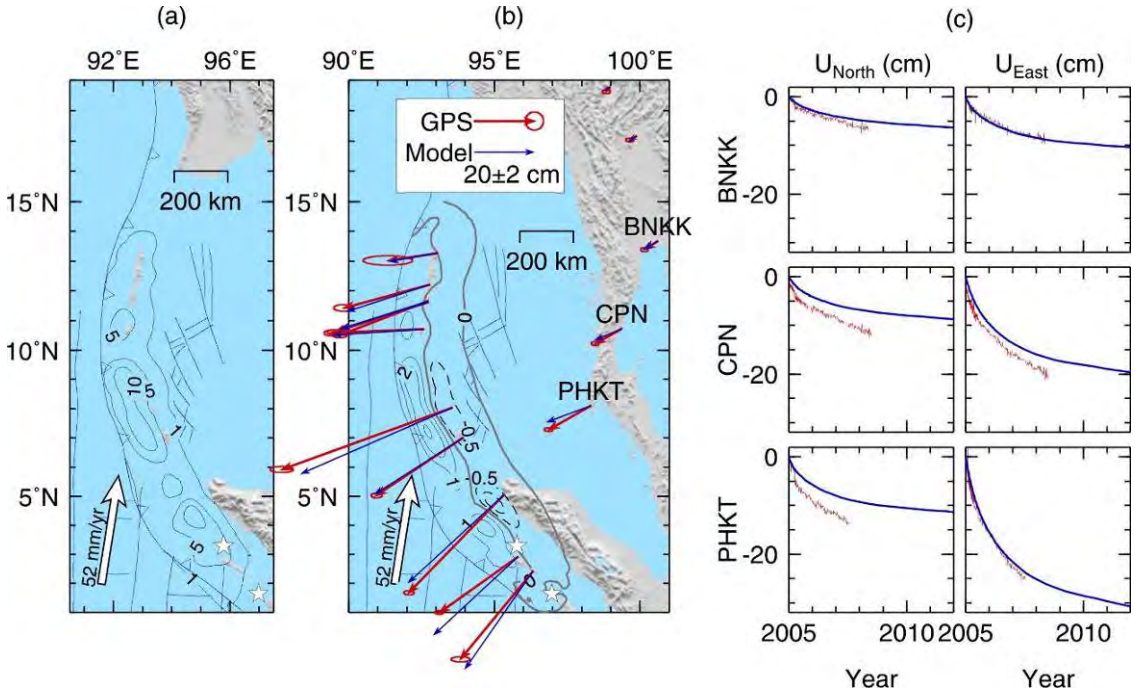

Figure 7.8. Comparison of GPS observations with postseismic deformation produced by the preferred model (Burghers and afterslip). GPS observations are the same as in Figure 7.3. (a) Total slip of the megathrust including the coseismic slip and afterslip. Except for the 1 m slip contour, contour intervals are 5 m. (b) Cumulative postseismic deformation from about 40 days to about 11 months after the 2004 Sumatra earthquake (*Pollitz et al.*, 2008). Solid and dashed contours represent surface uplift (1 m interval) and subsidence (0.5 m interval), respectively. Thick grey line represents the hinge line. (c) Time series at three continuously operating GPS stations, BNKK, CPN and PHKT (Panet et al., 2010). Red and blue represent GPS observations and model produced displacements, respectively.

continuously-operating stations reasonably well (Figure 7.8c). There is a shift in the northern component of stations CPN and PHKT, also shown as a slight clockwise rotation of the model-predicted displacement vector from the GPS vector at these two stations (Figure 7.8b). All the GPS data were corrected for the effect of the 2005 earthquake (*Pollitz et al.*, 2008; *Panet et al.*, 2010), of which the coseismic slip contours are shown in Figure 7.1. The shift in the northern component may be an artefact of data correction.

Similar to the over-correction at stations SAMP and LHWA by tens of centimetres (see discussion in section 7.2.2), an over-correction at CPN and PHKT could decrease the apparent southerly motion due to the postseismic deformation of the 2004 event.

Figure 6.21 in section 6.6 indicates that both the power-law function of $n = 3$ and the exponential function produce similar time series of the displacements and velocities. I construct a testing model (SUM1) to investigate whether the exponential decay of the afterslip in (6-6) produces the same fit to the GPS data as the power-law function. Model setup in SUM0 is the same as in the preferred model except that the decay function of the afterslip in SUM1 is exponential. SUM1 provides the same good fit to the 1-yr GPS data (Figure 7.9a). However, SUM1 greatly underestimates the rate of displacement changes with time at $t > 2$yr (Figure 7.9b). Based on the displacement curves in Figure 6.21, we may conclude that logarithmic or Ohmori's law decay functions of afterslip would provide even poorer fit to the GPS time series.

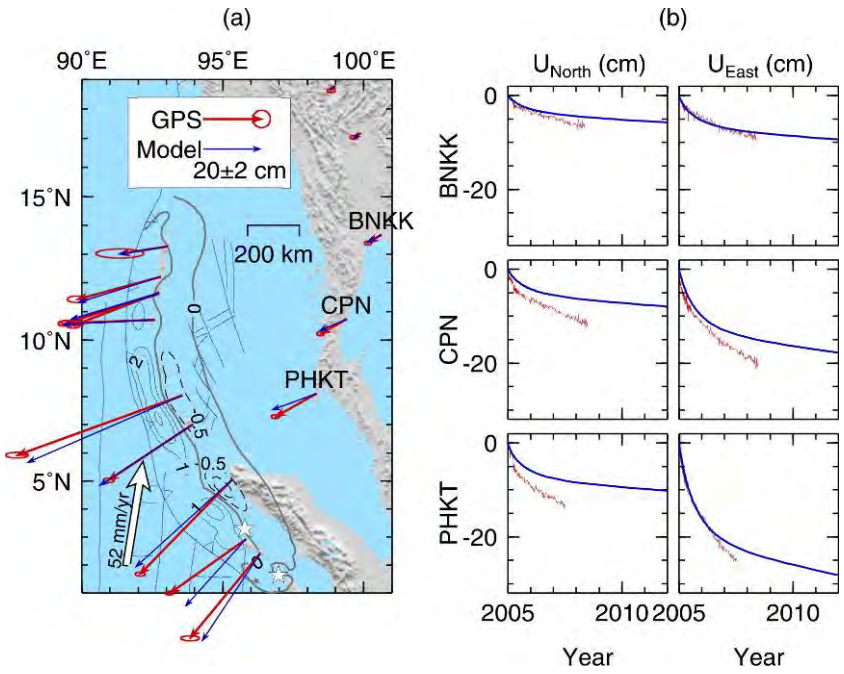

Figure 7.9. Similar to Figure 7.8, comparison of GPS observations with postseismic deformation produced by SUM1 (exponential decay of afterslip). (a) Cumulative postseismic deformation from about 40 days to about 11 months after the 2004 event (*Pollitz et al.*, 2008). (b) Time series at BNKK, CPN and PHKT (*Panet et al.*, 2010).

Another two tests are conducted to investigate the sensitivity of the model to the Maxwell component of the mantle viscosity η_M. In SUM2, $\eta_M = 5 \times 10^{18}$ Pa s, lower than the value in the preferred model by a factor of two. In SUM3, $\eta_M = 2 \times 10^{19}$ Pa s, higher than the value in the preferred model by a factor of two. Other parameters in SUM2 and SUM3 are the same as in the preferred model. SUM2 overestimates the rate of the displacement changes at sites BNKK and PHKT (right column of Figure 7.10a). With a larger η_M, SUM3 underestimates the rate at sites CPN and PHKT (right column of Figure 7.10b). Both SUM2 and SUM3 provide good fit to the first-order pattern of the 1-yr GPS data (left column of Figure 7.10). These two tests indicate that the η_M of no larger than 10^{19} Pa s is required to provide good fit to the GPS observations.

7.2.5. Tests of afterslip-alone and transient-rheology-alone models

To investigate whether the afterslip or transient rheology alone could explain the short-term postseismic deformation, I construct four testing models to compare model-predicted motion with observed postseismic deformation shown in Figure 7.3. Parameters of the mantle viscosity and afterslip of the fault are listed in Table 7.2.

In the first testing model (SUM4), afterslip of the fault is assumed, and the mantle rheology is only the steady-state Maxwell type. The mantle viscosity is the same 10^{19} Pa s as in the preferred model (Table 7.2). I have to increase the total afterslip from the preferred model by a factor of 5/3 to fit the near-field 1-yr GPS data (Figure 7.11b). However, the fit to the far-field data is rather poor (results not shown). In order to fit the far-field data, I have to add an afterslip patch landward of the near-field GPS data. The added afterslip patch extends from depths of ~65 km to ~100 km with slip values of up to 11 m (Figure 7.11a). SUM4-predicted deformation is shown in Figures 7.11b and 7.11c. This model of afterslip alone can explain the GPS motion for all the stations reasonably well, but afterslip at such great depths and with such large values is questionable.

Similar to SUM4, the second testing model (SUM5) includes only the afterslip of the fault and steady-state mantle rheology. Instead of adding an afterslip patch at greater depths in SUM4, I reduce the Maxwell viscosity of the upper mantle by one order of magnitude, that is, to 10^{18} Pa s ($T_M = 0.5$ yr) in order to fit the far-field GPS data (Figure 7.12b). In addition to the viscosity change, I had to increase the total afterslip from the

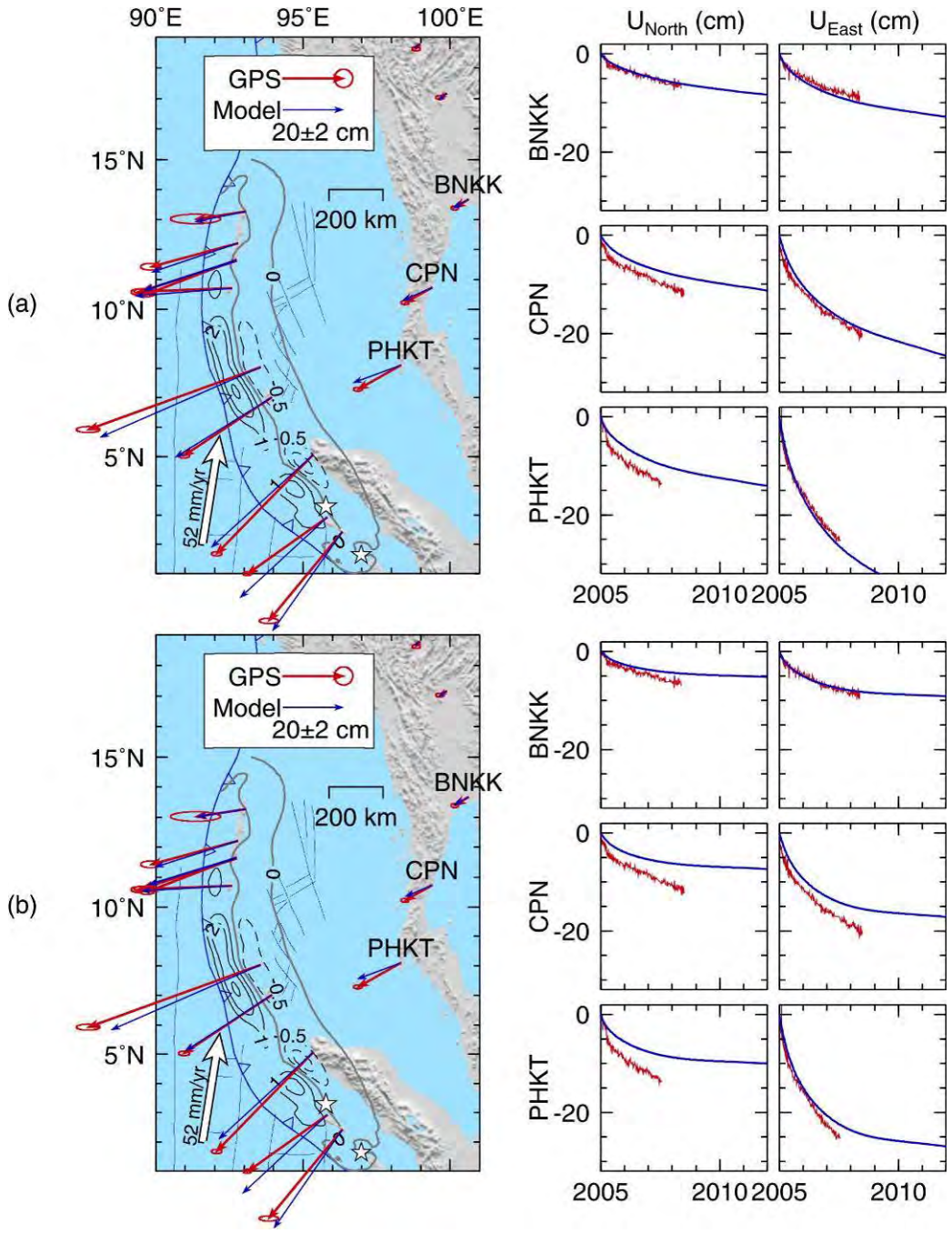

Figure 7.10. Similar to Figure 7.9, comparison of GPS observations with postseismic deformation produced by SUM1 ($\eta_M = 5 \times 10^{18}$ Pa s) (a) and SUM2 ($\eta_M = 2 \times 10^{19}$ Pa s) (b).

preferred model by a factor of 4/3 to fit the near-field data (Figure 7.12a). SUM5

provides the same good fit to the 1-yr GPS as SUM4 (Figure 7.12b), but Figure 7.12c shows that the predicted motion does an extremely poor job explaining the time series from the three continuous stations. In the comparison with the time series, it is the "shape" of the curves, that is, how the rate of the displacement changes with time, that is important. SUM5 consistently underestimates the rate of change within the first 1-2 yrs but grossly overestimates the rate afterwards. Besides, a steady-state viscosity as low as 10^{18} is very inconsistent with the values of around 10^{19} obtained in other Maxwell relaxation models for subduction earthquakes (see review by *Wang*, 2007).

Table 7.2. Mantle viscosity and afterslip of the fault. η_M and η_K are the viscosities (Pa s) of the Maxwell and Kelvin components, respectively.

Model	η_M	η_K	Afterslip	Notes
Preferred	10^{19}	5×10^{17}	√	Transient + afterslip
SUM4	10^{19}	∞	√	Steady-state + afterslip (afterslip at very large depths)
SUM5	10^{18}	∞	√	Steady-state + afterslip
SUM6	10^{19}	5×10^{17}	×	Transient, no afterslip
SUM7	10^{18}	5×10^{17}	×	Transient, no afterslip

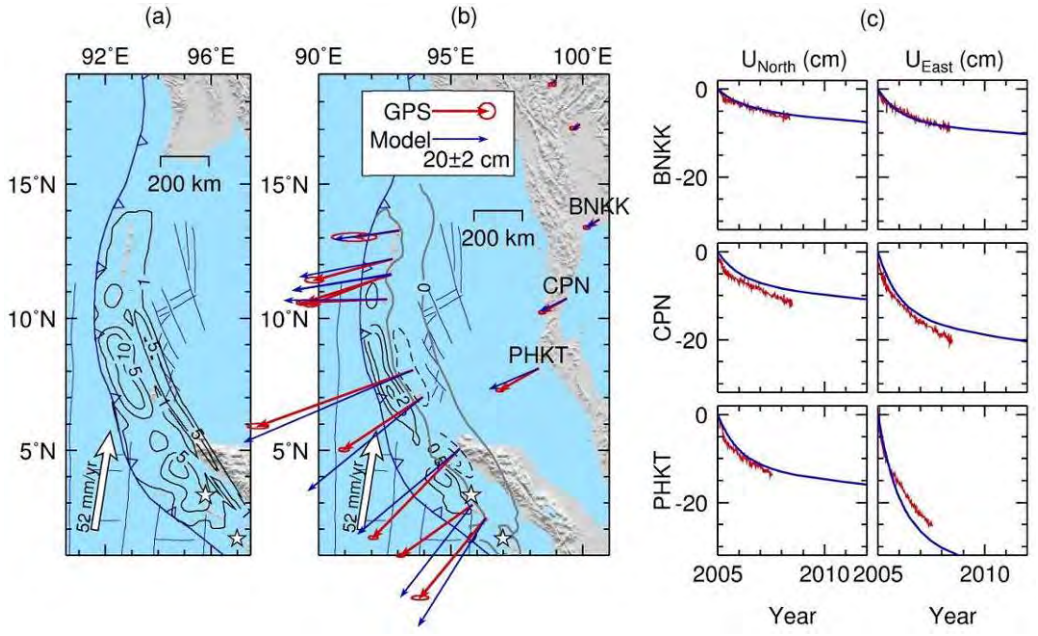

Figure 7.11. Similar to Figure 7.8, comparison of GPS observations with postseismic deformation produced by SUM4 (steady-state Maxwell rheology and afterslip). Afterslip of up to 11m at 65-100 km depths has to be added to fit the far-field GPS data.

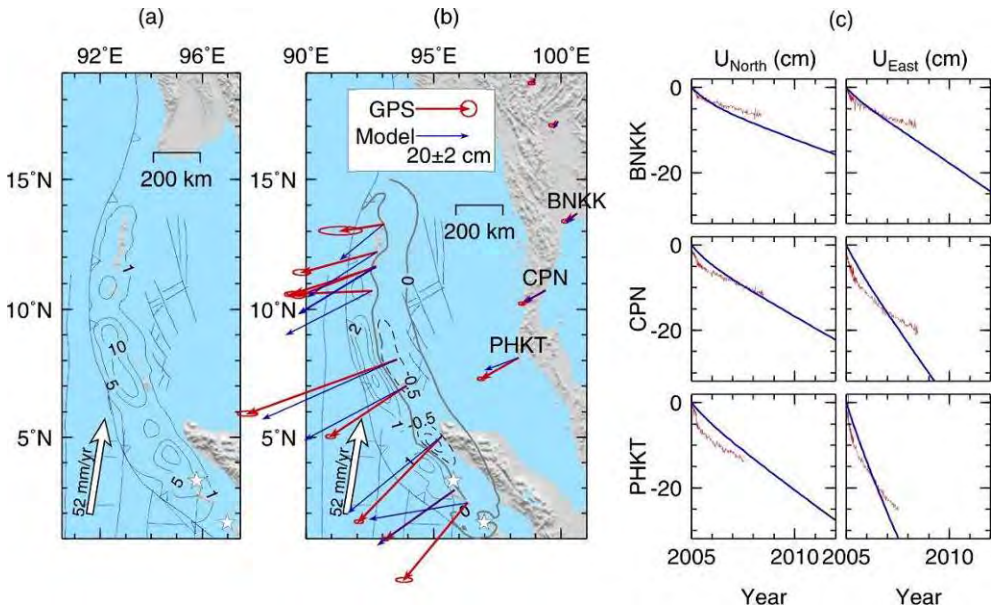

Figure 7.12. Similar to Figures 7.8 – 7.11, comparison of GPS observations with postseismic deformation produced by SUM5 (steady-state Maxwell rheology and afterslip). The upper mantle in SUM5 has a Maxwell viscosity 10^{18} Pa s (T_M = 0.6 yr).

In the third testing model (SUM6), the mantle rheology is the same biviscous Burghers type as in the preferred model, and there is no afterslip of the fault. SUM6 seriously under-predicts the motion of all the stations (Figure 7.13). Reducing the transient viscosity η_K by one order of magnitude (T_K = 0.05 yr) slightly increases the postseismic deformation within 1 yr and does not change the shape of time series at $t > 1$ yr (results not shown).

Similar to SUM6, the fourth testing model (SUM7) has the biviscous Burghers type and no afterslip of the fault. In SUM7, I reduce the steady-state (Maxwell) viscosity η_M by a factor of 10 from that of the preferred model, the same as in SUM5. Compared to SUM6, SUM7 has the same poor fit to the near-field GPS observations (Figure 7.14b). Compared to SUM5, the model of afterslip alone, SUM7 better explains the shape of the time series at the three continuous stations. However, it seriously under-predicts the motion of all the stations near the rupture zone within the first year (Figure 7.14b). Underestimating near-field velocities is a persistent problem with models of transient rheology alone, regardless of how I modified the values of η_K and η_M. *Pollitz et al.* (2008) derived a similar model of transient rheology alone and had the same problem

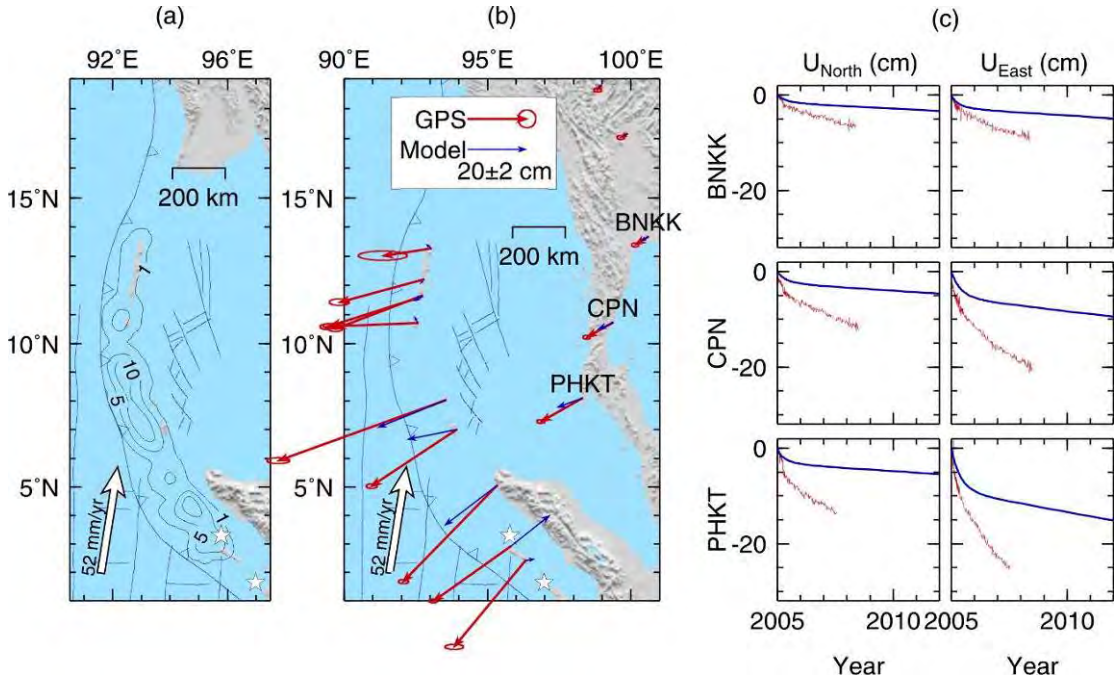

Figure 7.13. Similar to Figures 7.8 –7.12, comparison of GPS observations with postseismic deformation produced by SUM6 (biviscous Burghers type and no afterslip). The steady-state viscosity η_M in SUM6 is the same 10^{19} Pa s as in the preferred model.

with near-field deformation. In addition, due to limitations of the analytical approach they employed, they had to use a very crude coseismic rupture model consisting of several uniform-slip rectangular fault blocks. This also makes comparisons with near-field data difficult.

From these tests, we conclude that the afterslip and transient rheology are both required in order to explain the short-term postseismic deformation both in the near field and in the far field.

7.3. Chile: Decade-scale postseismic deformation

7.3.1. Tectonic background and observed crustal deformation

Based on GPS data, the Nazca plate subducts obliquely (directed N80ºE) beneath the South American plate at a rate of 66 mm/yr at 39°S (*Angermann et al.*, 1999; *Kendrick et al.*, 2003) (Figure 7.15). Constrained by spreading rates, transform fault azimuths, and earthquake slip vectors, a global plate motion model NUVEL-1a (*Demets et al.*, 1994)

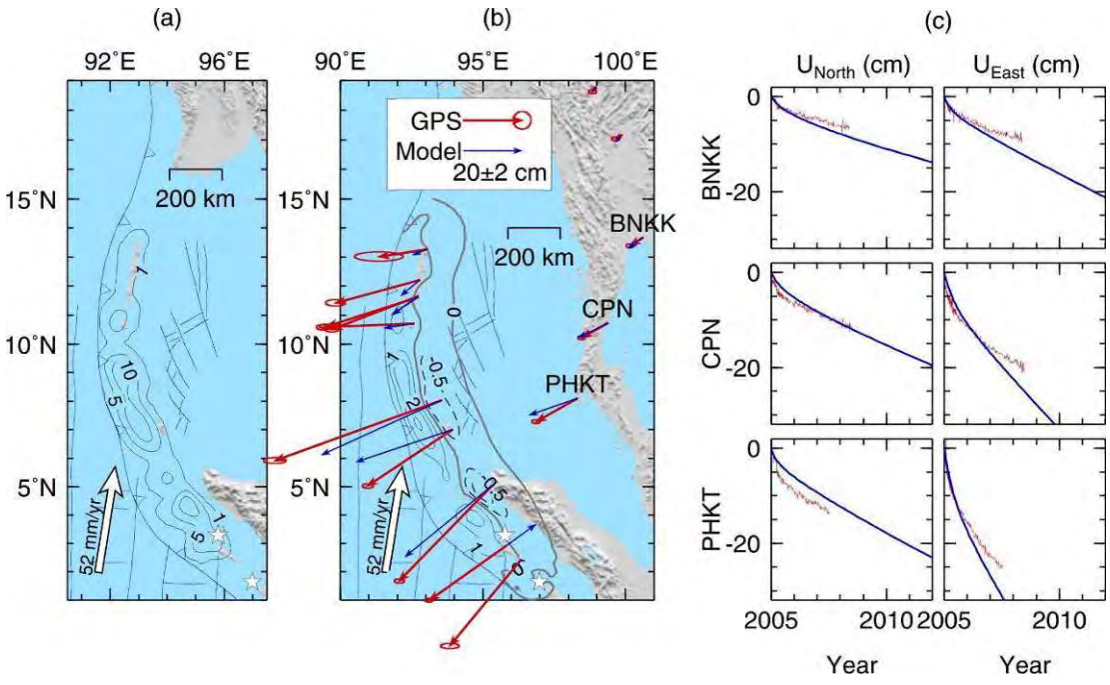

Figure 7.14. Similar to Figures 7.8 –7.13, comparison of GPS observations with postseismic deformation produced by SUM7 (biviscous Burghers type and no afterslip). The steady-state viscosity η_M in SUM7 is 10^{18} Pa s, one order of magnitude smaller than in the preferred model.

reported a larger rate of 80 mm/yr. Around latitude 47ºS, the Chile Ridge subducts beneath the South America plate. South of the triple junction, the Antarctica plate subducts beneath the South America plate at a rate of 18.5 mm/yr at 47ºS (*Sella et al.*, 2002; *Prawirodirdjo and Bock*, 2004).

A significant part of the margin-parallel motion of the upper plate associated with the oblique subduction of the Nazca plate is accommodated by a right-lateral shear motion fault system, the Liquine-Ofqui Fault Zone (LOFZ), of up to 100 km width co-located with the southern Andean volcanic arc (*Hoffmann-Rothe et al.*, 2006; *Rosenau et al.*, 2006). The southern termination of LOFZ at about 47°S is near the Chile triple junction where the Chile spreading ridge is being subducted. The interaction of the spreading

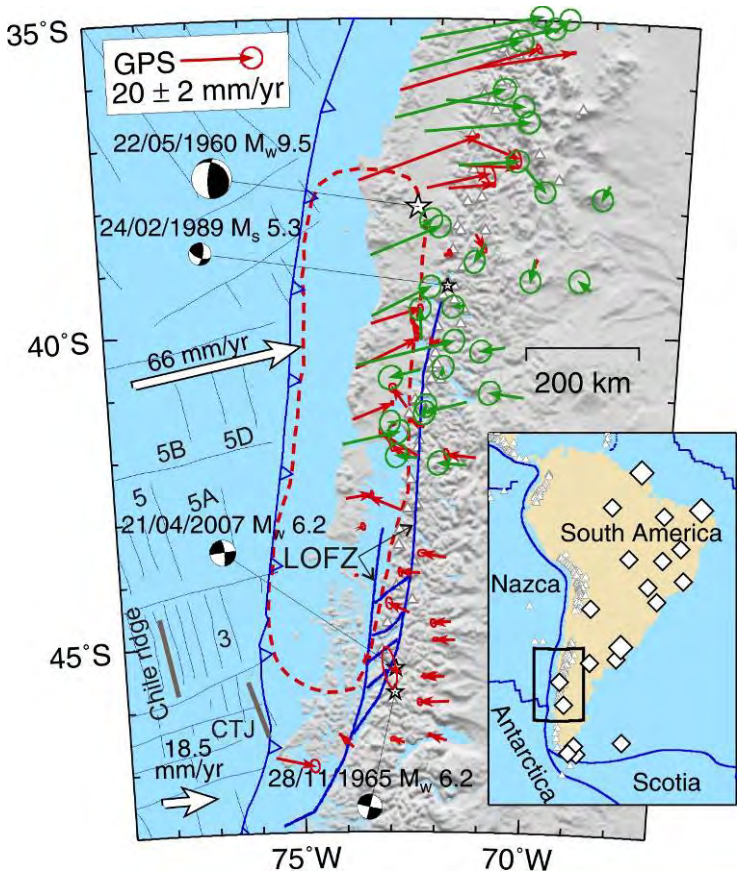

Figure 7.15. Tectonic settings and GPS observations in the Chile margin. Green and red vectors represent sliver-motion corrected GPS observations from *Klotz et al.* (2001) and from *Wang et al.* (2007), respectively. The red dashed line approximates the rupture zone of the M_w 9.5 1960 earthquake (*Plafker*, 1972). LOFZ: Liquine-Ofqui fault zone (*Cembrano et al.*, 2002). CTJ: Chile triple junction. Stars represent epicentres of the 1960 Chile earthquake and earthquakes along the LOFZ (*Barrientos and Acevedo-Aránguiz*, 1992; *Chinn and Isacks*, 1983; U.S. Geological Survey National Earthquake Information Center: http://neic.usgs.gov/neis/qed/). Inset shows the large-scale tectonic environment, with volcanoes indicated by open triangles. GPS stations used to define a South America reference for the GPS velocities of *Klotz et al.* (2001) and of *Wang et al.* (2007) are indicated using large and small open diamonds, respectively.

ridge with the continental forearc has had a strong impact on the motion of the southern LOFZ (*Nelson et al.*, 1994; *Cembrano et al.*, 2002; *Rosenau et al.*, 2006). On the basis of

recent GPS observations, *Wang et al.* (2007) first reported the contemporary dextral motion of the LOFZ. The rate of the sliver motion is 6.5 mm/yr between latitudes 42°S and 44°S and linearly tapers to zero northward from 42°S to the approximate northern end of the LOFZ at 39.5°S. The 6.5 mm/yr sliver motion is about 30% of the strike-slip component of the relative motion between the Nazca and South America plates.

The largest recorded megathrust earthquake occurred on this margin on May 22nd, 1960 (*Duda*, 1963; *Cifuentes*, 1989; *Cifuentes and Silver*, 1989). The great 1960 Chile earthquake and accompanying tsunami caused more than 2000 fatalities (*Housner*, 1963; *Sievers et al.*, 1963). The earthquake-induced tsunami propagated across the Pacific Ocean and produced waves up to about 5 m high along the Japanese coast (*Satake et al.*, 2003, 2007). *Cifuentes* (1989) estimated the rupture length of this event to be 920±100 km. The seismic moment of the 1960 Chile earthquake is estimated to be ~2.0×10^{23} N m (M_w 9.5) (*Kanamori and Cipar*, 1974; *Kanamori*, 1977).

On February 27th, 2010, the M_w 8.8 Maule earthquake ruptured this margin immediately north of the rupture zone of the 1960 event (US Geological Survey, http://earthquake.usgs.gov/earthquakes/eqinthenews/2010/us2010tfan/). The event caused significant seaward coseismic motion, similar to that of the 2004 Sumatra earthquake, detected at a number of GPS stations covering the entire latitude areas of the rupture zone. I have constructed a preliminary finite element model to study the coseismic and postseismic crustal deformation associated with this event. Our model predictions agree well with observed coseismic deformation (data collected by our US colleagues) (see discussion in section 8.2). Investigation on the postseismic deformation is ongoing. Because of the time limits, the ongoing work on the 2010 Maule earthquake is not presented in this thesis.

The great 1960 Chile earthquake caused crustal deformation still detectable at GPS stations decades after the event. Starting in 1993, the GeoForschungsZentrum (GFZ) Potsdam, Germany, within the framework of South American Geodynamic Activities (SAGA) project and in cooperation with numerous local host organizations, established a large-scale GPS campaign network in Chile and western Argentina. *Klotz et al.* (2001) published velocities at more than 200 GPS campaign stations in an area of about 2500 km long along the margin (from 22ºS to 44ºS) and 800 km wide. A subset of their GPS data

(green arrows in Figure 7.15) was collected in 1994 and 1996. The GPS data are referred to a nominal stable South American plate defined by three inland GPS stations (large open diamonds in Figure 7.15). Starting in 1993, Michael Bevis, presently at the Ohio State University, USA, led a GPS project (CAP) of which the network for the first time spanned the entire latitudinal range of the 1960 Chile earthquake. After initial and large campaigns in 1993 (north of ~ 42.5°S) and in 1994 (south of ~ 42.5°S) which barely overlapped, the network south of about 42°S was occupied on a piecemeal basis, often using just one or two roving GPS receivers, over extended periods of time between 1997 and 2005. The GPS data published in 2007 (*Wang et al.*, 2007) are referred to a nominal stable South American plate defined by 33 stations located in the South America and several adjacent plates (small open diamonds in Figure 7.15). Using the same approach as in *Wang et al.* (2007), the few GPS stations west of LOFZ between latitudes 44°S and 39.5°S are corrected for the sliver motion of the forearc due to the activity of LOFZ. The corrected GPS velocities are either very small or in the opposite direction of those at east of LOFZ. Other GPS stations are not affected by the motion of LOFZ.

Predominant features of the GPS observations shown in Figure 7.15 are as follows. (1) All the coastal stations are moving landward, obviously due to the re-locking of the fault, while the inland stations are moving seaward. The seaward motion of the inland area is similar to the coseismic and postseismic deformation observed in Sumatra. A similar pattern of this opposing motion is also observed in Alaska (*Savage et al.*, 1999; *Freymueller et al.*, 2000) where the 1964 M_w 9.2 Alaska earthquake occurred four decades ago. It is also expected to be observed in Sumatra in the very near future. The opposing motion indicates prolonged coseismic deformation in the inland area due to relaxation of the earthquake-induced stresses in the upper mantle (see description in section 5.2). *Klotz et al.* (2001) qualitatively attributed the opposing motion to the postseismic relaxation effects of the 1960 great earthquake. (2) Coastal areas at the latitudes of the 1960 earthquake are moving at velocities distinctly smaller than those to the north. (3) Velocities of the coastal areas at the latitudes of the 1960 earthquake decrease southward. Between latitudes of 43°S and 46°S, the coast areas move at small velocities of < 1 mm/yr.

The work described in this section is an expansion of my M.Sc. project (*Hu*, 2004).

For that project, I developed 3D viscoelastic finite element models in a flat Earth to investigate crustal deformation associated with the 1960 Chile M_w 9.5 earthquake, and with coauthors Wang, He, Klotz and Khazaradze, I published a paper for this work in the Journal of Geophysical Research (*Hu et al.*, 2004). Improvements to the previous model include three main aspects: incorporation of the transient rheology, incorporation of the afterslip of the fault, and the development of models in a spherical Earth. In addition to these improvements to the model, in this work I use more GPS data (Figure 7.15) and the recently obtained coseismic slip distribution of the 1960 earthquake inverted from geodetic data (*Moreno et al.*, 2009).

7.3.3. Fault slip and model mesh

At the time of the 1960 Chile earthquake, very limited geodetic data were available to define the distribution of its coseismic slip. *Plafker and Savage* (1970) measured sea-level changes at more than 150 locations in 1968, eight years after the earthquake. A more than 600 km long levelling line was first surveyed in 1957-1959 and was re-surveyed in 1963-1964. Eight triangulation surveys for the derivation of surface shear strain were carried out in 1950-1952 and in 1966-1968. The levelling and surface shear strain data were reported by *Barrientos and Ward* (1990). These geodetic data, obtained 3-8 years after the 1960 Chile earthquake, must include significant postseismic deformation. Because of limited information on the subduction interface at that time, *Barrientos and Ward* (1990) used a dislocation model with a planar fault geometry to invert these geodetic data. They reported a uniform slip planar model (USP) and a variable slip planar model (VSP). In their USP, a rectangular fault 850 km long and 130 km wide had a uniform displacement of seventeen metres. In their VSP, a main rupture zone at shallow depths had displacements up to 41 m, and three rupture patches at depths 80 – 110 km had slip up to 20 m. Based on the geodetic and teleseismic surface wave data, *Plafker* (1972) reported a uniform slip dislocation model in which a uniform 20 m slip occurred along a planar rectangular fault 1000 km long and 120 km wide. On the basis of the USP model by Barrientos and Ward (1990) and the uniform slip model by *Plafker* (1972), the earthquake in my master project was modelled as an instantaneous uniform slip of 20 m in the plate convergence direction over a rectangular rupture zone

900 km long and 120 km wide. In recent years, the geometry of the subduction interface has been better constrained from local seismological network (*Bohm et al.*, 2002; *Lange et al.*, 2007), deep seismic reflection and refraction profiles (*Lüth et al.*, 2003; *Groß et al.*, 2007), and gravity data (*Tassara et al.*, 2006; *Tašárová*, 2007). On the basis of recently derived slab geometry, *Moreno et al.* (2009) used a 3D elastic spherical-Earth finite element model to invert the same geodetic data as used by *Barrientos and Ward* (1990). *Moreno et al.* (2009) reported one rupture zone at depths <55 km with slip locally up to 40 m. Because a few years postseismic deformation is included in the geodetic data used for inversion, the obtained "coseismic" slip distribution must be overestimated although the exact amount of overestimate is unknown.

The model directly using the slip distribution from *Moreno et al.* (2009) overestimates seaward motion at inland stations as expected (results not shown). Similar to the model of the 2004 Sumatra earthquake in section 7.2, the model scaling down the coseismic slip from *Moreno et al.* (2009) by 80% provides best fit to the contemporary GPS data. The scaled coseismic distribution is shown in Figure 7.16a. Following the procedure of assigning afterslip of the fault in Sumatra, a value of ten percent of the residual slip, which is the difference between the peak coseismic slip in the whole rupture zone and the coseismic slip at every given nodal point, is assumed in the Chile margin. Because of the lack of geodetic data within a few years after the 1960 earthquake, the exact distribution of afterslip is unknown. For the purpose of modelling crustal deformation decades after the earthquake in this section, details of the afterslip distribution are not important (see discussion in section 6.7). The total slip of the fault including both coseismic slip and afterslip is shown in Figure 7.16b. Two latitude-parallel profiles at latitudes of 40.5°S (peak slip) and 44°S are shown in Figure 7.16c as examples.

Similar to my master project (*Hu et al.*, 2004), the megathrust is assumed to be locked along the entire margin in the strike direction. For the downdip direction, I previously assumed a uniform width for the locked zone, but this apparently does not produce a good match for the southward decreasing of the coast velocities shown in Figure 7.15. Following *Wang et al.* (2007), I assume a southward narrowing locked zone (Figure 7.17). This approach is consistent with the hypothesis that the downdip limit of the

seismogenic zone is thermally controlled (*Hyndman and Wang*, 1993; *Hyndman et al.*, 1997; *Oleskevich et al.*, 1999; *Hyndman and Peacock*, 2003). As we move south along the margin, the age of the Nazca plate gradually decreases to zero at CTJ (Figure 7.15), accompanied with an increase in heat flow (*Cande et al.*, 1987). Therefore, the downdip limit of the seismogenic zone must become shallower when approaching CTJ.

Similar to the procedures of deriving slab geometry in Sumatra, I tried to reconcile the available data in the literature in the manual derivation of twenty-five latitude-parallel profiles of the subducting slab along the Chile margin (Figure 7.18a). These data include relocated earthquakes (*Engdahl et al.*, 1998), previously published slab geometry (*Oleskevich et al.*, 1999; *Klotz et al.*, 2001; *Wang et al.*, 2007), and locations of the trench (*Bird*, 2003) and the arc (Figure 7.18b). These profiles were then used to construct the 3D mesh of the Chile margin. The finite element model spans longitudes 60°W – 84°W and latitudes 32°S – 52°S. It consists of 138,771 nodal points in 16,275 elements. The centre part of the finite element mesh is shown in Figure 7.19.

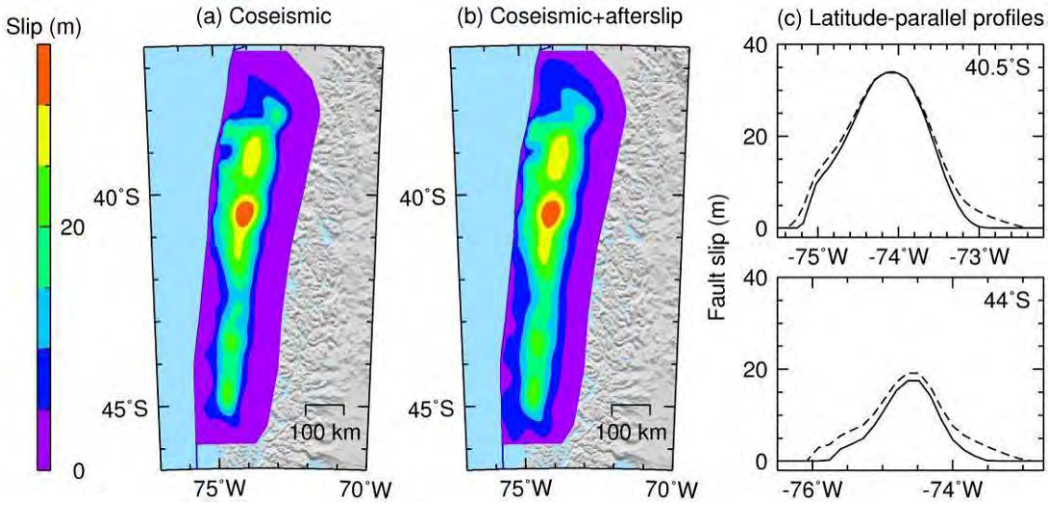

Figure 7.16. Slip distribution of the megathrust of the Chile margin. (a) Coseismic slip distribution of the 1960 M_w 9.5 Chile earthquake based on Moreno et al. (2009). (b) Total slip including coseismic slip and afterslip. (c) Coseismic (solid) and total (dashed) slips along two latitude-parallel profiles, 40.5°S (peak slip) and 44°S.

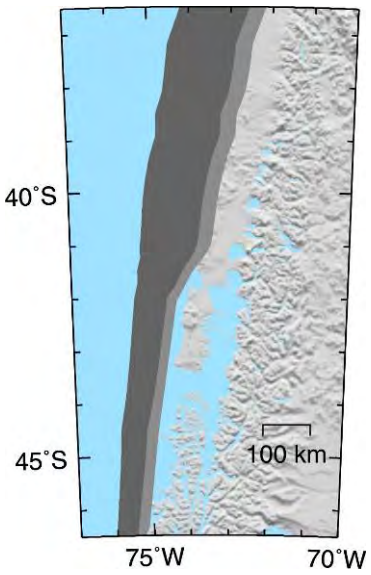

Figure 7.17. Locking of the megathrust in the Chile margin. Heavy shaded area represents the fully-locked region at the plate subduction rate. In the light shaded area, the subduction rate tapers linearly to zero.

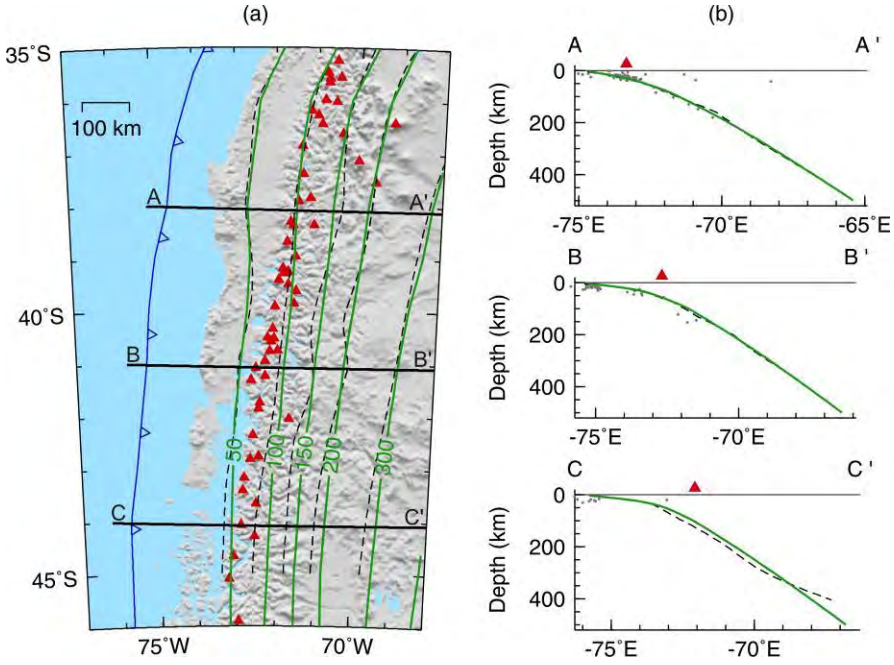

Figure 7.18. Geometry of the subduction interface in Chile. (a) Contour of the depth of the subduction interface. Solid green and dashed black lines represent this work and work of *Voelker et al.* (2007), respectively. Red triangles represent locations of the arc volcanoes. (b) Cross-sections of three slab profiles along lines of AA′, BB′ and CC′ in (a). The red triangle represents the location of the volcanoes of the arc closest to the slab profile. Small solid gray dots represent relocated earthquakes by *Engdahl et al.* (1998).

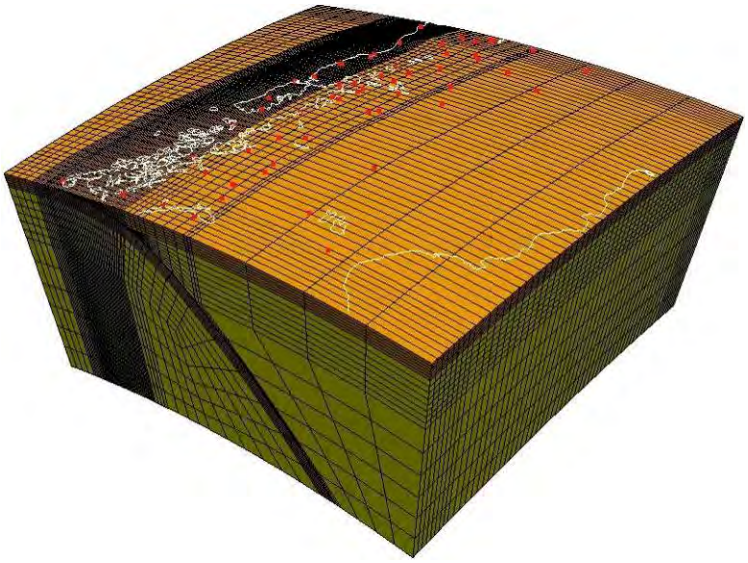

Figure 7.19. Central part of the finite element mesh. White lines on the top surface represent the coast lines in this region. Red dots represent locations of the GPS stations shown in Figure 7.15.

7.3.4. Model results

Model results are shown in Figure 7.20. The model well reproduces the first-order pattern of the GPS observations. For the coseismic vertical deformation, the hinge line is consistent with that observed by Plafker in 1968 (*Plafker and Savage*, 1970). In *Hu et al.* (2004), afterslip of the fault was lumped into the coseismic slip by assuming a wider rupture zone, and therefore the predicted hinge line was located farther landward. The new model predicts that the seaward motion of the inland stations will "disappear" about 18 T_M after the earthquake (when the seaward motion is < 1 mm/yr) (Figure 7.21). Note that the effect of the 2010 Maule earthquake is not included in this work (see section 8.2). Deformation north of the rupture zone of the 1960 earthquake is affected by the 2010 Maule earthquake, and hence seaward motion in this area has "re-appeared" in new GPS observations not included here.

Tests in section 7.2 demonstrate that both the transient rheology and afterslip of the fault must be at work immediately after the earthquake. Based on a simpler model of "2D" mesh, tests in section 6.5 indicate that at $t > 10\ T_M$, models of both the bi-viscous rheology and the Maxwell steady-state rheology produce similar crustal deformation. To

investigate whether the incorporation of the transient rheology (Kelvin body) has an effect also on deformation several decades after the earthquake, I construct a testing model CHL1 with the steady-state Maxwell rheology alone, the same as in *Hu et al.* (2004) except for the spherical Earth geometry. Model setup in CHL1 is the same as in the preferred model except that the mantle viscosity in CHL1 is of the steady-state Maxwell type with $\eta_M = 10^{19}$ Pa s.

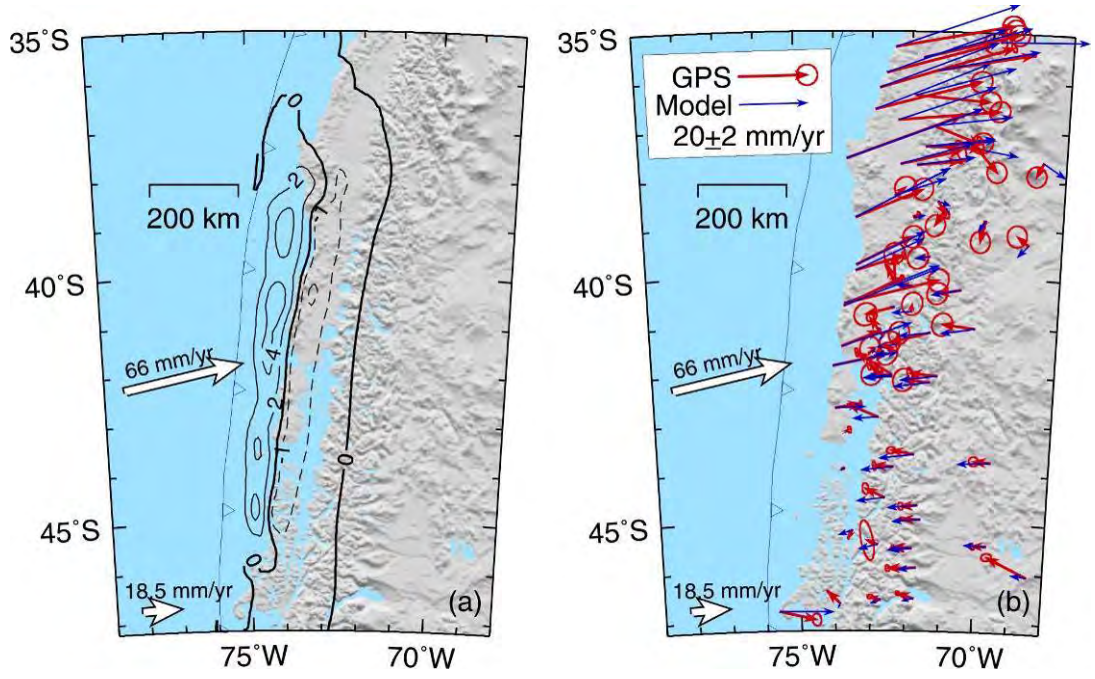

Figure 7.20. Preferred model for the 1960 Chile earthquake and its coseismic and postseismic deformation. (a) Model-predicted coseismic vertical surface deformation. Solid and dashed contours represent uplift (2 m intervals) and subsidence (1m intervals). Thick line is showing the 0 m vertical deformation. (b) Comparison of model-predicted surface velocities 40 years after the 1960 earthquake with GPS observations. Red and blue arrows represent GPS observations and model-predicted vectors, respectively. For the convenience of comparison, data from *Klotz et al.* (2001) are plotted also as red arrows (they were green arrows in Figure 7.15).

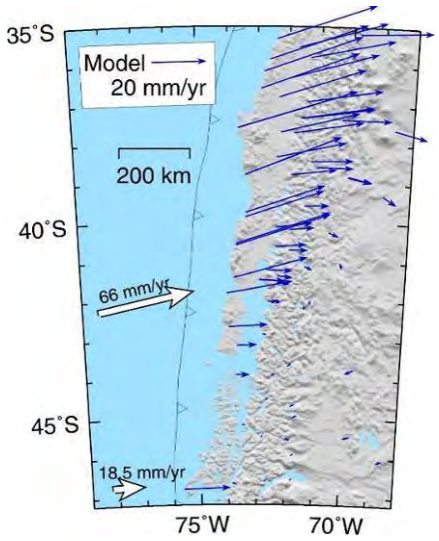

Figure 7.21. Model-predicted surface velocities 18 T_M (110 years) after the earthquake. The seaward motion in the inland area is less than 1 mm/yr.

CHL1 generally overestimates the seaward motion at the inland stations 7 T_{M} or 100 T_K (40 years) after the earthquake (Figure 7.22a). In order to improve the data fit in the inland area, a higher mantle viscosity, *e.g.*, 2.5×10^{19} Pa s as used in my previous MSc work, is required. At a short-time after the event (*e.g.*, $t < 10\ T_K$), CHL1 (steady-state Maxwell rheology) produces surface velocities generally much smaller than those of the preferred model (transient rheology) (results not shown). The fast decay of rapid deformation in the preferred transient-rheology model is consistent with the results in section 6.5. At longer times, surface velocities produced by the transient-rheology model are generally smaller than those of the steady-state rheology model, and a smaller mantle viscosity of the Maxwell component ($\eta_{\mathrm{M}} = 10^{19}$ Pa s) is thus required. Based on velocity evolution of two surface points, one at the coast and the other farther inland, differences in surface velocities between CHL1 and the preferred model are negligibly small at $t > 20\ T_M$ (Figure 7.22b).

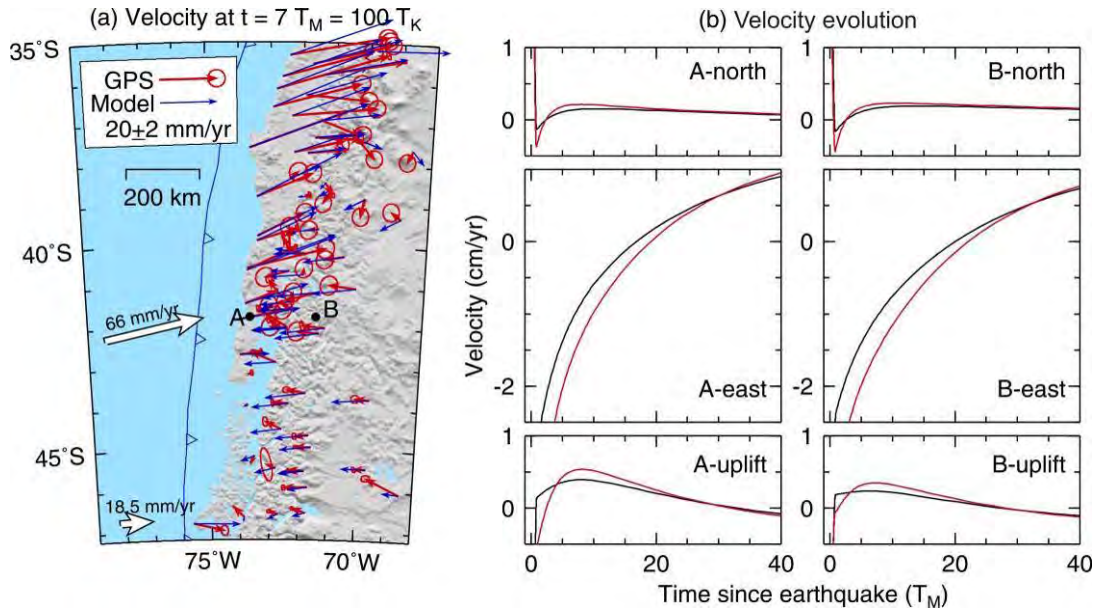

Figure 7.22. Comparison of CHL1 (steady-state rheology and afterslip) with GPS observations and the preferred Chile model. (a) Similar to Figure 7.20b, comparison of surface velocities produced by CHL1 with GPS observations. (b) Velocity evolution of two surface points A and B whose locations are plotted as solid black dots in (a). Black and red lines represent the preferred and CHL1 models, respectively.

The testing model VS3 in section 6.4 illustrates that the "cold" wedge corner represented by a steady-state viscosity one order of magnitude higher greatly affects the crustal deformation due to an earthquake alone at short times. I constructed another testing model CHL2 to investigate the effect of the "cold" wedge corner subjected to the earthquake and locking of the fault. Model setup in CHL2 is the same as in the preferred model except that the wedge corner has a steady-state viscosity 10^{20} Pa s, one order of magnitude larger than in the preferred model. The lateral variation of the steady-state viscosity in the continental upper mantle in CHL2 is the same as in VS3. CHL2 provides the same good fit to the GPS observations as the preferred model does (Figure 7.23a). For the deformation due to the earthquake alone, the differences in the surface velocities of the surface point A between CHL2 and the preferred model is large at short times after the earthquake (*e.g.*, $t < 30\ T_M$) but becomes small at longer times (Figure 7.23b). The pattern of velocity differences is consistent with the conclusion drawn in section 6.4. For

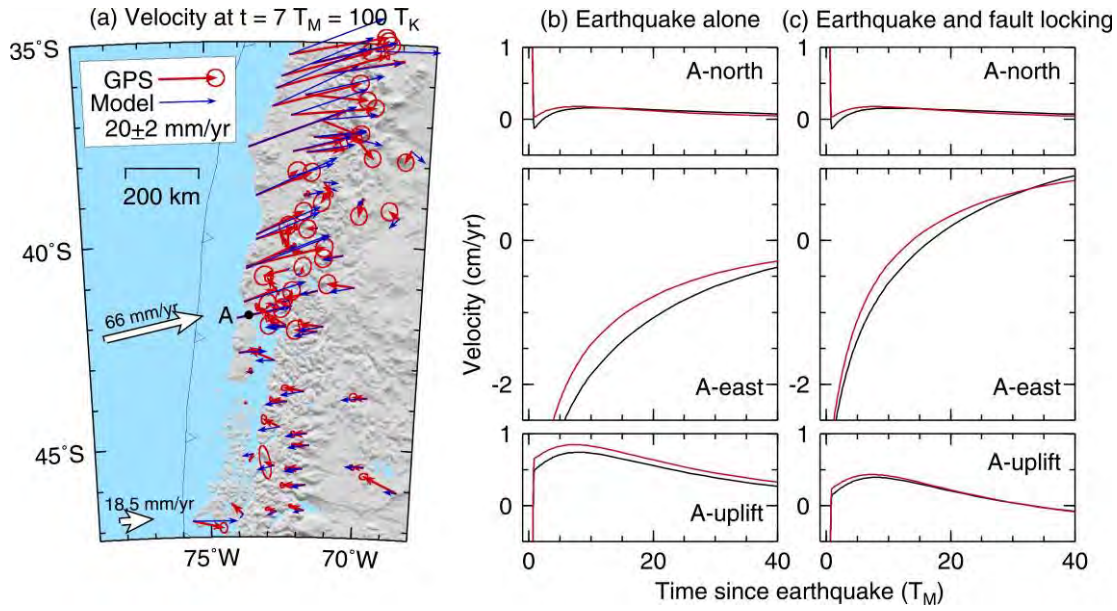

Figure 7.23. Similar to Figure 7.22, comparison of CHL2 (transient rheology and presence of a "cold" wedge corner) with GPS observations and the preferred Chile model. (a) Similar to Figure 7.20b, comparison of surface velocities produced by CHL2 with GPS observations. (b) Velocity evolution of the surface point A (solid black dots in (a) and Figure 7.22a) due to the earthquake alone. (c) Velocity evolution of A due to the earthquake and locking of the fault. Black and red lines represent the preferred and CHL2 models, respectively.

the deformation due to the earthquake and locking of the fault, the velocity differences are very small at both short and longer times, and hence the combined effects of the "cold" wedge corner largely cancel out.

Similar to the tests of the model sensitivity on the steady-state component (η_M) of the mantle viscosity, another two tests CHL3 and CHL4 are considered for the Chile margin, with $\eta_M = 5 \times 10^{18}$ Pa s and 2×10^{19} Pa s, respectively. Other parameters in CHL3 and CHL4 are the same as in the preferred model. Decreasing of η_M by a factor of two results overestimation of the seaward motion in the inland area (CHL3, Figure 7.24a), while increasing of η_M by a factor of two results underestimation of the seaward motion in the inland area (CHL4, Figure 7.24b). The landward motion of the coast areas (mainly due to

locking of the fault) is almost the same as in the preferred model and is less affected. Therefore, the η_M = 10^{19} Pa s in the preferred model is well constrained.

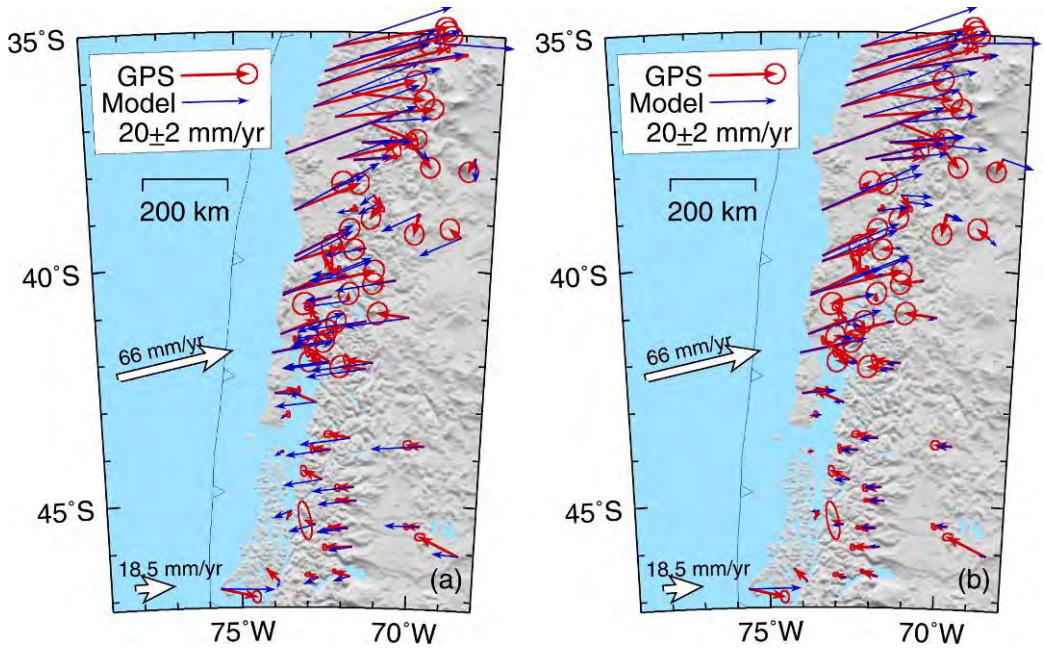

Figure 7.24. Comparison of testing models of different η_M with GPS observations. (a) Comparison of CHL3 (η_M = 5 × 10^{18} Pa s) with GPS observations. (b) Comparison of CHL4 (η_M = 2 × 10^{19} Pa s) with GPS observations. Note that in the preferred model (Figure 7.20), η_M = 10^{19} Pa s.

7.4. Cascadia: Century-scale interseismic deformation

7.4.1. Tectonic background and observed crustal deformation

In the Cascadia margin, the Juan de Fuca plate subducts obliquely (directed N54°E) beneath the North American (NA) plate at a convergence rate of 36 mm/yr at latitude 47°N (*Demets et al.*, 1994; *Wang et al.*, 2003) (Figure 7.25). In the upper plate, the southern Cascadia forearc moves northward and rotates clockwise as it moves north (*Wells et al.*, 1998; *Wells and Simpson*, 2001). Based on paleomagnetic, neotectonic, gravity and aeromagnetic observations, *Wells et al.* (1998) proposed that the forearc motion relative to the stable NA plate can be described as a rigid forearc sliver rotating around a Euler pole. The position of the forearc-NA pole was later refined by *Wells and*

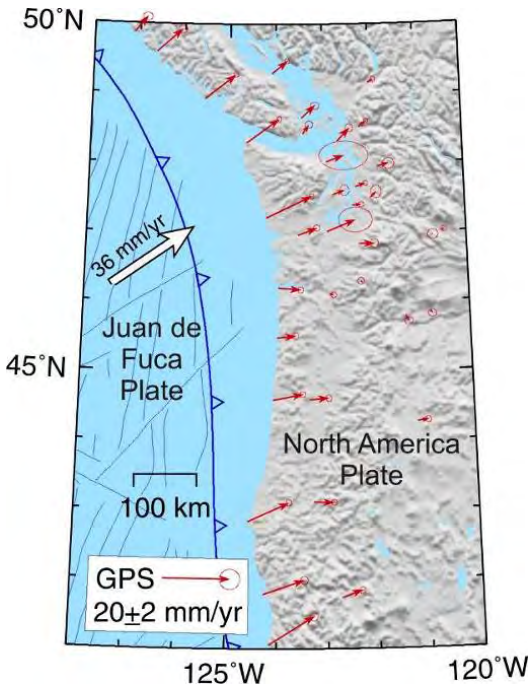

Figure 7.25. Tectonic settings and GPS observations in the Cascadia margin. Red arrows represent contemporary GPS observations 300 years after the 1700 earthquake (*Miller et al.*, 2001; *Wang et al.*, 2001; *Mazzotti et al.*, 2003; *McCaffrey et al.*, 2007).

Simpson (2001). Their model has been supported by GPS observations (*Savage et al.*, 2000; *Miller et al.*, 2001; *Mazzotti et al.*, 2002; *McCaffrey*, 2002). After correction for the forearc sliver motion, the contemporary GPS observations (*Wang et al.*, 2001) shows that all the stations are moving landward, that is, this margin is undergoing strain accumulation for the next megathrust event (Figure 7.25).

There is no written history of great earthquakes on this margin. Based on analysis of sediment cores collected along the continental margins of the western America, *Goldfinger et al.* (2003) concluded that 13 earthquake events ruptured the entire margin in the past 7700 years (see also *Leonard et al.*, 2010). They reported that the average recurrence of great megathrust earthquakes is about 500 years. The last giant event occurred 310 years ago, in 1700. This event caused a tsunami that propagated across the Pacific Ocean and caused damage along the Japanese coast where written records were kept. Based on the analyses of tsunami and modelling, this event occurred on Jan. 26,

1700 with moment magnitude 9.0 (*Satake et al.*, 1996; *Satake et al.*, 2003).

The interseismic deformation of the Cascadia forearc has been modelled using 2D and 3D elastic dislocation models (*Hyndman and Wang*, 1995; *Flück et al.*, 1997; *Wang et al.*, 2003) and viscoelastic finite element models (*Wang et al.*, 1994, 2001). Work of this section is an expansion of the work of *Wang et al.* (2001) (CASvis1) in the following aspects. (1) The 3D finite element model CASvis1 was constructed in a flat Earth and used steady-state rheology to represent the upper mantle. The model in this section is constructed in spherical Earth and incorporates the transient rheology. (2) Previous models (*Wang et al.*, 1994, 2001; *Wang*, 2007) assumed a thin viscoelastic layer between the elastic subducting slab and the elastic overlying plate to account for the effect of afterslip. The model of this section, consistent with models of the Sumatra and Chile margins, does not have such a thin layer. Instead, afterslip of the fault is included in the new model.

7.4.2. Fault slip and model mesh

Model setup including model geometry, rock physical properties and decay function of afterslip are the same as those described in section 7.1. The rupture zone of the 1700 earthquake is based on CASvis1 (*Wang et al.*, 2001). Unlike the uniform slip assumed in CASvis1, coseismic slip of the fault follows a bell-shaped function in the downdip direction (*Wang and He*, 2008; *Priest et al.*, 2009) and varies in strike direction depending on the plate convergence rate and direction (Figures 7.26a and 7.26c). Assignment of afterslip follows the approach of the previous two sections. The same ten percent of residual slip as in Chile is used in Cascadia (Figure 7.26b). Two latitude-parallel profiles at 44°N and 48°N are shown in Figure 7.26c as examples.

The locked zone of the fault is assumed to be the same as the rupture zone. Locking of the fault is modelled as back slip, that is, slip deficit, of the fault at the plate convergence rate. In the transition zone downdip, the full convergence rate follows a half bell-shaped function and tapers to zero. Contours of the back slip of the fault are shown in Figure 7.27.

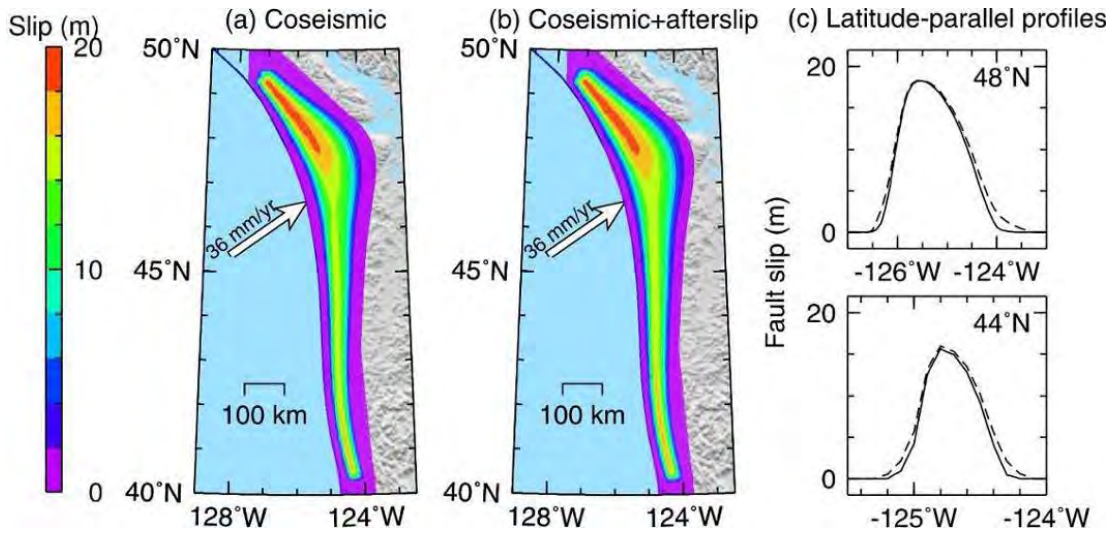

Figure 7.26. Slip distributions of the megathrust in Cascadia. (a) Coseismic slip distribution of the 1700 M_w 9.0 earthquake. (b) Total slip including coseismic slip and afterslip. (c) Coseismic (solid) and total (dashed) slips along two latitude-parallel profiles, 44°N and 48°N.

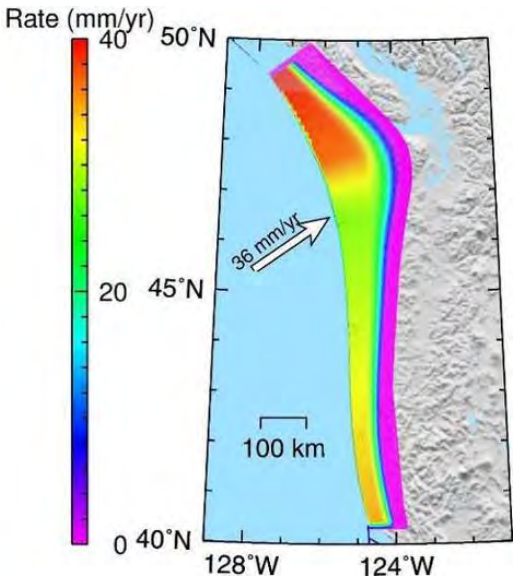

Figure 7.27. Locking of the megathrust in the Cascadia margin. Contours represent back slip rate of the fault depending on the plate convergence rate.

Similar to the procedures of deriving slab geometry in Sumatra (section 7.2.3) and in Chile (section 7.3.3), twenty-one latitude-parallel profiles of the subduction interface along the Cascadia margin are manually derived (Figure 7.28). These profiles were then used to construct the 3D mesh of the Cascadia margin. The Cascadia finite element model spans longitudes 114°W – 138°W and latitudes 35°N – 56°N. It consists of 133,329 nodal points in 15,624 elements. The central part of the finite element mesh is shown in Figure 7.29.

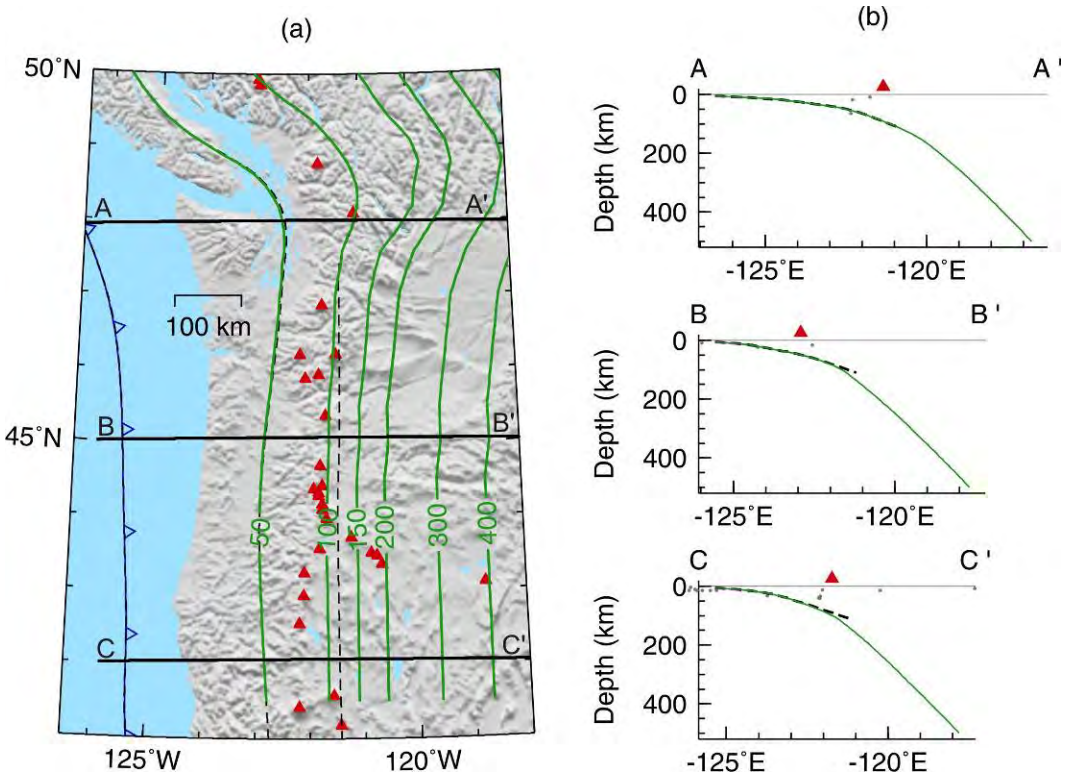

Figure 7.28. Geometry of the subduction interface in Cascadia. (a) Contour of the depth of the subduction interface. Solid green and dashed black lines represent this work and work of *McCrory et al.* (2004), respectively. Red triangles represent locations of the arc volcanoes. (b) Cross-sections of three slab profiles along lines of AA′, BB′ and CC′ in (a). The red triangle represents the location of the volcanoes of the arc closest to the slab profile. Small solid grey dots represent relocated earthquakes by *Engdahl et al.* (1998).

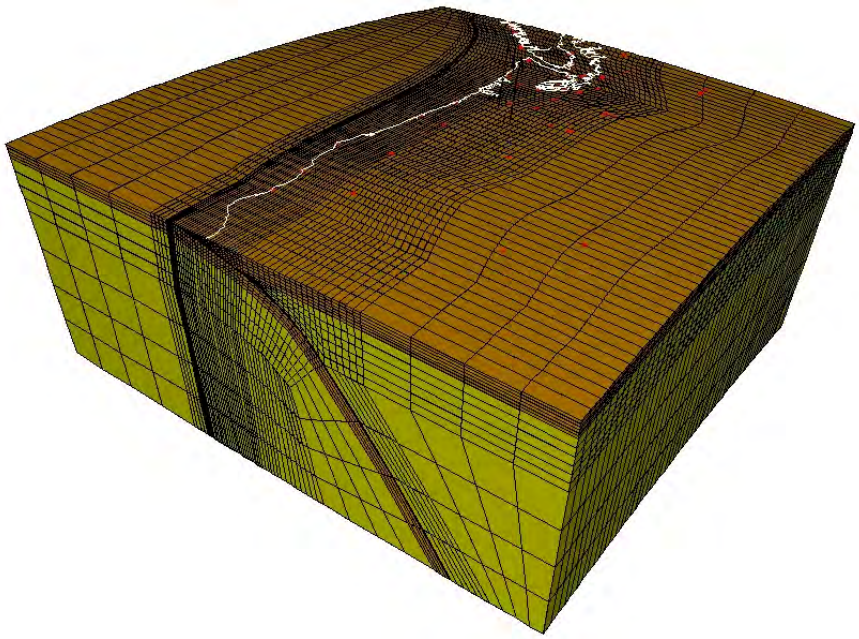

Figure 7.29. Central part of the finite element mesh of Cascadia. White lines on the top surface represent the coastal lines in this region. Red dots represent locations of the GPS stations shown in Figure 7.25.

7.4.4. Model results

More than three hundred years after the 1700 earthquake, the earthquake-induced stresses in the upper mantle must be mostly relaxed, and hence the surface velocities due to the earthquake alone are negligibly small as shown in Figure 7.30b. The landward motion at all the GPS stations reflects the fact that this margin is at a later stage of interseismic deformation. At this stage, the crustal deformation is mainly controlled by the locking of the fault. Figure 7.30c indicates that surface velocities due to the locking of the fault alone agree well with GPS observations. Surface velocities due to the combined effect of the earthquake and locking of the fault are almost the same as in Figure 7.30c. The fit to the GPS data is better than that of CASvis1. Model predicted coseismic vertical deformation shown in Figure 7.31a agrees with the estimates from paleoelevation studies by *Leonard et al.* (2004, 2010). The coseismic vertical deformation will be better constrained by new paleoseismic observations, an ongoing collaborative project with colleagues in the US. The general pattern of the uplift rate 300 years after the 1700

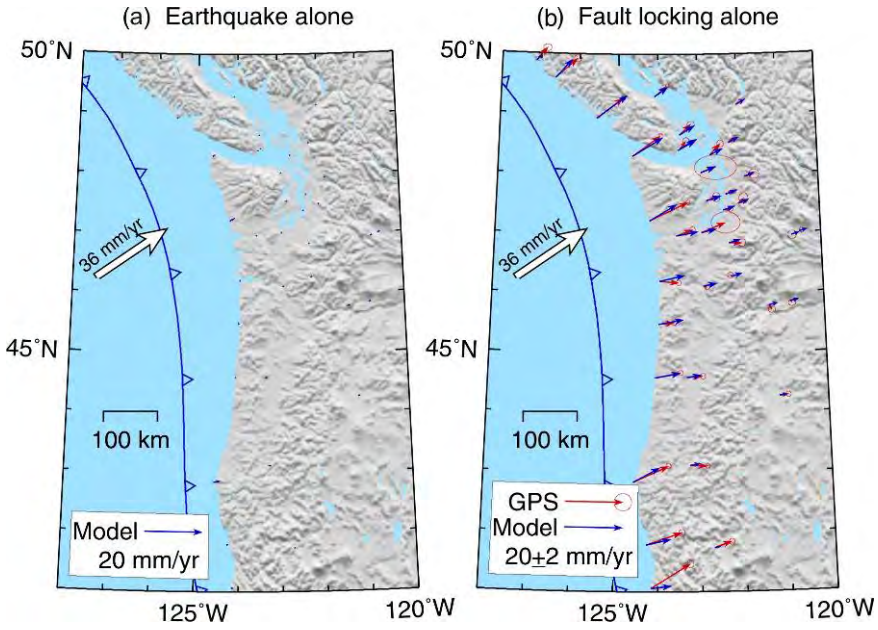

Figure 7.30. Model predicted surface velocities 300 years after the 1700 earthquake and their comparison with GPS observations. (a) Model predicted deformation due to the earthquake alone. (b) Comparison of model-predicted (blue arrows) surface velocities due to the locking of the fault alone with GPS observations (red arrows).

earthquake also agrees with present geodetic observations (see tide gauge and levelling data summarized by *Wang et al.*, 2003) (Figure 7.31b).

Shortly after the 1700 earthquake (*e.g.*, 2 yr in Figure 7.32a), the stations shown in Figure 7.30 would have been undergoing seaward motion, a scenario the same as the contemporary crustal deformation in Sumatra (section 7.2). Decades after the 1700 earthquake (*e.g.*, 40 yr in Figure 7.32b), the coastal stations would have been undergoing landward motion in contrast to seaward motion at inland stations, a scenario the same as the contemporary crustal deformation in Chile (section 7.3). On the other hand, deformation pattern hundreds of years after the earthquake in these two margins, Sumatra and Chile, will be similar to the contemporary deformation in Cascadia. Therefore, the crustal deformation in these three margins provides “snapshots” of the crustal deformation common in earthquake cycles.

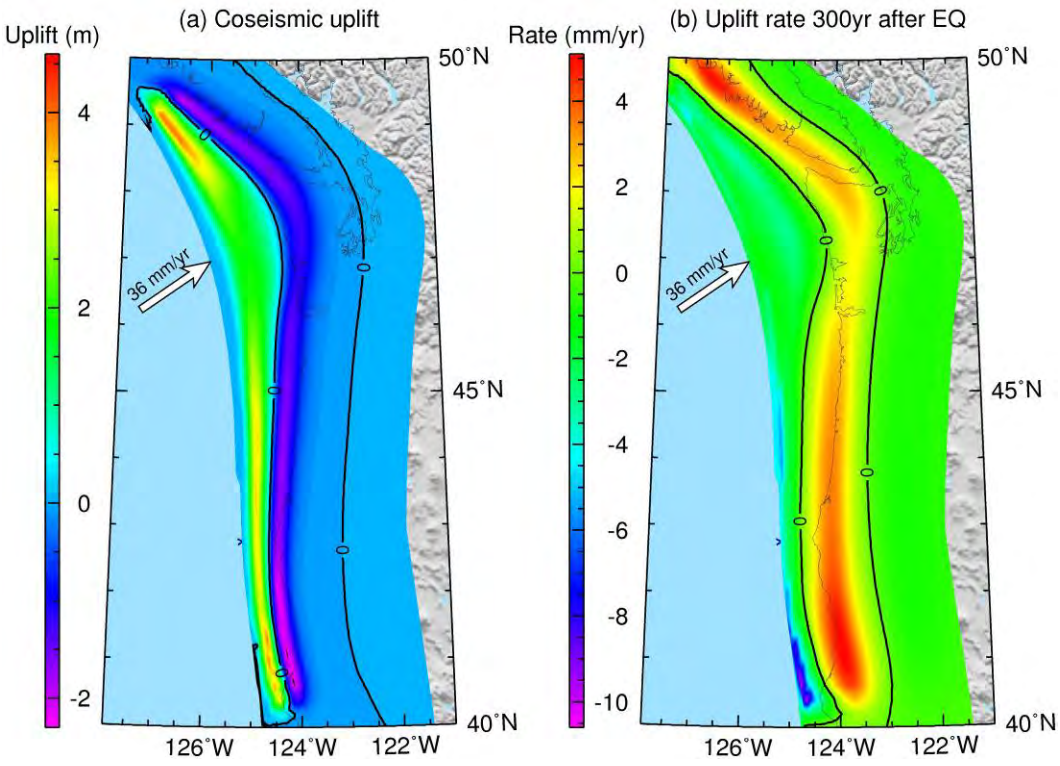

Figure 7.31. Model predicted vertical deformation. (a) Model-predicted coseismic vertical surface deformation. (b) Model predicted uplift rate 300 years after the earthquake. Thick black line represents the hinge line with no vertical deformation.

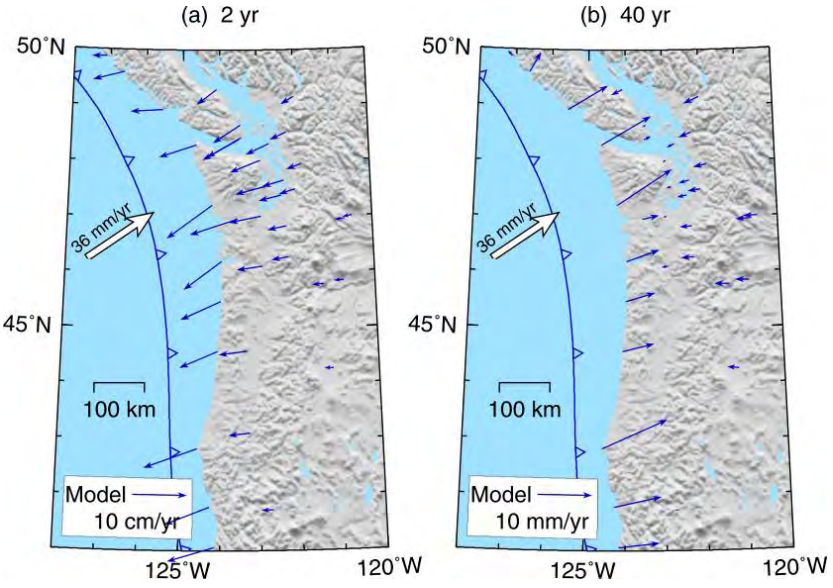

Figure 7.32. Model predicted surface velocities at GPS stations 2 years (a) and 40 years (b) after the earthquake due to the combined effects of the earthquake and locking of the fault.

Similar to the model sensitivity tests in sections 7.2 and 7.3, two tests are conducted to investigate if the long-term interseismic deformation is still sensitive to the change of steady-state component η_M of the mantle viscosity. The η_M in CAS1 and CAS2 are 5×10^{18} Pa s and 2×10^{19} Pa s, respectively. Other parameters in CAS1 and CAS2 are the same as in the preferred model. Figure 7.33 indicates that decreasing (CAS1) or increasing (CAS2) of the η_M in the preferred model by a factor of two results in almost the same long-term interseismic deformation. Therefore, at the later stage of the earthquake cycle, the crustal deformation is mainly controlled by the locking of the fault and is less affected by the stress relaxation of the upper mantle.

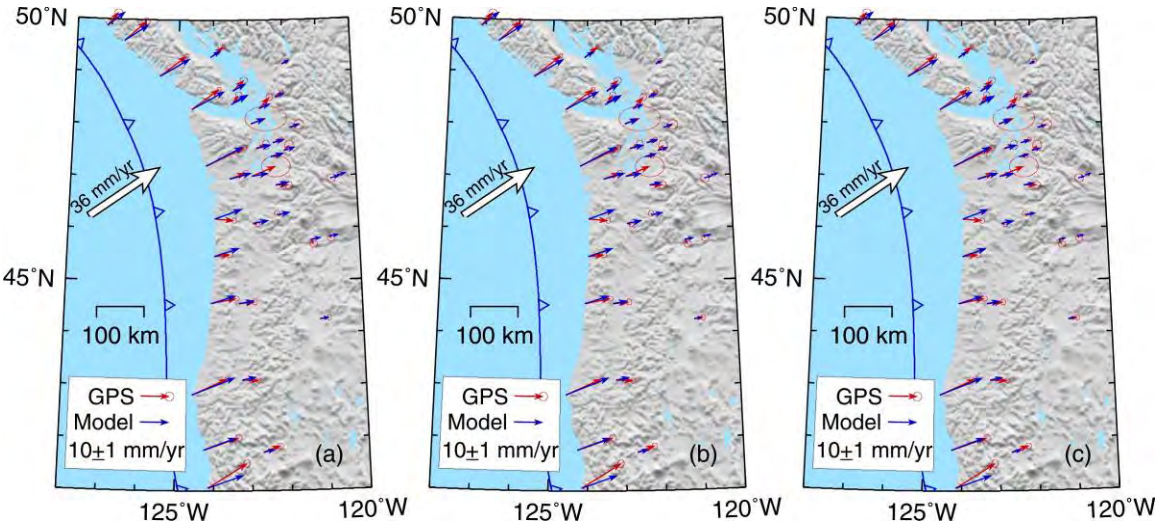

Figure 7.33. Comparison of the preferred and two testing models with GPS observations 300 years after the 1700 earthquake. (a) Comparison of CAS1 with GPS observations. In CAS1, $\eta_M = 5 \times 10^{18}$ Pa s. (b) Comparison of the preferred model with GPS observations. In the preferred model, $\eta_M = 10^{19}$ Pa s. (c) Comparison of CAS2 with GPS observations. In CAS2, $\eta_M = 2 \times 10^{19}$ Pa s.

Chapter 8. Conclusions and Recommendations for Future Research

8.1. Conclusions

Study of the deformation processes at subduction zones associated with great earthquakes helps to assess earthquake and tsunami hazards. Examining the deformation also contributes to the understanding of a wide range of other related processes, such as plate driving forces, mechanical properties of the mantle, dynamics of plate subduction, and so forth. This dissertation consists of two parts and investigates the deformation processes at different spatial scales. In the first part, I use elastic and elastic perfectly-Coulomb plastic models to examine how stress is transferred from the seismogenic zone to the updip zone and its effects on the stability of the overlying outer wedge. In the second part, I use viscoelastic finite element models to examine the crustal deformation of the forearc and back arc in subduction zone earthquake cycles. The scientific contributions of this dissertation include the following aspects.

For a given stress drop in the seismogenic zone during an earthquake, different degrees of the strengthening of the updip zone result in different states of the frictional failure of this zone (see section 2.3). The strengthening of the updip zone that causes rupture to be on the verge of breaking the trench is called the critical strengthening $\Delta\mu'_{b\_c}$ in this work. If strengthening of the updip zone $\Delta\mu'_b$ is smaller than $\Delta\mu'_{b\_c}$, the whole updip zone is at frictional failure. If $\Delta\mu'_b > \Delta\mu'_{b\_c}$, the strengthening is too large to allow the stress to be transferred to the entire updip zone, and its shallowest part is in a stress shadow.

Our model reveals a linear relationship between the critical strengthening of the updip zone $\Delta\mu'_{b\_c}$ and the total force drop ΔF of the seismogenic zone, defined as the product of the average stress drop and area of the seismogenic zone. For a given width of the updip zone, an earthquake with a larger ΔF requires a greater $\Delta\mu'_{b\_c}$ to prevent the rupture from breaking the trench. For the same earthquake force drop ΔF, a narrower updip zone requires a greater $\Delta\mu'_{b\_c}$, since a narrower updip zone is easier to be pushed to complete failure.

Previous studies of wedge mechanics, such as the classical theory of critically tapered Coulomb wedge (see section 3.1), only address long-term deformation of the subduction zone outer wedges averaged over numerous earthquake cycles. The dynamic Coulomb wedge theory (see section 3.3) describes how the long-term deformation is achieved through many earthquakes, that is, a wedge undergoes permanent plastic deformation mainly during earthquakes and mostly elastic deformation in interseismic periods. The dynamic Coulomb wedge theory postulates that the most seaward part of the frontal forearc (outer wedge) featuring much active plastic deformation and steep surface slope overlies the updip aseismic zone, and the further landward part of the forearc (inner wedge) featuring more stable geological formations and flatter surface slope overlies the seismogenic zone.

From published seismic-survey depth sections, I compiled the geometry of outer wedges at twelve accretionary margins and eleven erosional margins (see section 4.1). In the reference wedge model with an internal friction coefficient $\mu = 0.7$, internal pore fluid pressure ratio $\lambda = 0.8$, and basal effective friction coefficient $\mu_b' = 0.04$, outer wedges of most subduction zones are in a stable state although they are expected to be compressively critical (*Hu and Wang*, 2010; *Wang et al.*, 2010). For the weak-wedge model of *Lallemand et al.* (1994), $\mu = 0.52$, $\lambda = 0.88$, and $\mu_b' = 0.029$, most outer wedges are at stable or gravitationally unstable states. Therefore, the steady-state Coulomb wedge theory cannot fully explain the mechanics of the outer wedges. The dynamic Coulomb wedge theory can readily explain this paradox. At the interseismic stage, the outer wedges with a weak basal fault and comparably strong material are at a stable state. During earthquakes, strengthening of the updip zone at a moderate degree (see section 2.2) and/or slight weakening of the wedge material may drive the outer wedges into a compressively critical state (see section 4.2). It is great earthquakes that shape the geometry of the outer wedge. The inner wedge undergoes mostly elastic deformation in earthquake cycles.

After a great subduction zone earthquake, there are three primary processes that control the viscoelastic crustal deformation (see section 5.3). (1) After the earthquake, segments of the fault surrounding the rupture zone may undergo afterslip. Afterslip of the fault causes the upper plate to move towards the trench and decays rapidly with time. (2)

After the earthquake, the fault must be re-locked to accumulate strain for next events. The re-locking of the fault causes the upper plate to move slowly landward. (3) At the coseismic stage, the earthquake induces shear stresses in the upper mantle. The subsequent stress relaxation causes the prolonged seaward motion in areas farther away from the trench. The viscoelastic crustal deformation depends on the interplay of these three processes. Shortly after the earthquake (within a couple of characteristic time of afterslip T_A), the effect of the afterslip dominates (see section 6.6). The afterslip of the fault must follow the power-law decay function at the order of $n = 3$ with $T_A = 1.25$ yr in order to fit the near-field GPS displacements and the far-field GPS time series in Sumatra (see section 7.2.4). After a longer time but within a few Kelvin relaxation time T_K, the crustal deformation is controlled by the total effects of the afterslip and the transient relaxation of the mantle. The afterslip mainly affects the deformation of the forearc. The transient deformation of the mantle affects a broader area including the forearc and back arc. At time scales of a few to <20 Maxwell relaxation time T_M, the crustal deformation is controlled by the steady-state relaxation of the mantle and re-locking of the fault. The steady-state relaxation causes the backarc to move seaward, while the re-locking of the fault causes coast areas to move landward. After a long time when the earthquake-induced stresses are mostly relaxed, the re-locking of the fault dominates, and the entire upper plate moves slowly landward.

The upper mantle in the preferred model has the transient rheology. Viscosities of the steady-state component of the continental and oceanic mantle are 10^{19} Pa s and 10^{20} Pa s, respectively. The steady-state viscosity is about two orders of magnitude smaller than that of the global value obtained through global postglacial rebound modelling (*e.g.*, *Peltier*, 2004). This steady-state viscosity is well constrained in the Chile margin. Either decreasing or increasing of the preferred value by a factor of two results in a very poor fit to the GPS observations. In Sumatra, the preferred value is the maximum estimate, and the lower estimate of the mantle viscosity is 5×10^{18} Pa s. In Cascadia, the steady-state viscosity is constrained to be in the range of 5×10^{18} to 5×10^{19} Pa s.

The transient component of the continental and oceanic mantle is at present poorly constrained. In this work, the transient viscosity is assumed to be 5×10^{17} Pa s. Variation in the transient viscosity greatly affects the velocities within a few Kelvin relaxation time

T_K after a great earthquake. However, the transient relaxation still has a small effect decades after the event. For example, without the transient rheology the steady-state viscosity is 2.5 times the preferred value (*Hu et al.*, 2004; *Wang et al.*, 2007). A long time after the earthquake when the stresses of the Kelvin component are mostly relaxed, variation in the transient viscosity produces almost the same crustal deformation, and the mantle may be represented by either the transient rheology or the steady-state Maxwell rheology.

Modelling results in this work allow us to identify areas to make critical observations and thus provide guidance for the design of future field experiments. For example, the stress and strain analyses in this work assist the network design of ongoing and planned projects at the Nankai subduction zone, in addition to the NanTroSEIZE drilling project, particularly a planned network of borehole fluid pressure observatories. A finite element model of the 2010 M_w 8.8 Maule earthquake helps to design the network of campaign GPS stations.

8.2. Recommendations for future research

Because of the limited geodetic constraints, this dissertation uses a very preliminary model of the afterslip of the fault. The immediate future research is to investigate the detailed evolution and distribution of the afterslip. In addition to the GPS observations, more modern geodetic data such as interferometric synthetic aperture radar (InSAR) images, borehole strainmeter data and borehole pore fluid pressure data are becoming available. For example, InSAR measures the distance between a satellite and the Earth surface. Displacements of the land can be derived from two InSAR images (*e.g.*, *Rosen et al.*, 2004; *Konca et al.*, 2008; *Motagh et al.*, 2008; *Pritchard and Fielding*, 2008). The uncertainty of the InSAR data is a few centimetres (*e.g.*, *Motagh et al.*, 2008). The advantage of this method is that one satellite image may cover a very large area (10^4 – 10^6 km^2). The disadvantage is that how often the target area can be observed depends on the orbits of the satellite. Borehole strainmeters are used to measure the horizontal strain component with a precision of 10^{-10} (*e.g.*, *Gladwin*, 1984; *Asai et al.*, 2005; *Langbein et al.*, 2006; *Wang et al.*, 2008). Borehole hydrologic observatories monitor pore fluid pressure (*e.g.*, *Davis et al.*, 2006; *Davis et al.*, 2009), and the rate of the pressure changes

can be used to derive the rate of the volumetric strain. These modern geodetic methods may be used to constrain the motion of the crust and afterslip.

Well-established crustal deformation helps to investigate the underlying physical properties of the megathrust. For example, the 2010 M_w 8.8 Maule earthquake provides a unique opportunity to investigate the mechanics of the afterslip for the following two reasons. (1) For the first time, abundant modern GPS stations have covered the entire latitude range of the rupture zone (Figure 8.1). These stations have been continuously observing postseismic deformation associated with this event. (2) Portions of the rupture zone are right beneath the land where a few GPS stations locate (Figure 8.1a). The deformation observed at these GPS stations will help to constrain the evolution and distribution of the afterslip. We have been collaborating with our US colleagues (*e.g.*, *B. Brooks*, *M. Bevis*) who have been analysing GPS data in this margin. I have constructed a preliminary model that produces very good fit to the coseismic GPS observations (Figure 8.1). Further investigation on the postseismic crustal deformation and afterslip of the fault is ongoing. In addition to the great earthquake in the Chile margin, the M_w 9.0 Honshu earthquake occurred in Northeast Japan on March 11th, 2011 (http://earthquake.usgs.gov/earthquakes/eqinthenews/2011/usc0001xgp/). Comparison of the crustal deformation associated with these two margins may help to better understand the common subduction processes.

In addition to the stress transfer from the seismogenic zone to the updip and downdip zones during earthquakes (see Chapter 2), the earthquake-induced stresses must also transfer to the neighbouring segments of the megathrust in strike direction. Therefore, the neighbouring seismogenic zone may have a higher potential to reach frictional failure and thus nucleate earthquakes. For example, a few M_w 7 and M_w 8 earthquakes have occurred in the neighbouring segments of the 2004 M_w 9.1 Sumatra earthquake (Figure 7.1). However, the exact time sequence of these “stress-transfer triggered” earthquakes may depend on the pre-earthquake stress status of the megathrust, frictional properties of the fault, and rock rheology and is complicated. It will be still of great interests to study the distribution of the stresses induced by great earthquakes and its relationship with the subsequent earthquake occurrences.

In addition to the effect of the transient relaxation of the mantle, the viscoelastic

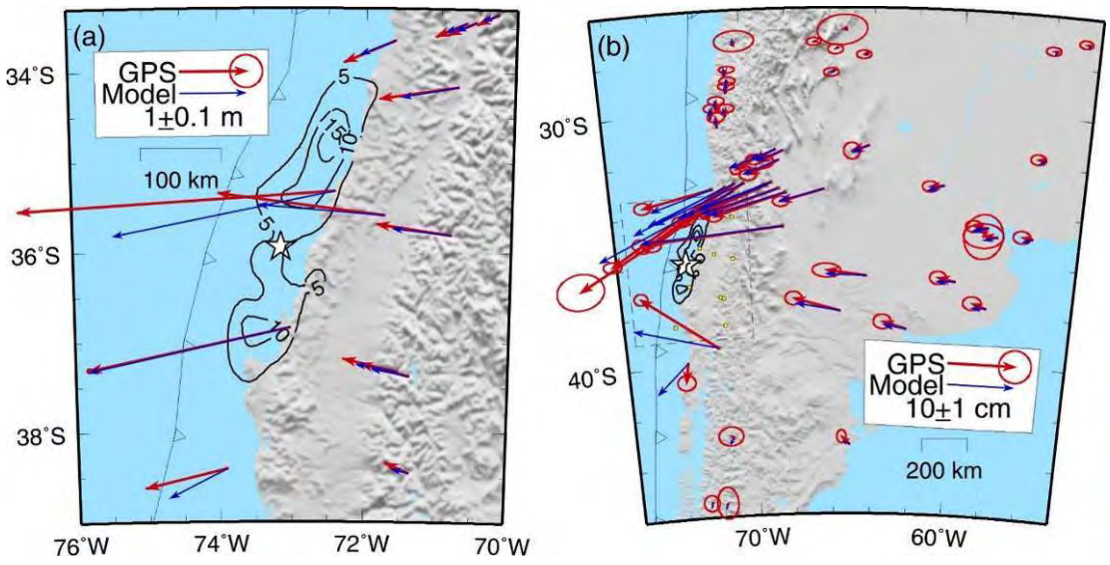

Figure 8.1. Comparison of model-produced coseismic deformation with GPS observations in the Chile margin. (a) Near-field coseismic displacements. (b) Far-field coseismic displacements. (a) is a zoom-in area in (b) highlighted by a box with dashed lines. Red and blue arrows represent model-produced and GPS (*Brooks*, 2010, personal communication) displacements, respectively. Contours of the coseismic slip of the fault are in intervals of 5 m (*Delouis et al.*, 2010). Open star is the epicentre of the 2010 Maule earthquake.

crustal deformation must also involve with other non-linear processes, such as the time-dependent stress transfer along the megathrust, the interactions between the afterslip and the overlying rock material and between the elastic upper plate and the mantle. The transient rheology is shown to be adequate to model the crustal deformation constrained by the available geodetic data (see section 7.2), and the non-linear processes thus may be secondary importance. However, physical mechanism and parameters of the transient rheology have yet to be much better constrained in laboratory experiments.

The vertical deformation is purposely not paid much attention to in this work because of the limited geodetic constraints in the vertical direction. However, some of the tests in Chapter 6 indicate that the vertical deformation is sensitive to the change in some model parameters. An ongoing project collaborating with US colleagues is to analyse new paleoseismic data to constrain the vertical deformation associated with the 1700 M_w 9

Cascadia earthquake. The new data will provide better understanding of the vertical deformation in earthquake cycles.

Future investigates on very low frequency earthquakes observed in outer wedges (*e.g.*, *Ito and Obara*, 2006) and on possible mechanisms responsible for normal faulting events observed in forearc basins (*e.g.*, *Moore et al.*,. 2007b) are summarized in sections 4.3.2 and 4.3.3, respectively.

Bibliography

Abe, K. (1973), Tsunami and mechanism of great earthquakes, *Physics of The Earth and Planetary Interiors*, *7*(2), 143-153.

Adam, J., and C. D. Reuther (2000), Crustal dynamics and active fault mechanics during subduction erosion: Application of frictional wedge analysis on to the North Chilean Forearc, *Tectonophys*, *321*, 297-325.

Altamimi, Z., P. Sillard, and C. Boucher1 (2002), ITRF2000: A new release of the International Terrestrial Reference Frame for earth science applications, *Journal of Geophysical Research*, *107*(B10), 2214, doi:10.1029/2001JB000561.

Ammon, C. J., C. Ji, H.-K. Thio, D. Robinson, S. Ni, V. Hjorleifsdottir, H. Kanamori, T. Lay, S. Das, D. Helmberger, G. Ichinose, J. Polet, and D. Wald (2005), Rupture Process of the 2004 Sumatra-Andaman Earthquake, *Science*, *308*, 1,133-1,139, doi:10.1126/science.1112260.

Ando, M. (1975), Source mechanisms and tectonic significance of historical earthquakes along the Nankai Trough, *Tectonophys*, *27*, 119-140.

Andrade, E. N. d. C. (1910), On the viscous flow in metals and allied phenomena, *Proceedings of the Royal Society of London, A 84*, 1-12.

Angermann, D., J. Klotz, and C. Reigber (1999), Space-geodetic estimation of the Nazca-South America Euler vector, *Earth and Planetary Science Letters*, 171, 329-334.

Apel, E. V., R. Bürgmann, P. Banerjee, and B. Nagarajan (2006), Geodetically constrained Indian Plate motion and implications for plate boundary deformation, *EOS, Transactions American geophysical Union*, *87*(52), T51B–1524.

Asai, Y., M. Okubo, H. Ishii, H. Aoki, T. Yamauchi, Y. Kitagawa, and N. Koizumi (2005), Co-seismic strain-steps associated with the 2004 off the Kii peninsula earthquakes–Observed with Ishii-type borehole strainmeters and quartz-tube extensometers, *Earth Planets Space*, *57*, 309–314.

Aubouin, J., J. Bourgois, and J. Azéma (1984), A new type of active margin: the convergent-extensional margin, as exemplified by the Middle America Trench off Guatemala, *Earth and Planetary Science Letters*, *67*, 211-218.

Banerjee, P., F. Pollitz, and R. Bürgmann (2005), The size and duration of the great 2004 Sumatra-Andaman earthquake from far-field static offsets, *Science*, *308*, 1,769-1,772, doi:10.1126/science.1113746.

Banerjee, P., F. Pollitz, B. Nagarajan, and R. (2007), Coseismic slip distribution of the 26 December 2004 Sumatra-Andaman and 28 March 2005 Nias earthquake from GPS static offsets, *Bulletin of the Seismological Society of American, 97*, S86-S102, doi:10.1785/0120050609.

Bangs, N. L. B., S. P. S. Gulick, and T. H. Shipley (2006), Seamount subduction erosion in the Nankai Trough and its potential impact on the seismogenic zone, *Geology*, *34*(8), 701-704, doi:10.1130/G22451.1.

Barrientos, S. E., and P. S. Acevedo-Aránguiz (1992), Seismological aspects of the 1988-1989 Lonquimay (Chile) volcanic eruption, *Journal of Volcanology and Geothermal Research*, 53, 73-87.

Barrientos, S. E., and S. N. Ward (1990), The 1960 Chile earthquake; inversion for slip distribution from surface deformation, *Geophysical Journal International*, *103*, 589-598.

Bellier, O., M. Sébrier, S. Pramumijoyo, T. Beaudouin, H. Harjono, I. Bahar, and O. Forni (1997), Paleoseismicitiy and seismic hazard along the great Sumatra fault (Indonesia), *Journal of Geodynamics*, *24*, 169-183.

Bilham, R. (2005), A flying start, then a slow slip, *Science*, *308*, 1,126-1,127, doi:10.1126/science.1113363.

Bilham, R., R. Engdahl, N. Feldl, and S. P. Satyabala (2005), Partial and Complete Rupture of the Indo-Andaman Plate Boundary 1847-2004, *Seismological Research Letters*, *76*(3), 299-311.

Bilek, S. L. (2009), Seismicity along the South American subduction zone: Review of large earthquakes, tsunamis, and subduction zone complexity, *Tectonophysics*, *495*(1-2), 2-14, doi:10.1016/j.tecto.2009.02.037.

Bilek, S. L., and T. Lay (2002), Tsunami earthquakes possibly widespread manifestations of frictional conditional stability, *Geophysical Research Letters*, *29*(14), doi:10.1029/2002GL015215.

Bird, P. (2003), An updated digital model of plate boundaries, *Geochemistry Geophysics Geosystems*, *4*(3), 1,027, doi:10.1029/2001GC000252.

Blenkinsop, T. (2000), Deformation microstructures and mechanisms in minerals and rocks, *Kluwer Academic Publishers*, Dordrecht, Netherlands, 150 pp.

Bohm, M., S. Lüth, H. Echtler, G. Asch, K. Bataille, C. Bruhn, A. Rietbrock, and P. Wigger (2002), The Southern Andes between 36°S and 40°S latitude: Seismicity and average velocities, *Tectonophysics*, *356*, 275–289.

Boschi, E., E. Casarotti, R. Devoti, D. Melini, A. Piersanti, G. Pietrantonio, and F. Riguzzi (2006), Coseismic deformation induced by the Sumatra earthquake, *Journal of Geodynamics*, *42*, 52–62, doi:10.1016/j.jog.2006.05.002.

Breen, N. A., and D. L. Orange (1992), The effects of fluid escape on accretionary wedges 1. Variable porosity and wedge convexity, *Journal of Geophysical Research*, *97*, 9,265-9,275.

Briggs, R. W., K. Sieh, A. J. Meltzner, D. Natawidjaja, J. Galetzka, B. Suwargadi, Y. -J. Hsu, M. Simons, N. Hananto, I. Suprihanto, D. Prayudi, J. -P. Avouc, L. Prawirodirdjo, and Y. Bock (2006), Deformation and slip along the Sunda megathrust in the great 2005 Nias-Simeulue earthquake, *Science*, *311*, 1897-1901.

Bruns, T. R., and R. von Huene (1986), Aleutian Trench, Shumagin segment, seismic section 104, in Seismic images of modern convergent margins tectonic structure, edited by R. von Huene, *AAPG Studies in Geology*, 26, 14-19.

Bürgmann, R., and G. Dresen (2008), Rheology of the lower crust and upper mantle: Evidence from rock mechanics, geodesy, and field observations, *Annual Review of Earth and Planetary Sciences*, *36*, 531–567, doi:10.1146/annurev.earth.36.031207.124326.

Byerlee, J. D. (1978), Friction of rocks, *Pure and Applied Geophysics*, *16*, 615-626.

Byrne, D. E., D. M. Davis, and L. R. Sykes (1988), Local and maximum size of thrust earthquakes and the mechanics of the shallow region of subduction zones, *Tectonics*, *7*, 833-857.

Cande, S. C., R. B. Leslie, J. C. Parra, and M. Hobart (1987), Interaction between the Chile ridge and Chile trench: Geophysical and geothermal evidence, *Journal of Geophysical Research*, *92*, 495-520.

Catherine, J. K., V. K. Gahalaut, and V. K. Sahu (2005), Constraints on rupture of the December 26, 2004, Sumatra earthquake from far-field GPS observations, *Earth and Planetary Science Letters*, *237*, 673–679, doi:10.1016/j.epsl.2005.07.012.

Cembrano, J., A. Lavenu, P. Reynolds, G. Arancibia, G. Lopez, and A. Sanhueza (2002), Late Cenozoic transpressional ductile deformation north of the Nazca—South America—Antarctica triple junction, *Tectonophysics*, 354, 289-314.

Cembrano, J., E. Schermer, A. Sanhueza, and A. Lavenu (2000), Along strike variations in the nature and timing of deformation along the intr-arc shear zone, the Liquine Ofqui fault zone, southern Chilean Andes, *Tectonophysics*, *319*, 129-149.

Chinn, D. S., and B. L. Isacks (1983), Accurate source depths and focal mechanisms of shallow earthquakes in western South America and in the New Hebrides island arc, *Tectonics*, *2*(6), 529-563.

Chlieh, M., J.-P. Avouac, V. Hjorleifsdottir, T.-R. A. Song, C. Ji, K. Sieh, A. Sladen, H. Hebert, L. Prawirodirdjo, Y. Bock, and J. Galetzka (2007), Coseismic slip and afterslip of the great *Mw* 9.15 Sumatra-Andaman earthquake of 2004, *Bulletin of the Seismological Society of America*, *97*(1A), S152 - S173.

Christeson, G. L., K. D. McIntosh, T. H. Shipley, E. R. Flueh, and H. Goedde (1999), Structure of the Costa Rica convergent margin, offshore Nicoya Peninsula, *Journal of Geophysical Research, 104*(B11), 25,443-25,468.

Cifuentes, I. L. (1989), The 1960 Chilean Earthquakes, *Journal of Geophysical Research*, *94*, 665-680.

Cifuentes, I. L., and P. G. Silver (1989), Low-frequency source characteristics of the great 1960 Chilean earthquake, *Journal of Geophysical Research*, *94*, 643-663.

Cisternas, M., B. F. Atwater, F. Torrejón, Y. Sawai, G. Machuca, M. Lagos, A. Eipert, C. Youlton, I. Salgado, T. Kamataki, M. Shishikura, C. P. Rajendran, J. K. Malik, Y. Rizal, and M. Husni (2005), Predecessors of the giant 1960 Chile earthquake, *Nature*, *437*, 404-407, doi:10.1038/nature03943.

Clift, P., and P. Vannucchi (2004), Controls on tectonic accretion versus erosion in subduction zones: Implications for the origin and recycling of the continental crust, *Reviews of Geophysics*, *42*, RG2001, doi:10.1029/2003RG000127.

Clift, P. D., I. Pecher, N. Kukowski, and A. Hampel (2003), Tectonic erosion of the Peruvian forearc, Lima Basin, by subduction and Nazca Ridge collision, *Tectonics*, *22*(3), doi:10.1029/2002TC001386.

Collins, B. P., and J. S. Watkins (1986), The Middle America Trench, in Seismic images of modern convergent margins tectonic structure, edited by R. von Huene, *AAPG Studies in Geology*, *26*, 30-32.

Collot, J. Y., B. Marcaillou, F. Sage, F. Michaud, W. Agudelo, P. Charvis, D. Graindorge, M. A. Gutscher, and G. Spence (2004), Are rupture zone limits of great subduction earthquakes controlled by upper plate structures? Evidence from multichannel seismic reflection data acquired across the northern Ecuador–southwest Colombia margin, *Journal of Geophysical Research*, *109*, B11103, doi:10.1029/2004JB003060.

Curray, J. R. (2005), Tectonics and history of the Andaman Sea region, *Journal of Asian Earth Sciences*, *25*, 187-232, doi:10.1016/j.jseaes.2004.09.001.

Currie, C. A., K. Wang, R. D. Hyndman, and J. He (2004), The thermal effects of steady-state slab-driven mantle flow above a subducting plate: the Cascadia subduction zone and backarc, *Earth and Planetary Science Letters*, *223*, 35– 48.

Dahlen, F. A. (1984), Noncohesive critical Coulomb wedges: An exact solution, *Journal of Geophysical Research*, *89*, 10,125-10,133.

Dahlen, F. A. (1990), Critical taper model of fold-and-thrust belts and accretionary wedges, *Annual Review of Earth and Planetary Sciences*, *18*, 55-99.

Dahlen, F. A., J. Suppe, and D. Davis (1984), Mechanics of fold-and-thrust belts and accretionary wedges: Cohesive Coulomb theory, *Journal of Geophysical Research*, *89*, 10,087-10,101.

Davey, F. J., K. Lewis, J. R. Childs, and M. A. Hampton (1986), Convergent margin off east coast of North Island, New Zealand, Parts I and II, in Seismic images of modern convergent margins tectonic structure, edited by R. von Huene, *AAPG Studies in Geology*, *26*, 49-53.

Davis, E. E., and R. D. Hyndman (1989), Accretion and recent deformation of sediments along the northern Cascadia subduction zone, *Geological Society of American Bulletin*, *101*, 1,465-1,480.

Davis, D., J. Suppe, and F. A. Dahlen (1983), Mechanics of fold-and-thrust belts and accretionary wedges, *Journal of Geophysical Research*, *88*, 1,153-1,172.

Davis, D. M., and R. von Huene (1987), Inferences on sediment strength and fault friction from structures at the Aleutian trench, *Geology*, *15*, 517-522.

Davis, E. E., K. Becker, K. Wang, and M. Kinoshita (2009), Co-seismic and post-seismic pore-fluid pressure changes in the Philippine Sea plate and Nankai decollement in response to a seismogenic strain event off Kii Peninsula, Japan, *Earth, Planets and Space*, *61*(6), 649-657.

Davis, E. E., K. Becker, K. Wang, K. Obara, and Y. Ito (2006), A discrete episode of seismic and aseismic deformation of the Nankai subduction zone accretionary prism and incoming Philippine Sea plate, *Earth and Planetary Science Letters, 242*, 73– 84.

Delouis, B., J.-M. Nocquet, and M. Vallée (2010), Slip distribution of the February 27, 2010 *Mw* = 8.8 Maule Earthquake, central Chile, from static and high-rate GPS, InSAR, and broadband teleseismic data, *Geophysical Research Letters, 37*, L17305, doi:10.1029/2010GL043899.

Delouis, B., H. Philip, L. Dorbath, and A. Cisternas (1998), Recent crustal deformation in the Antofagasta region (northern Chile) and the subduction process, *Geophysical Journal International, 132*, 302-338.

DeMets, C., R. G. Gordon, D. F. Argus, and S. Stein (1994), Effect of recent revisions to the geomagnetic reversal time scale on estimates of current plate motions, *Geophysical Research Letters, 21*(20), 2191-2194.

Dieterich, J. H. (1978), Time-dependent friction and the mechanics of stick-slip, *Pure and Applied Geophysics, 116*, 790-806.

Dieterich, J. H. (1992), Earthquake nucleation on faults with rate-dependent and state-dependent strength, *Tectonophysics, 211*, 115-134.

Dieterich, J. (1994), A constitutive law for rate of earthquake production and its application to earthquake clustering, *Journal of Geophysical Research, 99*(B2), 2,601-2,618.

Duda, S. J. (1963), Strain release in the circum-Pacific belt, Chile: 1960, *Journal of Geophysical Research, 68,* 5,531-5,544.

Dziewonski, A. M., and D. L. Anderson (1981), Preliminary reference Earth model, *Physics of the Earth and Planetary Interiors, 25*, 297- 356.

Engdahl, E. R., R. van der Hilst, and R. Buland (1998), Global teleseismic earthquake relocation with improved travel times and procedures for depth determination, *Bulletin of the Seismological Society of America, 88*(3), 722-743.

Enlow, R. L., and P. O. Koons (1998), Critical wedges in three dimensions: Analytical expressions from Mohr-Coulomb constrained perturbation analysis, *Journal of Geophysical Research, 103*(B3), 4897-4914.

Fitch, T. J. (1972), Plate convergence, transcurrent faults and internal deformation adjacent to southeast Asia and the western Pacific, *Journal of Geophysical Research,77*, 4432-4460.

Fletcher, R. C. (1989), Approximate analytical solutions for a cohesive fold-and-thrust wedge: Some results for lateral variation in wedge properties and for finite wedge angle, *Journal of Geophysical Research, 94*(B8), 10,347-10,354.

Flueh, E. R., M. A. Fisher, J. Bialas, J. R. Childs, D. Klaeschen, N. Kukowski, T. Parsons, D. W. Scholl, U. ten Brink, A. M. Trehu, and N. Vidal (1998), New seismic images of the Cascadia subduction zone from cruise SO108 - ORWELL, *Tectonophysics, 293*, 69-84.

Flück, P., R. D. Hyndman, and K. Wang (1997), Three-dimensional dislocation model for great earthquakes of the Cascadia subduction zone, *Journal of Geophysical Research, 102*, 20,539– 20,550.

Freed, A. M., R. Bürgmann, E. Calais, and J. Freymueller (2006), Stress-dependent power-law flow in the upper mantle following the 2002 Denali, Alaska, earthquake, *Earth and Planetary Science Letters*, *252*, 481-489.

Freed, A. M., T. Herring, and R. Bürgmann (2010), Steady-state laboratory flow laws alone fail to explain postseismic observations, *Earth and Planetary Science Letters, 300*, 1–10, doi:10.1016/j.epsl.2010.10.005.

Freymueller, J. T., S. C. Cohen, and H. J. Fletcher (2000), Spatial variations in present-day deformation, Kenai Peninsula, Alaska, and their implications, *Journal of Geophysical Research, 105*(B4), 8,079–8,101.

Fruehn, J., R. von Huene, and M. A. Fisher (1999), Accretion in the wake of terrane collision: The Neogene accretionary wedge off Kenai Peninsula, Alaska, *Tectonics, 18*(2), 263-277.

Fung, Y. C. (1965), Foundations of Solid Mechanics, Prentice-Hall, Englewood Cliffs, NJ, 525 pp.

Gagnon, K., C. D. Chadwell, and E. Norabuena (2005), Measuring the onset of locking in the Peru–Chile trench with GPS and acoustic measurements, *Nature, 434*, 205, doi:10.1038/nature03412.

Gahalaut, V. K., S. Jade, J. K. Catherine, R. Gireesh, M. B. Ananda, P. D. Kumar, M. Narsaiah, S. S. H. Jafri, A. Ambikapathy, A. Bansal, R. K. Chadha, D. C. Gupta, B. Nagarajan, and S. Kumar (2008), GPS measurements of postseismic deformation in the Andaman-Nicobar region following the giant 2004 Sumatra-Andaman earthquake, *Journal of Geophysical Research, 113*, B08401, doi:10.1029/2007JB005511.

Gahalaut, V. K., B. Nagarajan, J. K. Catherine, and S. Kumar (2006), Constraints on 2004 Sumatra–Andaman earthquake rupture from GPS measurements in Andaman–Nicobar Islands, *Earth and Planetary Science Letters*, *242*, 365–374, doi:10.1016/j.epsl.2005.11.051.

Geist, E. L., and S. L. Bilek (2001), Effect of depth‐dependent shear modulus on tsunami generation along subduction zones, *Geophysical Research Letters, 28*(7), 1,315-1,318, doi:10.1029/2000GL012385.

Geist, E. L., and R. Dmowska (1999), Local tsunamis and distributed slip at the source, *Pure and Applied Geophysics, 154*, 485-512.

Gerdom, M., A. M. Trehu, E. R. Flueh, and D. Klaeschen (2000), The continental margin off Oregon from seismic investigations, *Tectonophysics, 329*, 79-97.

Gladwin, M. T. (1984), High-precision multicomponent borehole deformation monitoring, *Review of Scientific Instruments, 55*(12), 2011–2016.

Goldfinger, C., C. H. Nelson, and J. E. Johnson (2003), Holocene earthquake records from the Cascadia subduction zone and northern San Andreas fault based on precise dating of offshore turbidites, *Annual Review of Earth and Planetary Sciences, 31*, 555-577, doi:10.1146/annurev.earth.31.100901.141246.

Groß, K., U. Micksch, and T. R. Group (2007), The reflection seismic survey of project TIPTEQ-the inventory of the Chilean subduction zone at 38.2°S, *Geophysical Journal International*, *172*(2), 565-571, doi:10.1111/j.1365-246x.2007.0.3680.x.

Gudmundsson, Ó., and M. Sambridge (1998), A regionalized upper mantle (RUM) seismic model, *Journal of Geophysical Research, 103*, 7,121-7,136.

Hashimoto, M., N. Choosakul, M. Hashizume, S. Takemoto, H. Hiroshi Takiguchi, Y. Fukuda, and K. Fujimori (2006), Crustal deformations associated with the great Sumatra-Andaman earthquake deduced from continuous GPS observation, *Earth Planets Space, 58*, 127–139.

Hayward, N., G. K. Westbrook, and S. Peacock (2003), Seismic velocity, anisotropy, and fluid pressure in the Barbados accretionary wedge from an offset vertical seismic profile with seabed sources, *Journal of Geophysical Research, 108*, 2515, doi:10.1029/2001JB001638.

Hippchen, S., and R. D. Hyndman (2008), Thermal and structural models of the Sumatra subduction zone: Implications for the megathrust seismogenic zone, *Journal of Geophysical Research*, *113*(B12), B12103, doi:10.1029/2008JB005698.

Hoffmann-Rothe, A., N. Kukowski, G. Dresen, H. Echtler, O. Oncken, J. Klotz, E. Scheuber, and A. Kellner (2006), Oblique convergence along the Chilean margin: Partitioning, margin-parallel faulting and force interaction at the plate interface, in *The Andes: Active subduction Orogeny*, edited by *O. Oncken, G. Chong, G. Franz, P. Giese, H.-J. Görtze, V. A. Ramos, M. R. Strecker, and P. Wigger*, *Springer-Verlag*, Berlin, 125-146, 586 pp.

Housner, G. W. (1963), An engineering report on the Chilean earthquakes of May, 1960, *Bulletin of the Seismological Society of America, 53*, 219-223.

Hsu, Y.-J., M. Simons, J.-P. Avouac, J. Galetzka, K. Sieh, M. Chlieh, D. Natawidjaja, L. Prawirodirdjo, and Y. Bock (2006), Frictional afterslip following the 2005 Nias-Simeulue earthquake, Sumatra, *Science, 312*, 1921-1926.

Hu, Y. (2004), 2-D and 3-D viscoelastic finite element models for subduction earthquake deformation, M.Sc. thesis, University of Victoria, Victoria, British Columbia, Canada.

Hu, Y., and K. Wang (2006), Bending-like behavior of wedge-shaped thin elastic fault blocks, *Journal of Geophysical Research, 111*, B06409, doi:10.1029/2005JB003987.

Hu, Y., K. Wang, J. He, J. Klotz, G. Khazaradze (2004), Three-dimensional viscoelastic finite element model for post-seismic deformation of the great 1960 Chile earthquake, *Journal of Geophysical Research, 109*, B12403, doi:10.1029/2004JB003163.

Hu, Y., and K. Wang (2008), Coseismic strengthening of the shallow portion of the subduction fault and the effects on the frontal prism taper, *Journal of Geophysical Research, 113*(B12), B12411, doi:10.1029/2008JB005724.

Hyndman, R. D., and S. M. Peacock (2003), Serpentinization of the forearc mantle, *Earth and Planetary Science Letters, 212*, 417-432, doi:10.1016/S0012-821X(03)00263-2.

Hyndman, R. D., and K. Wang (1993), Thermal constraints on the zone of major thrust earthquake failure: The Cascadia subduction zone, *Journal of Geophysical Research, 98*, 2039-2060.

Hyndman, R. D., and K. Wang (1995), Current deformation and thermal constraints on the zone of potential great earthquakes on the Cascadia subduction thrust, *Journal of Geophysical Research, 100*, 22,133–22,154.

Hyndman, R. D., K. Wang, T. Yuan, and G. D. Spence (1993), Tectonic sediment thickening, fluid expulsion, and the thermal Regime of subduction zone accretionary prisms: The Cascadia margin off Vancouver Island, *Journal of Geophysical Research, 98*(B12), 21,865-21,876.

Hyndman, R. D., M. Yamano, and D. A. Oleskevich (1997), The seismogenic zone of subduction thrust faults, *Island Arc, 6*(3), 244-260, doi:10.1111/j.1440-1738.1997.tb00175.x.

Ito, Y., and K. Obara (2006), Dynamic deformation of the accretionary prism excites very low frequency earthquakes, *Geophysical Research Letters, 33*, L02311, doi:10.1029/2005GL025270.

Jade, S., M. S. M. Vijayan, S. S. Gupta, P. D. Kumar, V. K. Gaur, and S. Arumugam (2007), Effect of the M 9.3 Sumatra–Andaman islands earthquake of 26 December 2004 at several permanent and campaign GPS stations in the Indian continent, *International Journal of Remote Sensing, 28*, 3045–3054.

James, T. S., and E. R. Ivins (1998), Predictions of Antarctic crustal motions driven by present-day ice sheet evolution and by isostatic memory of the Last Glacial Maximum, *Journal of Geophysical Research, 103*(B3), 4,993-5,017.

Jankaew, K., B. F. Atwater, Y. Sawai, M. Choowong, T. Charoentitirat, M. E. Martin, and A. Prendergast (2008), Medieval forewarning of the 2004 Indian Ocean tsunami in Thailand, *Nature, 455*, 1,228-1,231, doi:10.1038/nature07373.

Jarrard, R. D. (1986), Terrane motion by strike-slip faulting of forearc slivers, *Geology, 14*(9), 780-783.

Kanamori, H. (1972), Tectonic implications of the 1944 Tonankai and 1946 Nankaido earthquakes, *Physics of the Earth and Planetary Interiors, 5*, 129-139.

Kanamori, H. (1977), The energy release in great earthquake, *Journal of Geophysical Research, 82*, 2,981-2,987.

Kanamori, H. (1994), Mechanics of earthquakes, *Annual Review of Earth and Planetary Sciences, 22*, 207-237.

Kanamori, H., and J.J. Cipar (1974), Focal process of the great Chilean earthquake May 22, 1960, *Physics of the Earth and Planetary Interiors, 9*, 128-136.

Karato, S. (2008), Deformation of Earth materials: Introduction to the rheology of the solid Earth, *Cambridge University Press*, New York, 463 pp.

Karato, S. (2010), Rheology of the Earth's mantle: A historical review, *Gondwana Research, 18*, 17-45, doi:10.1016/j.gr.2010.03.004.

Karato, S., and P. Wu (1993), Rheology of the upper mantle: A synthesis, *Science, 260*, 771-778.

Kelsey, H. M., A. R. Nelson, E. Hemphill-Haley, and R. C. Witter (2005), Tsunami history of an Oregon coastal lake reveals a 4600 yr record of great earthquakes on the Cascadia subduction zone, *Bulletin of the Geological Society of America, 117*, 1,009-1,032, doi: 10.1130/B25452.1.

Kendrick, E., M. Bevis, R. Smalley Jr., B. Brooks, B, R. B. Vargas, E. Lauría, and L. P. S. Fortes (2003), The Nazca–South America Euler vector and its rate of change, *Journal of South American Earth Sciences, 16*, 125-131.

Khazaradze, G., K. Wang, J. Klotz, Y. Hu, and J. He, Prolonged post-seismic deformation of the 1960 great Chile earthquake and implications for mantle rheology, *Geophysical Research Letters, 29*, 7-1-7-4, 2002.

Kirby, S. H. (1983), Rheology of the lithosphere, *Reviews of Geophysics and Space Physics, 21*(6), 1,458-1,487.

Klaeschen, D., I. Belykh, H. Gnibidenko, S. Patrikeyev, and R. von Huene (1994), Structure of the Kuril Trench from seismic reflection records, *Journal of Geophysical Research, 99*, 24,173-24,188.

Klotz, J., D. Angermann, G. W. Michel, R. Porth, C. Reigber, J. Reinking, J. Viramonte, R. Perdomo, V. H. Rios, S. Barrientos, R. Barriga, and O. Cifuentes (1999), GPS-derived deformation of the Central Andes including the 1995 Antofagasta *Mw* = 8.0 earthquake, *Pure and Applied Geophysics, 154*, 3709-3730.

Klotz, J., G. Khazaradze, D. Angermann, C. Reigber, R. Perdomo, and O. Cifudentes (2001), Earthquake cycle dominates contemporary crustal deformation in Central and Southern Andes, *Earth and Planetary Science Letters, 193*, 437-446.

Kreemer, C., G. Blewitt, and F. Maerten (2006), Co- and postseismic deformation of the 28 March 2005 Nias *Mw* 8.7 earthquake from continuous GPS data, *Geophysical Research Letters, 33*, L07307, doi:10.1029/2005GL025566.

Kodaira, S., T. Iwasaki, T. Urabe, T. Kanazawa, F. Egloff, J. Makris, and H. Shimamura (1996), Crustal structure across the middle Ryukyu trench obtained from ocean bottom sesimographic data, *Tectonophysics, 263*, 39-60.

Konca, A. O., J.-P. Avouac, A. Sladen, A. J. Meltzner, K. Sieh, P. Fang, Z. Li, J. Galetzka, J. Genrich, M. Chlieh, D. H. Natawidjaja, Y. Bock, E. J. Fielding, C. Ji, and D. V. Helmberger (2008), Partial rupture of a locked patch of the Sumatra megathrust during the 2007 earthquake sequence, *Nature, 456*, 631-635, doi:10.1038/nature07572.

Kopp, C., J. Fruehn, E. R. Flueh, C. Reichert, N. Kukowski, J. Bialas, and D. Klaeschen (2000), Structure of the Makran subduction zone from wide-angle and reflection seismic data, *Tectonophysics*, *329*, 171-191.

Kopp, H., and N. Kukowski (2003), Backstop geometry and accretionary mechanics of the Sunda margin, *Tectonics*, *22*(6), 1072, doi:10.1029/2002TC001420.

Krabbenhöft, A., J. Bialas, H. Hopp, N. Kukowski, and C. Hübscher (2004), Crustal structure of the Peruvian continental margin from widge-angle seismic studies, *Geophysical Journal International*, *159*, 749-764.

Kukowski, N., and O. Oncken (2006), Subduction erosion—The "normal" mode of forearc material transfer along the Chilean margin?, in *The Andes: Active subduction orogeny*, edited by *O. Oncken, G. Chong, G. Franz, P. Giese, H.-J. Götze, V.A. Ramos, M.R. Strecker, P. Wigger*, *Springer-Verlag*, Berlin, 217–236, 568 pp.

Kukowski, N., T. Schillhorn, K. Huhn, U. von Rad, S. Husen, and E. Flueh (2001), Morphotectonics and mechanics of the central Makran accretionary wedge off Pakistan, *Marine Geology*, *173*, 1-19.

Lakki, A., R. Schaller, C. Carry, and W. Benoit (1998), High temperature anelastic and viscoelastic deformation of fine-grained MgO-doped Al_2O_3, *Acta Materialia*, *46*, 689-700.

Lallemand, S. E., P. Schnürle, and J. Malavieille (1994), Coulomb theory applied to accretionary and nonaccretionary wedges: Possible causes for tectonic erosion and/or frontal accretion, *Journal of Geophysical Research*, *99*(B6), 12,033-12,055.

Langbein, J., J. R. Murray, and H. A. Snyder (2006), Coseismic and Initial Postseismic Deformation from the 2004 Parkfield, California, Earthquake, Observed by Global Positioning System, Electronic Distance Meter, Creepmeters, and Borehole Strainmeters, *Bulletin of the Seismological Society of America*, *96*(4B), S304-S320, doi:10.1785/0120050823.

Lange, D., A. Rietbrock, C. Haberland, K. Bataille, T. Dahm, F. Tilmann, and E.R. Flueh (2007), Seismicity and geometry of the south Chilean subduction zone (41.5°S–43.5°S): Implications for controlling parameters, *Geophysical Research Letters*, *34*, L06311, doi:10.1029/2006GL029190.

Larson, K.M., J. T. Freymueller, and S. Philipsen (1997), Global plate velocities from the Global Positioning system, *Journal of Geophysical Research*, *102*(B5), 9,961-9,981.

Laursen, J., D. W. Scholl, and R. von Huene (2002), Neotectonic deformation of the central Chile margin: Deepwater forearc basin formation in response to hot spot ridge and seamount subduction, *Tectonics*, *21*(5), 2-1, doi:10.1029/2001TC901023.

Lay, T., H. Kanamori, C. J. Ammon, M. Nettles, S. N. Ward, R. C. Aster, S. L. Beck, S. L. Bilek, M. R. Brudzinski, R. Butler, H. R. Deshon, G. Ekström, K. Satake, and S. Sipkin (2005), The Great Sumatra-Andaman Earthquake of 26 December 2004, *Science*, *308*, 1,127-1,133, doi:10.1126/science.1112250.

Leonard, L. J., C. A. Currie, S. Mazzotti, and Roy D. Hyndman (2010), Rupture area and displacement of past Cascadia great earthquakes from coastal coseismic subsidence, *Geological Society of America Bulletin, 122*(11/12), 2,079–2,096, doi:10.1130/B30108.1.

Leonard, L. J., R. D. Hyndman, and S. Mazzotti (2004), Coseismic subsidence in the 1700 great Cascadia earthquake: Coastal estimates versus elastic dislocation models, *Geological Society of America Bulletin*, *116*(5/6), 655–670, doi:10.1130/B25369.1.

Liu, J. Y., and G. Ranalli (1992), Stresses in an overthrust sheet and propagation of thrusting: An Airy stress function solution, *Tectonics*, *11*, 549-559.

Liu, Y., and J. R. Rice (2007), Spontaneous and triggered aseismic deformation transients in a subduction fault model, *Journal of Geophysical Research*, *112*, B09404, doi:10.1029/2007JB004930.

López, C., G. Spence, R. Hyndman, and D. Kelley (2010), Frontal ridge slope failure at the northern Cascadia margin: Margin-normal fault and gas hydrate control, *Geology*, *38*(11), 967–970, doi:10.1130/G31136.1.

Lüth, S., P. Wigger, M. Araneda, G. Asch, K. Bataille, M. Bohm, C. Bruhn, P. Giese, J. Quezada, and A. Rietbrock (2003), A crustal model along 39°S from a seismic refraction profile-ISSA 2000, *Revista geológica de Chile*, *30*(1), 83– 94.

Luttrell, K. M., X. Tong, D. T. Sandwell, and B. A. Brooks (2010), Estimates of stress drop from the 27 February 2010 Chile earthquake and tectonic stress in the crust: Implications for fault strength, Abstract G33A-0840 presented at 2010 Fall Meeting, *American Geophysical Union*, San Francisco, California, 13-17 Dec.

Marone, C. (1998), Laboratory-derived friction laws and their application to seismic faulting, *Annual Review of Earth and Planetary Sciences*, *26*, 643-696, doi:10.1146/annurev.earth.26.1.643.

Marone, C., and D. M. Saffer (2007), Fault friction and the upper transition from seismic to aseismic faulting, in *The Seismogenic Zone of Subduction Thrust Faults*, edited by *T. H. Dixon and J. C. Moore*, *Columbia University Press*, New York, pp. 346–368.

Marone, C., C. H. Scholz, and R. Bilham (1991), On the mechanics of earthquake afterslip, Journal *of Geophysical Research*, *96*(B5), 8441-8452.

Mazzotti, S., H. Dragert, J. Henton, M. Schmidt, R. Hyndman, T. James, Y. Lu, and M. Craymer (2003), Current tectonics of northern Cascadia from a decade of GPS measurements, *Journal of Geophysical Research*, *108*(B12), 2554, doi:10.1029/2003JB002653.

Mazzotti, S., H. Dragert, R. D. Hyndman, M.M. Miller, and J.A. Henton (2002), GPS deformation in a region of high crustal seismicity: N. Cascadia forearc, *Earth and Planetary Science Letters*, *198*, 41– 48.

McCaffrey, R. (1994), Global variability in subduction thrust zone—forearc systems, *Pure and Applied Geophysics*, *142*(1), 173-224.

McCaffrey, R.(2002), Crustal block rotations and plate coupling, in *Plate boundary zones*, edited by *S. Stein* and *J. Freymueller*, *American Geophysical Union*, Washington DC, 101–122, doi:10.1029/030GD06.

McCaffrey, R. (2005), Block kinematics of the Pacific–North America plate boundary in the southwestern United States from inversion of GPS, seismological, and geologic data, *Journal of Geophysical Research*, *110*(B7), B07401, doi:10.1029/2004JB003307.

McCaffrey, R., P. C. Zwick, Y. Bock, L. Prawirodirdjo, J. F. Genrich, C. W. Stevens, S. S. O. Puntodewo, and C. Subarya (2000), Strain partitioning during oblique plate convergence in northern Sumatra: Geodetic and seismologic constraints and numerical modeling, *Journal of Geophysical Research*, *105*(B12), 28,363-28,376.

Melbourne, T. I., F. H. Webb, J. M. Stock, and C. Reigber (2002), Rapid postseismic transients in subduction zones from continuous GPS, *Journal of Geophysical Research*, *107*(B10), 2,241, doi:10.1029/2001JB000555.

Melosh, H. J. (1980), Rheology of the earth: Theory and observation, in *Physics of the Earth's Interior, Proceedings of the 1979 Enrico Fermi Summer School*, Varenna, Italy, edited by *A.M. Dziewonski and E. Boschi*, *Noord-Holland*, Amsterdam, pp. 318-336.

Melosh, H. J., and A. Raefsky (1981), A simple and efficient method for introducing faults into finite element computations, *Bulletin of the Seismological Society of America*, *71*, 1391-1400.

Melosh, H. J., and A. Raefsky (1983), Anelastic response of the Earth to a dip slip earthquake, *Journal of Geophysical Research*, *88*, 515-526.

Meltzner, A. J., K. Sieh, M. Abrams, D. C. Agnew, K. W. Hudnut, J.-P. Avouac, and D. H. Natawidjaja (2006). Uplift and subsidence associated with the great Aceh-Andaman earthquake of 2004, *Journal of Geophysical Research*, *111*, B02407, doi 10.1029/2005JB003891.

Miller, M. M., D. J. Johnson, C. M. Rubin, H. Dragert, K. Wang, A. Qamar, and C. Goldfinger (2001), GPS-determination of along-strike variation in Cascadia margin kinematics: Implications for relative plate motion, subduction zone coupling, and permanent deformation, *Tectonics*, *20*, 161– 176.

Miyashita, K. (1987), A model of plate convergence in Southwest Japan, inferred from levelling data associated with the 1946 Nankaido earthquake, *Journal of Physics of the Earth*, *35*, 449-467.

Monecke, K., W. Finger, D. Klarer, W. Kongko, B. G. Mcadoo, A. L. Moore, and S. U. Sudrajat (2008), A 1,000-year sediment record of tsunami recurrence in northern Sumatra, *Nature*, *455*, 1,232-1,234, doi:10.1038/nature07374.

Moore, G. F., N. L. Bangs, A. Taira, S. Kuramoto, E. Pangborn, and H. J. Tobin (2007a), How three-dimensional splay fault geometry fosters tsunami generation, *Science*, *318*, 1,128-1,131, doi:10.1126/science.1147195.

Moore, G. F., Y. Kido, K. T. Moe, A. Ibusuki, and S. Uraki (2007b), NanTroSEIZE Stage 1 (Part 2), Mechanical and hydrologic state of mega-splay faults: Implications for seismogenic faulting and tsunami generation, Safety Package for IODP Proposals 603B-Full2 and 603C-Rev.1.

Moore, G. F., Z. Zhao, T. H. Shipley, N. Bangs, and J. C. Moore (1995), Structural setting of the Leg 156 area, northern Barbados Ridge accretionary prism, in *Proceedings of the Ocean Drilling Program, Initial Reports, 156*, edited by *T. H. Shipley, Y. Ogawa, P. Blum, et al.*, *College Station*, TX (Ocean Drilling Program), pp. 13-27.

Moore, J. C., and D. Saffer (2001), Updip limit of the seismogenic zone beneath the accretionary prism of southwest Japan: An effect of diagenetic to low grade metamorphic processes and increasing effective stress, *Geology*, *29*, 183-186.

Moreno, M. S., J. Bolte, J. Klotz, and D. Melnick (2009), Impact of megathrust geometry on inversion of coseismic slip from geodetic data: Application to the 1960 Chile earthquake, *Geophysical Research Letters*, *36*, L16310, doi:10.1029/2009GL039276.

Motagh, M., R. Wang, T. R. Walter, R. Bürgmann, E. Fielding, J. Anderssohn, and J. Zschau (2008), Coseismic slip model of the 2007 August Pisco earthquake (Peru) as constrained by Wide Swath radar observations, *Geophysical Journal International*, *174*, 842–848, doi:10.1111/j.1365-246X.2008.03852.x.

Nelson, A. R., and W. F. Manley (1992), Holocene coseismic and aseismic uplift of Isla Mocha, South-central Chile, *Quarternary International*, *15/16*, 61-76.

Nelson, E., R. Forsythe, and I. Arit (1994), Ridge collision tectonics in terrane development, *Journal of South American Earth Sciences*, *7*, 271-278.

NewComb, K. R., and W. R. McCann (1987), Seismic history and seismotectonics of the Sunda arc, *Journal of Geophysical Research*, *92*(B1), 421-439.

Obara, K., and Y. Ito (2005), Very low frequency earthquakes excited by the 2004 off the Kii peninsula earthquakes: A dynamic process in the large accretionary prism, *Earth Planets Space*, *57*, 321-326.

Okada, Y. (1985), Surface deformation due to shear and tensile faults in a half-space, *Bulletin of the Seismological Society of America*, *75*, 1135-1154.

Okada, Y. (1992), Internal deformation due to shear and tensile faults in a half-space, *Bulletin of the Seismological Society of America*, *82*, 1,018-1,040.

Oleskevich, D., R. Hyndman, and K. Wang (1999), The updip and downdip limits to great subduction earthquakes: Thermal and structural models of Cascadia, south Alaska, SW Japan, and Chile, *Journal of Geophysical Research*, *104*(B7), 14,965-14,991.

Panet, I., F. Pollitz, V. Mikhailov, M. Diament, P. Banerjee, and K. Grijalva (2010), Upper mantle rheology from GRACE and GPS postseismic deformation after the 2004 Sumatra-Andaman earthquake, *Geochemistry Geophysics Geosystems*, *11*, Q06008, doi:10.1029/2009GC002905.

Park, J. O., T. Tsuru, S. Kodaira, P. R. Cummins, and Y. Kaneda (2002), Splay fault branching along the Nankai subduction zone, *Science*, *297*, 1,157-1,160.

Peacock, S. M., and R. D. Hyndman (1999), Hydrous minerals in the mantle wedge and the maximum depth of subduction zone earthquakes, *Geophysical Research Letters*, *26*, 2,517-2,520.

Peltier, W. R. (1974), The impulse response of a Maxwell Earth, *Reviews of Geophysics Space Physics*, *12*, 649-668.

Peltier, W. R. (2004), Global glacial isostasy and the surface of the ice-age earth: The ICE-5G (VM2) model and GRACE, *Annual review of earth and planetary sciences*, *32*, 111-149, doi:10.1146/annurev.earth.32.082503.144359.

Plafker, G. (1972), Alaskan Earthquake of 1964 and Chilean Earthquake of 1960: Implications for Arc Tectonics, *Journal of Geophysical Research*, *77*, 901-925.

Plafker, G., and J. C. Savage (1970), Mechanism of the Chilean earthquake of May 21 and 22, 1960, *Geological Society of America Bulletin*, *81*, 1001-1030.

Platt, J. P. (1993), Mechanics of oblique convergence, *Journal of Geophysical Research*, *98*, 16,239-16,256.

Pollitz, F. F. (1992), Postseismic relaxation theory on the spherical Earth, *Bulletin of the Seismological Society of America*, *82*, 422-453.

Pollitz, F. F. (1997), Gravitational-viscoelastic postseismic relaxation on a layered spherical Earth, *Journal of Geophysical Research*, *102*, 17,921-17,941.

Pollitz, F. F. (2003), Transient rheology of the uppermost mantle beneath the Mojave Desert, California, *Earth and Planetary Science Letters*, *215*, 89-104, doi:10.1016/S0012-821X(03)00432-1.

Pollitz, F. F., P. Banerjee, K. Grijalva, B. Nagarajan, and R. B. Bürgmann (2008), Effect of 3-D viscoelastic structure on post-seismic relaxation from the 2004 M= 9.2 Sumatra earthquake, *Geophysical Journal International*, *173*(1), 189-204, doi:10.1111/j.1365-246X.2007.03666.x.

Pollitz, F. F., R. Bürgmann, and P. Banerjee (2006), Post-seismic relaxation following the great 2004 Sumatra-Andaman earthquake on a compressible self-gravitating Earth, *Geophysical Journal International*, *167*, 397-420.

Pollitz, F. F., P. McCrory, D. Wilson, J. Svarc, C. Puskas, and R. B. Smith (2010), Viscoelastic-cycle model of interseismic deformation in the northwestern United States, *Geophysical Journal International*, *181*, 665-696, doi: 10.1111/j.1365-246X.2010.04546.x.

Prawirodirdjo, L., and Y. Bock (2004), Instantaneous global plate motion model from 12 years of continuous GPS observations, *Journal of Geophysical Research*, *109*, B08405, doi:10.1029/2003JB002944.

Priest, G. R., C. Goldfinger, K. Wang, R. C. Witter, Y. Zhang, and A. M. Baptista (2009), Confidence levels for tsunami-inundation limits in northern Oregon inferred from a

10,000-year history of great earthquakes at the Cascadia subduction zone, *Natural Hazards*, *54*(1), 27-73, doi:10.1007/s11069-009-9453-5.

Pritchard, M. E. and E. Fielding (2008), A study of the 2006 and 2007 earthquake sequence of Pisco, Peru, with InSAR and teleseismic data, *Geophysical Research Letters*, *35*, L09308, doi:10.1029/2008GL033374.

Rajendran, C. P., K. Rajendran, R. Anu, A. Earnest, T. Machado, P. M. Mohan, and J. Freymueller (2007), Crustal Deformation and Seismic History Associated with the 2004 Indian Ocean Earthquake: A Perspective from the Andaman–Nicobar Islands, *Bulletin of the Seismological Society of America*, *97*(1A), S174-S191, doi: 10.1785/0120050630.

Ranalli, G. (1995), Rheology of the Earth, 2nd ed., *Chapman and Hall*, London, 413 pp.

Ranalli, G., and H. H. Schloessin (1989), Role of episodic creep in global mantle deformation, in *Slow deformation and transition of stress in the Earth, Geophysical Monograph 49*, edited by *S.C. Cohen and P. Vanicek, American Geophysical Union*, Washington, D.C., pp. 55-63.

Ranero, C. R., I. Grevemeyer, H. Sahling, U. Barckhausen, C. Hensen, K. Wallmann, W. Weinrebe, P. Vannucchi, R. von Huene, and K. McIntosh (2008), Hydrogeological system of erosional convergent margins and its influence on tectonics and interplate seismogenesis, *Geochemistry Geophysics Geosystems*, *9*(3), Q03S04, doi:10.1029/2007GC001679.

Ranero, C. R., and R. von Huene (2000), Subduction erosion along the Middle America convergent margin, *Nature*, *404*, 748-755.

Ranero, C. R., R. von Huene, E. Flueh, M. Duarte, D. Baca, and K. McIntosh (2000), A cross section of the convergent Pacific margin of Nicaragua, *Tectonics*, *19*, 335-357.

Rosen, P. A., S. Henley, G. Peltzer, and M. Simons (2004), Updated Repeat Orbit Interferometry Package Released, *EOS Transactions American Geophysical Union*, *85*(5).

Rosenau, M., D. Melnick, and H. Echtler (2006), Kinematic constraints on intra-arc shear and strain partitioning in the southern Andes between 38°S and 42°S latitude, *Tectonics*, *25*, TC4013, doi:10.1029/2005TC001943.

Rudnicki, J. W., and M. Wu (1995), Mechanics of dip-slip faulting in an elastic half-space, *Journal of Geophysical Research*, *100*(11), 22,173-22,186.

Ruina, A. (1983), Slip instability and state variable friction law, *Journal of Geophysical Research*, *88*, 10,359-10,370.

Saffer, D. M., and B. A. Bekins (2002), Hydrologic controls on the morphology and mechanics of accretionary wedges, *Geology*, *30*, 271-274.

Sage, F., J.-Y. Collot, and C. R. Ranero (2006), Interplate patchiness and subduction-erosion mechanisms: Evidence from depth-migrated seismic images at the central Ecuador convergent margin, *Geology*, *34*, 997–1,000, doi:10.1130/G22790A.1.

Sagiya, T., and W. Thatcher (1999), Coseismic slip resolution along a plate boundary megathrust: The Nankai Trough, southwest Japan, *Journal of Geophysical Research, 104*, 1,111-1,129.

Sallarès, V., and C. R. Ranero (2005), Structure and tectonics of the erosional convergent margin off Antofagasta, north Chile (23°30´S), *Journal of Geophysical Research, 110*, B06101, doi:10.1029/2004JB003418.

Satake, K. (1993), Depth distribution of coseismic slip along the Nankai Trough, Japan, from joint inversion of geodetic and tsunami data, *Journal of Geophysical Research, 98*, 4,553-4,565.

Satake, K., and B. F. Atwater (2007), Long-Term Perspectives on Giant Earthquakes and Tsunamis at Subduction Zones, *Annual Review of Earth and Planetary Sciences*, *35*, 349–74, doi:10.1146/annurev.earth.35.031306.140302.

Satake, K., T. T. Aung, Y. Sawai, Y. Okamura, K. S. Wing, W. Swe, C. Swe, T. L. Swe, S. T. Tun, M. M. Soe, T. Z. Oo, and S. H. Zaw (2005), Report on post tsunami survey along the Myanmar coast for the December 2004 Sumatra-Andaman earthquake, *Annual Report on Active Fault and Paleoearthquake Researches, 5*, 161-188, in Japanese.

Satake, K., T. T. Aung, Y. Sawai, Y. Okamura, K. S. Wing, W. Swe, C. Swe, T. L. Swe, S. T. Tun, M. M. Soe, T. Z. Oo, and S. H. Zaw (2006), Tsunami heights and damage along the Myanmar coast from the December 2004 Sumatra-Andaman earthquake, *Earth Planets Space, 58*, 243–252.

Satake, K., K. Shimazaki, Y. Tsuji, and K. Ueda (1996), Time and size of a giant earthquake in Cascadia inferred from Japanese tsunami records of January 1700, *Nature, 379*, 246–249.

Satake, K., K. Wang, and B. F. Atwater (2003), Fault slip and seismic moment of the 1700 Cascadia earthquake inferred from Japanese tsunami descriptions, *Journal of Geophysical Research, 108*(B11), 2535, doi:10.1029/2003JB002521.

Savage, J. C. (1983), A dislocation model of strain accumulation and release at a subduction zone, *Journal of Geophysical Research, 88*, 4984-4996.

Savage, J. C., J. L. Svarc, and W. H. Prescott (1999), Deformation across the Alaska-Aleutian subduction zone near Kodiak, *Geophysical Research Letters, 26*, 2117-2120.

Savage, J. C., J. L. Svarc, W. H. Prescott, and M. H. Murray (2001), Deformation across the forearc of the Cascadia subduction zone at Cape Blanco, Oregon, *Journal of Geophysical Research, 105*, 3,095–3,120.

Schnürle, P., S. E. Lallemand, R. von Huene, and D. Klaeschen (1995), Tectonic regime of the southern Kurile Trench as revealed by multichannel seismic lines, *Tectonophysics, 241*, 259-277.

Scholl, D. W., J. McCarthy, and H. Ryan (1986), Forearc margin, central Aleutian Ridge, in *Seismic images of modern convergent margins tectonic structure*, edited by *R. von Huene, AAPG Studies in Geology, 26*, 10-13.

Scholz, C. H. (1998), Earthquakes and friction laws, *Nature*, *391*, 37– 42.

Scholz, C. H. (2003), The Mechanics of Earthquakes and Faulting (2nd Edition), *Cambridge University Press*, Cambridge, 471 pp.

Sella, G. F., T. H. Dixon, and A. Mao (2002), REVEL: A model for recent plate velocities from space geodesy, *Journal of Geophysical Research*, *107* (B4), doi:10.1029/2000JB000033.

Shipley, T. H., and R. T. Buffler (1986), Costa Rica continental margin: Line CR-7, in *Seismic images of modern convergent margins tectonic structure*, edited by *R. von Huene, AAPG Studies in Geology*, *26*, 33-36.

Sievers, H. A., G. Villegas, and G. Barros (1963), The seismic sea wave of 22 May 1960 along the Chilean coast, *Bulletin of the Seismological Society of America*, *53*, 1,125-1,190.

Snavely, P. D., Jr., R. von Huene, D. M. Mann, and J. Miller (1986), The central Oregon continental margin, Lines WO76-4 and WO76-5, in *Seismic images of modern convergent margins tectonic structure*, edited by *R. von Huene, AAPG Studies in Geology*, *26*, 24-29.

Spence, G. D., R. D. Hyndman, N. R. Chapman, and C. Cleary (2001), Fishing trawler nets massive 'catch' of methane hydrates, *EOS Transactions American Geophysical Union*, *82*(50), 621, 627.

Stein, S., and E. Okal (2005), Speed and size of the Sumatra earthquake, *Nature*, *434*, 581-582, doi:10.1038/434581a.

Subarya, C., M. Chlieh, L. Prawirodirdjo, J. P. Avouac, Y. Bock, K. Sieh, A. J. Meltzner, D. H. Natawidjaja, and R. McCaffrey (2006), Plate boundary deformation associated with the great Sumatra-Andaman earthquake, *Nature*, *440*, 46–51, doi:10.1038/nature04522.

Tašárová, Z. (2007), Towards understanding the lithospheric structure of the southern Chilean subduction zone (36°S–42°S) and its role in the gravity field, *Geophysical Journal International*, *170*, 995 – 1014, doi:10.1111/j.1365-246X.2007.03466.x.

Tassara, A., H.-J. Gö tze, S. Schmidt, and R. Hackney (2006), Three dimensional density model of the Nazca plate and the Andean continental margin, *Journal of Geophysical Research*, *111*, B09404, doi:10.1029/2005JB003976.

Thatcher, W. (1984), The earthquake DeformationC ycle at the Nankai Trough, Southwest Japan, *Journal of Geophysical Research*, *89*(B5), 3,087-3,101.

Thatcher, W., and J. B. Rundle (1984), A viscoelastic coupling model for the cyclic deformation due to periodically repeated earthquakes at subduction zones, *Journal of Geophysical Research*, *89*, 7631-7640.

Tonarini, S., S. Agostini, C. Doglioni, F. Innocenti, and P. Manetti (2007), Evidence for serpentinite fluid in convergent margin systems: The example of El Salvador (Central America) arc lavas, *Geochemistry Geophysics Geosystems*, *8*, Q09014, doi:10.1029/2006GC001508.

Turcotte, D. L. and G. Schubert (2002), Geodynamics, second edition, *Cambridge University Press*, Cambridge, UK, 456 pp.

Ueda, H., M. Ohtake, and H. Sato (2003), Postseismic crustal deformation following the 1993 Hokkaido Naseioki earthquake, northern Japan: Evidence for a low-viscosity zone in the uppermost mantle, *Journal of Geophysical Research*, *108*, 2151, doi:10.1029/2002JB002067.

Vanneste, L. E., and R. D. Larter (2002), Sediment subduction, subduction erosion, and strain regime in the northern South Sandwich forearc, *Journal of Geophysical Research*, *107*(B7), 2149, doi:10.1029/2001JB000396.

Vannucchi, P., S. Galeotti, P. D. Clift, C. R. Ranero, and R. von Huene (2004), Long-term subduction-erosion along the Guatemalan margin of the Middle America Trench, *Geology*, *32*(7), 617-620, doi:10.1130/G20422.1.

Vannucchi, P., R. Remitti, and G. Bettelli (2008), Geological record of fluid flow and seismogenesis along an erosive subducting plate boundary, *Nature*, *451*, 699–703, doi:10.1038/nature06486.

Vigny, C., W. J. F. Simons, S. Abu, R. Bamphenyu, C. Satirapod, N. Choosakul, C. Subarya, A. Socquet, K. Omar, H. Z. Abidin, and B. A. C. Ambrosius (2005), Insight into the 2004 Sumatra-Andaman earthquake from GPS measurements in southeast Asia, *Nature*, *436*, 201–206, doi:10.1038/nature03937.

Völker, David, I. Grevemeyer, J. He, K. Wang, and M. Heesemann (2007), Thermal regime of the Chilean Subduction Zone at 38°S and 43°S: modelling results and implications for seismicity, *Geophysical Research Abstracts*, *9*, 06274.

von Huene, R., and C. R. Ranero (2003), Subduction erosion and basal friction along the sediment-starved convergent margin off Antofagasta, Chile, *Journal of Geophysical Research*, *108*(B2), 2079, doi:10.1029/2001JB001569.

von Huene, R., and D. Klaeschen (1999), Opposing gradients of permanent strain in the aseismic zone and elastic strain across the seismogenic zone of the Kodiak shelf and slope, Alaska, *Tectonics*, *18*, 248-262.

von Huene, R, and D. W. Scholl (1991), Observations at convergent margins concerning sediment subduction, erosion, and the growth of continental crust, *Reviews of Geophysics*, *29*, 279-316.

von Huene, R., and S. Lallemand (1990), Tectonic erosion along the Japan and Peru convergent margin, *Geological Society of America Bulletin*, *102*, 704-720.

von Huene, R., C. R. Ranero, and P. Vannucchi (2004), Generic model of subduction erosion, *Geology*, *32*(10), 913-916.

von Huene, R., D. Klaeschen, B. Cropp, and J. Miller (1994), Tectonic structure across the accretionary and erosional parts of the Japan Trench margin, *Journal of Geophysical Research*, *99*(B11), 22,349-22,361.

von Huene, R., N. Nasu, and Y. Aoki (1986), The Japan Trench: Line ORI 78-4, in *Seismic images of modern convergent margins tectonic structure*, edited by *R. von Huene, AAPG Studies in Geology, 26*, 57-60.

Wada, I., and K. Wang (2009), Common depth of slab-mantle decoupling: Reconciling diversity and uniformity of subduction zones, *Geochemistry, Geophysics, Geosystems, 10*(10), Q10009, doi:10.1029/2009GC002570.

Wada, I., K. Wang, J. He, and R. D. Hyndman (2008), Weakening of the subduction interface and its effects on surface heat flow, slab dehydration, and mantle wedge serpentinization, *Journal of Geophysical Research, 113*(B4), B04402, doi:10.1029/2007JB005190.

Wahr, J., and M. Wyss (1980), Interpretation of postseismic deformation with a viscoelastic relaxation model, *Journal of Geophysical Research, 85*, 6471-6477.

Wang, K. (2007), Elastic and viscoelastic models of subduction earthquake cycles, in *The Seismogenic Zone of Subduction Thrust Faults*, edited by *T. H. Dixon and J. C. Moore, Columbia University Press*, New York.

Wang, K., and T. Dixon (2004), "Coupling" semantics and science in earthquake research (Forum article), *EOS, Transactions American geophysical Union, 85*, 180.

Wang, K., H. Dragert, H. Kao, and E. Roeloffs (2008), Characterizing an "uncharacteristic" ETS event in northern Cascadia, *Geophysical Research Letters, 35*, L15303, doi:10.1029/2008GL034415.

Wang, K., H. Dragert, and H. J. Melosh (1994), Finite element study of uplift and strain across Vancouver Island, *Canadian Journal of Earth Sciences, 31*, 1,510–1,522.

Wang, K., and J. He (1999), Mechanics of low-stress forearcs: Nankai and Cascadia, *Journal of Geophysical Research, 104*, 15,191-15,205.

Wang, K., and J. He (2008), Effects of frictional behavior and geometry of subduction fault on coseismic seafloor deformation, *Bulletin of the Seismological Society of America, 98*(2), 571-579, doi:10.1785/0120070097.

Wang, K., J. He, H. Dragert, and T.S. James (2001), Three-dimensional viscoelastic interseismic deformation model for the Cascadia subduction zone, *Earth Planet. Space, 53*, 295-306.

Wang, K., J. He, and Y. Hu (2006), A note on pore fluid pressure ratios in the Coulomb wedge theory, *Geophysical Research Letters, 33*, L19310, doi:10.1029/2006GL027233.

Wang, K., and Y. Hu (2006), Accretionary prisms in subduction earthquake cycles: The theory of dynamic Coulomb wedge, *Journal of Geophysical Research, 111*, B06410, doi:10.1029/2005JB004094.

Wang, K., Y. Hu, M. Bevis, E. Kendrick, R. Smalley Jr., R. B. Vargas, and E. Lauría (2007), Crustal motion in the zone of the 1960 Chile earthquake: Detangling earthquake-cycle deformation and forearc-sliver translation, *Geochemistry, Geophysics, and Geosystems, 8*(10), Q10010, doi:10.1029/2007GC001721.

Wang, K., Y. Hu, and J. He (2009), Wedge mechanics: Relation with subduction zone earthquakes and tsunamis, in Encyclopedia complexity and system science, *Volume x*, edited by *R. Meyers*, Springer, New York.

Wang, K., Y. Hu, R. von Huene, and N. Kukowski (2010), Interplate earthquakes as a driver of shallow subduction erosion, *Geology*, *38*(5), 431-434, doi: 10.1130/G30597.1.

Wang, K., R. E. Wells, S. Mazzotti, R. D. Hyndman, and T. Sagiya (2003), A revised dislocation model of interseismic deformation of the Cascadia subduction zone, *Journal of Geophysical Research*, *108*(B1), doi:10.1029/2001JB001227.

Wang, R., Z. Y. Ding, and Y. Q. Yin (1979), Foundations of solid mechanics, *Geological Publishing House*, China, 370 pp, in Chinese.

Wang, R., F. Lorenzo-Martín, and F. Roth (2003), Computation of deformation induced by earthquakes in a multi-layered elastic crust - FORTRAN programs EDGRN/EDCMP, *Computer and Geosciences*, *29*(2), 195-207.

Wang, R., F. Lorenzo-Martín, and F. Roth (2006), PSGRN/PSCMP - a new code for calculating co- and post-seismic deformation, geoid and gravity changes based on the viscoelastic-gravitational dislocation theory, *Computers and Geosciences*, *32*(4), 527-541, doi:10.1016/j.cageo.2005.08.006.

Wang, W. H., and D. M. Davis (1996), Sandbox model simulation of forearc evolution and noncritical wedges, *Journal of Geophysical Research*, *101*, 11,329-11,339.

Weertman, J. (1955), Theory of steady state creep based on dislocation climb, *Journal of Applied Physics*, *26*, 1,213-1,217.

Weertman, J., and J. R. Weertman (1975), High temperature creep of rock and mantle viscosity, *Annual Review of Earth and Planetary Sciences*, *3*, 293-315.

Wells, R. E., and R. W. Simpson (2001), Northward migration of the Cascadia forearc in the northwestern U. S. and implications for subduction deformation, *Earth Planets Space*, *53*, 275– 283.

Wells, R. E., C. S. Weaver, and R. J. Blakely (1998), Forearc migration in Cascadia and its neotectonic significance, *Geology*, *26*, 759-762.

Wells, R. E., R. J. Blakely, Y. Sugiyama, D. W. Scholl, and P. A. Dinterman (2003), Basin-centered asperities in great subduction zone earthquakes: A link between slip, subsidence, and subduction erosion? *Journal of Geophysical Research*, *108*(B10), doi:10.1029/2002JB002072.

Wells, R. E., and R. W. Simpson (2001), Northward migration of the Cascadia forearc in the northwestern U. S. and implications for subduction deformation, *Earth Planets Space*, *53*, 275– 283.

Willett, S., C. Beaumont, and P. Fullsack (1993), Mechanical model for the tectonics of doubly vergent compressional orogens, *Geology*, *21*, 371-374.

Wu, P. (1992), Deformation of an incompressible viscoelastic flat earth with power-law creep: A finite element approach, *Geophysical Journal International*, *108*, 35-51.

Xiao, H. B., F. A. Dahlen, and J. Suppe (1991), Mechanics of extensional wedges, *Journal of Geophysical Research*, *96*, 10,301-10,318.

Xie, X., and Z.X. Yao (1989). A generalized reflection-transmission coefficient matrix method to calculate static displacement field of a dislocation source in a stratified half space, *Chinese J. Geophys.*, *32*, 191–205.

Xu, Z. L. (1979), Elasticity (Volume I), *People's Education Publishing House*, Beijing, 396 pp, in Chinese.

Yamanaka, Y., and M. Kikuchi (2004), Asperity map along the subduction zone in northeastern Japan inferred from regional seismic data, *Journal of Geophysical Research*, *109*, B07307, doi:10.1029/2003JB002683.

Ye, S., J. Bialas, E. R. Flueh, A. Stavenhagen, R. von Huene, G. Leandro, and K. Hinz (1996), Crustal structure of the Middle American Trench off Costa Rica from wide-angle seismic data, *Tectonics*, *15*, 1,006-1,021.

Yin, A. (1993), Mechanics of wedge-shaped fault blocks, 1. An elastic solution for compressive wedges, *Journal of Geophysical Research*, *98*, 14,245-14,256.

Yin, A., and T. K. Kelty (2000), An elastic wedge model for the development of coeval normal and thrust faulting in the Mauna Loa-Kilauea rift system in Hawaii, *Journal of Geophysical Research*, *105*, 25,909-25,925.

Yu, G., S. Wesnousky, and G. Ekström (1993), Slip partitioning along major convergence plate boundaries, *Pure and Applied Geophysics*, *140*(2). 183-210.

Yuen, D. A., R. Sabadini, and E.V. Boschi (1982), On transient rheology and glacial isostasy, *Journal of Geophysical Research*, *91*, 11,420-11,438.

Zachariasen, J., K. Sieh, F. W. Taylor, and W. S. Hantoro (2000), Modern vertical deformation above the Sumatran subduction zone: Paleogeodetic insights from coral microatolls, *Bulletin of the Seismological Society of America*, *90*, 897– 913.

Zhao, W. L., D. M. Davis, F. A. Dahlen, and J. Suppe (1986), Origin of convex accretionary wedges: Evidence from Barbados, *Journal of Geophysical Research*, *91*, 10,246-10,258.

Zheng, G., R. Dmowska, and J. R. Rice (1996), Modeling earthquake cycles in the Shumagin segment, Alaska, with seismic and geodetic constraints, *Journal of Geophysical Research*, *101*, 8383-8392.

Zweck, C., J. T. Freymueller, and S. C. Cohen (2002), Three-dimensional elastic dislocation modeling of the postseismic response to the 1964 Alaska earthquake, *Journal of Geophysical Research*, *107*(B4), 2064, doi:10.1029/2001JB000409.

Appendix A. Comparison of the Stress Transfer Model in Chapter 2 With the Dislocation Model and the Crack Model

Temporal and spatial changes in friction cause stress drop and increase along the subduction fault during earthquakes. The stress changes control coseismic slip distribution along the fault, and the fault motion induces deformation on the ground surface. Depending on the purpose of research, different models can be used to model different aspects of this process. Dislocation models are widely used to model crustal deformation by kinematically prescribing coseismic slip along the fault without considering realistic stress changes. Crack models are often used to model coseismic fault slip and resultant surface deformation by prescribing a stress drop in the rupture zone independent of the initial stress and without considering how the stress drop is controlled by changes in fault friction. Our stress transfer model prescribes a change in fault friction and calculates the resultant stress change from an initial state and the consequent fault slip and surface deformation.

Here we compare these three approaches using simple models: a uniform-slip dislocation model, a uniform-stress-drop crack model, and a uniform-friction-change stress transfer model. In this comparison, we assume a linear subduction fault dipping at 15º in an elastic half-space, with the seismogenic zone extending from 30 km to 150 km from the trench (Figure A1a). Vertical and horizontal dimensions are made very large to approximate the half-space assumption. Parameters are chosen so that the thrust earthquakes simulated using the three models have the same seismic moment.

For the uniform-slip dislocation model, we use the analytical solution of *Okada* (1992) for a buried rectangular fault. The 2D results (dotted line in Figure A1d) are obtained by assuming an extremely large strike-length for the rectangular fault. Stress changes along the fault associated with the deformation are then determined from the calculated strain. The prescribed discontinuous slip along the subduction fault results in stress singularities at the updip and downdip edges of the rupture zone.

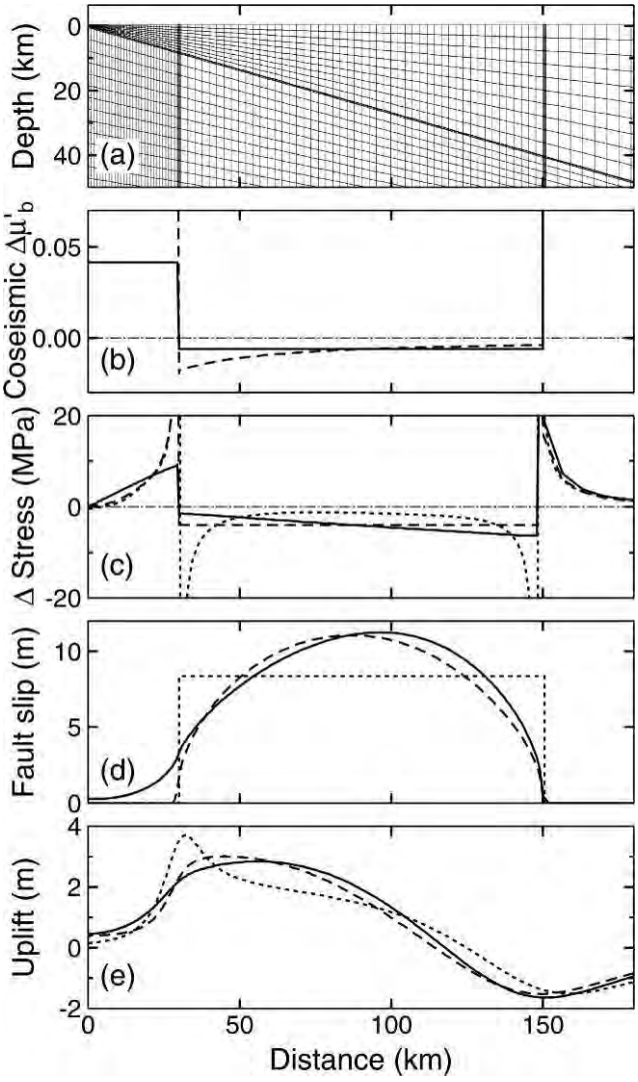

Figure A1. Comparison of a stress transfer model (solid line) with a uniform-stress-drop crack model (dashed line) and a uniform-slip dislocation model (dotted line). The earthquakes simulated using the three models have the same moment magnitude. (a) Central part of the finite element mesh for the stress transfer and crack models. The "solid line" along the subduction fault and the two vertical "solid lines" bracketing the megathrust seismogenic zone are actually groups of densely spaced small elements. (b) Coseismic $\Delta\mu_b'$ along the fault (irrelevant to the dislocation model). (c) Stress drop (or increase) along the fault. (d) Slip distribution along the fault. (e) Vertical displacement at the surface.

The crack model is readily simulated by modifying our finite element stress transfer model, although there are various more precise analytical and numerical solutions (*Rudnick and Wu*, 1995; *Geist and Dmowska*, 1999). To produce a uniform stress drop in the rupture zone, we need to device a variable $\Delta\mu_b'$ (dashed line in Figure A1b). To prevent any slip beyond the rupture zone, a situation portrayed by the most conventional crack model, we simply assign very large $\Delta\mu_b'$ values to the updip and downdip zones. In the uniform-stress-drop crack model, fault slip at the edges of the rupture zone is continuous, but the stress is singular, although the singularity is milder than in the uniform-slip dislocation model. Numerically, we have approximated the singularity behavior with a very sharp stress gradient handled using very small elements.

For the stress transfer model, a uniform $\Delta\mu_b' = -0.006$ is applied to the seismogenic zone to produce an averaged stress drop of 4 MPa, and a strengthening of $\Delta\mu_b' = 0.042$ is assigned to the updip zone. Coseismic slip can extend into the updip zone (solid line in Figure A1d). The termination of the slip updip of the seismogenic zone is more gradual than in the crack model and is not accompanied with a stress singularity. For simplicity, we have purposely made the downdip termination of the slip identical to that of the crack model. In reality, the termination should be in a gradual fashion similar to the updip termination.

The three models produce similar surface deformation patterns over the downdip edge of the rupture zone and farther away from the trench. Because the downdip edge is rather deeply buried, surface deformation is not very sensitive to the details of the slip termination. However, the manner of the slip termination around the more shallowly buried updip end of the seismogenic zone has a greater impact on surface deformation, with the most abrupt termination (the uniform-slip dislocation model) producing the largest localized uplift.

Appendix B: Comparison of the Stress Function Solution in Chapter 3 with Previously Published Elastic Wedge Solutions

Comparison with previously published solutions serves three purposes: (1) It provides a rigorous check for the new solution because a correct general solution should reduce to simpler forms for more specific conditions, (2) it demonstrates how the new solution may be applied to problems that do not have the same boundary conditions as ours, and (3) it provides a critique of previous solutions that contain errors.

A stress solution for a triangular hanging beam (Figure B1a) is available in *Xu* (1979). To apply our new solution, let $\rho_w = a = \lambda = \alpha = 0$. Therefore $k_2 = 1/\tan\theta$ and $k_4 = -2/\tan^2\theta$. Stresses in the hanging beam are then,

$$\sigma_x = \frac{\rho g (x \tan\theta - 2y)}{\tan^2\theta}$$
$$\sigma_y = -\rho g y \qquad \text{(B1)}$$
$$\tau_{xy} = -\frac{\rho g y}{\tan\theta}$$

(B1) is the solution given in *Xu* (1979). A more general solution can be obtained using (3-23) if $\alpha \neq 0$.

Another solution available in *Xu* (1979) is for a triangular dam subject to water

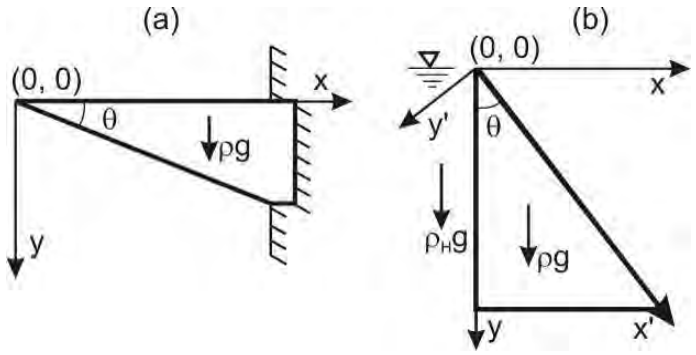

Figure B1. Geometries of two simple problems in *Xu* (1979) (from *Hu and Wang*, 2006). (a) A triangular hanging beam subject to its own weight ρg. (b) A triangular dam subject to water pressure $\rho_H g$ on its vertical side. Coordinate system (x', y') is used with solution (3-23), and system (x, y) is used in *Xu* (1979).

pressure $\rho_H gy$ on its vertical side (Figure B1b). To apply our solution, we need to set up the coordinate system (x', y') as shown in Figure B1b and let $\rho_w = \lambda = \mu_b = 0$. In this system, $\alpha = \theta - 90^o$ and $\beta = 90^o$. At the "lower" (water side) boundary, $\overline{\sigma}_n = \sigma_n = -\rho_H g x'/\cos\theta$. Comparing this with (3-16), we obtain $a = \rho_H/(\rho\sin\theta)$. Stresses in the ($x'$, y') system are then

$$\begin{aligned}
\sigma_{x'} &= -\frac{\rho_H g x'}{\tan\theta\sin\theta} + \left[\frac{\rho_H\left(3\cos^2\theta - 1\right)}{\sin^3\theta} - \frac{\rho\cos\theta}{\tan\theta}\right] g y' \\
\sigma_{y'} &= -\rho g y' \sin\theta \\
\tau_{x'y'} &= -\left[\rho\cos\theta - \frac{\rho_H}{\tan\theta\sin\theta}\right] g y'
\end{aligned} \tag{B2}$$

Writing x' and y′ in terms of x and y and rotating the coordinate system into (x, y), we obtain the solution given in *Xu* (1979):

$$\begin{aligned}
\sigma_x &= -\rho_H g y \\
\sigma_y &= \left(\frac{\rho}{\tan\theta} - \frac{2\rho_H}{\tan^3\theta}\right) g x + \left(\frac{\rho_H}{\tan^2\theta} - \rho\right) g y \\
\tau_{xy} &= -\frac{\rho_H g x}{\tan^2\theta}
\end{aligned} \tag{B3}$$

Liu and Ranalli (1992) derived a stress solution for an elastic trapezoid. Although they did not have a frictional basal boundary, their solution can be cast into a form similar to ours if the trapezoid is reduced to a wedge.

Solutions by *Yin* (1993) and *Yin and Kelty* (2000) are for a finite wedge, similar to that in Figure 1b of *Hu and Wang* (2006) but with $\phi = 90°$. If an arbitrary constant term that violates the basal friction condition is removed from the σ_x expression of *Yin* (1993), his solution should be similar to the solution with linear boundary conditions in *Yin and Kelty* (2000). Unfortunately, an error in dealing with pore fluid pressure gradient terms $\partial P_f/\partial x$ and $\partial P_f/\partial y$ occurred to both solutions when the stress equilibrium equations were written in terms of effective stresses. For the special case of zero pore fluid pressure, their solutions should have a similar form to ours since the boundary conditions can be shown to be the same as ours. Because their graphical illustrations showed results incompatible with boundary conditions, *e.g.*, basal shear and normal tractions do not agree with friction coefficients in several figures, possibly due to plotting errors, we did not proceed with a

more specific comparison.

Appendix C: Benchmarking of the new Finite Element Source Code Used in Part II

There are no three-dimensional (3-D) viscoelastic analytical solutions in the literature that incorporate transient rheology in a spherical Earth. Therefore, a direct comparison of our new finite element method (FEM) code including the transient rheology (PGCvise2) with analytical solutions is not possible. In this section, I setup simpler models by changing material physical parameters or varying model dimensions such that comparison with other simpler analytical or numerical solutions is possible.

The default material properties in the following tests include a Young's modulus E of 160 GPa, a Poisson's ratio υ of 0.25 and a rock density ρ of 3300 Kg/m^3.

C1. Comparison with simpler analytical solutions

C1.1. Rectangular fault in an elastic half space

Okada (1985, 1992) presented a complete set of analytical expressions for surface and internal displacements due to shear and/or tensile faulting in an elastic half-space for both point and finite (rectangular) sources. The analytical solution for a $W \times L$ km rectangular fault dipping 60º with an oblique slip U_0 (Figure C1a) is used to compare with finite element modelling results in this section. Surface displacements in the dip direction (Figure C2a) and in the strike direction (Figure C2b) agree well with those of the Okada solution. The poorer agreement in the vicinities of the fault edges is due to the numerical limits in modelling the singularity of slip termination.

C1.2. Viscoelastic creeping under constant uniaxial stress load

Viscosity η is defined as

$$\sigma'_{ij} = 2\eta\dot{\varepsilon}'_{ij} \tag{C1}$$

where $\sigma'_{ij} = \sigma_{ij} - \delta_{ij}\sigma_{kk}/3$ is deviatoric stress, and $\dot{\varepsilon}'_{ij} = \varepsilon_{ij} - \delta_{ij}\varepsilon_{kk}/3$ is rate of deviatoric strain. For a constant uniaxial stress load σ_0, the normal stress in the axial direction σ_{11} is σ_0, and the other two normal stresses are $\sigma_{22} = \sigma_{33} = 0$. The elastic deformation occurs upon the initial loading and is constant. For a Maxwell body (Figure 5.2a), the subsequent deformation is purely viscous and incompressible. For a Kelvin body

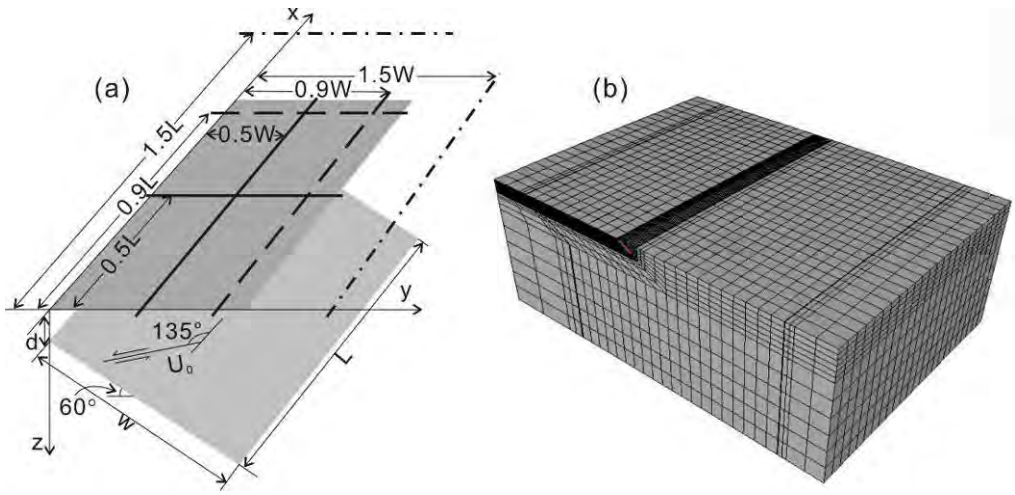

Figure C1. Comparison of PGCvise2 with the analytical solution of *Okada* (1992) for a uniform slip along a $W \times L$ km rectangular fault in an elastic half space. (a) Cartoon show of the fault dipping 60º and location of profiles on surface to be plotted in Figures C2a and C2b. (b) Central part of the finite element mesh. Location of the fault is highlighted with red color.

(Figure 5.2b), the subsequent deformation is viscoelastic, and only the deformation corresponding to the deviatoric strain is incompressible. The volumetric strain of the Kelvin body is elastic and compressible. However, if the hydrostatic (or lithostatic) component of the stress tensor is subtracted, that is, the approach of this work, the volumetric strain of the Kelvin body must be small and may be ignored. Therefore, if the rate of the axial strain ε_{11} is $\dot{\varepsilon}$, the strain rates of the other two directions can be written as $\dot{\varepsilon}_{22} = \dot{\varepsilon}_{33} = -\dot{\varepsilon}/2$ because the rate of the volumetric strain is zero. In the axial direction, we have $\sigma'_{11} = 2\eta\varepsilon'_{11} = 2\eta\varepsilon_{11}$, that is, $\sigma_0 = 3\eta\dot{\varepsilon}$. The axial strain ε_M of the Maxwell body can be written as

$$\varepsilon_M = \frac{\sigma_0}{\mu_M}\left[\frac{1}{2(1+\upsilon)} + \frac{t}{3T_M}\right] \tag{C2a}$$

where μ_M is shear modulus of the Maxwell body, υ is Poisson's ratio, and $T_M = \eta_M / \mu_M$ is Maxwell relaxation time with η_M being the viscosity of the Maxwell body. Similar to (C2a), the axial strain ε_K of the Kelvin body can be written as

$$\varepsilon_K = \frac{\sigma_0}{2\mu_K(1+\upsilon)}\left[1-\exp\left(\frac{2t(1+\upsilon)}{3T_K}\right)\right] \tag{C2b}$$

where μ_K is shear modulus of the Kelvin body, and $T_K = \eta_K / \mu_K$ is Kelvin relaxation time with η_K being the viscosity of the Kelvin body. Combining (C2a) and (C2b), we obtain the axial strain ε_B of the Burghers body (Figure C3a)

$$\varepsilon_B = \varepsilon_M + \varepsilon_K = \frac{\sigma_0}{2(1+\upsilon)}\left[\frac{1}{\mu_M}+\frac{2(1+\upsilon)t}{3T_M}+\frac{1}{\mu_K}-\exp\left(-\frac{2(1+\upsilon)t}{3T_K}\right)\right] \tag{C2c}$$

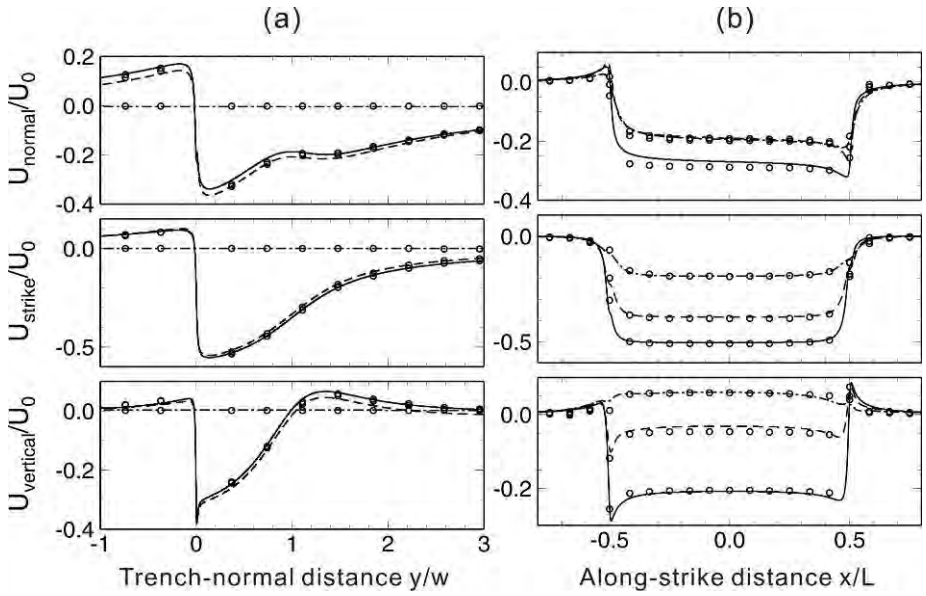

Figure C2. Surface displacements produced by PGCvise2 and the analytical solution presented by *Okada* (1985, 1992). (a) Displacements produced by *Okada* analytical solution along three trench-normal profiles (along-strike distance of 0.5L, 0.9L and 1.5L in Figure C1a), are represented by solid, dashed and dot-dashed lines, respectively. Corresponding displacements produced by PGCvise2 along those profiles are represented by open circles. The trench-normal distance is normalized by *W*. (b) Similar with (a), comparison of displacements along three along-strike profiles (trench-normal distance of 0.5W, 0.9W and 1.5W in Figure C1a). The along-strike distance is normalized by *L*.

For the comparison of the finite element code PGCvise2 with the solution (C2c), I construct a testing model. The deformation in a laterally unconstrained cube under uniform vertical stress is symmetric with respect to its vertical central axis, and thus only one quarter of the cube is modelled. Dimensions of the testing model are 10 km in the depth direction and 0.01 degrees in both the latitude and longitude directions. A uniform and constant load of 10 MPa is applied to the top surface. The bottom and the two symmetry surfaces are fixed in their normal directions and free in the other two directions. The other surfaces are free in all three directions. The Burghers body illustrated in Figure C3a can be reduced to other simpler materials, such as Maxwell, elastic and standard linear solid bodies by allowing infinite large viscosity of the Maxwell and/or the Kelvin components. Parameters that are used in the tests are listed in Table C1. The results produced by PGCvise2 agree well with the analytical solution (C1) (Figure C3).

Table C1. Viscosities of the Burghers body in the testing models M1-4. Comparison of these models is presented in Figure C3.

	η_M (Pa s)	η_K (Pa s)	Equivalent physical bodies
M1	10^{19}	10^{18}	Burghers body (μ_M, η_M; μ_K, η_K)
M2	10^{19}	∞	Maxwell body (μ_M, η_M)
M3	∞	10^{18}	standard linear solid body (μ_M; μ_K, η_K)
M4	∞	∞	elastic body (μ_M)

C2. Comparison with FEM program using Maxwell rheology in Cartesian coordinate system

In order to compare with PGCvise1 of which Maxwell rheology is assumed, an infinite large viscosity is assigned to η_K in PGCvise2. Viscosity values given in this section are thus only for the Maxwell body η_M. For models of small sizes and at very shallow depths, the curvature of the spherical Earth can be, and thus a direct comparison between these two models using the spherical and Cartesian systems is possible.

In the first part of this section, I will investigate the consistency of modelling results produced by the two programs through a model of constant surface stress load. Geometry effects between the two coordinate systems will also be elucidated afterwards. In the

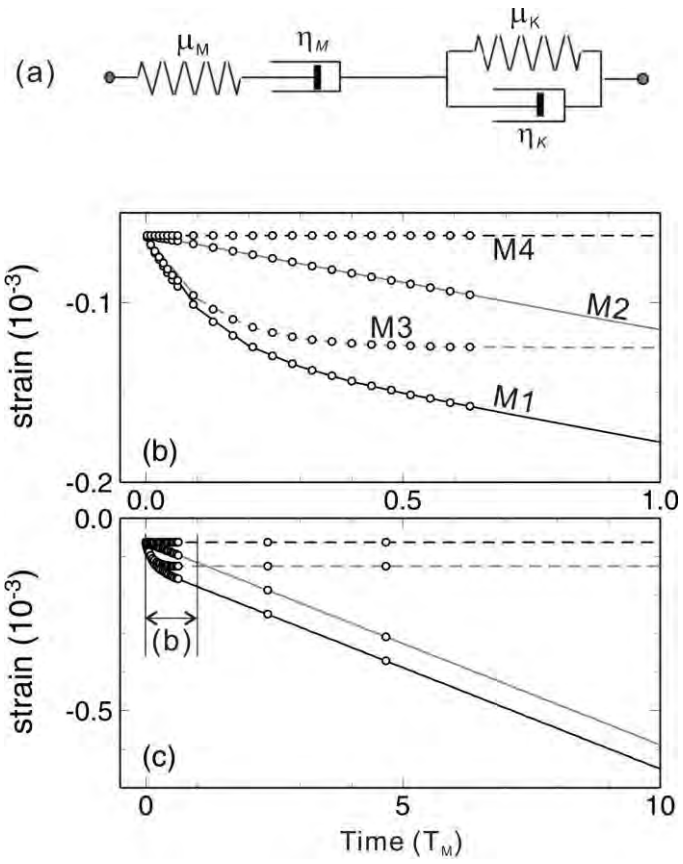

Figure C3. Comparison of PGCvise2 (open circles) with the analytical solution (lines) of uniaxial constant stress load (C2c). Viscosities for the Maxwell and Kelvin elements of the four models M1-4 are listed in Table C1. The Maxwell relaxation time T_M is ~5 years. The top panel illustrates the Burghers body (a). The lower two panels present the same results with time window spanning from 1 T_M (b) to 10 T_M (c).

second part, I will investigate the consistency through a model of uniform coseismic slip over a rectangular fault in 2-D plan-strain models reduced from 3-D models by fixing displacement in one direction.

C2. 1. Constant surface stress load

Viscosity for both PGCvise1 and PGCvise2 is 10^{19} Pa s which gives a Maxwell relaxation time T_M of ~5 yr. Similar to the model setup in section C1.2, a constant stress 10 MPa is applied to the top surface of a 10-km cube. The bottom and surrounding

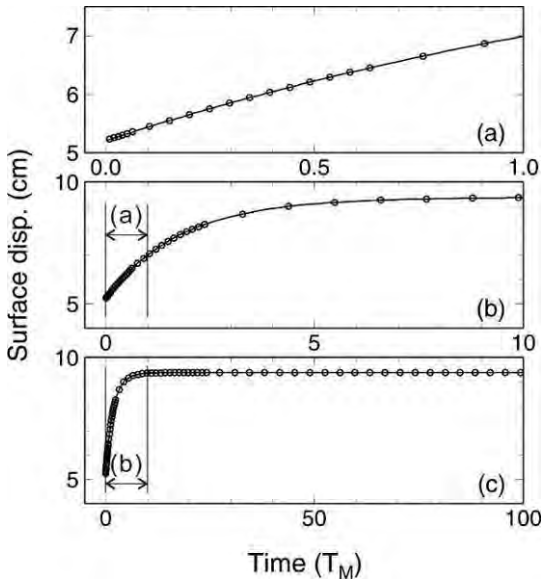

Figure C4. Surface displacement evolution produced by PGCvise2 (open circles) and PGCvise1 (solid line) for a model of constant surface stress load. The Maxwell relaxation time T_M is ~5 years. Modelling results are the same in these three panels, except that time window spans from 1 T_M (a) to 100 T_M (c).

surfaces are fixed in the direction perpendicular to the surface and free in the other two directions. The instantaneous response to the 10 MPa surface stress load is elastic. Subsequently, viscous deformation takes place (Figure C4a). When the stresses induced by the surface load are complete relaxed, the system reaches a hydrostatic state in which stresses in all the three directions are the same as the surface load, and thus viscous deformation stops (*e.g.*, time after 10 T_M in Figure C4c). Figure C4 indicates that two programs produce the same results.

For a cube of $L\times L\times L$ in a Cartesian system, the area of a cross-section perpendicular to any one of the three axes is the same. If a stress load M_0 is applied to the top surface, the internal stress in the depth direction is M_0 and does not vary with depth. A similar "cube" of $L\times L/s\times L/s$ (depth×latitude×longitude) where s transfers the length in the Cartesian system into arc length in the spherical Earth is part of a spherical shell. If the same M_0 is applied to the top surface, the internal stress increases with depth because the cross-section area is smaller at greater depths, and given the same force, the stress is

larger at greater depths. The vertical instantaneous response to M_0 (elastic deformation) is therefore larger than that of the Cartesian system because of the larger averaged vertical stress. For viscous deformation, $\eta = \frac{\sigma}{2\dot{\varepsilon}} \propto \frac{\sigma}{\Delta V / V}$ where V is the volume, ΔV is the volumetric change. For the same σ and η, ΔV in the spherical Earth is smaller than that of the Cartesian system because of its smaller V. Therefore, the displacement due to the viscous deformation is also smaller.

Model scale L is gradually increased from 1 km to 500 km to investigate the geometry effects discussed above. Normalized difference of surface displacement, defined as the difference of surface displacements produced by PGCvise2 and PGCvise1 normalized by L, scales linearly with L (Figure C5a). At short times, elastic deformation dominates, and the displacement in the spherical Earth U_s is larger than that of the Cartesian system (solid line in Figure C5a). After a long time (*e.g.*, $10T_M$), viscous deformation dominates, and U_s is smaller (dashed and dot-dashed lines in Figure C5a). Velocity V_s in the spherical Earth is smaller than that of the Cartesian system (negative values in Figure C5b). Velocity difference between these two coordinate systems increases exponentially with L at short times (*e.g.*, 0.1 T_M and 1 T_M in Figure C5b). After a long time (*e.g.* 10 T_M), stresses induced by M_0 are relaxed, and the velocity is nearly zero (dot-dashed line in Figure C5b).

C2.2. Uniform coseismic slip over a rectangular fault

Comparison with PGCvise1 is also made on a model that includes a 30 km elastic layer overlying a 1000km viscoelastic layer (Figure C6a). Rock physical properties follow the default values. One-metre uniform coseismic slip is applied over a w = 10-km wide rupture zone dipping 15°. The along-strike length is 100 km. Results are presented along the trench-normal surface line bisecting the rupture zone. Both programs produce approximately the same displacements shown in Figures C6b and C6c (along-strike component is zero and not shown). The loading area in this model, that is, unit slip over the 10-km wide fault, is very small although the model scale is made very large (10^3 km) to reduce boundary effects. At such a small loading area, the curvature of the real Earth may be ignored, and thus these two models produce the same results. The slightly-less

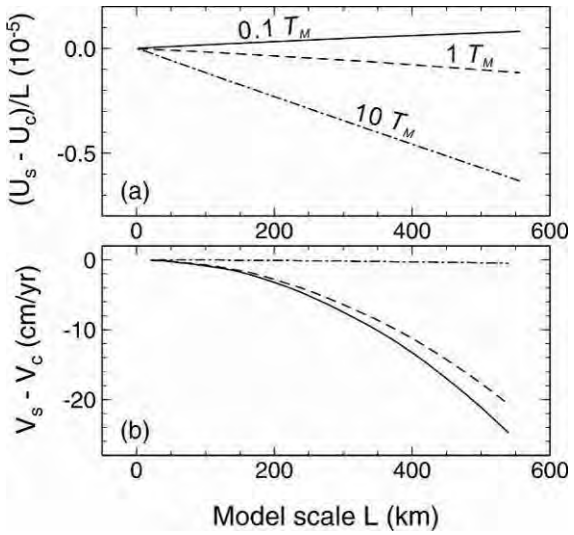

Figure C5. Comparison of PGCvise2 with PGCvise1 to investigate the geometry effects. Model scale L is the size of the cubic mesh ($L \times L \times L$). Solid, dashed and dotdashed lines denote data produced at times of 0.1 T_M, 1 T_M and 10 T_M, respectively. (a) Surface displacement difference normalized by model scale L. U_s and U_c are surface displacement produced by PGCvise2 and PGCvise1, respectively. (b) Surface velocity difference. V_s and V_c are surface velocity produced by PGCvise2 and PGCvise1, respectively.

agreement in areas further away from the fault zone may be due to the geometric effects (see section 6.2).

C3. Comparison with an analytical solution for postseismic deformation in a spherically layered Earth using transient rheology

Pollitz (1992, 1997) presented a complete set of analytical expressions for viscoelastic postseismic relaxation in a spherically-layered Earth. Comparison with Pollitz solution is made on the same model as in the previous section C2.2 except that the model in this section is developed in the real Earth, and its viscoelastic layer has the transient rheology (Figure C7a). Viscosities of the lower layer are 10^{19} Pa s and 10^{18} Pa s for the Maxwell and Kelvin components, respectively. Probably due to a viscosity

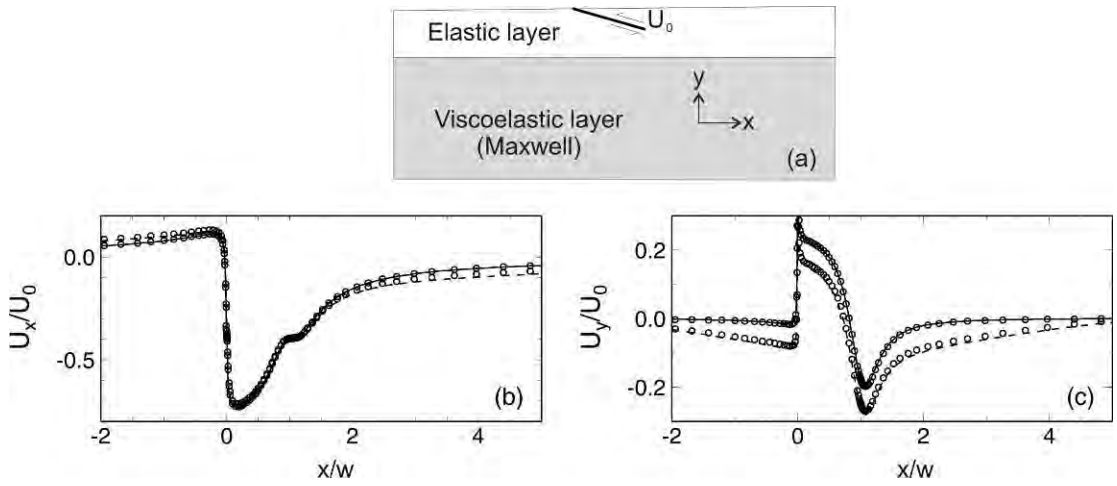

Figure C6. Comparison of PGCvise2 with FEM program using Maxwell rheology in Cartesian (lines) and spherical (circles) coordinate systems for a model of uniform coseismic slip over a rectangular fault. (a) A model includes a 30 km elastic layer, and a 1000 km viscoelastic layer. One-metre uniform coseismic slip is applied over a rectangular fault dipping 15°. Comparison of surface horizontal and vertical displacements is illustrated in (b) and (c), respectively. Displacements produced by PGCvise1 at times of 1 T_M and 10 T_M, are represented by solid and dashed lines, respectively. Open circles represent corresponding displacements produced by PGCvise2 in the spherical Earth. Along-strike component is zero and not shown. The width of the fault is w = 10 km.

definition in *Pollitz*'s solution different from (C1) and/or due to the assumption of the incompressible Kelvin rheology in this work, the viscosities of this work have to be scaled by a factor of ~1.5 to produce a good agreement with *Pollitz*'s solution. After the viscosity correction, the postseismic deformation, defined as a residual of the total deformation and the coseismic deformation, modelled by PGCvise2 agrees well with that of *Pollitz*'s solution (Figures C7b and C7c). In PGCvise2, the mesh density in vicinities of the fault edges is purposely made very high (element size is 0.2 km) to model the slip singularity in these regions, and the mesh density in areas away from the fault is low (element size is up to 400 km). In *Pollitz*'s code, the spherical harmonic degrees for all the layers are the same and may not be high enough to model the slip termination at the

fault edges. The different approaches in handling the slip singularity by these two programs may lead to the poor agreement above the downdip edge of the fault (Figure C7c).

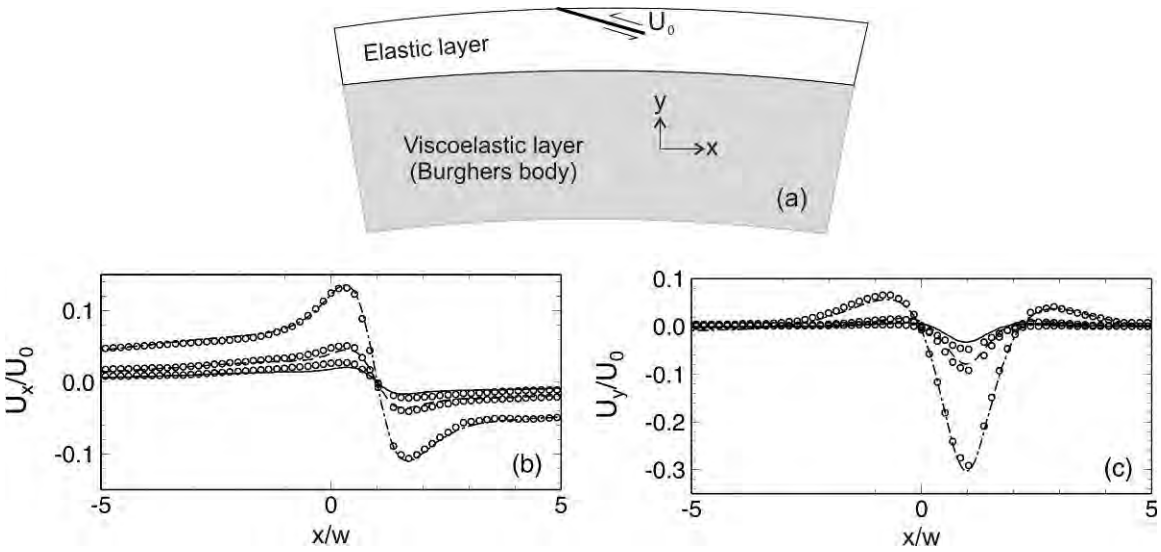

Figure C7. Comparison of PGCvise2 with the analytical solution of *Pollitz* (1992, 1997) for postseismic deformation in a spherically layered Earth using transient rheology. (a) The same model as in section C2 (Figure C6) except that of the spherical coordinate system and of the viscoelastic layer of the transient rheology. Horizontal (b) and vertical (c) postseismic displacements produced by *Pollitz*'s solution at times of 0.1 T_M, 1 T_M and 10 T_M are represented by solid, dashed and dot-dashed lines, respectively. Corresponding displacements produced by PGCvise2 are denoted by open circles. The width of the fault is w = 10 km. Viscosities of this work scaled by a factor of 1.5 are used in *Pollitz*'s solution.